UNIVERSITY OF OKLAHOMA

GRADUATE COLLEGE

THE MIDDLE SURFACE CONCEPT AND ITS APPLICATION TO CONSTITUTIVE MODELING OF SOILS

A Dissertation

Submitted to the Graduate College

In Partial Fulfillment of the Requirements for the

Degree of

Doctor of Philosophy

By

Yunming Yang

Norman, Oklahoma

2003

Downloaded from SHAREOK. Persistent Handle URL: https://hdl.handle.net/11244/647

UMI Number: 3107287

INFORMATION TO USERS

The quality of this reproduction is dependent upon the quality of the copy submitted. Broken or indistinct print, colored or poor quality illustrations and photographs, print bleed-through, substandard margins, and improper alignment can adversely affect reproduction.

In the unlikely event that the author did not send a complete manuscript and there are missing pages, these will be noted. Also, if unauthorized copyright material had to be removed, a note will indicate the deletion.

UMI®

UMI Microform 3107287

Copyright 2004 by ProQuest Information and Learning Company.

All rights reserved. This microform edition is protected against unauthorized copying under Title 17, United States Code.

ProQuest Information and Learning Company
300 North Zeeb Road
P.O. Box 1346
Ann Arbor, MI 48106-1346

© Copyright by Yunming Yang 2003
All Rights Reserved

THE MIDDLE SURFACE CONCEPT AND ITS APPLICATION TO CONSTITUTIVE MODELING OF SOILS

A Dissertation APPROVED FOR THE
SCHOOL OF CIVIL ENGINEERING AND ENVIRONMENTAL SCIENCE

BY

K. K. M 11/11/03
Kanthasamy K Muraleetharan

Younane Abousleiman

John P. Albert
John P Albert

Gerald A. Miller
Gerald A Miller

Md. Musharraf Zaman
Musharraf Zaman

DEDICATION

This dissertation is dedicated to my parents and brother

ACKNOWLEDGEMENTS

I would like to express my greatest gratitude to Dr. Muraleetharan for his valuable and inspiring academic instruction and indispensable mental support throughout my Ph.D. study. His encouragement to attempt new avenues for my research area helped me set the basis for my dissertation. His encouragement for me to try-out different research topics broadened my geotechnical engineering knowledge. He taught me how to prepare good manuscripts for publication by continuously encouraging me to pay attention to details, big and small.

I would also like to extend my gratitude to my other committee members: Dr. Miller, Dr. Zaman, Dr. Abousleiman, and Dr. Albert. I thank them for spending their valuable time in reading and commenting on my dissertation. I also appreciate their valuable advice that helped me finalize my dissertation.

Finally I want to thank all the fellow graduate students in OU geotechnical engineering group, especially Dr. Wei, for their friendship and collaboration.

The research reported in this dissertation is supported by two grants (CMS-9501718 and CMS-0112950) from the U.S. National Science Foundation, and this support is acknowledged.

TABLE OF CONTENTS

Page

Dedication iv
Acknowledgements v
Table of Contents vi
List of Tables ix
List of Figures x
Abstract xv

Chapter 1 Middle Surface Concept and Its Application to Elastoplastic Behavior of Saturated Sands 1

1.1 Introduction 1
1.2 Theory 4
1.2.1 Pseudo Yield Surfaces 6
1.2.2 True Yield Surface 8
1.3 Model Performance 14
1.4 Calibration and Validation 18
1.4.1 Determination of the Critical State Line 19
1.4.2 Model Calibration 21
1.4.3 Model Validation 23
1.5 Conclusions 26
1.6 References 28
Tables and Figures 33

Chapter 2 General Stress Space Implementation of the Middle Surface Concept (MSC) for Saturated Sands 56

2.1 Introduction 56
2.2 Theory 57
2.2.1 Pseudo Yield Surfaces 60
2.2.2 Construction of the True Yield Surface 66
2.3 Model Prediction 78
2.4 Conclusions 82
2.5 References 84
Tables and Figures 86

Chapter 3 Single Element Numerical Implementation of the MSC Sand Model for Finite Element Applications 104

3.1 Introduction 104
3.2 Numerical Implemented Formulations of the MSC Sand Model 107
3.3 Numerical Implementation of the Constitutive Relations 112
3.3.1 Global Problem 112
3.3.2 Numerical Integration 114

3.3.3 The Development of the Consistent Tangent Stiffness Matrix..... 117
3.4 Numerical Examples..... 118
3.5 Conclusions..... 122
3.6 References..... 124
Tables and Figures..... 126

Chapter 4 Solution Existence Conditions for Elastoplastic Constitutive Models of Granular Materials..... 136

4.1 Introduction..... 136
4.2 Conditions for the Solution Existence..... 137
4.3 Solution Existence Conditions for Granular Material Models..... 142
4.3.1 Granular Material Models..... 142
4.3.2 Examination of Rowe's and Roscoe's Flow Rules..... 146
4.3.3 Examination of Modified Rowe's and Roscoe's Flow Rules..... 150
4.3.4 Consideration of Elastic Anisotropy..... 155
4.4 Conclusions and Discussions..... 157
4.5 References..... 159
Tables and Figures..... 162

Chapter 5 Modeling the Stress-Strain Behavior of Unsaturated Soils Using the Middle Surface Concept..... 172

5.1 Introduction..... 172
5.2 Model Formulations..... 174
5.2.1 The Pseudo Yield Surface in $p'-q$ space..... 174
5.2.2 The Pseudo Yield Surfaces in $s-q$ space..... 176
5.2.3 The Development of the True Response..... 179
5.3 Model Calibration and Prediction..... 181
5.4 Conclusions..... 183
5.5 References..... 184
Tables and Figures..... 186

Chapter 6 Application of the MSC Based Sand Model in Dynamic Boundary Value Problems..... 190

6.1 Introduction..... 190
6.2 The Fully Coupled Finite Element Method (FEM)..... 190
6.3 Prediction for a Centrifuge Model Test..... 191
6.3.1 Model Test Specification..... 191
6.3.2 Predictions and Test Results..... 193
6.4 Conclusions..... 197
6.5 References..... 198
Figures..... 200

Appendix I: Conversion of the Model Parameters From Triaxial Space to General Stress Space..... 214

Appendix II: the Computation of $\frac{\partial \mathbf{R}}{\partial \mathbf{X}}$ 216

LIST OF TABLES

page

Table 1.1: Model Constants Model Performance, Nevada Sand, Toyoura Sand and Oklahoma #1 Sand..... 33

Table 1.2: Various Values of Model Parameters Used in the Parametric Study..... 33

Table 2.1: Model Constants for Nevada Sand..... 86

Table 2.2: Model Constants for Toyoura Sand..... 87

Table 3.1: The Convergence of Global Iteration..... 126

Table 3.2: The Convergence of Local Iterations for Drained Triaxial Simulation at the 4th step..... 127

Table 4.1: Modified Rowe's Flow Rule Parameters for Sacramento River Sand and Toyoura Sand (After Guo, 2000)..... 162

Table 4.2: The Critical Poisson's Ratios and Stress Ratios for Sacramento River Sand Under Various Conditions with Modified Rowe's Flow Rule..... 162

Table 4.3: The Critical Poisson's Ratios and Stress Ratios for Toyoura Sand Under Various Conditions with Modified Rowe's Flow Rule..... 162

Table 4.4: Modified Rowe's Flow Rule Parameters for Ottawa Sand..... 163

Table 4.5: The Critical Poisson's Ratios and Stress Ratios for Ottawa Sand Under Various Conditions with Modified Rowe's Flow Rule..... 163

Table 4.6: Modified Roscoe's Flow Rule Parameters for Nevada Sand and Toyoura Sand..... 163

Table 4.7: The Critical Poisson's Ratio and Stress Ratio for Nevada Sand Under Various Conditions with Modified Roscoe's Flow Rule..... 164

Table 4.8: The Critical Poisson's Ratio and Stress Ratio for Toyoura Sand Under Various Conditions with Modified Roscoe's Flow Rule..... 164

Table 5.1: The Model Parameters for Aeolian Silt..... 186

LIST OF FIGURES

Page

Figure 1.1: The True and Pseudo Responses During a Constant p (40 kPa) Drained Test for a Dense Sand (Initial State Parameter = -0.13)..... 34

Figure 1.2: Simulation of Conventional Triaxial Drained Compression Test (Initial State Parameter = -0.13)..... 35

Figure 1.3: The True and Pseudo Responses During a Constant p (40 kPa) Drained Test for a Loose Sand (Initial State Parameter = 0.10)..... 36

Figure 1.4: The Effects of Model Parameters on Hardening Behavior..... 37

Figure 1.5: The Effects of Model Parameters on Volumetric Evolutions..... 38

Figure 1.6: The Effects of Model Parameters on State Parameter Evolutions..... 39

Figure 1.7: Critical State Line for Nevada Sand..... 40

Figure 1.8: Comparisons of the Model Predictions and Test Results for Constant Confining Pressure Drained Tests for Nevad Sand with Dr = 40%..... 41

Figure 1.9: Comparisons of the Model Predictions and Test Results for Constant Confining Pressure Drained Tests for Nevada Sand with Dr = 60%..... 42

Figure 1.10: Comparisons of the Model Predictions and Test Results for Conventional Triaxial Undrained Compression Tests for Nevada Sand with Dr = 60%..... 43

Figure 1.11: Comparisons of the Model Predictions and Test Results for Conventional Triaxial Drained Tests for Toyoura Sand Under Lateral Stress of 100 kPa..... 44

Figure 1.12: Comparisons of the Model Predictions and Test Results for Conventional Triaxial Drained Tests for Toyoura Sand Under Lateral Stress of 500 kPa..... 45

Figure 1.13: Comparisons of the Model Predictions and Test Results for Conventional Triaxial Undrained Tests for Toyoura Sand with a Void Ratio of 0.735 and Varying Initial Confining Pressures..... 46

Figure 1.14: Comparisons of the Model Predictions and Test Results for Conventional Triaxial Undrained Tests for Toyoura Sand with

a Void Ratio of 0.833 and Varying Initial Confining Pressures..... 47

Figure 1.15: Comparisons of the Model Predictions and Test Results for Conventional Triaxial Undrained Tests for Toyoura Sand with a Void Ratio of 0.907 and Varying Confining Pressures..... 48

Figure 1.16: Comparison of the Model Predictions and Test Results for Conventional Triaxial Drained Tests for Oklahoma #1 Sand Under Varying Initial Confining Pressures..... 49

Figure 1.17: Comparison of the Model Predictions and Test Results for Conventional Triaxial Undrained Tests for Oklahoma #1 Sand Under Initial Confining Pressure of 300 psi (2.1 MPa)..... 50

Figure 1.18: Comparison of the Model Predictions and Test Results for Conventional Triaxial Undrained Tests for Oklahoma #1 Sand Under Initial Confining Pressure of 1000 psi (6.9 MPa)..... 51

Figure 1.19: Comparison of the Model Predictions and Test Results for Conventional Triaxial Undrained Tests for Oklahoma #1 Sand Under Initial Confining Pressure of 2100 psi (14.5 MPa)..... 52

Figure 1.20: Comparison of the Model Predictions and Test Results for Conventional Triaxial Undrained Tests for Oklahoma #1 Sand Under Initial Confining Pressure of 3200 psi (22.1 MPa)..... 53

Figure 1.21: Comparison of the Model Predictions and Test Results for Conventional Triaxial Undrained Tests for Oklahoma #1 Sand Under Initial Confining Pressure of 4200 psi (29 MPa)..... 54

Figure 1.22: Comparison of the Model Predictions and Test Results for Conventional Triaxial Undrained Tests for Oklahoma #1 Sand Under Initial Confining Pressure of 5950 psi (41 MPa)..... 55

Figure 2.1: Bounding and Dilatancy Surfaces for the First pseudo Yield Surface..... 88

Figure 2.2: The Role of the Second Pseudo Yield Surface..... 89

Figure 2.3: Undrained Cyclic Triaxial Test Results for Nevada Sand with a Relative Density of 60% (Initial Confining Stress = 80 kPa)..... 91

Figure 2.4: Undrained Cyclic Triaxial Test Predictions for Nevada Sand with a Relative Density of 60% (Initial Confining Stress = 80 kPa)..... 92

Figure 2.5: Undrained Cyclic Triaxial Test Results for Nevada Sand with a Relative Density of 40% (Initial Confining Stress = 80 kPa)..... 93

Figure 2.6: Undrained Cyclic Triaxial Test Predictions for Nevada Sand with a Relative Density of 40% (Initial Confining Stress = 80 kPa)..... 94

Figure 2.7: Undrained Cyclic Triaxial Test Predictions for Nevada Sand with a Relative Density of 60% Using the First Pseudo Yield Surface..... 95

Figure 2.8: Undrained Cyclic Triaxial Test Predictions for Nevada Sand with a Relative Density of 60% Using the Modified First Pseudo Yield Surface..... 96

Figure 2.9: Undrained Cyclic Simple Shear Test Results for Nevada Sand with a Relative Density of 60% (Initial Axial Stress = 80 kPa)..... 97

Figure 2.10: Undrained Cyclic Simple Shear Test Predictions for Nevada Sand with a Relative Density of 60% (Initial Axial Stress = 80 kPa)..... 98

Figure 2.11: Undrained Cyclic Simple Shear Test Results for Nevada Sand with a Relative Density of 40% (Initial Axial Stress = 80 kPa)..... 99

Figure 2.12: Undrained Cyclic Simple Shear Test Predictions for Nevada Sand with a Relative Density of 40% (Initial Axial Stress = 80 kPa)..... 100

Figure 2.13: Undrained Cyclic Triaxial Test Results and Predictions for Toyoura Sand with a Relative Density of 50% (Initial Confining Stress = 200 kPa)..... 101

Figure 2.14: Undrained Cyclic Triaxial Test Results and Predictions for Toyoura Sand with a Relative Density of 50% (Initial Confining Stress = 400 kPa)..... 102

Figure 2.15: Undrained Cyclic Triaxial Test results and Predictions for Toyoura Sand with a Relative Density of 30% (Initial Confining Stress = 400 kPa)..... 103

Figure 3.1: The Simulation for Conventional Drained Triaxial Loading..... 128

Figure 3.2: The Simulation for Conventional Undrained Triaxial Loading..... 129

Figure 3.3: The Simulation for Drained Simple Shear Loading..... 130

Figure 3.4: The Simulation for Undrained Simple Shear Loading..... 131

Figure 3.5: The Integration Error for Conventional Drained Triaxial Loading..... 132

Figure 3.6: The Integration Error for Conventional Undrained Triaxial Loading..... 133

Figure 3.7: The Integration Error for Drained Simple Shear Loading..... 134

Figure 3.8: The Integration Error for Undrained Simple Shear Loading..... 135

Figure 4.1: $\widetilde{B}^* - q/p$ and the Conditions for Solution Existence..... 165

Figure 4.2: $y - x(\nu)$ and the Conditions for Solution Existence..... 166

Figure 4.3: The Critical Poisson's Ratio and Stress Ratio for
Rowe's and Modified Rowe's Flow Rule..... 167

Figure 4.4: The Evolution of $\widetilde{B}^*$ with the Poisson's Ratio..... 168

Figure 4.5: The Critical Poisson's Ratio and Stress Ratio for
Roscoe's and Modified Roscoe's Flow Rule ($A = 1$)..... 169

Figure 4.6: The Effects of Fabric Anisotropy on Volumetric Changes..... 170

Figure 4.7: The Effects of Anisotropic Elasticity on the
Critical Poisson's Ratio and Stress Ratio..... 171

Figure 5.1: Shear Strength Due to Suction..... 186

Figure 5.2: The Predictions and Test Results of Constant Suction Shearing..... 187

Figure 5.3: Simulation of Suction Decrease for Loose Silt..... 188

Figure 5.4: Simulation of Suction Decrease for Dense Silt..... 189

Figure 6.1: The Configuration and Instrumentation of Centrifuge Model..... 200

Figure 6.2: Base Motion of Acceleration for the Centrifuge Model..... 201

Figure 6.3: Elements, Nodes and Boundary Conditions in FEM..... 202

Figure 6.4: The Measured and Predicted P.W.P. at the Bottom Level
in the Centrifuge Model..... 203

Figure 6.5: The Measured and Predicted P.W.P. at the Middle Level
in the Centrifuge Model..... 204

Figure 6.6: The Measured and Predicted P.W.P. at the Top Level
in the Centrifuge Model..... 205

Figure 6.7: Pore Water Pressure Contour at 5th Second..... 206

Figure 6.8: Pore Water Pressure Contour at 7.5th Second..... 207

Figure 6.9: Pore Water Pressure Contour at 10th Second..... 208

Figure 6.10: The Measured and Predicted Acc. at the Top Level
For Loose Sand in the Centrifuge Model..... 209

Figure 6.11: The Measured and Predicted Acc. at the Top Level
For Dense Sand in the Centrifuge Model..... 210

Figure 6.12: The Measured and Predicted Lateral Displacement
in the Centrifuge Model..... 211

Figure 6.13: The Measured and Predicted Settlement in the Centrifuge Model..... 213

ABSTRACT

The modeling of stress-strain behavior of geomaterials, such as soils, is key to the accurate analyses of complicated geotechnical engineering structures. Traditional elastoplastic modeling concepts, characterized by a single yield surface, however, limit our ability to model complex stress-strain responses. In this dissertation, a novel modeling concept called the Middle Surface Concept (MSC), is developed using multiple pseudo yield surfaces. The MSC is first developed to model saturated sand behavior under monotonic triaxial loading conditions and then extended to the general stress space. Single element model predictions are compared to laboratory tests results for three different types of sands subjected to various loading conditions and reasonable comparisons are obtained. In order to implement the general stress space MSC sand model into a finite element method, the consistent tangent stiffness matrix is developed and the model is numerically integrated using the generalized trapezoidal rule. Some useful restrictions in terms of Poisson's ratio for various flow rules used in constitutive models for granular materials are also developed. The MSC sand model is implemented into a fully coupled computer code, DYSAC2, and predictions are made for a centrifuge model subjected to base shaking. Reasonable comparisons between DYSAC2 predictions and centrifuge model test results are obtained validating the performance of the MSC sand model in boundary value problems. Finally, the MSC is expanded to model unsaturated sand or silt behavior under triaxial monotonic loading conditions. Two pseudo yield surfaces are utilized to model the effects of suction on the stress-strain behavior of unsaturated sands and silts.

Chapter 1

Middle Surface Concept and Its Application to Elastoplastic Behavior of Saturated Sands

1.1 Introduction

Although it has been well known that the behavior of sands varies with both density and confining pressure, most of the currently available constitutive models do not properly take the effects of density and confining pressure into consideration. Most of the currently available constitutive models treat a sand with different densities as different materials with different set of model constants (Lade, 1977; Vermeer, 1978; Poorooshasb and Pietruszczak, 1986; Wang et al., 1990; Crouch and Wolf, 1994). This type of approach raises questions regarding appropriateness of model constants during loading paths that cause volume and therefore density change. A unified way to take into account the density and confining pressure, first introduced by Wroth and Bassett (1965) and generalized and validated by Been and Jefferies (1985), opened up a new avenue to incorporate the effects of density and confining pressure into constitutive modeling of sands. In the above mentioned works an attempt was made to represent the sand behavior by using the difference in void ratio between the current void ratio and the void ratio at the critical state under the current confining pressure. This difference in void ratio was named the "state parameter" by Been and Jefferies (1985). Been and Jefferies' (1985) experimental results and subsequent applications of this concept by others validated this postulate (Been et al., 1986, 1987; Carriglio et al., 1990; Collins et al., 1992; Yu, 1994,

1996). The explicit incorporation of the state parameter concept into constitutive models can be seen in Bardet (1986), Jefferies (1993), and Wood et al. (1994) and more recently in Manzari and Dafalias (1997), Yu (1998), Gajo and Wood (1999a, 1999b), and Li and Dafalias (2000). Although the state parameter concept presented an attractive way to incorporate the effect of density and confining pressure in a unified way, the explicit incorporation of the state parameter concept into a constitutive model presented number of implementation difficulties. For instance, Bardet (1986) used the state parameter only within his dilatancy rule. Jefferies (1993) and Wood et al. (1994) limited their models only to the cases with constant confining pressure loading paths rendering the model not useful for practical applications. Manzari and Dafalias (1997) presented a comprehensive model that incorporated the state parameter and avoided number of problems encountered by previous models; however, they still had to resort to special techniques and restrictions to handle loading along a constant stress ratio path under certain conditions. For example, Manzari and Dafalias (1997) had to add special restrictions to avoid predicting initial dilation of looser than critical samples under certain loading conditions. In Yu's state parameter model, an extended Cam Clay model is used to represent the behavior of sand (Yu, 1998). Furthermore, this model requires the definition of a normal consolidation line for sand. It is difficult to define a unique normal consolidation line for sands and the Cam Clay model is not well suited to model the behavior of sands, especially for cyclic loading paths. In Gajo and Wood's model (1999a, 1999b), locating the so-called "image" stress is a difficult task. Moreover, in their model, at the end of loading, there is no guarantee that the void ratio will reach the value at the critical state. Another problem with Gajo and Wood's (1999a, 1999b) model is that their yield surface is curved in the

stress ratio (q/p) effective mean normal stress (p) plot. Although the actual yield surface for sands maybe somewhat curved, the specific functional form in the Gajo and Wood's (1999a, 1999b) model may not be justifiable. The above described models encountered difficulties in incorporating the state parameter because of two reasons. If the state parameter is used as a hardening parameter, the confining pressure involved in the definition of the state parameter is difficult to handle through hardening in the classical elastoplasticity theory. This is the reason that Jefferies (1993) and Wood et al. (1994) only considered constant confining pressure loading paths. Secondly, if the state parameter is included in the plastic modulus, it is difficult to render the response to end at the critical state. It should be noted that the above mentioned problems with the inclusion of the state parameter into constitutive models within the critical state soil mechanics framework has nothing to do with the state parameter concept or the critical state concept. The problems are related to the modeling techniques used in these models.

In order to easily incorporate the state parameter concept into a constitutive model for sands within the framework of critical state soil mechanics, an original modeling technique is presented in this chapter. The concept presented is straightforward and avoids the above mentioned problems encountered by the previous models. The model constants are also easy to calibrate. In the first part of the development, the model is developed for monotonic loading conditions within the triaxial stress space. Yang and Muraleetharan (2002, 2003) also presented the triaxial stress space development of this model for saturated sands.

1.2 Theory

As stated above, the proposed constitutive model uses the critical state and the state parameter concepts for sands. Although there is a lot of debate about the critical state for sands (Been and Jefferies, 1985; Poulos, 1981), in this chapter, it is assumed that a unique critical state line exists for sands both in terms of stress ratio and void ratio. The state parameter is defined as the difference in void ratio between the current void ratio and the void ratio at the critical state under the current confining pressure.

Since it is difficult to incorporate the state parameter into the model and make the response reach the critical state at the end of loading with one yield surface, the task is divided between three yield surfaces. Among these three yield surfaces, only one yield surface represents the true response of a material and the other two yield surfaces are used to assist the true yield surface to incorporate the state parameter and bring the response path to the critical state at the end of loading. These three yield surfaces are not completely independent. They all start from the same initial state and are linked through some common quantities and conditions. The true yield surface is a combination of the other two yield surfaces. This is the central concept of the proposed model. The two yield surfaces other than the true yield surface are named "pseudo yield surfaces". The one serving to assist the true response to reach the critical state is called the "first pseudo yield surface" and the other one assisting the true yield surface to include the effects of the state parameter on the hardening response is called the "second pseudo yield surface". The responses represented by these two pseudo yield surfaces are named "pseudo responses". The true yield surface lies between these two pseudo yield surfaces and hence

this concept is named the "*Middle Surface Concept (MSC)*". It is worth noting that all these three yield surfaces have their own stress and strain states during any point in a loading path. Only the stress and strain states for the true yield surface represent the true response of a material. These three yield surfaces also have all the features defined in the classical plasticity theory. That is, they all have their own hardening rules and flow rules and all satisfy the consistency condition. The main difference from the classical plasticity theory is that these yield surfaces are linked by selected common quantities and conditions.

Although similar concepts have been used in the past to obtain the true response as a combination of several different responses (for example, Kabilamany and Ishihara, 1990; Desai, 1974; Park and Desai, 2000), what is unique about MSC is the careful selection of hardening and flow rules and common quantities between the three yield surfaces to separate the modeling demands caused by number of unique concepts such as the state parameter and the critical state into manageable subtasks. The motivations for the above mentioned works and the MSC are also quite different. For example, Kabilamany and Ishihara (1990) were interested in splitting the response between various physical mechanisms such as a consolidation mechanism and three shear mechanisms. The Disturbed State Concept (DSC) used by Desai and his coworkers (Desai, 1974; Park and Desai, 2000) is motivated by the concept of damage and describes the true behavior as a combination of behavior of two states, intact and ultimate (or fully adjusted) states. Elastoplastic concepts are only applied to the intact state. On the other hand, MSC is motivated by the need to have flexibility in modeling number of unique concepts and uses the elastoplasticity theory consistently, and provides a framework to incorporate

more than two pseudo responses, if necessary. Furthermore, Kabilamany and Ishihara (1990) and Park and Desai (2000) models use parameters that depend on density of a sand, and they suffer from difficulties described previously.

1.2.1 Pseudo Yield Surfaces

The first pseudo yield surface that makes the stress ratio reach the critical state at the end of loading, takes the following form:

$$f_1 = q_1 / p_1 - \alpha_1 = 0 \tag{1.1}$$

$$\alpha_1 = M \frac{\varepsilon_{q1}^p}{a + \varepsilon_{q1}^p} \tag{1.2}$$

where, α_1 and ε_{q1}^p, respectively, are the hardening parameter and plastic deviatoric strain for the first pseudo yield surface; M is the critical stress ratio; a is a model constant; and p_1 and q_1, respectively, represent the first pseudo effective isotropic and deviatoric stresses in the triaxial stress space. The shape of the yield surface for sands represented with equation (1.1) is linear in p-q plot, which has been validated by Tatsuoka and Ishihara (1974) and widely accepted as a simplified yield function for sands (Wood et al., 1994; Manzari and Dafalias, 1999; Li and Dafalias, 2000). This type of yield function cannot, however, predict the plastic deformation under constant stress ratio loading paths. Given the fact that relatively small plastic deformation occurs for sands during constant stress ratio loading, the yield function given by equation (1.1) is a reasonable simple approximation. If needed, a cap can be easily added to the yield surface similar to Vermeer (1978) and Wang et al. (1990).

The hardening parameter represented by equation (1.2) takes the form of Vermeer (1978) that guarantees that the stress ratio will approach the critical state value M when the deviatoric plastic strain is large. The plastic modulus for the first pseudo yield surface can be obtained using the classical plasticity theory as follows:

$$K_{p1} = M \frac{a}{(a + \varepsilon_{q1}^{p})^2} \tag{1.3}$$

where, for convenience, the deviatoric part of the plastic strain increment direction is set to unity here and in derivation of other plastic moduli presented later.

The second pseudo yield surface takes the following form and incorporates the state parameter:

$$f_2 = q_2 / p_2 - \alpha_2 = 0 \tag{1.4}$$

$$K_{p2} = M \exp(-k_1 \psi_2) \frac{a}{(\varepsilon_{q2}^{p} + a)^2} \tag{1.5}$$

where, ψ_2 is the state parameter for the second pseudo yield surface, which is defined together with ψ_1 for the first pseudo yield surface and ψ for the true yield surface as:

$$\psi_i = e_i - e_{cri} = e_i - (e_{ref} - \lambda \ln(p_i / p_{ref})) \qquad (i = true, 1, 2) \tag{1.6}$$

In equation (1.4), α_2 is the hardening parameter for the second pseudo yield surface, and p_2 and q_2, respectively, represent the second pseudo isotropic and deviatoric stresses in the triaxial stress space. In equation (1.5) k_1 is a strength hardening parameter related to the state parameter and ε_{q2}^{p} is the plastic deviatoric strain for the second pseudo yield surface. Parameter a is the same parameter as used for the first pseudo yield surface. From equation (1.5), one can see that the plastic modulus for the second pseudo yield surface differs from that of the first one because of the inclusion of the state parameter

ψ_2. For example, loose sands with positive state parameter values will have a lower plastic modulus for the second pseudo yield surface compared to that for the first pseudo yield surface. Thus, the definition of the plastic modulus for the second pseudo yield surface takes into account the effects of the state parameter on the stress-strain response. In order to avoid the direct inclusion of the state parameter in the hardening rule, the definition of the second pseudo yield surface starts with the plastic modulus rather than the hardening parameter α_2. The hardening parameter α_2 is not known until the flow rule is defined as described later. In equation (1.6), e_i and e_{cri} are the current void ratio and void ratio at the critical state under the current effective confining pressure for these three yield surfaces. Once the reference pressure, p_{ref}, is fixed the quantities e_{ref} and λ are model constants related to the critical state line on the e-ln p plot. Other equations can also be used to represent the critical state line on the e-ln p plot, for example, see Li and Wang (1998).

1.2.2 True Yield Surface

Based on the pseudo yield surfaces the true yield surface can be defined. Before formulating the true yield surface, it is necessary to establish the links between the true yield surface and the pseudo yield surfaces. It is proposed that these three yield surfaces have the same confining pressure and plastic deviatoric strain at any point during loading, which in turn implies that increments in confining pressure and plastic deviatoric strain are also same throughout the loading, i.e., $p = p_1 = p_2$, $\varepsilon_q^p = \varepsilon_{q1}^p = \varepsilon_{q2}^p$ and $dp = dp_1 = dp_2$, $d\varepsilon_q^p = d\varepsilon_{q1}^p = d\varepsilon_{q2}^p$. The proposition that the confining pressure and

plastic deviatoric strain are the same for all three yield surfaces produces the additional four equations necessary to solve the system of equations. However, the choice of these quantities and not the others produces a simplified and physically more meaningful model. The definition of the same plastic deviatoric strain between the pseudo yield surfaces leads to the fact that the plastic moduli of these two yield surfaces differ only by the state parameter of the second yield surface (see eqs. (1.3) and (1.5)). This fits the original objective of delegating the task of including the effects of the state parameter to the second pseudo yield surface. The definition of the same confining pressure between the three yield surfaces simplifies the implementation of the model, especially for the general stress space. In addition, these three yield surfaces will have a common initial state and links between their hardening parameter and state parameter relationships. The link between the hardening parameters will be used to define the plastic modulus for the true yield surface and the link between the state parameters will be used to define the flow rule for the true yield surface. The link between the hardening parameters is presented first. The true yield surface's hardening parameter is defined as:

$$\alpha = \frac{\varepsilon_q^p}{b+\varepsilon_q^p}\alpha_1 + \frac{b}{b+\varepsilon_q^p}\alpha_2 \tag{1.7}$$

The true yield surface is defined as:

$$f = q/p - \alpha = 0 \tag{1.8}$$

In equation (1.7), b is a model constant determining, based on the value of the plastic deviatoric strain, how much the hardening parameter for the true yield surface depends on the hardening parameter for the first pseudo yield surface or the second pseudo yield surface. The larger the deviatoric plastic strain, the closer the true stress response to the

first pseudo response, and the stress ratio approaches the critical state (eqs. (1.1) and (1.2)). The plastic modulus for the true yield surface can be obtained using equations (1.7), (1.3) and (1.5) as described below.

Differentiating both sides of equation (1.7), one can obtain:

$$d\alpha = \alpha_1 \frac{b}{(b+\varepsilon_q^p)^2} d\varepsilon_q^p + \frac{\varepsilon_q^p}{b+\varepsilon_q^p} d\alpha_1 - \alpha_2 \frac{b}{(b+\varepsilon_q^p)^2} d\varepsilon_q^p + \frac{b}{b+\varepsilon_q^p} d\alpha_2 \tag{1.9}$$

Consistency condition gives:

$$\frac{\partial f}{\partial \sigma} d\sigma + \frac{\partial f}{\partial \alpha} d\alpha = 0 \tag{1.10}$$

Setting the deviatoric part of the plastic strain increment direction to unity, the deviatoric plastic strain increment is:

$$d\varepsilon_q^p = \frac{1}{K_p} \frac{\partial f}{\partial \sigma} d\sigma \tag{1.11}$$

From equations (1.8), (1.10) and (1.11), the following relationship can be obtained:

$$d\alpha = K_p d\varepsilon_q^p \tag{1.12}$$

Similarly for the pseudo yield surfaces:

$$d\alpha_1 = K_{p1} d\varepsilon_q^p \tag{1.13}$$

$$d\alpha_2 = K_{p2} d\varepsilon_q^p \tag{1.14}$$

Substituting equations (1.12), (1.13) and (1.14) into equation (1.9), the plastic modulus for the true yield surface can be obtained as:

$$K_p = \frac{b}{(b+\varepsilon_q^p)^2} \alpha_1 + \frac{\varepsilon_q^p}{b+\varepsilon_q^p} K_{p1} - \frac{b}{(b+\varepsilon_q^p)^2} \alpha_2 + \frac{b}{b+\varepsilon_q^p} K_{p2} \tag{1.15}$$

If one substitutes equations (1.2), (1.3) and (1.5) into equation (1.15), K_p can be also written as:

$$K_p = M\frac{b}{(b+\varepsilon_q^p)^2}\frac{\varepsilon_q^p}{a+\varepsilon_q^p} + M\frac{\varepsilon_q^p}{b+\varepsilon_q^p}\frac{a}{(a+\varepsilon_q^p)^2} - \frac{b}{(b+\varepsilon_q^p)^2}\alpha_2 + (M-k_1\psi_2)\frac{b}{b+\varepsilon_q^p}\frac{a}{(a+\varepsilon_q^p)^2} \tag{1.16}$$

The derivation of the flow rules is presented next. The flow rules for the pseudo yield surfaces will be defined first. The flow rules must be able to bring the void ratio for the true response to the critical state and incorporate the effects of the state parameter (for example, Li et al., 1999). Guided by these requirements the flow rules for the pseudo yield surfaces are defined as:

$$D_1 = \frac{d\varepsilon_{p1}^p}{d\varepsilon_q^p} = A(M + k_2\psi_1 - q_1/p) \tag{1.17}$$

$$D_2 = \frac{d\varepsilon_{p2}^p}{d\varepsilon_q^p} = A(M + k_2\psi_2 - q_2/p) \tag{1.18}$$

where, A and k_2 are the model constants for the description of dilatancy, ψ_1 and ψ_2 are the state parameters corresponding to the pseudo yield surfaces, and ε_{pi}^p $(i = 1, 2)$ are plastic volumetric strains. Throughout this chapter and this thesis, volumetric contraction is taken positive and volumetric expansion is taken negative. The inclusion of state parameter into the flow rule was first introduced by Manzari and Dafalias (1997) and was further validated by Li et al. (1999) and Li and Dafalias (2000). The approach to incorporate the confining pressure and void ratio, in a different way, into the flow rule can be seen in Faruque et al. (1992). For loose sands under larger confining pressures having larger positive state parameter values, equations (1.17) and (1.18) give larger

positive dilatancy ratios indicating larger volumetric contraction. In contrast, for dense sands under smaller confining pressures having larger negative state parameter values, the above two equations give larger negative dilatancy ratios indicating larger volumetric expansion. Thus, the effects of confining pressure and density for sands are incorporated in the above defined flow rules. In addition, the definition of the flow rule for the first pseudo yield surface (eq. (1.17)) guarantees that its state parameter will approach zero as its stress ratio approaches the critical state at the end of loading and therefore ensures its void ratio will reach the critical state.

The determination of the flow rule for the true yield surface is pursued through establishing the relationship between the state parameters of the three yield surfaces. Similar to equation (1.7), the link between the state parameter for the true yield surface and those for the pseudo yield surfaces is defined as:

$$\psi = \frac{\varepsilon_q^p}{c + \varepsilon_q^p}\psi_1 + \frac{c}{c + \varepsilon_q^p}\psi_2 \tag{1.19}$$

where, c is a model constant defining how much the true state parameter depends on the state parameter for the first or second pseudo yield surface. In equation (1.19), during the later stages of loading, for larger ε_q^p, the true state parameter ψ approaches the first pseudo ψ_1 and therefore the critical state (eq. (1.17)). In order to obtain the flow rule for the true yield surface, differentiating both sides of equation (1.19) gives:

$$d\psi = \frac{\varepsilon_q^p}{c + \varepsilon_q^p}d\psi_1 + \frac{c\psi_1}{(c + \varepsilon_q^p)^2}d\varepsilon_q^p + \frac{c}{c + \varepsilon_q^p}d\psi_2 - \frac{c\psi_2}{(c + \varepsilon_q^p)^2}d\varepsilon_q^p \tag{1.20}$$

Substituting the differential form of the state parameter expressions in equation (1.6) and the relationship $de = -(1 + e_0)d\varepsilon_p$ into equation (1.20), one can obtain:

$$d\varepsilon_p = \frac{\varepsilon_q^p}{c+\varepsilon_q^p} d\varepsilon_{p1} - \frac{1}{(1+e_0)} \frac{c}{(c+\varepsilon_q^p)^2} \psi_1 d\varepsilon_q^p + \frac{c}{c+\varepsilon_q^p} d\varepsilon_{p2} + \frac{1}{(1+e_0)} \frac{c}{(c+\varepsilon_q^p)^2} \psi_2 d\varepsilon_q^p \tag{1.21}$$

The fact that these three yield surfaces have a common confining pressure is used in deriving equation (1.21). The volumetric strain increments in equation (1.21) are composed of elastic and plastic parts and elastic volumetric strain increments depend on the confining pressure and its increment. Confining pressure and its increment are same for all the yield surfaces and therefore the elastic parts of volumetric strain increments in equation (1.21) will vanish. As a result, equation (1.21) can be expressed as:

$$d\varepsilon_p^p = \frac{\varepsilon_q^p}{c+\varepsilon_q^p} d\varepsilon_{p1}^p - \frac{1}{(1+e_0)} \frac{c}{(c+\varepsilon_q^p)^2} \psi_1 d\varepsilon_q^p + \frac{c}{c+\varepsilon_q^p} d\varepsilon_{p2}^p + \frac{1}{(1+e_0)} \frac{c}{(c+\varepsilon_q^p)^2} \psi_2 d\varepsilon_q^p \tag{1.22}$$

Dividing both sides of equation (1.22) with the common plastic deviatoric strain increment and using the flow rules for the pseudo yield surfaces in equations (1.17) and (1.18), one can obtain the flow rule for the true yield surface as:

$$D = \frac{d\varepsilon_p^p}{d\varepsilon_q^p} = \frac{\varepsilon_q^p}{c+\varepsilon_q^p} D_1 + \frac{1}{1+e_0} \frac{c}{(c+\varepsilon_q^p)^2} (\psi_2 - \psi_1) + \frac{c}{c+\varepsilon_q^p} D_2 \tag{1.23}$$

The formulation presented above implies that plastic deformation occurs from the beginning of loading and this is a reasonable assumption for sands. In order to calculate the elastoplastic behavior, the elastic behavior is defined as follows (Manzari and Dafalias, 1997):

$$d\varepsilon_p^e = dp / K_e \tag{1.24}$$

$$d\varepsilon_{qi}^e = dq_i / (3G_e) \qquad (i = true, 1, 2) \tag{1.25}$$

where, $d\varepsilon_p^e$ and $d\varepsilon_{qi}^e$ represent isotropic and deviatoric parts of elastic strain increments, K_e and G_e represent elastic bulk and shear modulus, respectively. These moduli are defined as:

$$K_e = K_0(p/p_{at})^n \tag{1.26}$$

$$G_e = G_0(p/p_{at})^n \tag{1.27}$$

where, K_0, G_0 and n are model's elastic constants, p_{at} is the atmospheric pressure used as the reference pressure.

In summary, the plastic moduli of the three yield surfaces are given by equations (1.3), (1.5) and (1.15); flow rules are represented by equations (1.17), (1.18) and (1.23); and hardening rules are given by equations (1.12)-(1.14). The elastic behavior is represented with equations (1.24)-(1.27). Within the framework of the classical elastoplasticity theory and two common quantities (confining pressure and plastic deviatoric strain) between the three yield surfaces, the stress-strain relationship for the three yield surfaces can be obtained.

1.3 Model Performance

The performance of the model is investigated under variety of conditions using the model constants given in Table 1.1. First, a dense sand with a negative initial state parameter under a constant confining pressure loading is considered. The initial void ratio and the confining pressure used are 0.66 and 40 kPa, respectively. The corresponding value of the initial state parameter is –0.13. Model simulations under a constant confining pressure (40 kPa) and drained loading conditions are shown in Figure 1.1. In Figure 1.1, the first pseudo deviatoric stress-strain response is always below the critical state value

and reaches the critical state value at the end of loading. On the other hand, the second pseudo deviatoric stress-strain response ends up above the critical state at the end of loading and has a stiffer initial response compared with the first one due to the effect of the negative initial state parameter value. The combination of the two pseudo responses makes the true response reach the critical state value along with the first pseudo response. As far as the volumetric response is concerned, the first pseudo void ratio reaches the critical state at the end of loading through dilation. This can be seen from the zero state parameter value at the end of the loading for the first pseudo response. The second pseudo response has a larger dilation than the first one and ends up with a positive state parameter value at the end of the loading. The true response is closer to the second pseudo response during the early stages of loading. With increasing axial strain, the true response moves away from the second pseudo response and approaches the first pseudo response and finally reaches the critical state as intended during the development of the model.

In order to demonstrate the model's capabilities under varying confining pressures, simulation of a conventional triaxial drained compression test was carried out and the results are shown in Figure 1.2. In this simulation the axial strain is increased while keeping the radial stress constant at 40 kPa. This results in confining pressure changing during the loading. The initial void ratio and the state parameter values are again 0.66 and –0.13, respectively. From Figure 1.2, it can be seen that the model performs equally well under varying confining pressure conditions.

Simulations for a constant confining pressure loading with a positive initial state parameter value representing a loose sand are shown in Figure 1.3. The initial void ratio

and the confining pressure are taken as 0.89 and 40 kPa, respectively. The corresponding value of the initial state parameter is 0.1. Model constants given in Table 1.1 are again used. As shown in Figure 1.3, the second pseudo deviatoric stress-strain response for e = 0.89 lies below the first pseudo response. However, for e = 0.66 the second pseudo response lies above the first pseudo response (Figure 1.1). Since the first pseudo response is not controlled by the state parameter, this response is the same for both e = 0.89 and 0.66. By comparing Figures 1.1 and 1.3 one can also see the differences in the volumetric responses and evolution of state parameters between negative and positive initial state parameter values. The volumetric response with positive initial state parameter reaches the critical state through contraction. In contrast, the volumetric response with negative initial state parameter reaches the critical state through dilation. The simulations presented in Figures 1.1-1.3 demonstrate the model's capability under variety of loading and initial conditions.

It is worth noting that this model works equally well under more complicated loading paths as well as above mentioned loading paths. It has been known that excessive volumetric dilation and softening may occur, which brings the soil to an unstable state, in certain state parameter models for sands under some particular loading paths (Manzari and Dafalias, 1997). Therefore, special numerical techniques have to be used to deal with such problems. However, in this model, the true stress ratio always lies between the two pseudo stress ratios (eq. (1.7)), and the two pseudo stress ratios can serve the purpose of bounding the softening to a limited degree. In addition, the true volumetric change is mainly dependent on the first pseudo's when the plastic deviatoric strain is relatively

large (eq. (1.23)). The first pseudo yield surface won't develop excessive volumetric dilation as the first pseudo stress ratio is always lower than the critical state stress ratio.

The parameters required to describe the stress-strain behavior using this model are a, b, k_1 for hardening, and A, c, k_2 for dilatancy, the elastic parameters K_0, G_0, n, and the critical state parameters λ, M and e_{ref}. The roles of the parameters specific to the proposed model (a, b, k_1, A, c, k_2) will be described below. The model constants are given in Table 1.1 unless specified. The initial void ratio and the confining pressure used in the parametric study are 0.66 and 40 kPa, respectively. The corresponding value of the initial state parameter is –0.13. The confining pressure is held constant at 40 kPa throughout the loading for all the simulations in the parametric study. Various values of model parameters a, b, k_1, A, c, k_2 used in the parametric study are listed in Table 1.2. The roles of a, b, k_1 on the hardening response are shown in Figure 1.4. In Figure 1.4, the stiffness and strength can be reduced by increasing the value of a and decreasing the values of k_1 and b. However, these three model constants control the stress-strain behavior in different ways. Model constant a influences both the first and the second pseudo responses. Model constant k_1 influences the true response through its effect on the second pseudo response. Constant b influences the true response by specifying how fast the true response moves from the second pseudo response to the first pseudo response. The smaller the value of b the quicker the true response will reach that of the first pseudo response. The constant a has a greater influence than k_1 and b in changing the stiffness and strength. The parameters a, b, k_1 have little effect on the volumetric response.

The effects of parameters A, c, k_2 on the volumetric response are shown in Figures 1.5 and 1.6. These parameters have little influence on the deviatoric stress-strain response. Figure 1.5 shows that larger values of A and k_2 cause larger dilation for dense sands with negative initial state parameter values. The parameter k_2 influences the behavior through the state parameter. The value of k_2 also determines the position of the phase transformation lines. Increasing the value of A not only increases dilation but also increases the initial contraction when the stress state is below the phase transformation line. However, increasing the value of k_2 will lower the phase transformation line and leads to smaller contraction and larger dilation. Similar to the role of the hardening parameter b, parameter c determines how fast the volumetric response reaches the critical state. Evolution of the state parameter values corresponding to the volumetric responses in Figure 1.5 are shown in Figure 1.6. It can be seen from Figure 1.6 that larger values of A and k_2 and a smaller value of c make the state parameter reach zero at a faster rate.

1.4 Calibration and Validation

In this section, the determination of the critical state line will be first described followed by the calibration of the parameters specific to this model (a, b, k_1, A, c, k_2) and comparisons between simulations and experimental data. Laboratory tests conducted on Nevada sand (Arulmoli et al., 1992), Toyoura sand (Verdugo and Ishihara, 1996) and Oklahoma #1 sand (Kmeid, 2003) are used for calibration and predictions.

Nevada sand (D_{50} = 0.15 mm) has a maximum dry density of 17.33 kN/m^3, a minimum dry density of 13.87 kN/m^3, and a specific gravity of 2.67. Monotonic triaxial tests with different densities and confining pressures under drained and undrained loading conditions are available (Arulmoli et al., 1992). Drained tests were carried out under constant confining pressures. The tests were mainly performed on samples with relative densities (Dr) of 40% and 60% under confining pressures of 40, 80 and 160 kPa. The void ratios corresponding to Dr = 40% and Dr = 60% are 0.740 and 0.660, respectively. The Toyoura sand has a maximum void ratio of 0.977, a minimum void ratio of 0.597, and a specific gravity of 2.65. A series of conventional drained triaxial tests were carried out with different void ratios ranging from 0.810 to 0.996 under constant lateral stresses of 100 kPa and 500 kPa (Verdugo and Ishihara, 1996). Triaxial undrained tests were carried out with void ratios ranging from 0.735 to 0.907 under different initial confining pressures varying from 0.1 MPa to 3 MPa. The drained and undrained conventional triaxial compression tests on Oklahoma # 1 sand under relatively high initial effective confining pressures ranging from 300 psi (2 Mpa) to 5950 psi (41 Mpa) were performed by Kmeid (2003). Experimental results showed that sands in this range of large confining pressures were susceptible to grain crushing during shearing. In contrast to the broad range of confining pressures in the tests, the range of porosities is narrow, from 0.37 to 0.44.

1.4.1 Determination of the Critical State Line

Since the state parameter is defined based on the critical state line the determination of the critical state line is an important task. There is a lot of debate about

the critical state line for sands. Some argue that there is no unique critical state line for sands (Konrad, 1990; Riemer and Seed, 1997). Some argue that there is a unique critical state line (Poulos, 1981). Others even proposed that the critical state exists only for the stress ratio and not in the confining pressure-void ratio space (Vaid et al., 1990; Mooney et al., 1998). These controversies mainly resulted from the complexity of sand behavior and testing difficulties. Measuring critical state for sands is a difficult task due to the problems such as localization. The uniqueness of the critical state for sands is, however, assumed in the development of the proposed model.

Critical state lines for Nevada sand for stress ratio and in the confining pressure-void ratio space are shown in Figure 1.7. The critical state line for Nevada sand for stress ratio has a slope (M) of 1.3. It has been observed by various researchers that the critical state line in the confining pressure and void ratio space is curved. The slope of the critical state line increases with the confining pressure and there is usually a break point from which the slope of the critical state line in the confining pressure and void ratio space increases sharply (Been et al., 1991; Yamamuro and Lade, 1997; Li and Wang, 1998). In this chapter, the critical state line in the confining pressure and void ratio space for Nevada sand is assumed to be bilinear (for example, Been et al., 1991). The first part is a flat line with the critical state void ratio of 0.78 for confining pressures smaller than 160 kPa. This part is determined from drained tests for different initial void ratios and confining pressures. The second part is represented by line with a slope of 0.04 for confining pressures larger than 160 kPa. This portion is determined from the undrained tests. The initial state parameters values of –0.043 and –0.12, respectively, can be

obtained for Dr = 40% and Dr = 60% from the critical state line shown in Figure 1.7(a) for confining pressures less than 160 kPa.

The critical state line for Toyoura sand can be represented by

$$e_{cr} = e_{ref} - \lambda(p / p_{at})^{\xi} \tag{1.28}$$

where e_{ref}, λ and ξ are material constants and p_{at} is the atmospheric pressure, used for normalization (Li and Dafalias, 2000). These parameters together with the critical stress ratio slope M are obtained from drained test results for Toyoura sand and are shown in Table 1.1.

The slope of the critical state line in $p-q$ space for Oklahoma #1 sand is obtained by averaging the stress ratios of four drained tests at the end of loading. Its critical state line in $ln\, p-e$ space is represented with a straight line, and the corresponding parameters e_{ref} and λ are obtained by using two drained test results at the end of loading. These parameters are listed in Table 1.1. It should be noted that the slope λ (0.178) for the critical state line in $ln\, p-e$ space is larger than the values used for other two sands. This is attributed to the grain crushing behavior of sands under relatively large confining pressures, which causes dramatic compression during shearing.

1.4.2 Model Calibration

From equation (1.7), it can be seen that the second pseudo yield surface plays a dominant role in the true hardening response when the plastic deviatoric strain is relatively small compared with the value of the parameter b. In this case, parameters a and k_1 play the main role in determining the hardening response. Given two test results

with different initial state parameters, a and k_1 can be determined by trial and error procedure through comparing their hardening responses during the early stages of loading. The stiffness and strength can be reduced by increasing the value of a and decreasing the value of k_1. In the same way, A and k_2 can be determined through examining the volumetric responses for two different initial state parameters during the early stages of loading. Increasing the value of A will increase both the volumetric contraction and dilation, and increasing k_2 will increase the dilation and decrease the contraction. For a loose sand, the undrained response will give the best estimation of the values of A and k_2 because pore pressure increase during undrained test is much more pronounced and easier to measure than the volume change during drained test for a loose sand. The parameters k_1 and k_2 control the difference in responses for two different state parameter values, since they are the only parameters directly related to sand's state parameters in this model. Constant b influences the true response by specifying how fast the deviatoric stress-strain true response moves from the second pseudo response to the first pseudo response. The smaller the value of b the quicker the true response will reach that of the first pseudo response. Similarly the parameter c determines how fast the volumetric response reaches the critical state. A smaller value of c will bring the volumetric response faster to the critical state. Therefore parameters b and c can be obtained through curve fitting by examining the responses during later stages of loading. Parameter b mainly controls the later stages of the hardening response including peak value. The peak of the hardening response includes the value of peak deviatoric stress and the position. Parameters a, b, and k_1 have little effect on the volumetric behavior and

parameters A, c, and k_2 have little effect on the stress-strain response. This separation helps the calibration process and is one of the strengths of the proposed model.

The model parameters for Nevada sand are obtained from drained test results at relative densities of 40% and 60% shown in Figures 1.8 and 1.9. It should be noted that when the confining pressure is smaller than 160 kPa for Nevada sand, the state parameter is independent of confining pressure, as described above. The parameters for Toyoura Sand are obtained by using drained test results under 500 kPa lateral stress for void ratio of 0.96 shown in Figure 1.12, and under 100 kPa lateral stress for void ratio of 0.831 shown in Figure 1.11. The two cases correspond to the largest and smallest state parameters among all the drained tests examined for Toyoura sand. The model parameters for Oklahoma #1 sand are obtained by using drained test results under the initial confining pressure of 500 psi (3.4 MPa) and 1500 psi (10.3 MPa), respectively, shown in Figure 1.16. All the values of the model parameters for Nevada sand, Toyoura sand and Oklahoma #1 sand obtained using this calibration procedure are listed in Table 1.1.

1.4.3 Model Validation

Stress-strain and volumetric responses for Nevada sand with Dr of 40% and 60% under drained loading conditions are shown in Figures 1.8 and 1.9, respectively. Denser sands have a stiffer hardening response, higher peak value and larger dilation as shown in Figure 1.9, as opposed to looser sand responses shown in Figure 1.8. For example, the peak strength for Dr of 40% under 160 kPa confining pressure is 220 kPa, compared to 270 kPa for Dr of 60% under 160 kPa confining pressure. Denser sands also show a

much more pronounced softening following the peak deviatoric stress. In Figure 1.9, under 160 kPa confining pressure, softening brings the deviatoric stress down to 240 kPa from the peak strength of 270 kPa. The sample for Dr of 40% experiences 3% volumetric expansion, compared with 5% volumetric expansion for Dr of 60%. In addition, a considerable amount of volumetric contraction can be observed for Dr of 40% during the early stages of loading. The model reflects the above phenomena very well. The model predictions shown in Figures 1.8 and 1.9 indicate that the volumetric response is independent of the confining pressures. The reason for these predictions is that the critical state line was assumed a flat line for confining pressures below 160 kPa (Figure 1.7). This assumption implies that for confining pressures smaller than 160 kPa the initial state parameter value is independent of confining pressures and depends only on the initial void ratio. It is quite obvious that confining pressures greater than 160 kPa will yield different initial state parameter values even when the initial void ratio is a constant and consequently will lead to volumetric responses that depend on confining pressures. The model predictions and conventional undrained compression test results for Nevada sand with Dr of 60% is shown in Figure 1.10. The pore water pressure in Figure 1.10 decreases throughout the loading due to the plastic volumetric expansion, which resulted in the increase of effective confining pressure and deviatoric stress. In general, the test results and model simulations are in good agreement.

The drained and undrained triaxial test results and model predictions for Toyoura sand are shown in Figures 1.11-1.15. The comparisons between test results and model predictions again show a good agreement. The tests cover a wide range of confining pressures varying from 100 kPa to 3000 kPa and void ratios varying from 0.907 to 0.735,

which correspond to a wide range of state parameters. For the drained tests in Figures 1.11 and 1.12, denser sands experience stiffer stress-strain response, higher peak strength and larger volumetric expansion. For the undrained tests in Figures 1.13 – 1.15, denser sands under smaller initial confining pressures show greater pore water pressure decrease than looser sands under higher initial confining pressures. It is worth noting that even for the densest sand with a void ratio of 0.735 in Figure 1.13, a considerable amount of pore water pressure increase can be observed during the early stages of loading when the initial confining pressure is very high (for example, 3000 kPa). This is in accordance with the state parameter concept in which the combination of void ratio and confining pressure determines sand behavior. In Figure 1.15, in which the void ratio is very high (0.907), liquefaction (zero confining pressure) can be observed.

Figures 1.16 shows the test results and predictions for Oklahoma #1 sand under drained loading conditions for the initial confining pressures from 500 psi (3.5 MPa) to 2000 psi (13.8 MPa). It can be seen that predictions and test results are in a reasonable good agreement. Larger confining pressures lead to larger shear strength and larger compression. It should be noted that the measured deviatoric stress and volumetric evolutions for relatively large initial confining pressures, for example at 1500 psi (10 MPa) and 2000 psi (14 MPa), are not stable and continue increasing at a constant rate even when the axial strain reaches 30%. This is caused by the continuous sand grain crushing under relatively large confining pressures. The volumetric strain evolutions are available only for the tests under initial confining pressures of 500 psi (3.5 MPa) and 1500 psi (10 MPa) in Figure 1.16 because the data acquisition system didn't operate properly under initial confining pressures of 1000 psi (6.9 MPa) and 2000 psi (14 MPa).

Figures 1.17-1.22 show the undrained test results and predictions under initial effective confining pressures varying from 300 psi (2.1 MPa) to 5950 psi (41 MPa). Both test results and predictions show that under smaller confining pressures the pore water pressures increase first, followed by a decrease, such as in Figures 1.17 and 1.18. Correspondingly, the effective confining pressures decrease first, followed by an increase. This results from the negative state parameters under smaller confining pressure. Under higher confining pressures, the pore water pressures increase throughout loading, which results in effective confining pressure decreasing throughout loading, such as in Figures 1.19 – 1.22. This results from the positive state parameters under higher confining pressures. It should be noted that the predicted deviatoric stresses experience greater softening than the measured ones under larger confining pressures. This discrepancy is likely due to the grain crushing of sands and corresponding localization of samples during shearing.

1.5 Conclusions

A novel modeling technique named the *"Middle Surface Concept (MSC)"* is presented to take into account the state parameter and the critical state concepts within the classical elastoplasticity theory. By dividing the modeling task between two pseudo yield surfaces the difficulties faced by previous models in incorporating the state parameter and achieving the critical state are avoided. The true response is a combination of the two pseudo responses. The true yield surface lies between the two pseudo yield surfaces and hence the name Middle Surface Concept. All three yield surfaces share a common confining pressure, plastic deviatoric strains and their increments, and are

further linked by relationships relating the hardening and dilatancy rules. The model parameters are meaningful, easy to calibrate, and are independent of the density of a sand.

The application of this concept to the monotonic loading of saturated sands within the triaxial space is presented. The model is shown to be capable of modeling various loading conditions and capturing unique features such as softening of dense sands following the peak deviatoric stress under drained loading. Reasonable comparisons between model predictions and laboratory test results are achieved for three different sands.

The Middle Surface Concept is quite general and can be applied to materials other than sand in that it can model more than one unique concept by dividing the task among multiple pseudo yield surfaces.

1.6 References

Arulmoli, K., Muraleetharan, K. K., Hossain, M. M. & Fruth, L. S. (1992), *VELACS: Verification of Liquefaction Analysis by Centrifuge Studies, Laboratory Testing Program, Soil Data Report.* Technical Report, the Earth Technology Corporation, Irvine, California

Bardet, J. P. (1986), Bounding Surface Plasticity Model for Sands, *Journal of Engineering Mechanics* **112**, No.11, 1198-1217

Been, K. & Jefferies, M. G. (1985), A State Parameter for Sands, *Geotechnique* **35**, No. 2, 99-102

Been, K., Crooks, J. H. A., Becker, D. E. & Jefferies, M. G. (1986), The Cone Penetration Test in Sands: Part I, State Parameter Interpretation, *Geotechnique* **36**, No. 2, 239-249

Been, K., Jefferies, M. G., Crooks, J. H. A. & Rothenburg, L. (1987), The Cone Penetration Test in Sands: Part II, General Inference of State, *Geotechnique* **37**, No. 3, 285-299

Been, K., Jefferies, M. G., & Hachey, J. (1991), The Critical State of Sands, *Geotechnique* **41**, No. 3, 365-381

Carriglio, F., Ghionna, V. N., Jamiolkowski, M. & Lancellotta, R. (1990), Stiffness and Penetration Resistance of Sands Versus State Parameter, *Journal of Geotechnical Engineering* **116**, No. 6, 1015-1020

Collins, I. F., Pender, M. J. & Wang, Y. (1992), Cavity Expansion in Sands Under Drained Loading Conditions, *International Journal for Numerical and Analytical Methods in Geomechanics* **16**, 3-23

Crouch, R. S. & Wolf, J. P. (1994), Unified 3D Critical State Bounding-Surface Plasticity Model for Soils Incorporating Continuous Plastic Loading Under Cyclic Paths, *International Journal for Numerical and Analytical Methods in Geomechanics* **18**, 735-758

Desai, C.S. (1974), A Consistent Finite Element Technique for Work-Softening Behavior, *Proc., Int. Conf. on Computational Methods in Nonlinear Mech.*, University of Texas at Austin, Austin, Texas

Faruque, O., Zaman, M. M. & Abdumrahee, A. (1992), On Modeling Stress-Strain and Dilatant Behavior of Cohesionless Soil, *Indian Geotechnical Journal* **22**, No. 3, 175-195

Gajo, A. & Wood, D. M. (1999a), A Kinematic Hardening Constitutive Model for Sands: The Multiaxial Formulation, *International Journal for Numerical and Analytical Methods in Geomechanics* **23**, 925-965

Gajo, A. & Wood, D. M. (1999b), Severn-Trent Sand: A Kinematic-Hardening Constitutive Model: the q-p Formulation, *Geotechnique* **49**, No. 5, 595-614

Jefferies, M. G. (1993), Nor-Sand: A Simple Critical State Model for Sand, *Geotechnique* **43**, No. 1, 91-103

Kabilamany, K. & Ishihara, K. (1990), Stress Dilatancy and Hardening Laws for Rigid Granular Model of Sand, *Soil Dynamics and Earthquake Engineering* **9**, No. 2, 66-77

Kmeid, E.T. (2003), *Experimental Study of Unconsolidated Sand Under High Confining Pressures*, M.S. Thesis, School of Civil Engineering and Environmental Science, University of Oklahoma, Norman, Oklahoma

Konrad, J. M. (1990), Minimum Undrained Strength of Two Sands, *Journal of Geotechnical Engineering* **116**, No. 6, 933-947

Lade, V. P. (1977), Elasto-Plastic Stress-Strain Theory for Cohesionless Soil with Curved Yield Surfaces, *Int. J. Solids Structures* **13**, 1019-1035

Li, X. S. & Wang, Y. (1998), Linear Representation of Steady-State Line for Sand, *Journal of Geotechnical and Geoenvironmental Engineering* **124**, No. 12, 1215-1217

Li, X. S., Dafalias, Y. F. & Wang, Z. L. (1999), State-Dependent Dilatancy in Critical-State Constitutive Modeling of Sand, *Canadian Geotechnical Journal* **36**, 599-611

Li, X. S., & Dafalias, Y. F. (2000), Dilatancy for Cohesionless Soils, *Geotechnique* **50**, No. 4, 449-460

Manzari, M. T. & Dafalias, Y. F. (1997), A Critical State Two-Surface Plasticity Model for Sands, *Geotechnique* **47**, No. 2, 255-272

Mooney, M. A., Finno, R. J., & Viggiani, M. G. (1998), A Unique Critical State for Sand? *Journal of Geotechnical and Geoenvironmental Engineering* **124**, No. 11, 1100-1108

Park, Inn-Joon & Desai, C. S. (2000), Cyclic Behavior and Liquefaction of Sand Using Disturbed State Concept, *Journal of Geotechnical and Geoenvironmental Engineering* **126**, No. 9, 834-846

Poorooshasb, H. B. & Pietruszczak, S. (1986), A Generalized Flow Theory for Sand, *Soil and Foundations* **26,** No. 2, 1-15

Poulos, S. J. (1981), The Steady State of Deformation, *Journal of the Geotechnical Engineering Division* **107**, No. 5, 553-562

Riemer, M. F. & Seed, R. B. (1997), Factors Affecting Apparent Position of Steady-State line, *Journal of Geotechnical and Geoenvironmental Engineering* **123**, No. 3, 281-287

Tatsuoka, F. & Ishihara, K. (1974), Yielding of Sand in Triaxial Compression, *Soils and Foundations* **14**, No. 2, 63-76

Vaid, Y. P., Chung, E. K. F. & Kuerbis, R. H. (1990), Stress Path and Steady State, *Canadian Geotechnical Journal* **27**, 1-7

Verdugo, R. & Ishihara, K. (1996), The Steady State of Sandy Soils, *Soils and Foundations* **36**, No. 2, 81-91

Vermeer, P. A. (1978), A Double Hardening Model for Sand, *Geotechnique* **28**, No. 4, 413-433

Wang, Z. L., Dafalias, Y. F., & Shen, C. K. (1990), Bounding Surface Hypoplasticity Model for Sand, *Journal of Engineering Mechanics* **116**, No. 5, 983-1001

Wood, D. M., Belkheir, K. & Liu, D. F. (1994), Strain Softening and State Parameter for Sand Modeling, *Geotechnique* **44**, No. 2, 335-339

Wroth, C. P. & Bassett, N. (1965), A Stress-Strain Relationship for the Shearing Behavior of Sand, *Geotechnique* **15**, No. 1, 32-56

Yamamuro, J. A., & Lade, P. V. (1997), Static Liquefaction of Very Loose Sands, *Canadian Geotechnical Journal* **34**, 905-917

Yang, Y. & Muraleetharan, K.K. (2002), The Middle Surface Concept and Its Application in Geomaterials, Proceedings (in CD ROM), *15th ASCE Engineering Mechanics Division Conference*, 2002, New York

Yang, Y. & Muraleetharan, K.K. (2003), Middle Surface Concept and Its Application to Elastoplastic Behavior of Saturated Sands, *Geotechnique* **53**, No. 4, 421-431

Yu, H. S. (1994), State Parameter from Self-Boring Pressuremeter Tests in Sand, *Journal of Geotechnical Engineering* **120**, No. 12, 2118-2135

Yu, H. S. (1996), Interpretation of Pressuremeter Unloading Tests in Sands, *Geotechnique* **46**, No. 1, 17-31

Yu, H. S. (1998), CASM: A Unified State Parameter Model for Clay and Sand, *International Journal for Numerical and Analytical Methods in Geomechanics* **22**, 621-653

Table 1.1. Model Constants for Model Performance, Nevada Sand, Toyoura Sand and Oklahoma #1 Sand

		Model performance	Nevada sand	Toyoura sand	Oklahoma #1 sand
Elasticity	G_0 (kPa)	3×10^4	2.0×10^4	2.0×10^4	2.0×10^4
	K_0 (kPa)	3×10^4	2.0×10^4	2.0×10^4	2.0×10^4
	n	0.6	0.6	0.5	0.6
Critical state	M	1.30	1.30	1.27	1.3
	λ	0.025	0 (p<160 kPa) or 0.04 (p>160 kPa)	0.019	0.178
	e_{ref}	0.760	0.780	0.934	1.0135
	p_{ref} (kPa) or ξ	160	160	0.7	1000
Hardening and softening	a	0.0010	0.0025	0.0045	0.0035
	k_1	3.0	4.0	4.0	6
	b	0.05	0.06	0.04	0
Dilatancy	A	1.0	0.8	0.7	0.8
	k_2	6	11	6	4
	c	0.050	0.002	0.002	0

Table 1.2. Various Values of Model Parameters Used in the Parametric Study

Hardening and Softening									Dilatancy								
a			k_1			b			A			k_2			c		
0.001	0.01	0.05	3	6	9	0.002	0.01	0.05	1	2	3	3	6	12	0.002	0.01	0.05

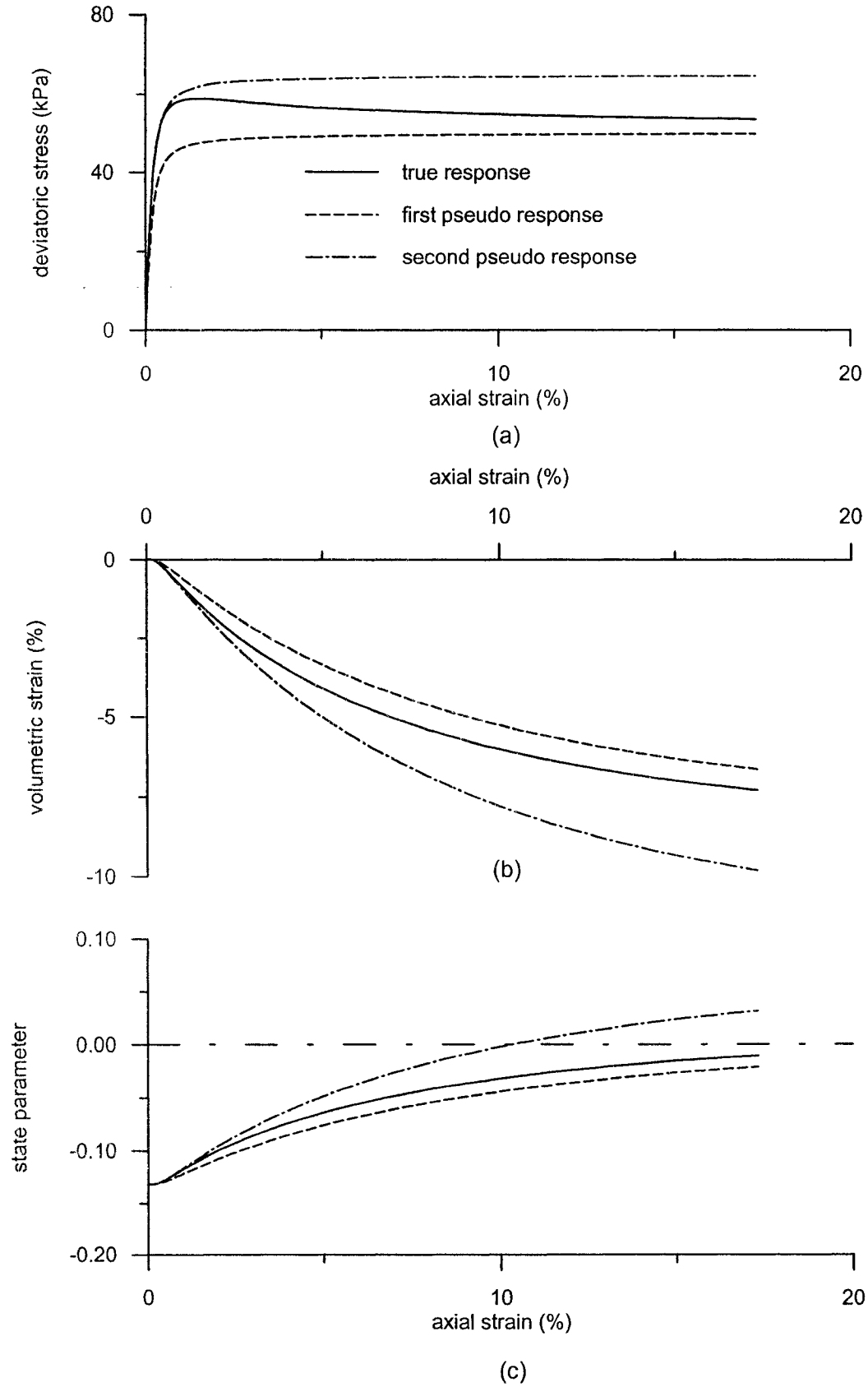

Figure 1.1: the true and pseudo responses during a constant p (40 kPa) drained test for a dense sand (initial state parameter = -0.13)

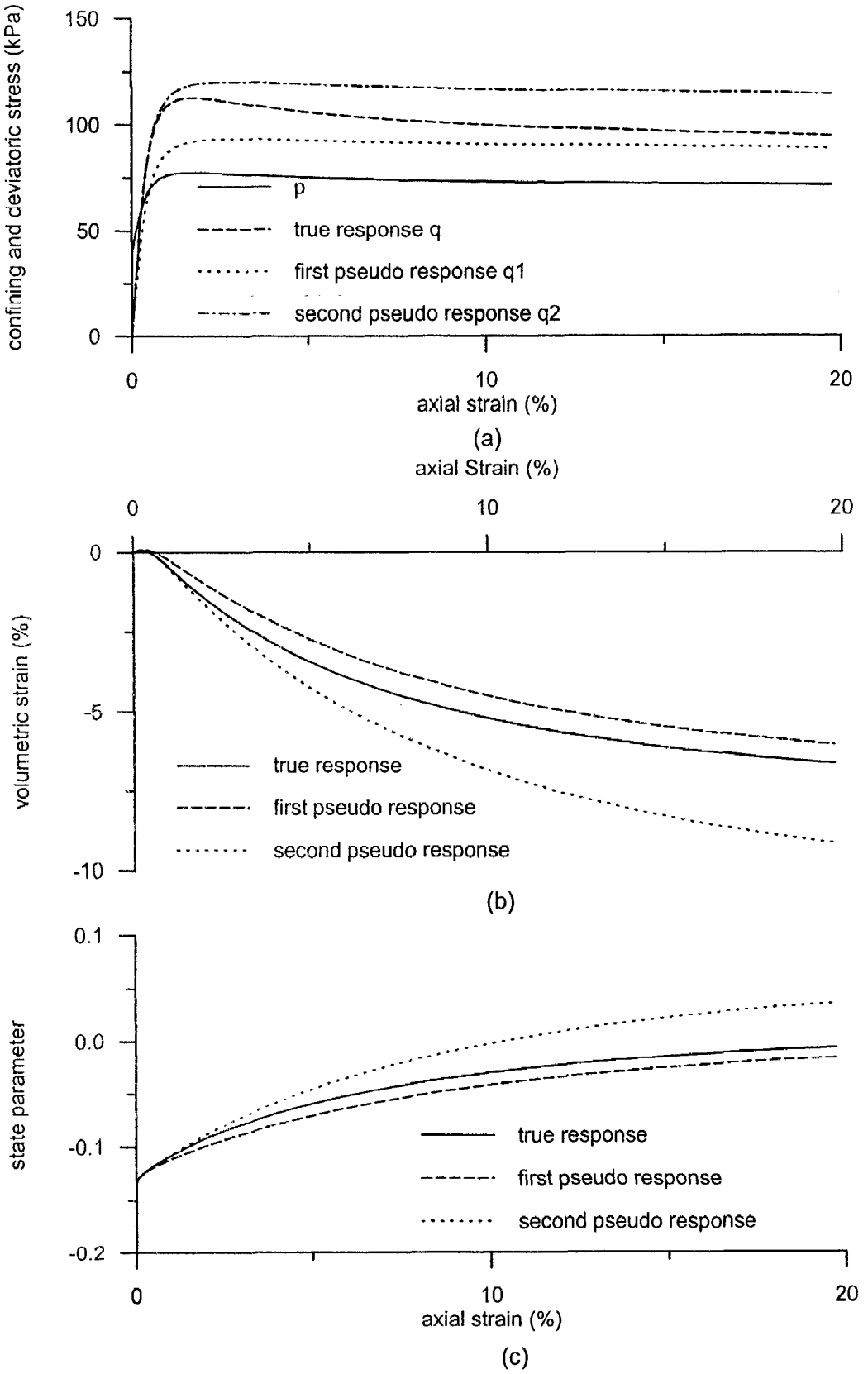

Figure 1.2: simulation of conventional triaxial drained compression test (initial state parameter = -0.13)

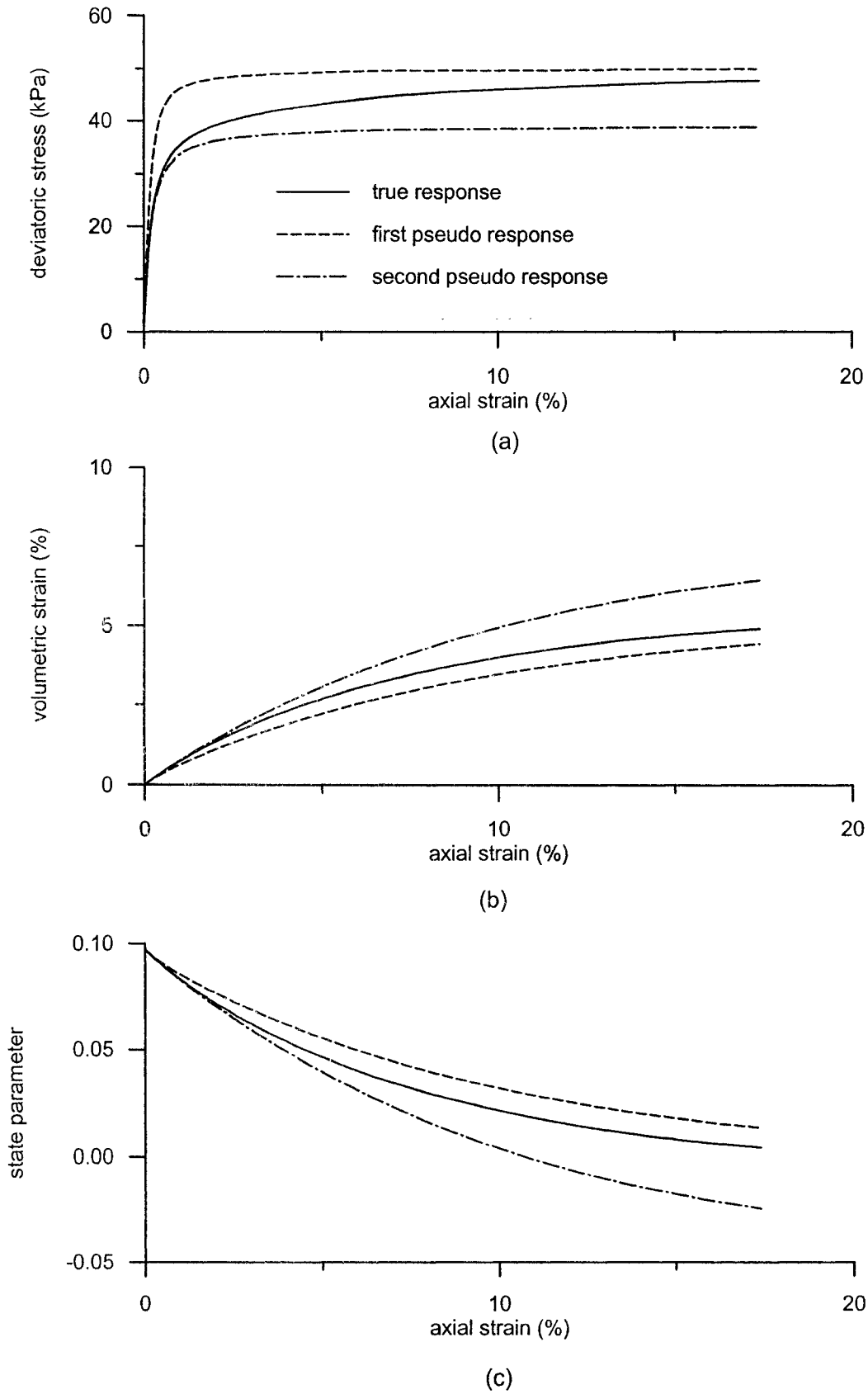

Figure 1.3: the true and pseudo responses during a constant p (40 kPa) drained test for a loose sand (initial state parameter = 0.10)

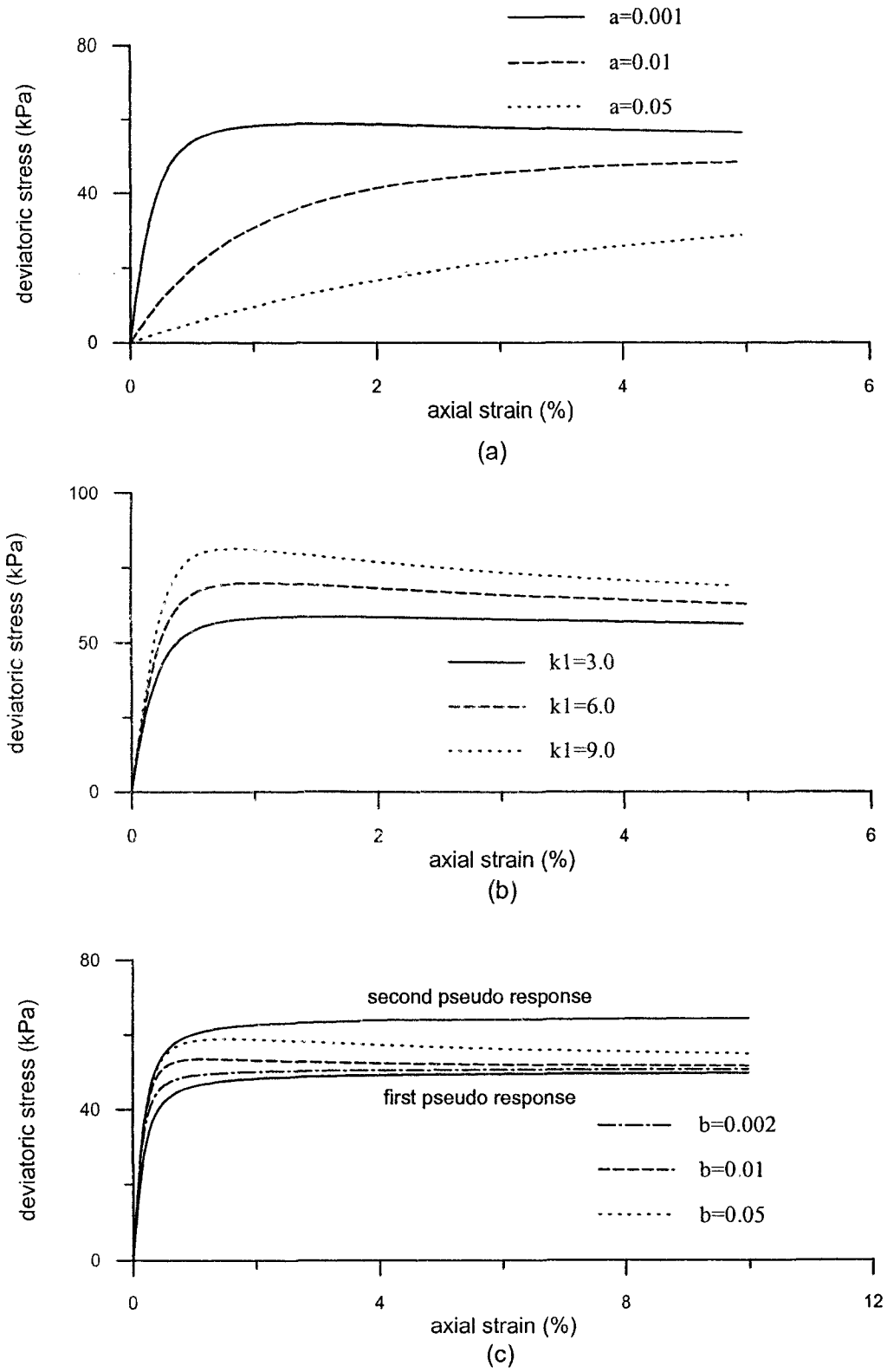

Figure 1.4: the effects of model parameters on hardening behavior

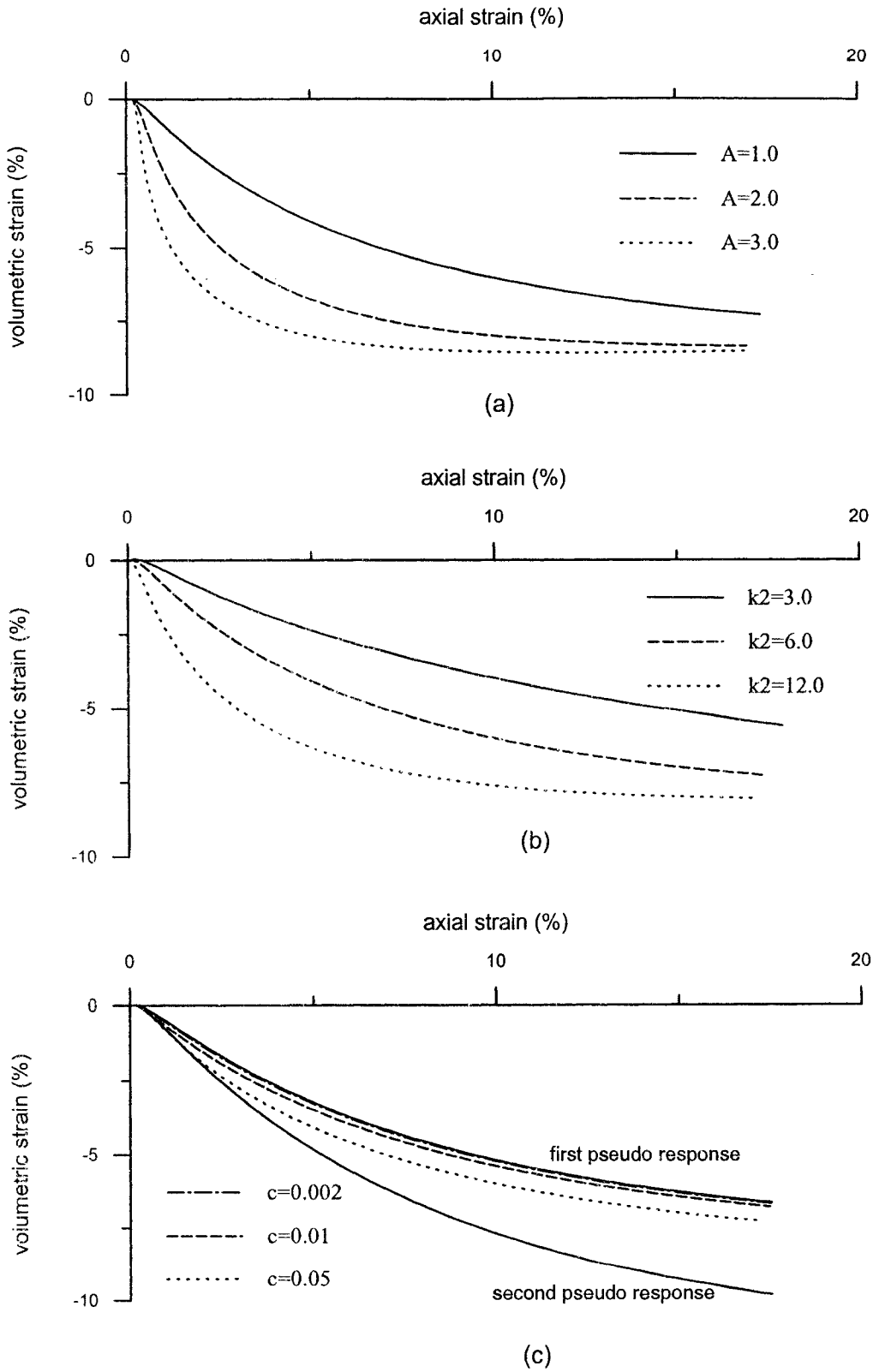

Figure 1.5: the effects of model parameters on volumetric evolutions

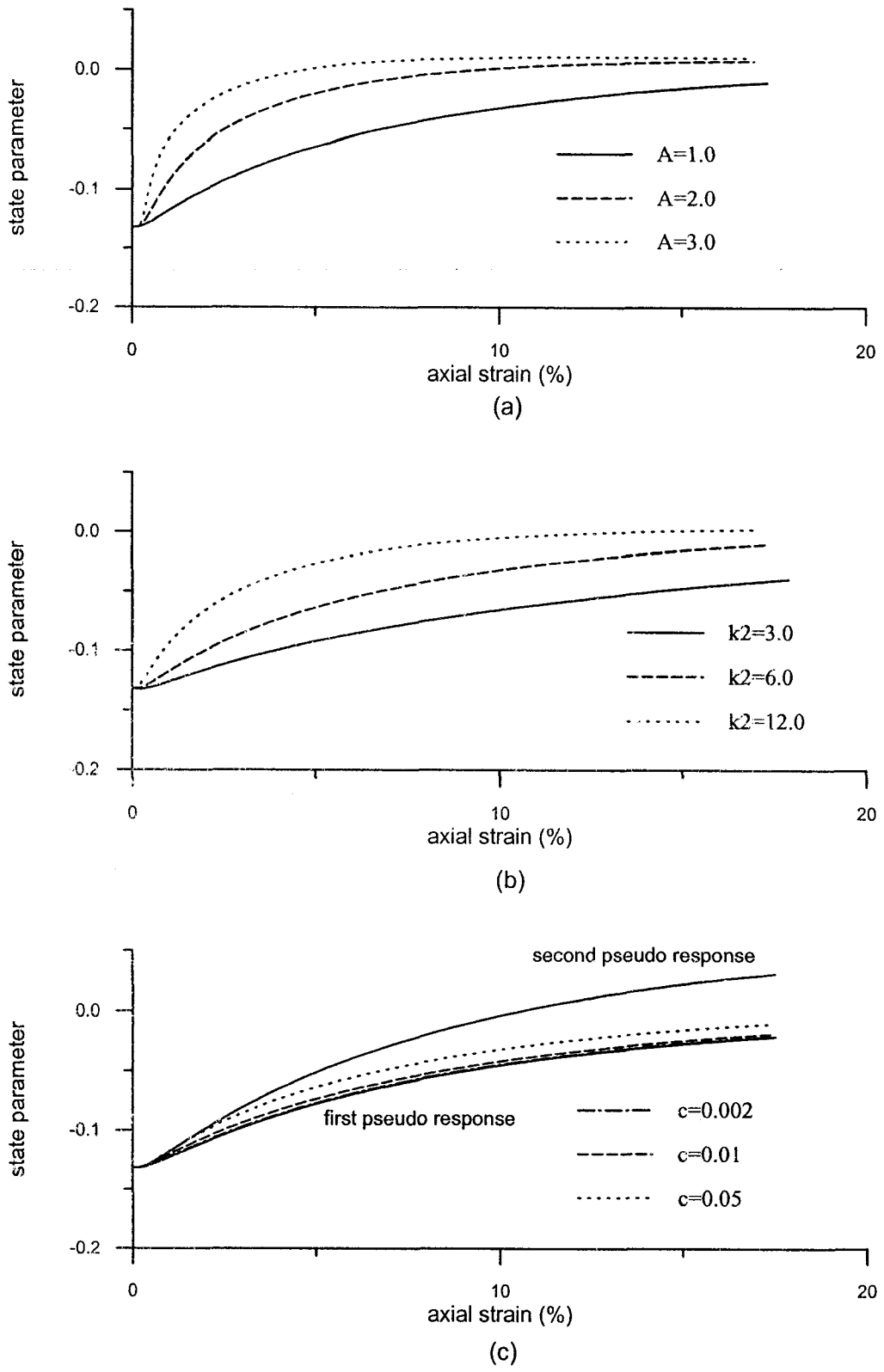

Figure 1.6: the effects of model parameters on state parameter evolutions

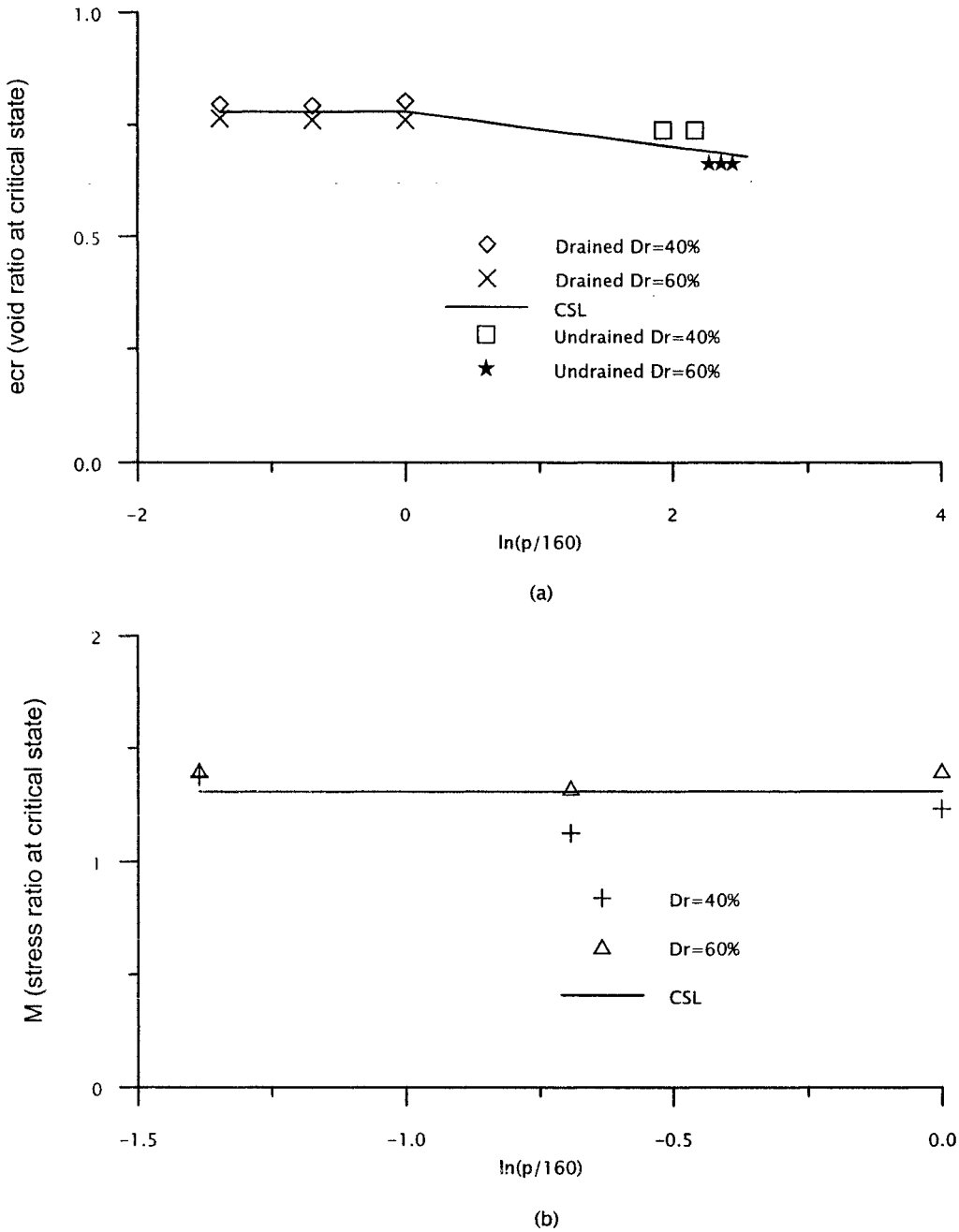

Figure 1.7: critical state line for Nevada Sand

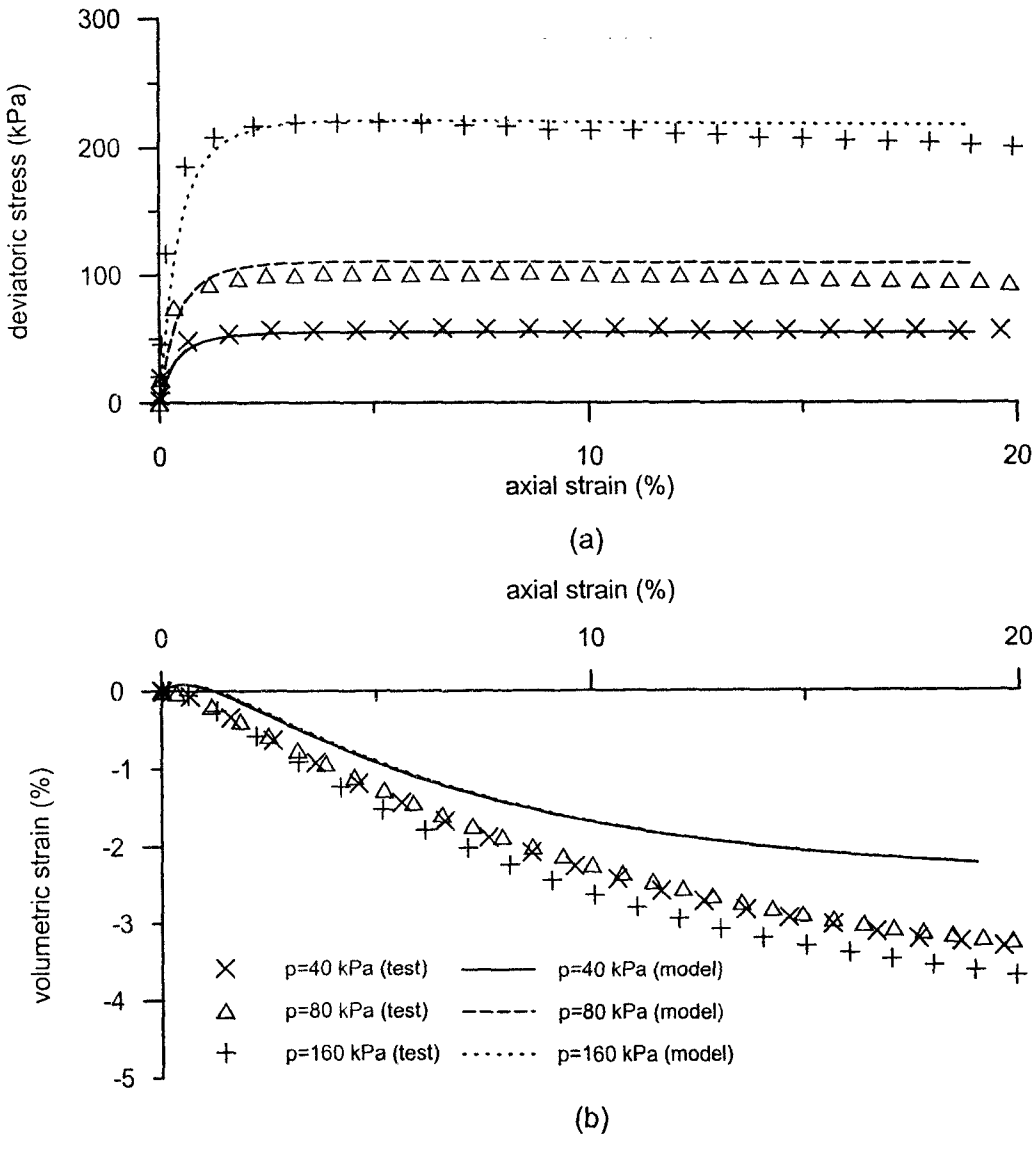

Figure 1.8: comparisons of the model predictions and test results for constant confining pressure drained tests for Nevad sand with Dr = 40% (test data after Arulmoli, et al., 1992; test data used for model calibration)

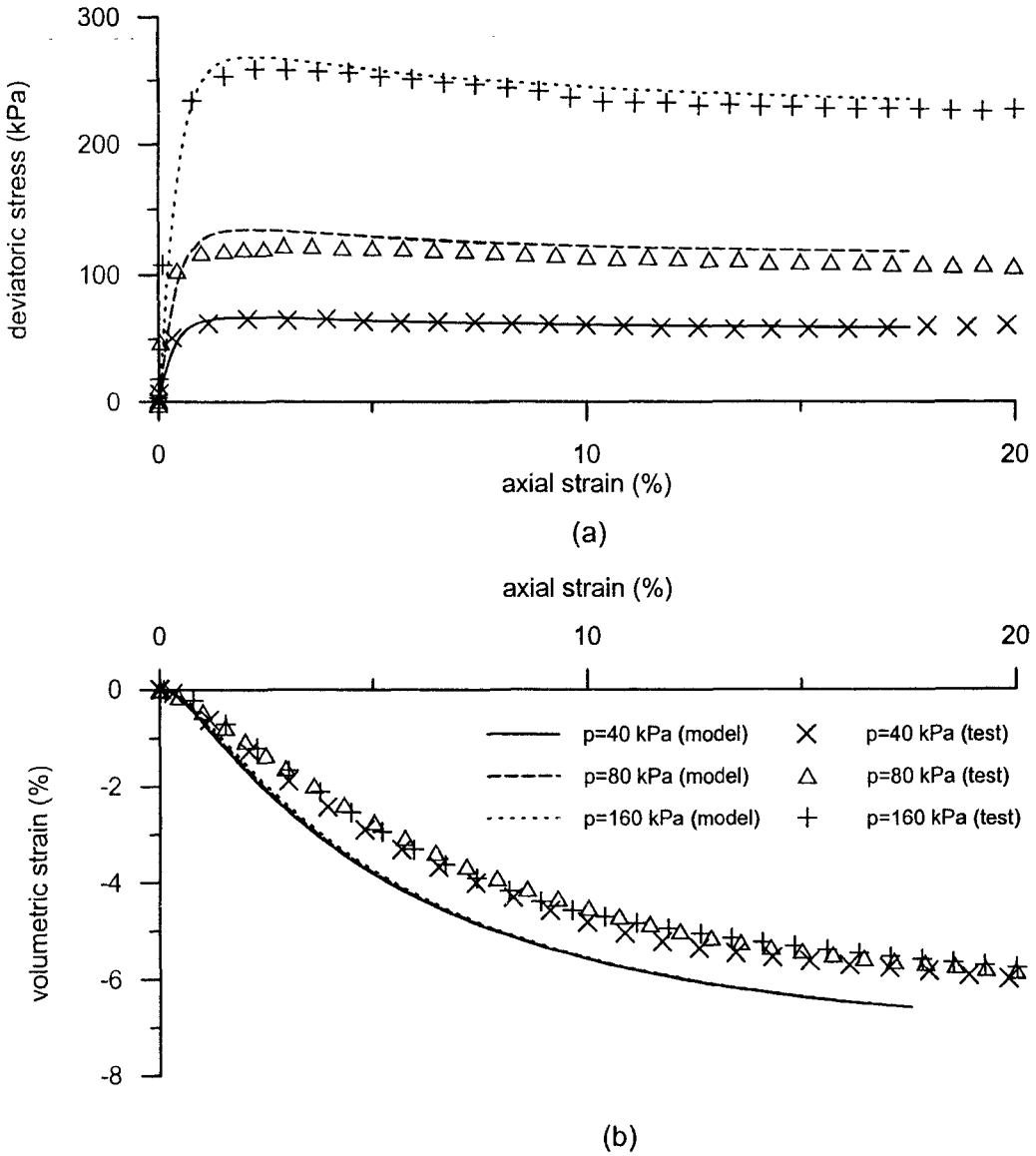

Figure 1.9: comparisons of the model predictions and test results for constant confining pressure drained tests for Nevada sand with Dr = 60% (test data after Arulmoli, et al., 1992; test data used for model calibration)

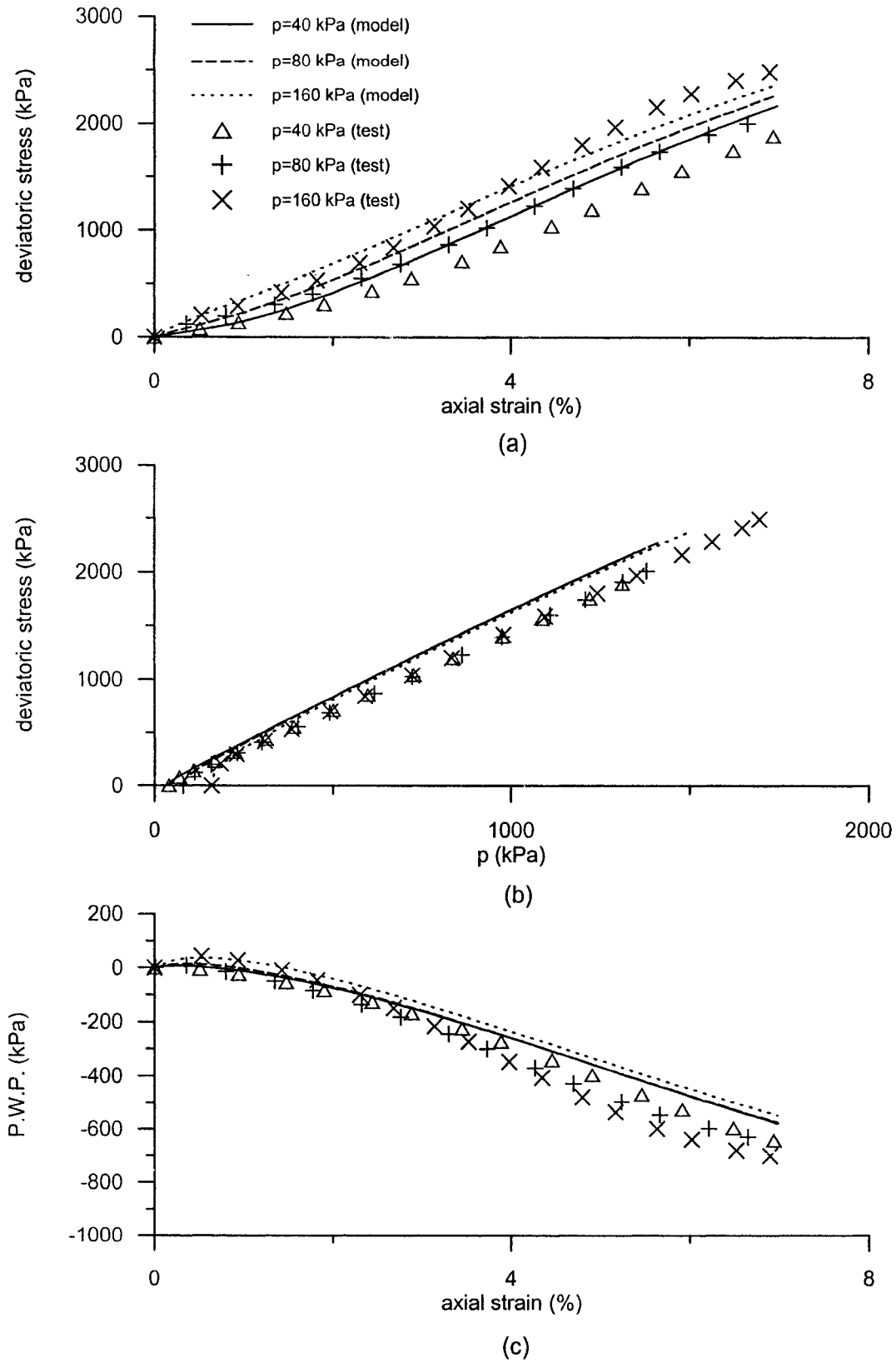

Figure 1.10: comparisons of the model predictions and test results for conventional triaxial undrained compression tests for Nevada sand with Dr = 60% (test data after Arulmoli, et al., 1992)

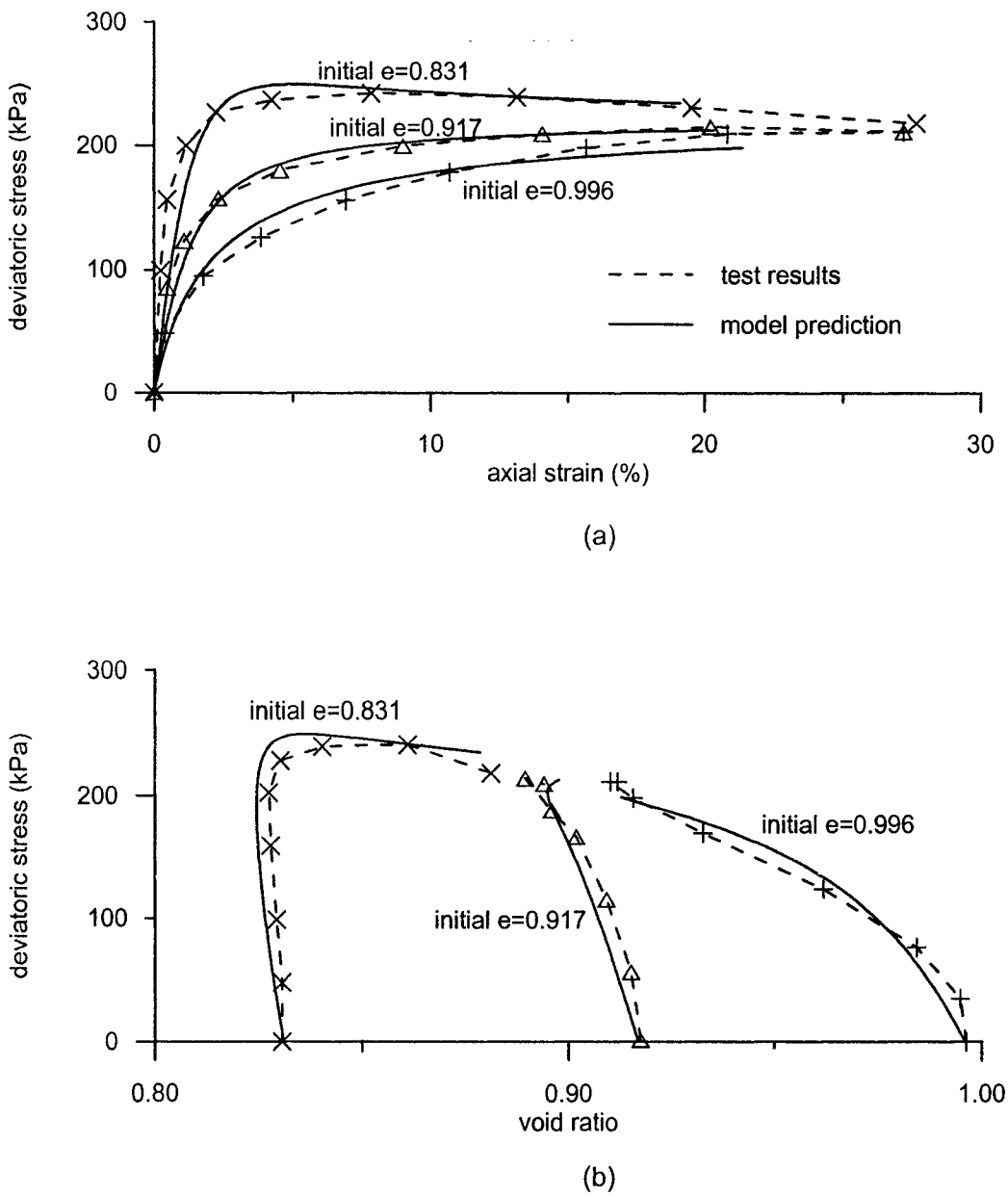

Figure 1.11: comparisons of the model predictions and test results for conventional triaxial drained tests for Toyoura sand under lateral stress of 100 kPa
(test data after Verdugo & Ishihara, 1996; e0=0.831 data used for model calibration)

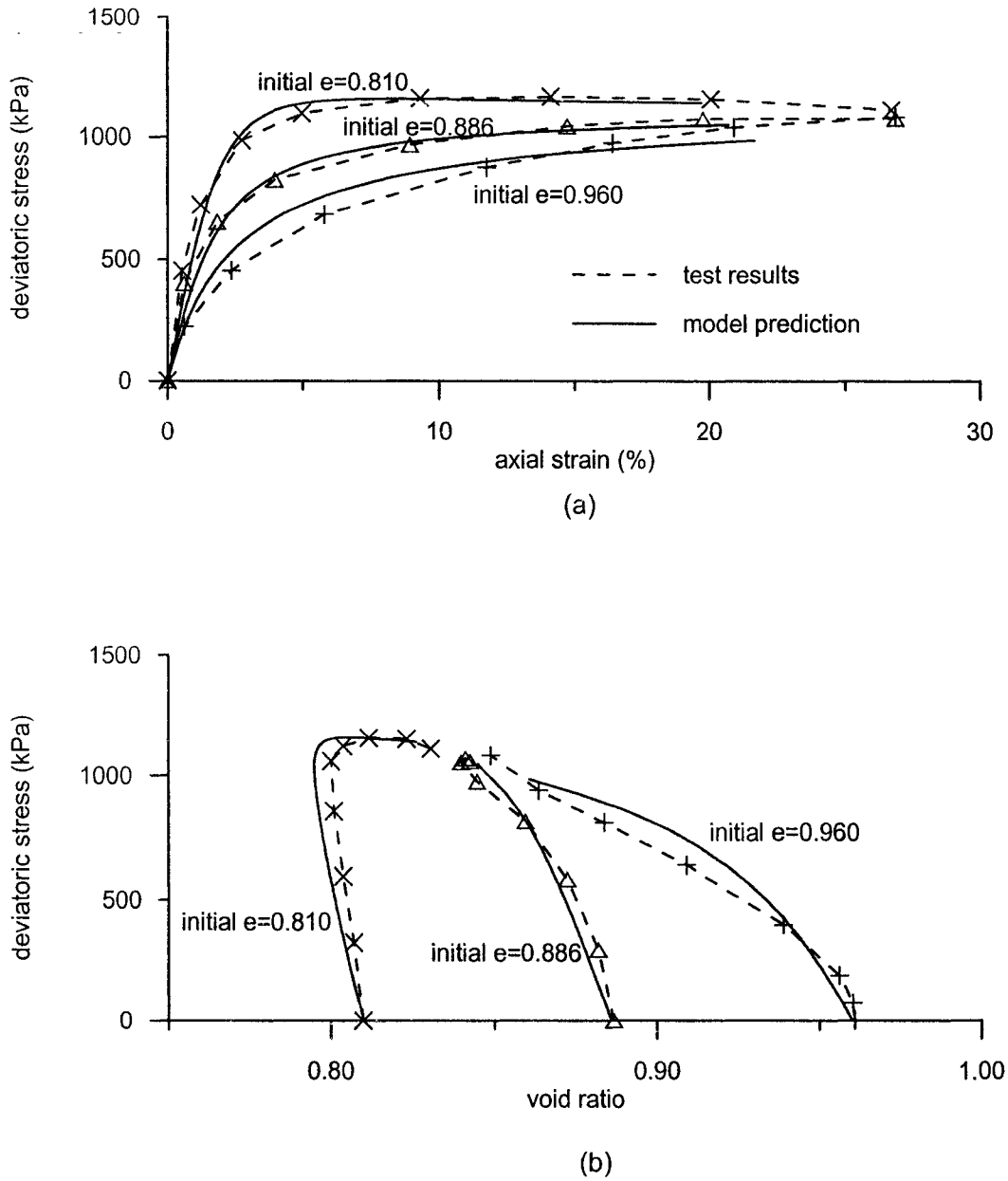

Figure 1.12: comparisons of the model predictions and test results for conventional triaxial drained tests for Toyoura sand under lateral stress of 500 kPa (test data after Verdugo & Ishihara, 1996; e0=0.960 data used for model calibration)

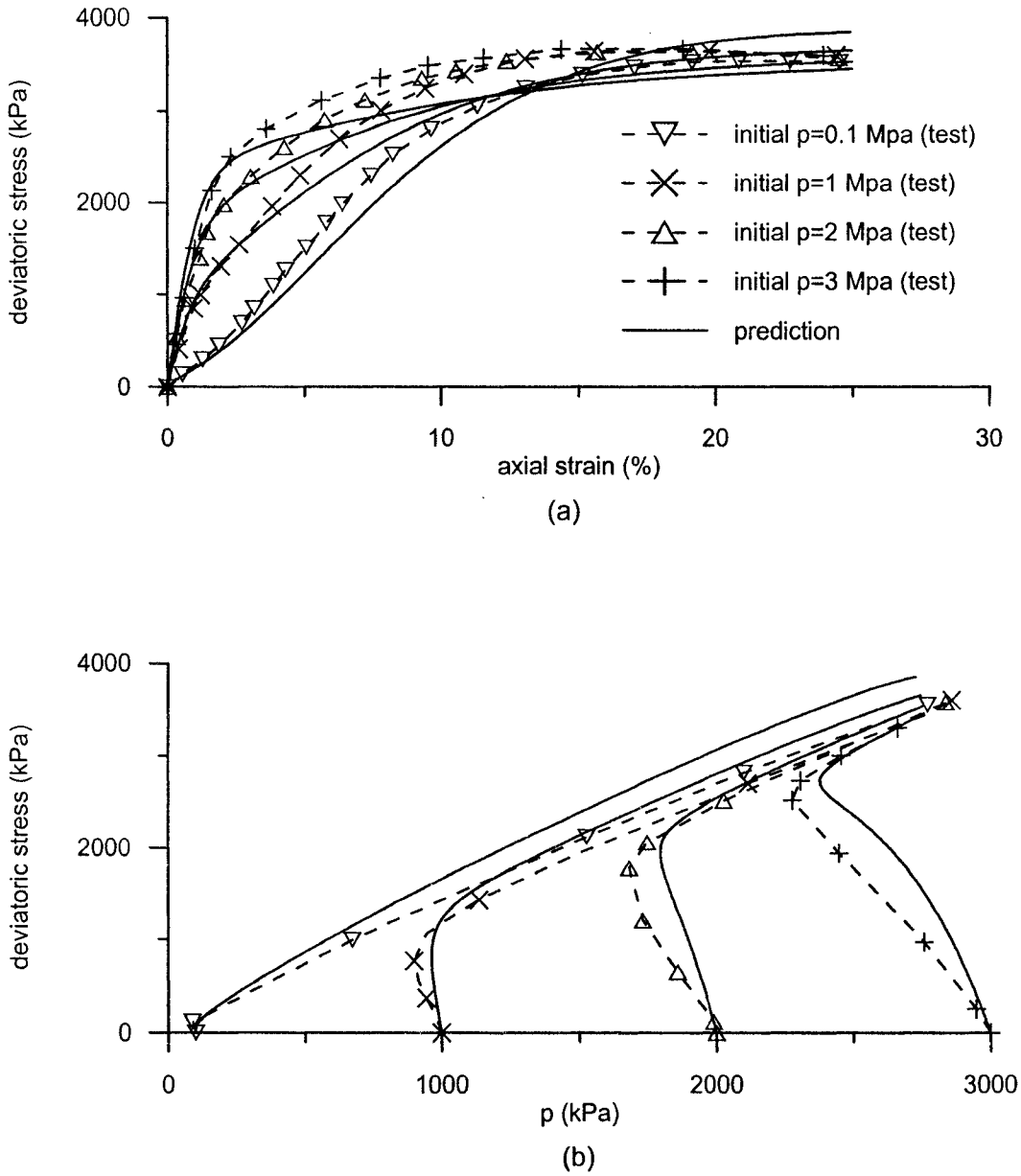

Figure 1.13: comparisons of the model predictions and test results for conventional triaxial undrained tests for Toyoura sand with a void ratio of 0.735 and varying initial confining pressures (test data after Verdugo & Ishihara, 1996)

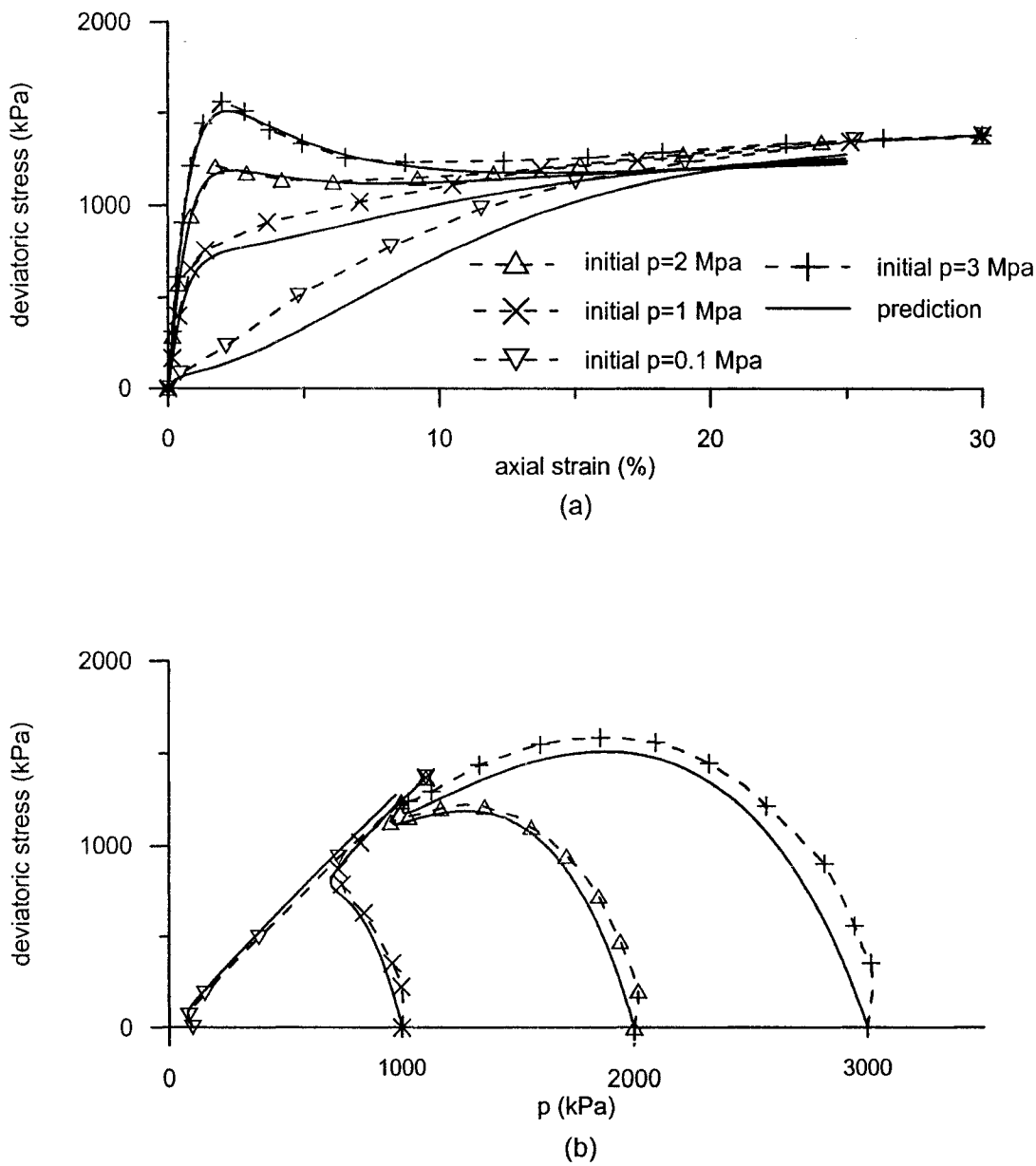

Figure 1.14: comparisons of the model predictions and test results for conventional triaxial undrained tests for Toyoura sand with a void ratio of 0.833 and varying initial confining pressures (test data after Verdugo & Ishihara, 1996)

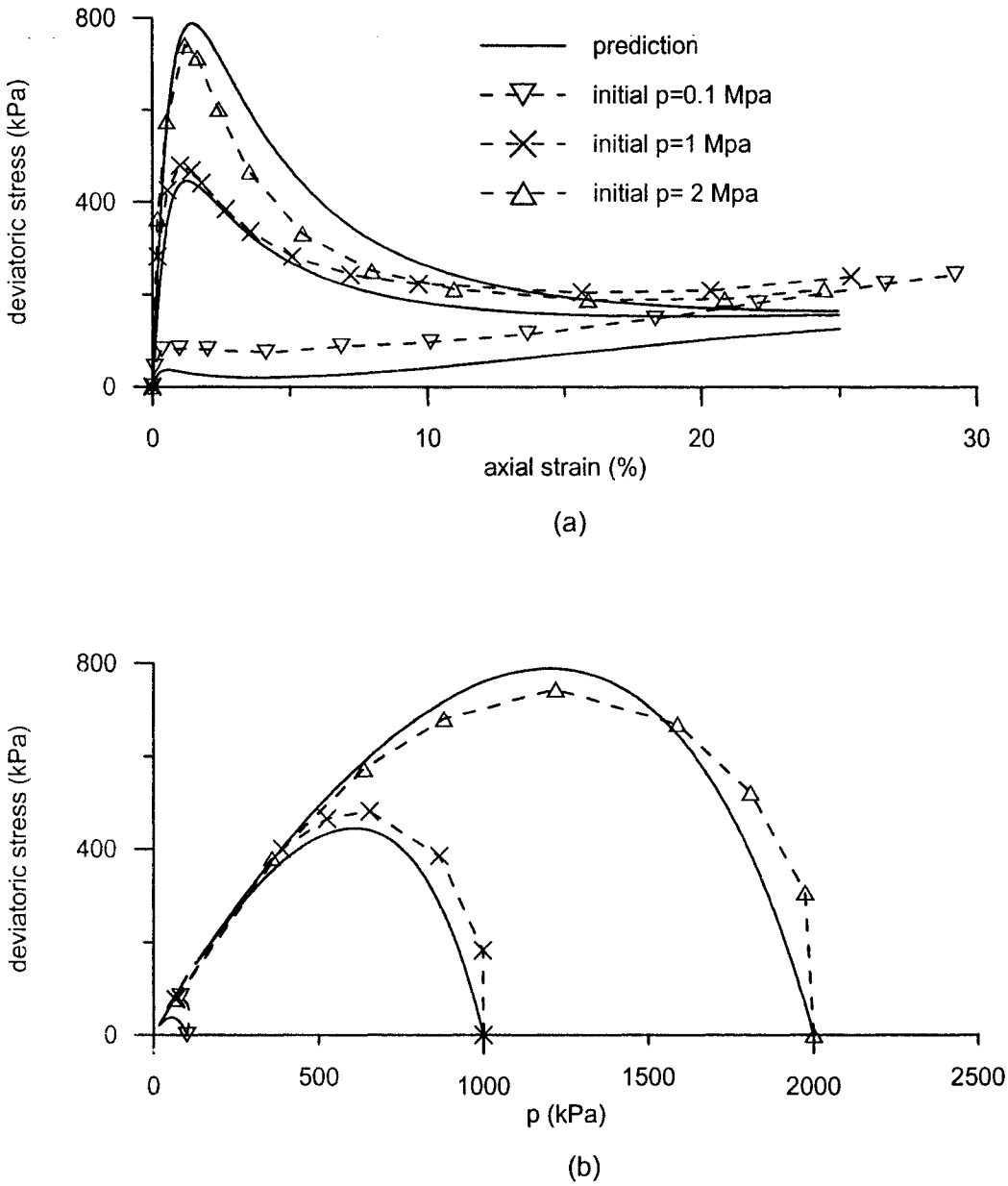

Figure 1.15: comparisons of the model predictions and test results for conventional triaxial undrained tests for Toyoura sand with a void ratio of 0.907 and varying confining pressures (test data after Verdugo & Ishihara, 1996)

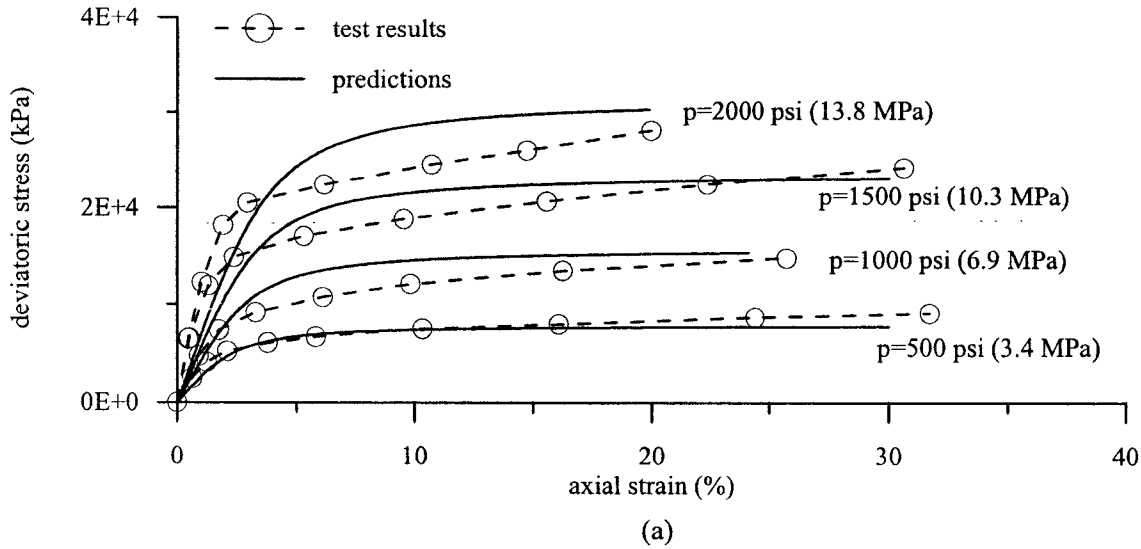

(a)

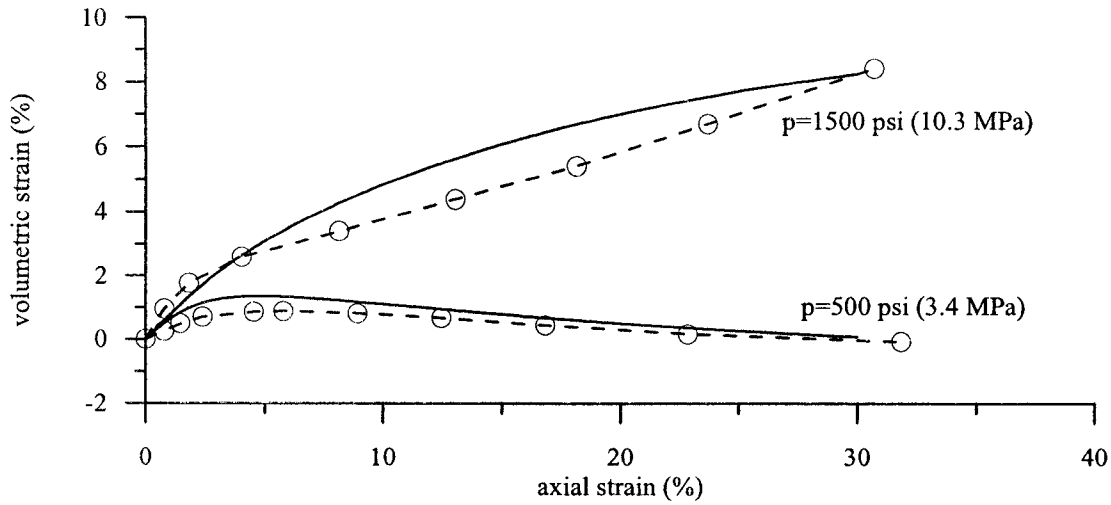

(b)

Figure 1.16: comparison of the model predictions and test results for conventional triaxial drained tests for Oklahoma #1 sand under varying initial confining pressures (test data after Kmeid, 2003) (p=500 and 1500 psi data used for model calibration)

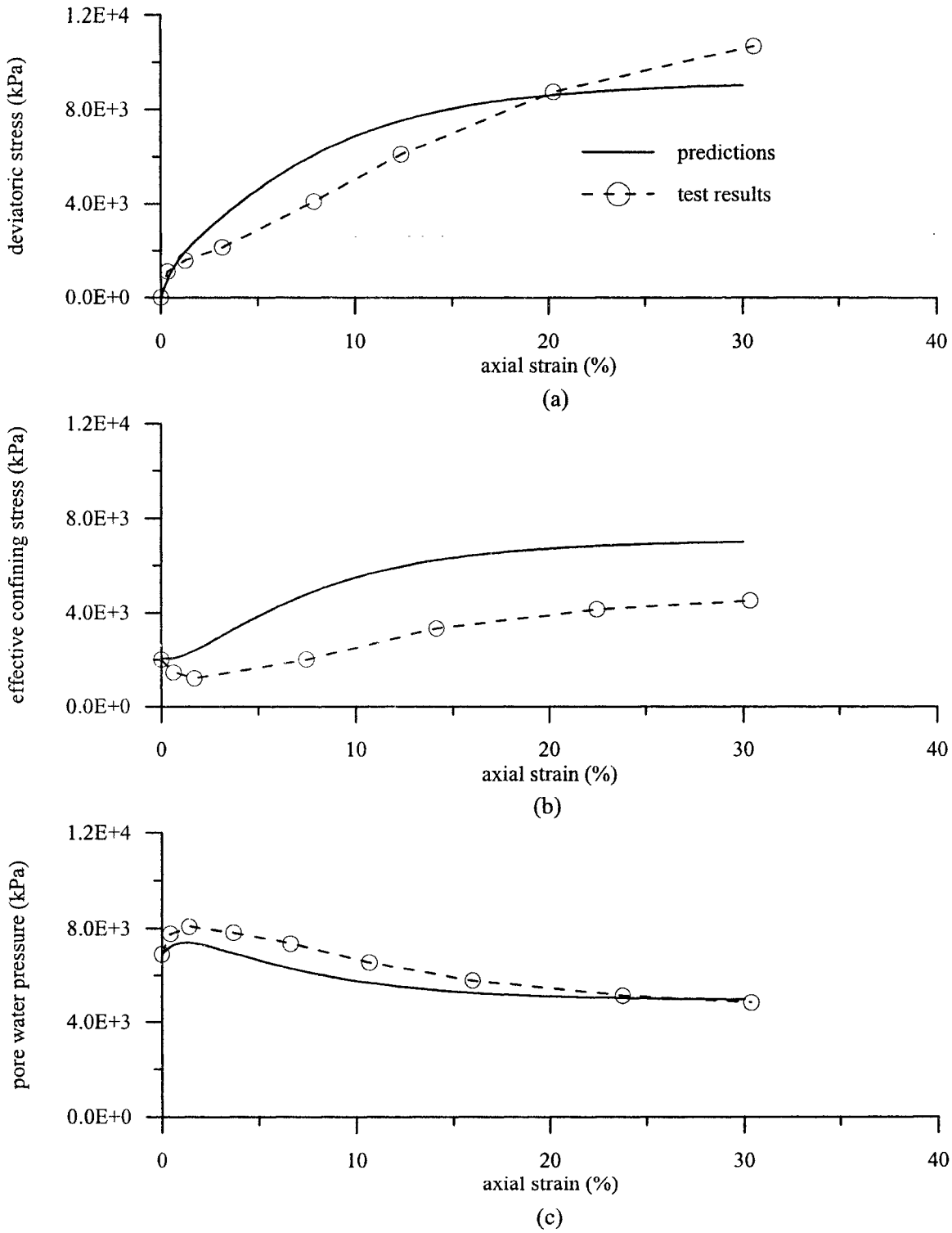

Figure 1.17: comparison of the model predictions and test results for conventional triaxial undrained tests for Oklahoma #1 sand under initial confining pressure of 300 psi (2.1 MPa) (test data after Kmeid, 2003)

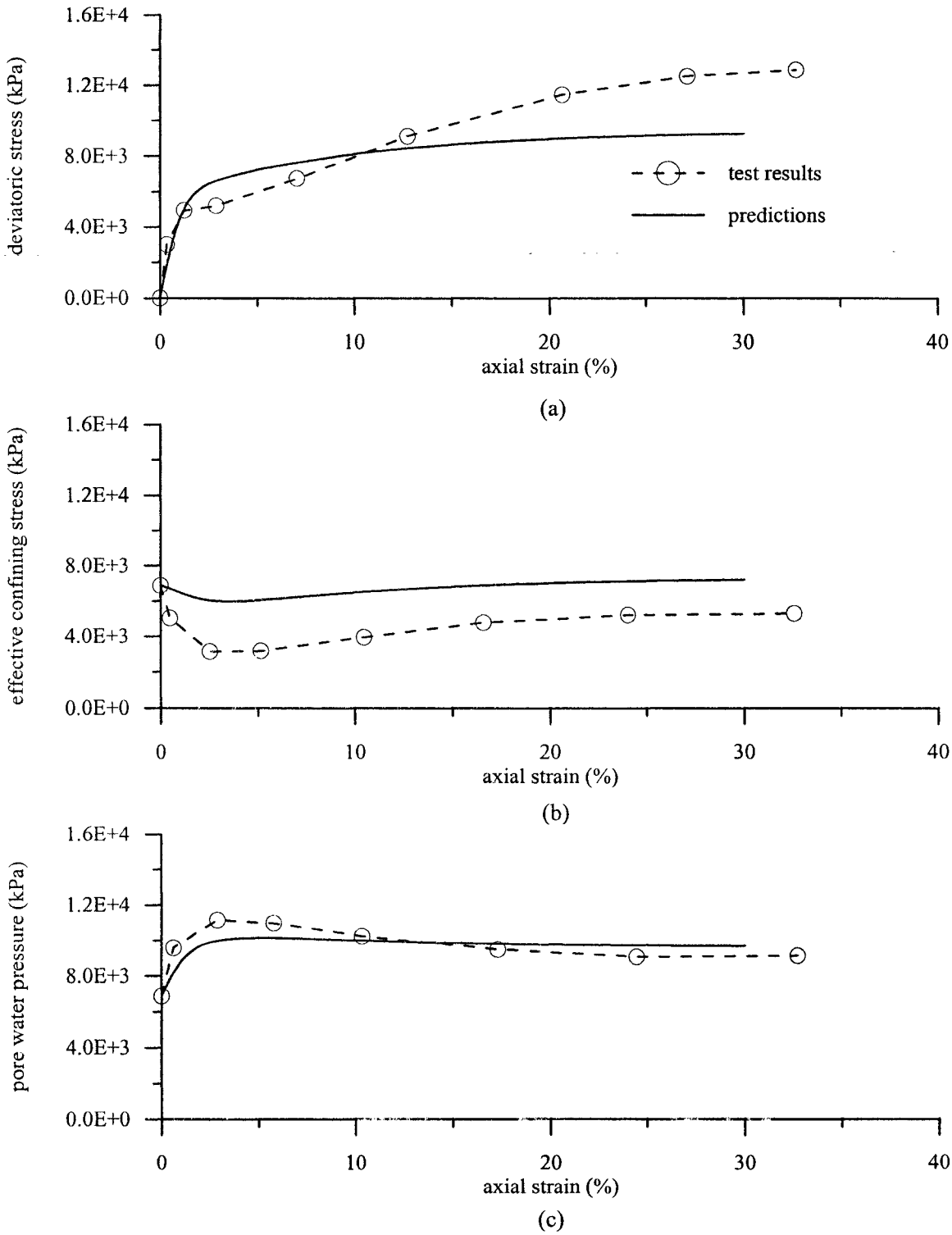

Figure 1.18: comparison of the model predictions and test results for conventional triaxial undrained tests for Oklahoma #1 sand under initial confining pressure of 1000 psi (6.9 MPa) (test data after Kmeid, 2003)

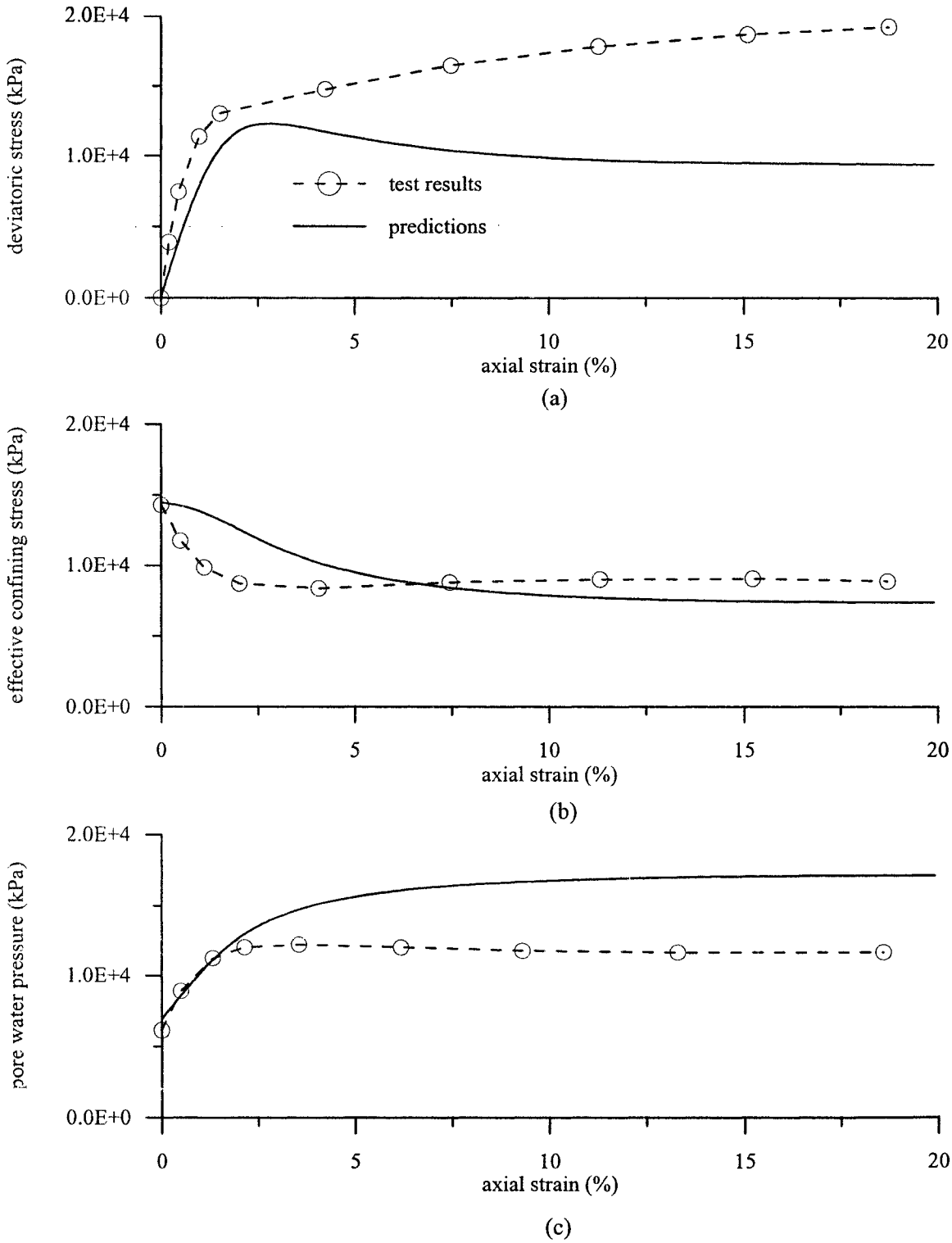

Figure 1.19: comparison of the model predictions and test results for conventional triaxial undrained tests for Oklahoma #1 sand under initial confining pressure of 2100 psi (14.5 MPa) (test data after Kmeid, 2003)

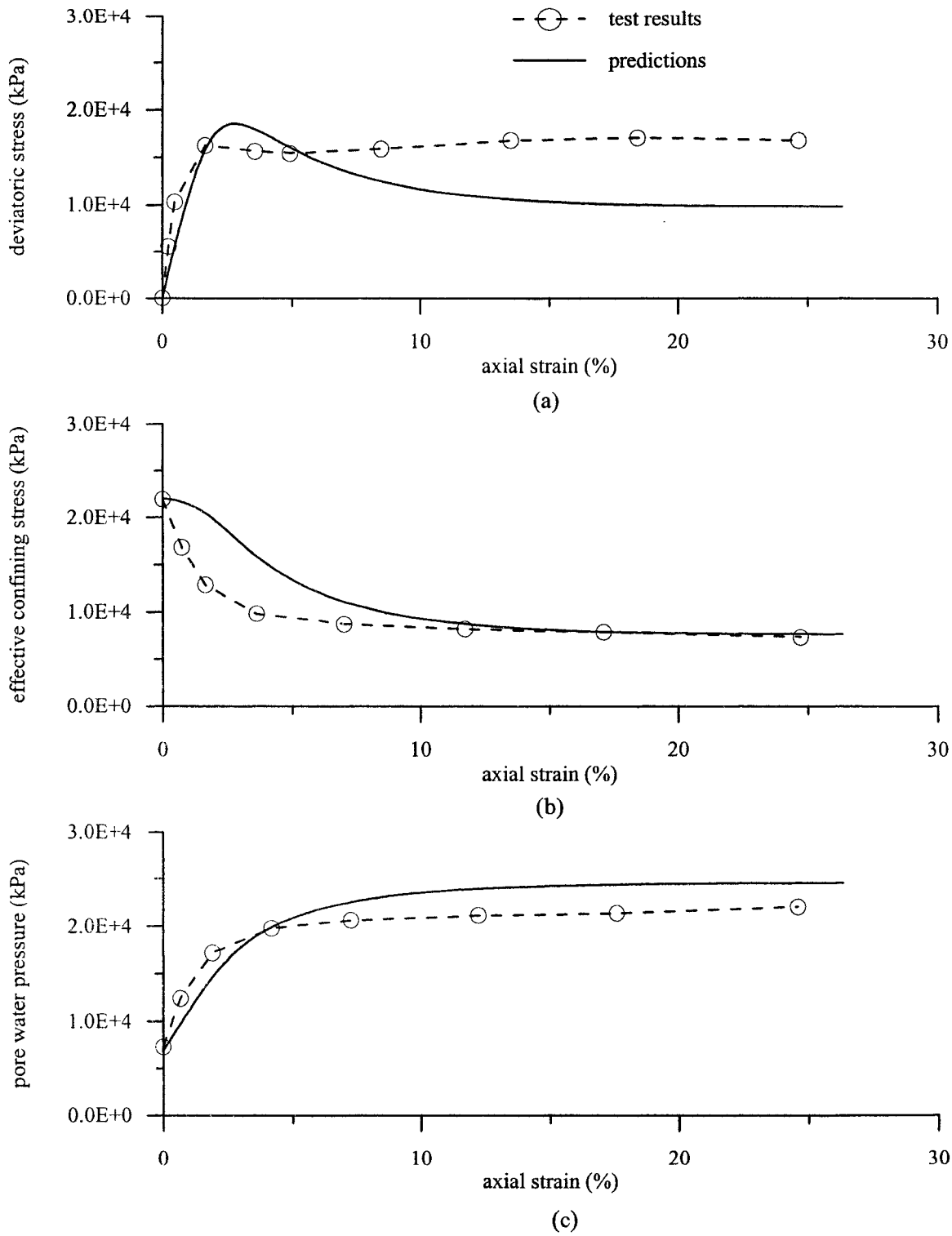

Figure 1.20: comparison of the model predictions and test results for conventional triaxial undrained tests for Oklahoma #1 sand under initial confining pressure of 3200 psi (22.1 MPa) (test data after Kmeid, 2003)

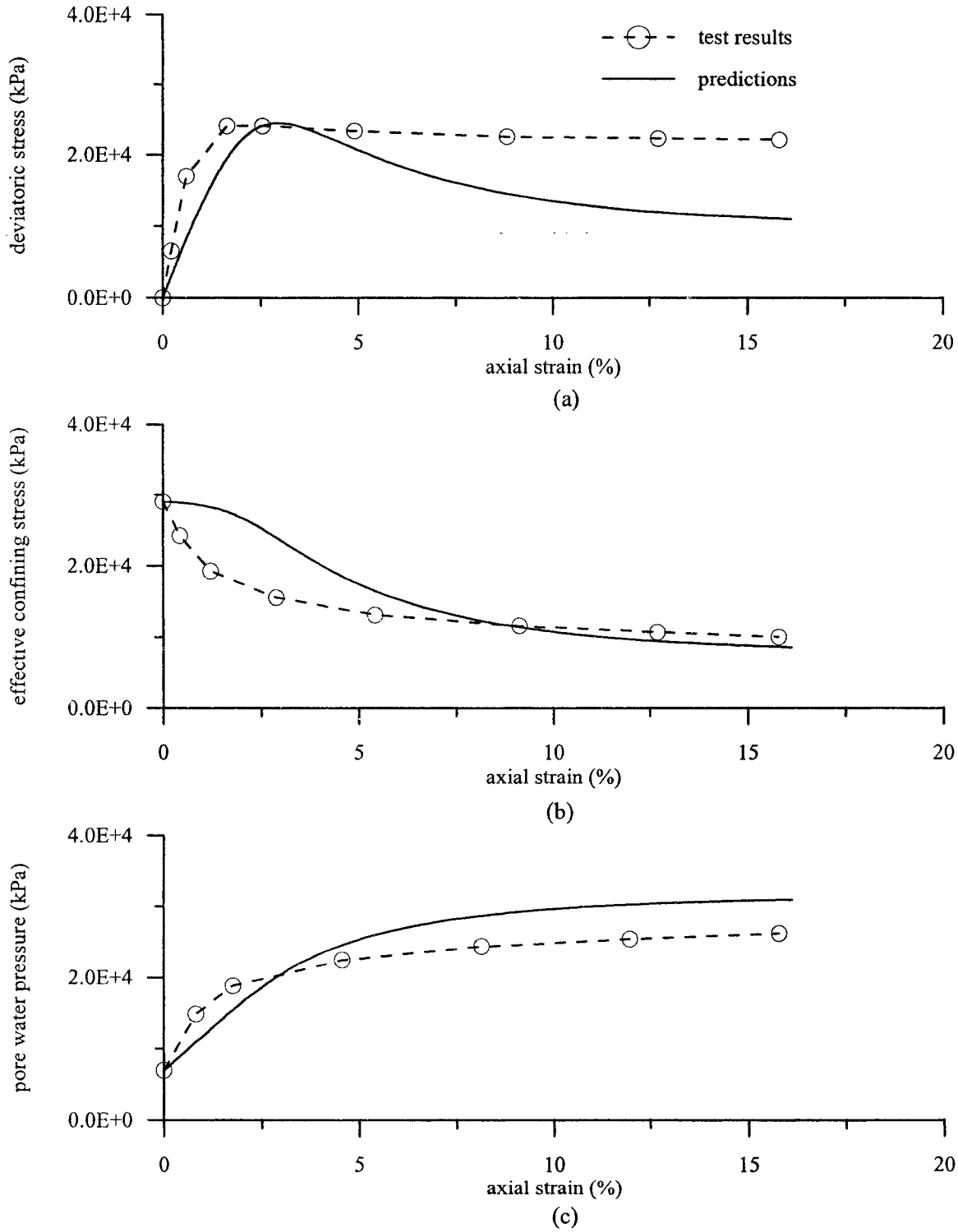

Figure 1.21: comparison of the model predictions and test results for conventional triaxial undrained tests for Oklahoma #1 sand under initial confining pressure of 4200 psi (29 MPa) (test data after Kmeid, 2003)

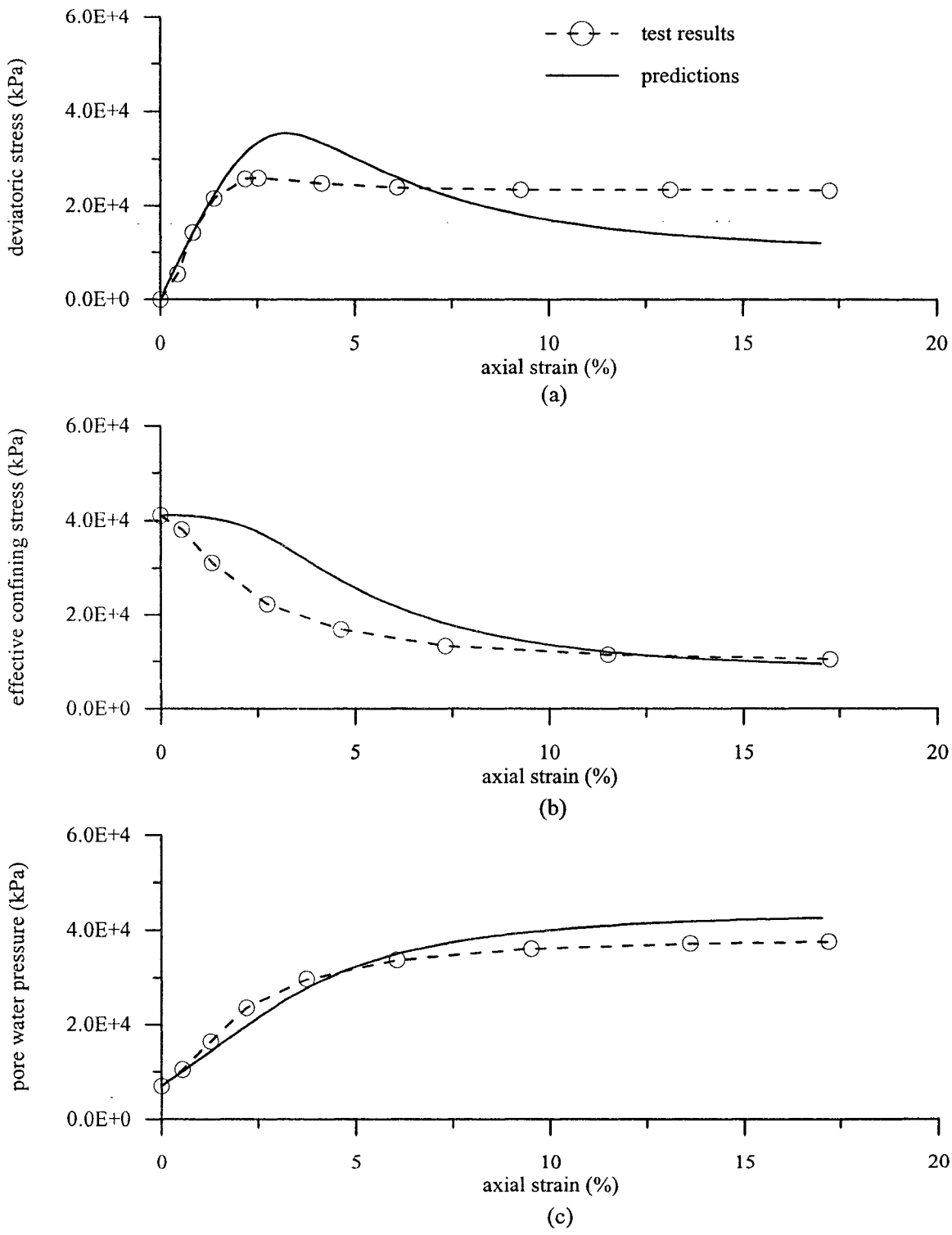

Figure 1.22: comparison of the model predictions and test results for conventional triaxial undrained tests for Oklahoma #1 sand under initial confining pressure of 5950 psi (41 MPa) (test data after Kmeid, 2003)

Chapter 2

General Stress Space Implementation of the Middle Surface Concept (MSC) for Saturated Sands

2.1 Introduction

In addition to the characteristics of sand response in monotonic triaxial loading conditions, described in Chapter 1, in general stress space considerable plastic deformation occurs during unloading and reloading. For example, during unloading, after the loading path crosses the phase transformation line, the volumetric contraction is so large that liquefaction or cyclic mobility may occur under undrained conditions (Ishihara et al., 1975). In addition, sand is an assemblage of particles and therefore the fabric – particle contact orientations – of a sand influences its stress-strain behavior significantly. A typical sand in the field or a sand sample prepared in the laboratory has an anisotropic fabric. That is, the particle contact orientations have a preferential direction. Even for an initially isotropic sand, an anisotropic fabric is produced during shearing. This type of anisotropy is called the stress-induced anisotropy. A significant portion of stress-induced anisotropy remains even after unloading. It has been observed (Oda, 1972; Arthur et al., 1986; Dean, 2003) that, although initially there were very little differences, shearing along different directions following a loading-unloading cycle gives different responses in terms of hardening and volumetric change. In this Chapter, extending the MSC sand model in monotonic triaxial conditions, the application of the MSC incorporating the effects of fabric anisotropy and cyclic loading response to general stress space is

presented. All the model parameters under monotonic loading conditions remain the same for the general stress space. This general stress space implementation provides further insights into the MSC and highlights its versatility as a general material modeling concept. Reference

2.2 Theory

The MSC was originally developed with three yield surfaces for triaxial monotonic loading conditions in Chapter 1. Among these three yield surfaces, one is the true yield surface and the other two are pseudo yield surfaces used to represent the critical state concept and the effects of the state parameter. In the original development, the true yield surface lies in between two pseudo yield surfaces and hence the name the "Middle Surface Concept". It is, however, not necessary for the MSC to have exactly three yield surfaces and the true yield surface doesn't necessarily have to lie in between the pseudo yield surfaces. In the general stress space model, four yield surfaces composed of one true yield surface and three pseudo yield surfaces are used. The first pseudo yield surface is used to represent the critical state concept of soils and unloading and reloading plastic deformation. The second pseudo yield surface is used to represent the development of fabric anisotropy. The influence of fabric anisotropy on sand behavior is represented with the combination of the first and second pseudo yield surfaces. The third pseudo yield surface is used to represent the effect of the state parameter on the hardening and softening response. Based on the test results (Tatsuoka and Ishihara, 1974), all the yield surfaces in the present model have a cone shape in the general stress space. In order to represent the differences in sand response along different

loading directions under isotropic fabric condition, some model parameters are made to depend on the Lode angle. In view of the fact that the state parameter significantly affects the dilatancy ratio, the phase transformation lines for all the pseudo yield surfaces are made to depend on their state parameters.

Common features of all the yield surfaces are first introduced and then specific details of different yield surfaces are developed. Following standard notations, the bold characters denote tensors.

For all the yield surfaces, the stress and strain rates consist of hydrostatic part and deviatoric part and are given as:

$$\dot{\boldsymbol{\sigma}} = \dot{\boldsymbol{s}} + \dot{p}\mathbf{I} \tag{2.1}$$

$$\dot{\boldsymbol{\varepsilon}} = \dot{\boldsymbol{e}} + \frac{1}{3}\dot{\varepsilon}_v \mathbf{I} \tag{2.2}$$

where p and ε_v denote hydrostatic part of stress and strain, respectively, and $\boldsymbol{s}$ and $\boldsymbol{e}$ denote deviatoric part of stress and strain tensors, respectively. The quantity $\mathbf{I}$ is the second-order isotropic tensor. All the yield surfaces have the shape of a cone in the general stress space and given by:

$$f = [(\boldsymbol{s} - p\boldsymbol{\alpha}) : (\boldsymbol{s} - p\boldsymbol{\alpha})]^{1/2} - mp = 0 \tag{2.3}$$

where $\boldsymbol{\alpha}$ denotes the position of the axis of the cone and mp is the radius of the cone. m is a relatively small constant and all the yield surfaces share the same value of m. In accordance with the classical elastoplasticity theory, the plastic strain rate $\dot{\boldsymbol{\varepsilon}}^p$ for all the yield surfaces is defined as:

$$\dot{\boldsymbol{\varepsilon}}^p = \dot{\boldsymbol{e}}^p + \frac{1}{3}\dot{\varepsilon}_v^p \mathbf{I} = \langle L \rangle \boldsymbol{R} \tag{2.4}$$

$$L = \frac{1}{K_p}\left(\frac{\partial f}{\partial \boldsymbol{\sigma}}\dot{\boldsymbol{\sigma}}\right) \tag{2.5}$$

where $\dot{\boldsymbol{e}}^p$, $\dot{\varepsilon}_v^p$ denote the deviatoric and hydrostatic parts of the plastic strain rate, respectively; $\boldsymbol{R}$ denotes the direction of the plastic strain rate; K_p denotes the plastic modulus; L denotes the loading index; and $\langle\ \rangle$ denotes Macauley brackets. When L is positive, $\langle L \rangle$ is equal to L. When L is negative, $\langle L \rangle$ is zero. In the classical elastoplasticity theory, all the yield surfaces satisfy the consistency condition, given as:

$$df = \frac{\partial f}{\partial \boldsymbol{\sigma}}\dot{\boldsymbol{\sigma}} + \frac{\partial f}{\partial \boldsymbol{\alpha}}\dot{\boldsymbol{\alpha}} = 0 \tag{2.6}$$

Usually, it is convenient to develop the formulations for cone type of yield surfaces on the stress ratio π-plane where the stress ratio is denoted by $\boldsymbol{r} = \boldsymbol{s}/p$ (see for example, Manzari and Dafalias, 1997). The deviatoric part of the normal to the yield surface on the stress ratio π plane is:

$$\boldsymbol{n} = \frac{\boldsymbol{r} - \boldsymbol{\alpha}}{m} \tag{2.7}$$

where $\boldsymbol{n}$ is a unity tensor. Correspondingly, the normal to the yield surface is:

$$\frac{\partial f}{\partial \boldsymbol{\sigma}} = \boldsymbol{n} - \frac{1}{3}N\mathbf{I} \tag{2.8}$$

where $N = \boldsymbol{n} : \boldsymbol{r}$. The loading index L can be rewritten as:

$$L = \frac{1}{K_p}(p\boldsymbol{n} : \dot{\boldsymbol{r}}) = \frac{1}{K_p}(\boldsymbol{n} : \dot{\boldsymbol{s}} - N\dot{p}) \tag{2.9}$$

The associative flow rule can be used for the deviatoric part of the plastic strain rate on the stress ratio π-plane and $\boldsymbol{R}$ can be rewritten as:

$$\boldsymbol{R} = \boldsymbol{n} + \frac{1}{3} D\mathbf{I} \tag{2.10}$$

where D denotes the dilatancy ratio. According to equations (2.4) and (2.10), the deviatoric part and hydrostatic part of the plastic strain rate can be split as:

$$\dot{\boldsymbol{e}}^{p} = \langle L \rangle \boldsymbol{n} \tag{2.11}$$

$$\dot{\varepsilon}_{v}^{p} = \langle L \rangle D \tag{2.12}$$

The consistency condition represented with equation (2.6) can be rewritten as:

$$\boldsymbol{n} : \dot{\boldsymbol{r}} = \boldsymbol{n} : \dot{\boldsymbol{\alpha}} \tag{2.13}$$

The elastic responses for the true and three pseudo yield surfaces are defined as:

$$\dot{\boldsymbol{e}}^{e} = \frac{\dot{\boldsymbol{s}}}{2G} \tag{2.14}$$

$$\dot{\varepsilon}_{v}^{e} = \frac{\dot{p}}{K} \tag{2.15}$$

where $\boldsymbol{e}^{e}$ and ε_{v}^{e} are the deviatoric and hydrostatic parts of the elastic strain, respectively. K and G are bulk and shear modulus, respectively, and are defined as:

$$K = K_0 (p / p_{at})^{a0} \tag{2.16}$$

$$G = G_0 (p / p_{at})^{a0} \tag{2.17}$$

where, K_0, G_0 and a_0 are elastic model parameters, and p_{at} is the atmospheric pressure used as the reference pressure.

2.2.1 Pseudo Yield Surfaces

The first pseudo yield surface employs the bounding surface concept to represent cyclic loading response and the critical state behavior. The bounding surface is chosen as

a cone in the general stress space with its axis as the hydrostatic stress axis. Its radius is $M'p_1$, where p_1 denotes the hydrostatic stress for the first pseudo yield surface. M' represents the critical state stress ratio M minus the radius of the yield surface m on the stress ratio π-plane. The plastic modulus for the first pseudo yield surface is defined based on $\boldsymbol{d}_1$, the distance tensor, on the stress ratio π-plane, between $\boldsymbol{\alpha}_1$ and the projection of the first pseudo stress state ($\boldsymbol{r}_1$) on the bounding surface, where $\boldsymbol{\alpha}_1$ denotes the center of the first pseudo yield surface. Figure 2.1 shows the relative positions of the first pseudo yield surface, the bounding surface, and the definition of $\boldsymbol{d}_1$ on the stress ratio π-plane. The projection of the first pseudo stress state ($\boldsymbol{r}_1$) on the bounding surface is obtained using the normal $\boldsymbol{n}_1$. The first pseudo plastic modulus K_{p1} is defined as:

$$K_{p1} = \frac{d_1^{\,2}}{(a/2)(M'_d - d_1)} p_1 \tag{2.18}$$

where, a is a model constant and M'_d is the diameter of the bounding surface on the stress ratio π-plane. d_1 denotes the trace of the product of $\boldsymbol{d}_1$ and $\boldsymbol{n}_1$, that is, $\boldsymbol{d}_1 : \boldsymbol{n}_1 = tr(\boldsymbol{d}_1 \boldsymbol{n}_1)$. According to the above definition, the closer the $\boldsymbol{\alpha}_1$ is to the projection of $\boldsymbol{r}_1$ on the bounding surface, the smaller the plastic modulus is. $\boldsymbol{\alpha}_1$ can approach but never go beyond the bounding surface so that the critical state behavior of sands can be represented. On the other hand, relatively large distance between $\boldsymbol{\alpha}_1$ and the projection of $\boldsymbol{r}_1$ on the bounding surface gives larger plastic modulus, such as during unloading. Similar definitions of bounding surface and plastic modulus can be found in Wang et al. (1990) and Manzari and Dafalias (1997). What is unique about the current definition of bounding surface is that the radius of the bounding surface is a constant M'. This fixed

bounding surface definition can avoid the difficulties associated with controlling the evolution of the bounding surface under complicated loading conditions, such as constant stress ratio loading and cyclic simple shear loading.

In order to determine the dilatancy ratio for the first pseudo yield surface, a dilatancy surface is developed. The radius of the dilatancy surface on the stress ratio π-plane is $M' + k_2\psi_1$, where k_2 is a model constant and ψ_1 is the state parameter for the first pseudo yield surface given together with those for the true and other pseudo yield surfaces as:

$$\psi_i = e_i - e_{cri} \qquad (i = true, 1, 2, 3) \tag{2.19a}$$

$$e_{cri} = e_{ref} - \lambda \ln(p_i / p_{ref}) \tag{2.19b}$$

where e_i denotes the void ratio and e_{cri} denotes the void ratio on the critical state line under the current confining pressure for a particular yield surface; λ, p_{ref}, and e_{ref} are model parameters for defining the critical state void ratio. There are alternative formulations for the critical void ratio. For example, Li and Dafalias (2000) used:

$$e_{cr} = e_{ref} - \lambda(p / p_{at})^{\xi} \tag{2.19c}$$

where ξ is a model parameter. The dilatancy surface is also illustrated in Figure 2.1. The dilatancy ratio is defined based on the distance tensor $\boldsymbol{c}_1$ between the center of the first pseudo yield surface and the projection of the first pseudo stress state on the dilatancy surface. The dilatancy ratio is given as:

$$D_1 = Ac_1 \tag{2.20}$$

where, A is a model constant and $c_1 = \boldsymbol{c}_1 : \boldsymbol{n}_1$. From Figure 2.1 and equation (2.20), it can be seen that, when $\boldsymbol{\alpha}_1$ is inside of the dilatancy surface, D_1 is always positive and

represents volumetric contraction. When $\boldsymbol{\alpha}_1$ is outside of the dilatancy surface, the sign of D_1 depends on the loading direction. For example, during the triaxial compression, when $\boldsymbol{\alpha}_1$ goes outside of the dilatancy surface, the directions of $\boldsymbol{c}_1$ and $\boldsymbol{n}_1$ are opposite and gives negative c_1, representing volumetric dilation. On the other hand, for unloading following the triaxial compression, when the stress point is outside the dilatancy surface, the directions of $\boldsymbol{c}_1$ and $\boldsymbol{n}_1$ are the same and gives positive c_1, representing volumetric contraction. In this case, c_1 is larger than that for the initial triaxial compression loading and leads to larger volumetric contraction. This is consistent with the test results by Pradhan and Tatsuoka (1989). Similar to the formulation of the dilatancy ratio under monotonic loading conditions in Chapter 1, the dilatancy ratio in equation (2.20) is dependent on the state parameter. As described above, the stress ratio for the first pseudo yield surface will eventually reach the critical state at the end of loading. Correspondingly, the above defined dilatancy surface will coincide with the bounding surface and leads to a state parameter value of zero indicating that the void ratio has reached the critical state. The evolution of the hardening parameter for the first pseudo yield surface will be defined together with the true hardening parameter in a later section.

The second pseudo yield surface is designed to capture the influence of anisotropic fabric of sands. A sample of sand is an assembly of numerous particles, and the distribution of particle contacts, also named fabric, may not be the same along different directions. This anisotropic fabric, named the initial anisotropy, may be set in a sand sample during the course of deposition in the field or sample preparation in the laboratory. Anisotropic fabric can also result during the course of loading. Such anisotropic fabric resulting from loading is called the stress-induced anisotropy. Both

initial and stress-induced anisotropy are represented with the second pseudo yield surface. The influence of anisotropic fabric on the stress-strain behavior of sands will be represented by modifying the first pseudo yield surface using the second pseudo yield surface, which will be described in a later section. It was discovered that the stress-induced anisotropic fabric can be best represented with the plastic deviatoric strain (Arthur et al., 1986; Calvetti et al., 1997). Arthur et al.'s (1986) tests involved a change in major principal stress direction for reloading following the initial loading and unloading to zero deviatoric stress. They found that the reloading behavior was greatly influenced by the previously incurred changes in the particle contact distribution that was related to the plastic deviatoric strain incurred during the previous loading. Calvetti et al. (1997) studied the stress-induced anisotropy more thoroughly using both analytical and experimental techniques under complex loading conditions including continuous rotation of the principal stress direction. They concluded that the variation of contact distribution in a granular material could be approximately represented by the incremental strain tensor with plastic deviatoric strain increment playing the main role. In accordance with above studies, the second pseudo hardening parameter is defined as:

$$\alpha_2 = M' \frac{\boldsymbol{e}_2^p + \boldsymbol{F}_0}{a + \left|\boldsymbol{e}_2^p + \boldsymbol{F}_0\right|} \tag{2.21}$$

where a and M' are the same model constants as in the first pseudo yield surface, and $|\ |$ denotes the magnitude of a tensor. $\boldsymbol{F}_0$ denotes the initial anisotropy, which becomes zero for the initially isotropic samples. The flow rule for the second pseudo yield surface is defined similar to that for the first pseudo yield surface and is given as:

$$D_2 = Ac_2 \tag{2.22}$$

where A is the same model constant as in the first pseudo yield surface. $c_2 = \boldsymbol{c}_2 : \boldsymbol{n}_2$, where $\boldsymbol{c}_2$ is the distance tensor between $\boldsymbol{\alpha}_2$ and the projection of the second pseudo stress state on the second pseudo dilatancy surface with the radius of $M' + k_2\psi_2$ on the stress ratio π-plane. The selection of this specific form for the second pseudo yield surface will be validated in a later section.

The third pseudo yield surface is designed to take into account the effect of the state parameter on the hardening response. The combination of the third and the first pseudo yield surfaces can be used to represent the softening response for dense sands during the later stages of loading. The effect of the state parameter is incorporated into the plastic modulus for the third pseudo yield surface given by:

$$K_{p3} = \exp(-k_1\psi_3) K_{p1} \tag{2.23}$$

where k_1 is a model constant and K_{p1} is the plastic modulus for the first pseudo yield surface. Because the state parameter for medium dense and dense sands is usually negative, from equation (2.23), the plastic modulus for the third pseudo yield surface is larger than that for the first pseudo yield surface. In contrast, loose sands with a positive state parameter will have a smaller plastic modulus for the third pseudo yield surface than that for the first one. Similar to the first and second pseudo yield surfaces, the dilatancy ratio for the third pseudo yield surface is defined as:

$$D_3 = Ac_3 \tag{2.24}$$

where $c_3 = \boldsymbol{c}_3 : \boldsymbol{n}_3$. c_3 denotes the distance tensor between $\boldsymbol{\alpha}_3$ and the projection of the third pseudo stress state on the third pseudo dilatancy surface with the radius of $M' + k_2\psi_3$ on the stress ratio π-plane. The hardening parameter for the third pseudo yield

surface will be defined in a later section together with the hardening parameters for the first pseudo and true yield surfaces.

2.2.2 Construction of the True Yield Surface

The true yield surface will be next constructed by using the three pseudo yield surfaces and various links between the yield surfaces. The links should be selected to make the problem solvable and minimize the computational effort. In addition, the selection of links is supposed to assist these three pseudo yield surfaces and their combinations to fulfill their designed functions. In this MSC sand model, at the beginning of loading, all the yield surfaces share the same initial conditions. During the course of loading, there are two types of links corresponding to purely elastic response when stress points are inside the yield surfaces and elastoplastic response when stress points are on the yield surfaces. The links for elastoplastic response are introduced first. For elastoplastic loading, the links consist of certain common quantities shared by all the yield surfaces and relationships between their dilatancy ratios, hardening rules, and plastic moduli. The common quantities for the elastoplastic response are selected as the hydrostatic stress p and the plastic deviatoric strain tensor $\boldsymbol{e}^p$, that is:

$$p = p_1 = p_2 = p_3 \tag{2.25}$$

$$\boldsymbol{e}^p = \boldsymbol{e}_1^p = \boldsymbol{e}_2^p = \boldsymbol{e}_3^p \tag{2.26}$$

Since all the yield surfaces are defined on the stress ratio ($\boldsymbol{r} = \boldsymbol{s}/p$) π-plane a common p can significantly reduce the computational effort. In addition, p is a scalar and easy to manipulate. The reason to select the same $\boldsymbol{e}^p$ for all the yield surfaces is that the accumulated deviatoric plastic strain is the basis to construct the links between the

hardening rules and dilatancy rules as described subsequently. From equations (2.26) and (2.11), it is evident that the deviatoric part of the normal to all the yield surfaces and the loading indices for all the yield surfaces are the same, given as:

$$\boldsymbol{n} = \boldsymbol{n}_1 = \boldsymbol{n}_2 = \boldsymbol{n}_3 \tag{2.27}$$

$$L = L_1 = L_2 = L_3 \tag{2.28}$$

From equations (2.27) and (2.28), another advantage for selecting the same $\boldsymbol{e}^p$ can be seen. The same $\boldsymbol{e}^p$ for all the yield surfaces results in the same $\boldsymbol{n}$ and L for all the yield surfaces thereby reducing the computational effort.

The construction of the true yield surface is composed of two steps. The first step is to modify the first pseudo yield surface by using the second pseudo yield surface. The second step is to develop the formulations for the true yield surface based on the modified first pseudo yield surface and the third pseudo yield surface. The first step is described in this section. After incorporating the influence of the second pseudo yield surface, the first pseudo yield surface is renamed "the modified first pseudo yield surface." Recall that the first pseudo yield surface is designed to represent the critical state behavior, and unloading and reloading plastic deformation of sands. The second pseudo yield surface is designed to describe the evolution of the anisotropic fabric of sands. The modified first pseudo yield surface retains the functions of the first pseudo yield surface, and at the same time, represents the effects of anisotropic fabric on sand behavior. The hardening parameter for the modified first pseudo yield surface is denoted by $\boldsymbol{\alpha}_{12}$, where the subscript "12" refers to the quantities for the modified first pseudo yield surface.

The modified first pseudo plastic modulus is defined as:

$$K_{p12} = \frac{d_{12}^{\ 2}}{(a/2)(M_d' - d_{12})} p + f_K |(\boldsymbol{\alpha}_2 - \boldsymbol{\alpha}_{12}) : \boldsymbol{n}| \tag{2.29a}$$

$$f_K = h_1 p \frac{(\boldsymbol{\alpha}_2 - \boldsymbol{\alpha}_{12}) : \boldsymbol{n}}{|(\boldsymbol{\alpha}_2 - \boldsymbol{\alpha}_{12}) : \boldsymbol{n}|} \tag{2.29b}$$

The modified first pseudo dilatancy ratio is defined as:

$$D_{12} = Ac_{12} + f_D |(\boldsymbol{\alpha}_2 - \boldsymbol{\alpha}_{12}) : \boldsymbol{n}| \tag{2.30a}$$

$$f_D = h_2 D_2 \tag{2.30b}$$

For the first term on the right hand side of equations (2.29a) and (2.30a), the definitions of d_{12} and c_{12} are similar to d_1 and c_1. $d_{12} = \boldsymbol{d}_{12} : \boldsymbol{n}$ where $\boldsymbol{d}_{12}$ represents the distance tensor between $\boldsymbol{\alpha}_{12}$ and the projection of the modified first pseudo stress state on the bounding surface. $c_{12} = \boldsymbol{c}_{12} : \boldsymbol{n}$ where $\boldsymbol{c}_{12}$ represents the distance tensor between $\boldsymbol{\alpha}_{12}$ and the projection of the modified first pseudo stress state on the modified first dilatancy surface. The second term on the right hand side of equations (2.29a) and (2.30a) represents the influence of the second pseudo yield surface, and therefore, the effect of fabric anisotropy on sand behavior. In equations (2.29b) and (2.30b), h_1 and h_2 are model constants. It is the relative distance between the hardening parameters of the second and the modified first pseudo yield surfaces, $\boldsymbol{\alpha}_2 - \boldsymbol{\alpha}_{12}$, that plays the key role for representing the effects of fabric on sand behavior. If the effects of the fabric are ignored, the modified first pseudo yield surface is identical to the first pseudo yield surface. The incorporation of the effect of the second pseudo yield surface into the first pseudo yield surface doesn't affect the ability of the modified first pseudo yield surface to reach the critical state at the end of loading, because the second pseudo yield surface also reaches the critical state at the end of loading. Because the modified first pseudo yield surface is

used to replace the first pseudo yield surface, the plastic modulus for the third pseudo yield surface in equation (2.23) is changed to:

$$K_{p3} = \exp(-k_1 \psi_3) K_{p12} \tag{2.31}$$

To demonstrate how the effects of fabric are represented by using equations (2.29) and (2.30), without the loss of generality, consider the responses for drained triaxial compression loading, followed by unloading to zero deviatoric stress and reloading along triaxial compression and extension. The influence of the fabric anisotropy can be clearly demonstrated by comparing the responses for the first pseudo and the modified first pseudo yield surface. In this example, the hydrostatic stress remains constant, and the initial state of the fabric is assumed to be isotropic so that only the effect of stress-induced anisotropy is considered. Figure 2.2 shows the simulated responses from the first, second and the modified first pseudo yield surfaces, where the elastic responses are neglected. Figures 2.2 (a) and (b) show the hardening responses and volume changes, respectively, for initial compression loading and unloading. Figures 2.2 (c) and (d) show the hardening responses and volume changes, respectively, for compression reloading and extension reloading. Note that all the yield surfaces share the same plastic deviatoric strain.

During the initial triaxial compression in Figure 2.2 (a), the second pseudo hardening response goes up along the hyperbolic curve represented by equation (2.21). Although an anisotropic fabric is created during the initial triaxial compression loading, this fabric has little influence on the modified first pseudo response. The reason is that the first, second and modified first pseudo hardening responses are almost identical and $\alpha_2 - \alpha_{12}$ is negligible. The nearly identical hardening responses can be explained by

comparing the plastic moduli between the first pseudo, the second pseudo and the modified first pseudo yield surfaces. For the triaxial compression loading, the plastic modulus for the second pseudo yield surface can be rewritten in the form of the first and modified first pseudo yield surfaces by using equations (2.9), (2.11), (2.13) and (2.21), given as:

$$K_{p2} = \frac{d_2^2}{(a/2)M_d'} p \tag{2.32}$$

where d_2 denotes the distance between α_2 and the projection of the second pseudo stress state on the bounding surface. Comparison of equations (2.18), (2.29) and (2.32) shows that K_{p1}, K_{p2} and K_{p12} are almost identical, given the relatively small values of d_1, d_2 and d_{12} for initial triaxial compression loading. The same argument applies to the volumetric changes that are almost identical for all the three pseudo yield surfaces as shown in Figure 2.2 (b).

During the unloading, the second pseudo yield surface goes down along the same hyperbolic curve until zero deviatoric stress is reached by the first and the modified first pseudo yield surfaces in Figure 2.2 (a). At this point, the deviatoric plastic strain is not zero, indicating the existence of anisotropic fabric. In Figure 2.2 (a), the modified first pseudo yield surface moves down at a faster rate than the second pseudo yield surface. Correspondingly, a large distance tensor $\alpha_2 - \alpha_{12}$ directed upward is induced between the second pseudo and the modified first pseudo yield surfaces. As $\boldsymbol{n}$ is directed downward, $(\alpha_2 - \alpha_{12}) : \boldsymbol{n}$ is negative. From equations 2.29 (a) and (b), this negative value hinders the downward movement of the modified first pseudo yield surface by decreasing its plastic modulus compared with that for the first pseudo yield surface. As for the plastic

volumetric change during unloading, the large distance between the second pseudo yield surface and its phase transformation line gives a considerable volumetric contraction represented with D_2. Thus, the inclusion of D_2 in equations 2.30 (a) and (b) significantly increases the volumetric contraction for the modified first pseudo yield surface compared with that for the first pseudo yield surface as shown in Figure 2.2 (b).

Following the unloading to zero deviatoric stress, separate reloading is carried out along triaxial compression and extension. The second pseudo yield surface still moves upward and downward, respectively, corresponding to compression and extension reloading along the same hyperbolic curve. For the triaxial compression reloading, the second pseudo yield surface lies above the modified first pseudo yield surface as shown in Figure 2.2 (c). $\boldsymbol{\alpha}_2 - \boldsymbol{\alpha}_{12}$ and $\boldsymbol{n}$ are both directed upward and their product is positive. Therefore, the second pseudo yield surface enhances the hardening of the modified first pseudo response compared with that for the first pseudo yield surface as shown in Figure 2.2 (c). During the triaxial compression reloading, the second pseudo yield surface is usually above its phase transformation line and leads to negative D_2 indicating volumetric dilation. Thus, the inclusion of D_2 into the modified first pseudo dilatancy rule in equation (2.30) reduces its volumetric contraction, compared with that for the first pseudo yield surface in Figure 2.2 (d). In contrast, for the triaxial extension reloading, the second pseudo yield surface lies below the modified first pseudo yield surface in Figure 2.2 (c). $\boldsymbol{\alpha}_2 - \boldsymbol{\alpha}_{12}$ and $\boldsymbol{n}$ have opposite directions and their product is negative. This hinders the hardening response of the modified first pseudo yield surface, compared with that for the first pseudo yield surface as shown in Figure 2.2 (c). Similar to unloading, the relatively large volumetric contraction from the second pseudo yield surface and large

distance $(\alpha_2 - \alpha_{12}) : n$ significantly increase the volumetric contraction for the modified first pseudo yield surface, compared with that for the first pseudo yield surface as shown in Figure 2.2 (d). It should be noted that, during the course of reloading, the modified first pseudo yield surface keeps approaching the second pseudo yield surface and the distance between them keeps decreasing. It indicates that the effects of anisotropic fabric on the reloading response keep decreasing until the modified first pseudo yield surface meets the second pseudo yield surface, where the effects of anisotropic fabric disappear. The decrease of the anisotropic fabric effects with the increase of reloading has been verified in experimental studies (Arthur et al., 1980).

From the above example and equations (2.29) and (2.30), it is evident that the effects of anisotropic fabric depend on $(\alpha_2 - \alpha_{12}) : n$ and D_2. The negative $(\alpha_2 - \alpha_{12}) : n$ and positive D_2 hinder the hardening response and enhance the plastic volumetric contraction during the unloading and extension reloading. In the case of undrained loading condition, if the initial triaxial compression loading is large enough (for example, goes over the phase transformation line), the reduction of the hardening response and increase of the plastic volumetric contraction by the second pseudo yield surface during the unloading and extension reloading may induce liquefaction.

The true yield surface is developed based on the modified first pseudo and the third pseudo yield surfaces, and lies in between them. The true hardening parameter together with the hardening parameters for the modified first and the third pseudo yield surfaces is defined as:

$$\alpha = \frac{\xi^p}{b + \xi^p} \alpha_{12} + \frac{b}{b + \xi^p} \alpha_3 \tag{2.33}$$

$$\dot{\boldsymbol{\alpha}} = \langle L \rangle \frac{K_p}{p} \boldsymbol{n} \tag{2.34}$$

$$\boldsymbol{\alpha}_{12} = g_{12} \boldsymbol{\alpha} \tag{2.35}$$

$$\boldsymbol{\alpha}_3 = g_3 \boldsymbol{\alpha} \tag{2.36}$$

where b is a model constant and ξ^p is a scalar, representing the accumulated plastic deviatoric strain. In equation (2.33), the true hardening parameter is close to the third pseudo hardening parameter during the early stages of loading when ξ^p is relatively small. Recall that the third pseudo hardening response depends on the state parameter. Thus, the effect of the state parameter on the true hardening response is reflected during the early stages of loading. During the later stages of loading, where ξ^p is relatively large, the true hardening parameter approaches the modified first pseudo hardening parameter as shown in equation (2.33). As the modified first pseudo stress ratio is designed to reach the critical state at the end of loading, it brings the true stress ratio to reach the critical state. In equations (2.35) and (2.36), the modified first and third pseudo hardening parameters are related with the true hardening parameter through two scalars g_{12} and g_3, respectively. This can significantly reduce the computational effort without affecting their designed functions, because two tensors $\boldsymbol{\alpha}_{12}$ and $\boldsymbol{\alpha}_3$ are simplified and replaced with two scalars g_{12} and g_3. In addition, as $\boldsymbol{\alpha}_{12}$, $\boldsymbol{\alpha}_3$ and $\boldsymbol{\alpha}$ remain along the same direction on the stress ratio π-plane, their evolutions are easier to control.

Differentiating both sides of equation (2.33), one can obtain:

$$\dot{\boldsymbol{\alpha}} = \frac{\xi^p}{b+\xi^p} \dot{\boldsymbol{\alpha}}_{12} + \frac{b}{b+\xi^p} \dot{\boldsymbol{\alpha}}_3 + \frac{b}{(b+\xi^p)^2} (\boldsymbol{\alpha}_{12} - \boldsymbol{\alpha}_3) \dot{e}^p \tag{2.37}$$

where, $\dot{e}^p$ is the magnitude of the plastic deviatoric strain rate tensor. Multiplying by $\boldsymbol{n}$ the both sides of equation (2.37) and using equation (2.13), one can obtain:

$$\boldsymbol{n} : \dot{\boldsymbol{r}} = \frac{\xi^p}{b+\xi^p} \boldsymbol{n} : \dot{\boldsymbol{r}}_{12} + \frac{b}{b+\xi^p} \boldsymbol{n} : \dot{\boldsymbol{r}}_3 + \frac{b}{(b+\xi^p)^2} \boldsymbol{n} : (\boldsymbol{\alpha}_{12} - \boldsymbol{\alpha}_3) \dot{e}^p \tag{2.38}$$

Using equations (2.9), (2.11) and common quantities for all the yield surfaces, one can obtain the plastic modulus for the true yield surface from equation (2.38) as:

$$K_p = \frac{\xi^p}{b+\xi^p} K_{p12} + \frac{b}{b+\xi^p} K_{p3} + p \frac{b}{(b+\xi^p)^2} \boldsymbol{n} : (\boldsymbol{\alpha}_{12} - \boldsymbol{\alpha}_3) \tag{2.39}$$

Differentiating both sides of equations (2.35) and (2.36), along the same line as the above given derivation, one can obtain:

$$\dot{g}_i = \frac{\langle L \rangle}{p(\boldsymbol{\alpha} : \boldsymbol{n})} (K_{pi} - g_i K_p) \qquad (i = 12, 3) \quad when\ \boldsymbol{\alpha} : \boldsymbol{n} \neq 0 \tag{2.40}$$

It should be noted that, in equation (2.40), when the product of $\boldsymbol{\alpha}$ and $\boldsymbol{n}$ is close to zero, the progress of g_i is difficult to control. Under these circumstances, without affecting the overall performance of the model, g_i is assumed not to change.

The dilatancy ratio for the true yield surface is determined through a relationship between the state parameters of the true, modified first, and the third pseudo yield surfaces as given by:

$$\psi = \frac{\xi^p}{c+\xi^p} \psi_{12} + \frac{c}{c+\xi^p} \psi_3 \tag{2.41}$$

where c is a model constant. In equation (2.41), the true state parameter approaches that of the modified first pseudo yield surface as the accumulated plastic deviatoric strain increases. As described above, the state parameter for the modified first pseudo yield surface reaches zero at the end of loading. Correspondingly, it also brings the true state

parameter to zero. This indicates that the true void ratio reaches the critical state at the end of loading together with that for the modified first pseudo yield surface. Differentiating equation (2.41), with the definition of state parameters in equation (2.19), one can obtain:

$$\dot{e} - \dot{e}_{cr} = \frac{\xi^p}{c+\xi^p}(\dot{e}_{12} - \dot{e}_{cr12}) + \frac{c}{c+\xi^p}(\dot{e}_3 - \dot{e}_{cr3}) + \frac{c}{(c+\xi^p)^2}(\psi_{12} - \psi_3)\dot{e}^p \quad (2.42a)$$

$$\dot{e}_i = -(1+e_0)\dot{\varepsilon}_{vi} \qquad (i = true, 12, 3) \quad (2.42b)$$

where e_0 is the initial void ratio. Because all the yield surfaces share the same hydrostatic stress, the elastic part of volumetric strain rate and the critical state void ratio are the same for all the yield surfaces in equation (2.42a). Canceling the elastic part of volumetric changes and the critical state void ratios on both sides of equation (2.42a) and dividing equation (2.42a) with the magnitude of deviatoric plastic strain rate $\dot{e}^p$, one can obtain the dilatancy ratio for the true yield surface as:

$$D = \frac{\xi^p}{c+\xi^p} D_{12} + \frac{c}{c+\xi^p} D_3 - \frac{1}{(1+e_0)} \frac{c}{(c+\xi^p)^2}(\psi_{12} - \psi_3) \quad (2.43)$$

There are three pseudo dilatancy surfaces, three pseudo state parameters, and three pseudo flow rules in the formulation presented above. All of them are used to represent the dependence of volumetric change on the state parameter. It was found that the flow rule for the modified first pseudo yield surface alone can represent the state parameter dependence of the volumetric change, except for extremely loose or dense sands. Therefore, for the sands with a normal relative density, the dilatancy ratio for the true yield surface can be simplified to be equal to that for the modified first pseudo yield surface, given as:

$$D = D_{12} \tag{2.44a}$$

According to equations (2.41) and (2.43), this leads to

$$D_3 = D_{12} \tag{2.44b}$$

$$\psi_3 = \psi_{12} \tag{2.44c}$$

$$\psi = \psi_{12} \tag{2.44d}$$

Further simplification can be made without greatly affecting the functions of the pseudo yield surfaces by replacing the second pseudo dilatancy surface with the dilatancy surface for the modified first pseudo yield surface. Thus, there is only one dilatancy surface, the modified first pseudo dilatancy surface, in the simplified version of the model formulation.

It is well known that sand response is different along different loading directions even for initially isotropic fabric condition, such as different responses in triaxial compression and extension. In order to reflect this difference, some model constants are made to depend on the Lode angle, given as:

$$Q_\theta = g(\theta, c_e) Q_c \tag{2.45a}$$

$$g(\theta, c_e) = \frac{2c_e}{(1+c_e) - (1-c_e)\cos 3\theta} \tag{2.45b}$$

$$c_e = \frac{Q_e}{Q_c} \tag{2.45c}$$

where Q_θ represents a model constant that depends on the Lode Angle θ, Q_c and Q_e denote the value of that model constant in triaxial compression and extension, respectively. The Lode angle at any stress state is defined as:

$$\cos 3\theta = \frac{3\sqrt{3}}{2}\left(\frac{\bar{S}}{\bar{J}}\right)^3 \tag{2.46a}$$

$$\bar{J} = \left(\frac{1}{2} tr\bar{\boldsymbol{r}}\right)^{1/2} \tag{2.46b}$$

$$\bar{S} = \left(\frac{1}{3} tr\bar{\boldsymbol{r}}\right)^{1/3} \tag{2.46c}$$

$$\bar{\boldsymbol{r}} = \boldsymbol{r} - \boldsymbol{\alpha} \tag{2.46d}$$

where $\bar{J}$ and $\bar{S}$ are the second and third invariants of the stress tensor. By calibrating the model parameters based on triaxial compression and extension test results, it was found that the model parameters a (for hardening response), k_2 (for volumetric change), and M (for critical stress ratio) are those that depend on the Lode angle the most.

The above described is the formulation for elastoplastic response. The problem is not complete until the links between various yield surfaces are defined in purely elastic response. For the elastic response when the stress paths move inside yield surfaces, in addition to the same hydrostatic stress as described in equation (2.25), it is proposed that all the yield surfaces have the same deviatoric stress tensor rate, which is given as:

$$\dot{\boldsymbol{s}} = \dot{\boldsymbol{s}}_{12} = \dot{\boldsymbol{s}}_2 = \dot{\boldsymbol{s}}_3 \tag{2.47}$$

Because all the yield surfaces share the same hydrostatic stress, the same rate of deviatoric stress tensor, and the same radius of yield surface, following the elastic response, the true and all the pseudo stress paths will reach the same position on their respective yield surfaces, and share the same $\boldsymbol{n}$. This is consistent with the proposition of the same $\boldsymbol{n}$ for all the yield surfaces in the elastoplastic response.

2.3 Model Prediction

The proposed model is used to predict the responses of two different types of sands, Nevada sand and Toyoura sand, under cyclic triaxial and simple shear loading conditions (Arulmoli et al., 1992; Uchida and Stedman, 2001). The model parameters in Chapter 1 are used for predictions except h_1 and h_2 representing the effects of stress-induced anisotropy and F_0 representing the effects of the initial anisotropy. Because the densities of the tested samples are in the normal range, the simplified model described above is used. F_0 can be calibrated by comparing the triaxial test results in which the loading is applied along different angles with respect to the particle contact orientation angle of the sample. Alternatively, F_0 can also be obtained by using indirect methods such as electrical methods (Arulmoli et al., 1985; Dafalias and Arulanandan 1979). Due to the lack of test results for Nevada sand, F_0 is set zero for the predictions presented here. The calibration of h_1 and h_2 was performed by using the undrained cyclic loading response. During the early stages of cyclic loading, the induced plastic deviatoric strain is relatively small, resulting in relatively small anisotropic fabric. With increasing number of cycles, the induced plastic deviatoric strain begins to increase producing a relatively large anisotropic fabric. Therefore, the calibration of h_1 and h_2 can be made during the later stages of cyclic loading. The parameter h_1 is responsible for the effect of fabric on the stiffness. The parameter h_2 is responsible for the effect of fabric on the volumetric change and is reflected by the decrease in effective confining pressure in cyclic undrained loading.

Table 2.1 lists all the model constants for Nevada sand under triaxial stress space and general stress space. The conversion of the model parameters from triaxial stress space to general stress space is given in the Appendix I. In addition to the model parameters calibrated in Chapter 1, h_1 and h_2 are calibrated by using the test result for relative density of 60% under the initial confining pressure of 80 kPa, shown in Figure 2.3. The test results and predictions for cyclic triaxial undrained loading for a sample with a relative density of 40% and an initial confining pressure of 80 kPa are shown in Figures 2.5 and 2.6, respectively. Good comparisons between the model predictions and test results are achieved for both 40% and 60% relative densities using the *same set of model parameters*. The magnitude of deviatoric stress change in these two tests is about the same, around ±30 kPa, and as expected, the sample with a 40% relative density reaches liquefaction in fewer number of cycles than the 60% relative density sample. The proposed model captures this dependence of liquefaction potential on the relative density of sands very well.

For the Nevada sand with a relative density of 60%, in addition to the model predictions with the true yield surface shown in Figure 2.4, the predicted responses using only the first pseudo and modified first pseudo yield surfaces are also shown in Figures 2.7 and 2.8, respectively. These predictions are shown in order to demonstrate the roles of the second and third pseudo yield surfaces during undrained cyclic loading. Comparing Figures 2.7 and 2.8, one can identify the influence of the second pseudo yield surface on undrained cyclic response. During the early stages of cyclic loading, the responses represented with the first and modified first pseudo yield surfaces are almost identical because the deviatoric plastic strain is relatively small, resulting in smaller anisotropic

fabric. With the increase in number of cycles, the deviatoric plastic strain increases and the role of the second pseudo yield surface becomes greater. Consequently, liquefaction is reached by using the modified first pseudo yield surface as shown in Figure 2.8. In contrast, the effective confining pressure doesn't reach zero when using the first pseudo yield surface as shown in Figure 2.7. As shown in Figure 2.2, larger contraction predicted by the modified first pseudo yield surface during unloading and extension reloading is the reason for the sample reaching liquefaction as shown in Figure 2.8. From Figure 2.7, it can also be seen that, although the liquefaction is not reached by using the first pseudo yield surface, the axial strain keeps increasing. This results from the different plastic modulus between compression and extension loading. This considerable strain value increase is unrealistic considering the fact that liquefaction is not reached. Comparing Figures 2.8 and 2.4, one can see the effect of the third pseudo yield surface on the undrained cyclic loading response. In effective p-q space, the difference between with and without the third pseudo yield surface is not very significant. However, the axial strain predicted with the inclusion of the third pseudo yield surface is smaller than otherwise and simulates the test results better during the early stages of loading. This is because the inclusion of a negative state parameter in the third pseudo plastic modulus enhances the hardening response.

Predictions are also made for undrained cyclic simple shear response for Nevada sand with relative densities of 40% and 60% under an initial axial stress of 80 kPa. The test results and predictions for a sample with a relative density of 60% are shown in Figures 2.9 and 2.10, respectively. The tests results and predictions for a sample with a relatively density of 40% are shown in Figures 2.11 and 2.12, respectively. The

magnitude of the applied shear stress is ±13 kPa for the sample with a 60% relative density, and ±8 kPa for the sample with a 40% relative density. Since it is difficult to measure the static lateral pressure coefficient for simple shear tests, a typical value of 0.6 is assumed at the start of shearing. The same model parameters as for the triaxial loading predictions given in Table 2.1 are used again. Again, the model predictions agree reasonably well with the test results. Similar to triaxial loading conditions, the looser sand is predicted to have a larger liquefaction potential than the denser sand under simple shear conditions. Under the applied shear stress of ±13 kPa, it takes 6 cycles for the sample with 60% relative density to reach liquefaction. Under the shear stress of ±8 kPa, it takes 5 cycles for the sample with 40% relative density to reach liquefaction.

Uchida and Stedman (2001) performed cyclic triaxial undrained loading tests on Toyoura sand. In each test, certain magnitude of cyclic axial strain is applied in each cycle until the liquefaction is reached. The test results and predictions for a sample with a 50% relative density under an initial confining pressure of 200 kPa subjected to 1% axial strain change are shown in Figures 2.13 (a) and (b), respectively. The test results and predictions for a sample with a 50% relative density under an initial confining pressure of 400 kPa subject to 0.6% axial strain change are shown in Figure 2.14 (a) and (b), respectively. The test results and predictions for a sample with a 30% relative density under an initial confining pressure of 400 kPa subject to 1% axial strain change are shown in Figure 2.15 (a) and (b), respectively. All the model parameters except h_1 and h_2 are obtained from monotonic triaxial tests described in Chapter 1. The model parameters h_1 and h_2 are calibrated using the test results with relative density of 50% under initial confining pressure of 200 kPa, shown in Figure 2.13. All the model

parameters are listed in Table 2.2. It should be mentioned that the model constants for triaxial extension are assumed to be identical to those for triaxial compression due to lack of triaxial extension test results. Equation 2.19 (c) is used to define the critical void ratio for Toyoura sand. As shown in Figures 2.13 – 2.15, the predictions agree very well with the test results. In addition, the fact that the looser Toyoura sand under higher confining pressure has a greater liquefaction potential is captured well by the model. While it takes 5 cycles for the sample with a relative density of 50% to reach liquefaction in Figures 2.13 and 2.14, it takes as few as 2 cycles for the sample with a relative density of 30% to reach liquefaction in Figure 2.15.

2.4 Conclusions

The Middle Surface Concept for saturated sand modeling under monotonic loading conditions is extended to model sand behavior in general stress space. Three pseudo yield surfaces are used to represent the well known response features of sands such as state parameter and fabric dependence, critical state behavior, and large volumetric contraction during unloading. The true yield surface is constructed based on these three pseudo yield surfaces through the appropriate selection of links between various yield surfaces. Only two more model parameters are added to the monotonic triaxial formulation to extend the model to the general stress space. This shows that although multiple yield surfaces are used, appropriate selection of links between various yield surfaces help to keep the model simple. The good agreement between model predictions and test results on two types of sands under a variety of loading conditions proves the capability of the proposed model. The successful application of the proposed

model to represent the behavior of sands in general stress space demonstrates that it is indeed possible to use MSC to represent a complex material behavior by dividing different response features into different pseudo yield surfaces without overloading a single yield surface. The expansion of MSC to model the behavior of other materials seems promising.

2.5 References

Arthur, J. R. F., Chua, K. S., Dunstan, T. & Juan I. Rodriguez del C. (1980), Principal Stress Rotation: A Missing Parameter, *Journal of the Geotechnical Engineering Division, ASCE* **106**, No. 4, 419-433

Arthur, J. R. F., Koenders, M. A. & Wong, R. K. S. (1986), Anisotropy in Particle Contacts Associated with Shearing in Granular Media, *Acta Mechanica* **64**, 19-29

Arulmoli, K., Arulanandan, K., & Seed, H. B. (1985), New Method for Evaluating Liquefaction Potential, *Journal of the Geotechnical Engineering Division, ASCE* **111**, No. 1, 95-114

Arulmoli, K., Muraleetharan, K. K., Hossain, M. M. & Fruth, L. S. (1992), *VELACS: Verification of Liquefaction Analysis by Centrifuge Studies, Laboratory Testing Program, Soil Data Report,* Technical Report, the Earth Technology Corporation, Irvine, California

Calvetti, F., Combe, G. & Lanier, J. (1997), Experimental Micromechanical Analysis of a 2D Granular Material: Relation Between Structure Evolution and Loading Path, *Mechanics of Cohesive-Frictional Material* **2**, 121-163

Dafalias, Y. F. & Arulanandan, K. (1979), Electrical Characterization of Transversely Isotropic Sands, *Archives of Mechanics* **31**, No. 5, 723-739

Dean, E. T. R. (2003), Patterns, Fabric and Soil Elasto-Plasticity, *International Conference on Plasticity*, Quebec, 7-11 July 2003

Ishihara, K., Tatsuoka, F. & Yasuda, S. (1975), Undrained Deformation and Liquefaction for Sand Under Cyclic Stresses, *Soils and Foundations* **15**, No. 1, 29-44

Li, X. S., & Dafalias, Y. F. (2000). Dilatancy for Cohesionless Soils, *Geotechnique* **50**, No. 4, 449-460

Manzari, M. T. & Dafalias, Y. F. (1997), A Critical State Two-Surface Plasticity Model for Sands, *Geotechnique* **47**, No. 2, 255-272

Oda, M. (1972), Initial Fabrics and Their Relations to the Mechanical Properties of Granular Material, *Soils and Foundations* **14**, No. 4, 45-63

Pradhan, B. S. & Tatsuoka, F. (1989), On Stress-Dilatancy Equations of Sand Subjected to Cyclic Loading, *Soils and Foundations* **29**, No. 1, 65-81

Tatsuoka, F. & Ishihara, K. (1974), Yielding of Sand in Triaxial Compression, *Soils and Foundations* **14**, No. 2, 63-76

Uchida, K. & Stedman, J.D. (2001), Liquefaction Behavior of Toyoura Sand Under Cyclic Strain Controlled Triaxial Loading, *Proceedings of the Eleventh (2001) International Offshore and Polar Engineering Conference*, Stavanger, Norway, June 17-22, 2001

Wang, Z. L., Dafalias, Y. F., & Shen, C. K. (1990), Bounding Surface Hypoplasticity Model for Sand, *Journal of Engineering Mechanics* **116**, No. 5, 983-1001

Table 2.1. Model Constants for Nevada Sand

Nevada Sand		General Space	Triaxial Space
Elasticity	G_0 (kPa)	2.0×10^4	2.0×10^4
	K_0 (kPa)	2.0×10^4	2.0×10^4
	a_0	0.6	0.6
Critical State	M (*comp*)	1.06	1.30
	M (*ext*)	0.63	0.78
	λ	0 (p<160 kPa) or 0.04 (p>160 kPa)	0 (p<160 kPa) or 0.04 (p>160 kPa)
	e_{ref}	0.78	0.78
	p_{ref} (kPa)	160	160
Hardening and Softening	a (*comp*)	0.0031	0.0025
	a (*ext*)	0.0012	0.001
	k_1	4.0	4.0
	b	0.07	0.06
Dilatancy	A	0.8	0.8
	k_2 (*comp*)	9.0	11
	k_2 (*ext*)	0.82	1.0
Anisotropic Fabric	h_1	163	200
	h_2	1.5	1.2

Table 2.2. Model Constants for Toyoura Sand

Toyoura Sand		General Space	Triaxial Space
Elasticity	G_0 (kPa)	2.0×10^4	2.0×10^4
	K_0 (kPa)	2.0×10^4	2.0×10^4
	a_0	0.5	0.5
Critical State	M	1.04	1.27
	λ	0.019	0.019
	e_{ref}	0.934	0.934
	ξ	0.7	0.7
Hardening and Softening	a	0.0055	0.0045
	k_1	4.0	4.0
	b	0.049	0.04
Dilatancy	A	0.7	0.7
	k_2	4.9	6
Anisotropic Fabric	h_1	163	200
	h_2	1.22	1.0

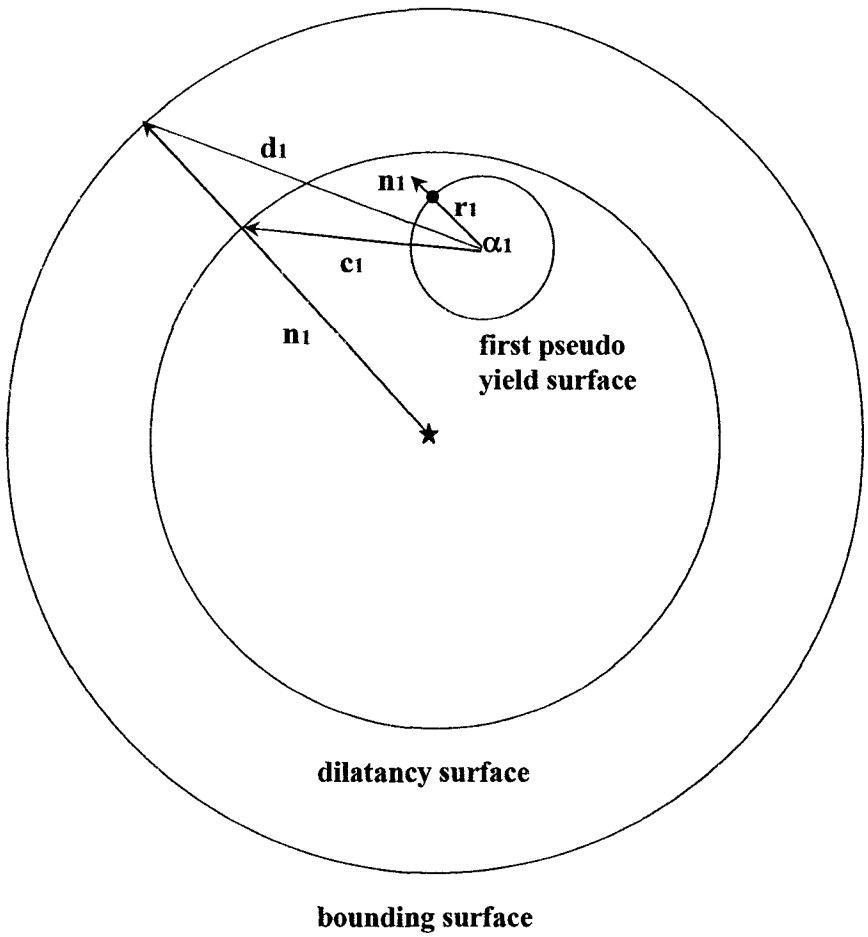

Figure 2.1: bounding and dilatancy surfaces for the first pseudo yield surface

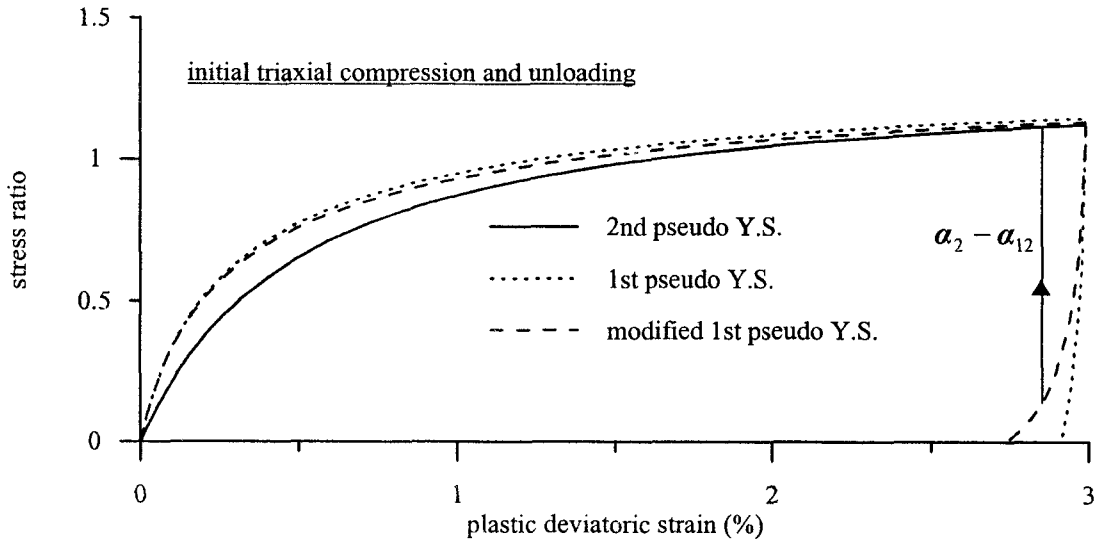

(a)

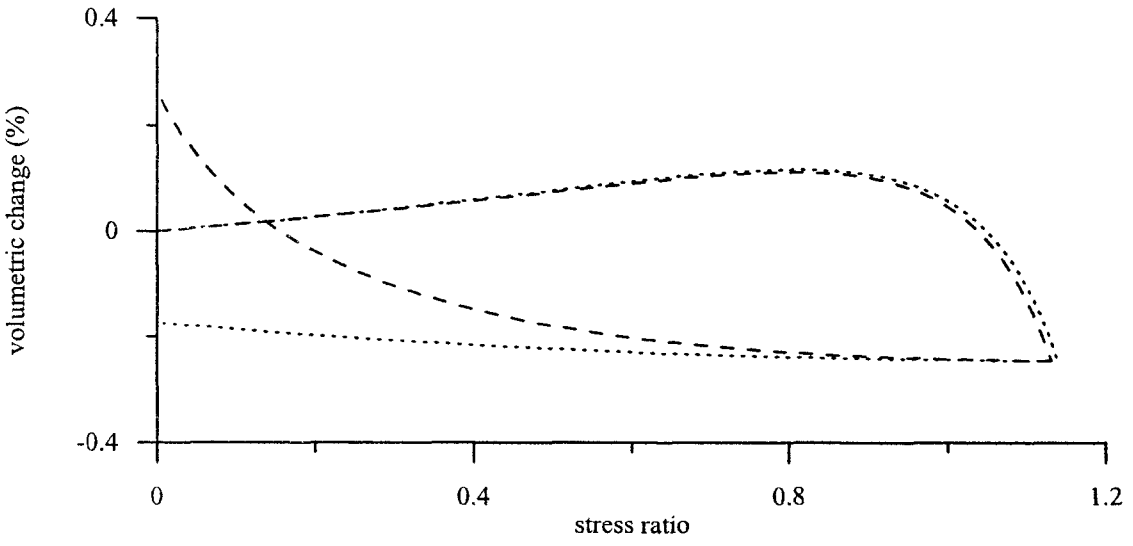

(b)

Figure 2.2: the role of the second pseudo yield surface

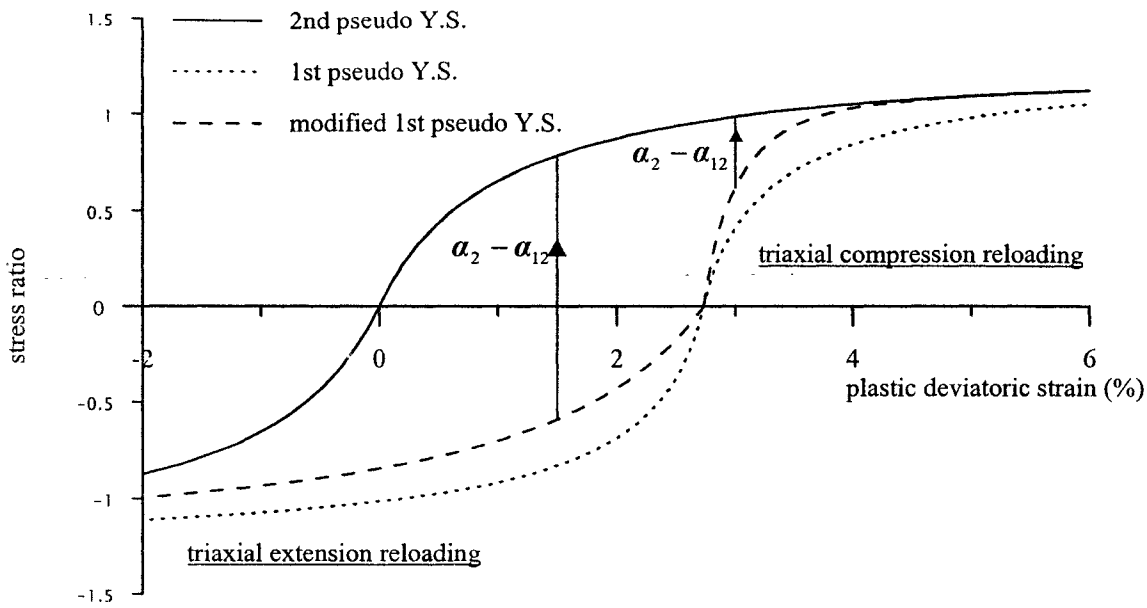

(c)

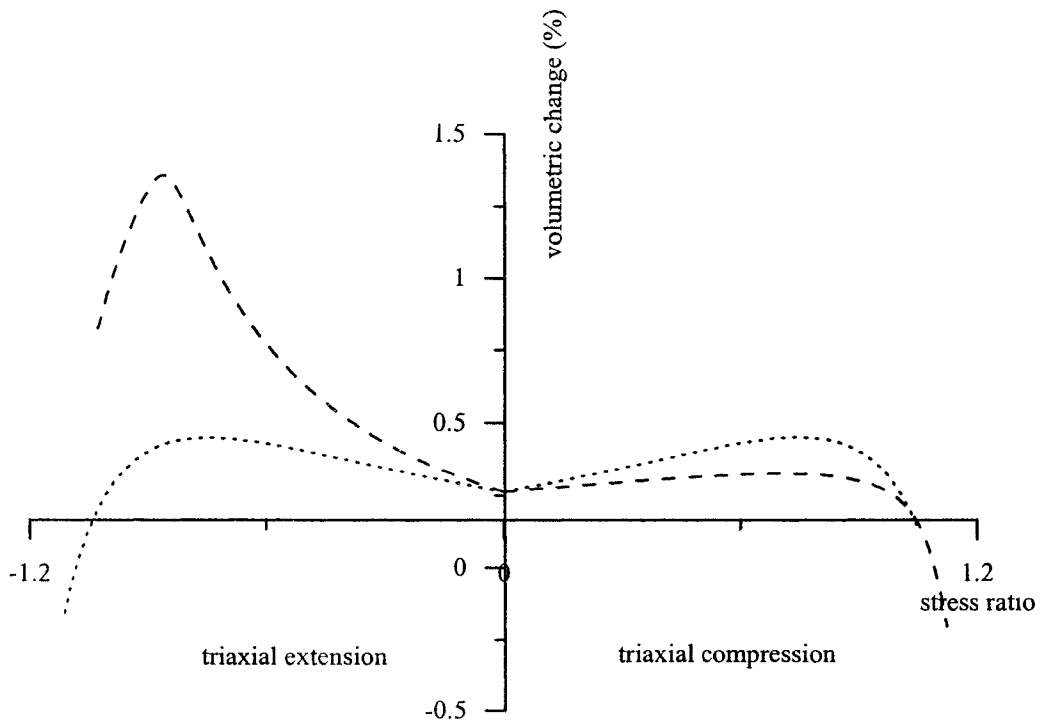

(d)

(cont.) Figure 2.2: the role of the second pseudo yield surface

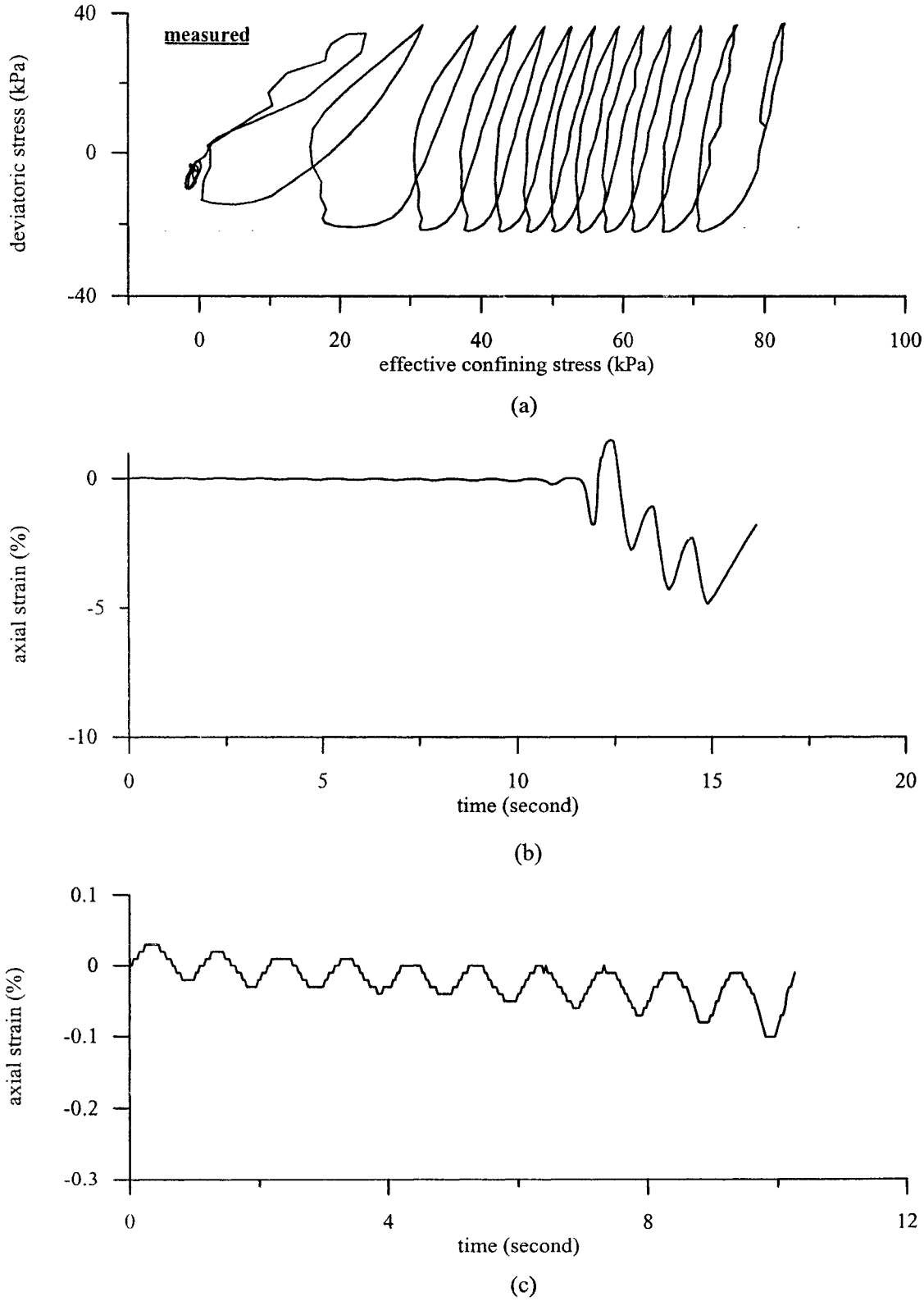

Figure 2.3: undrained cyclic triaxial test results for Nevada sand with a relative density of 60% (initial confining stress = 80 kPa)
(test data after Arulmoli et al., 1992)
(test data used for calibrating parameters h1 and h2)

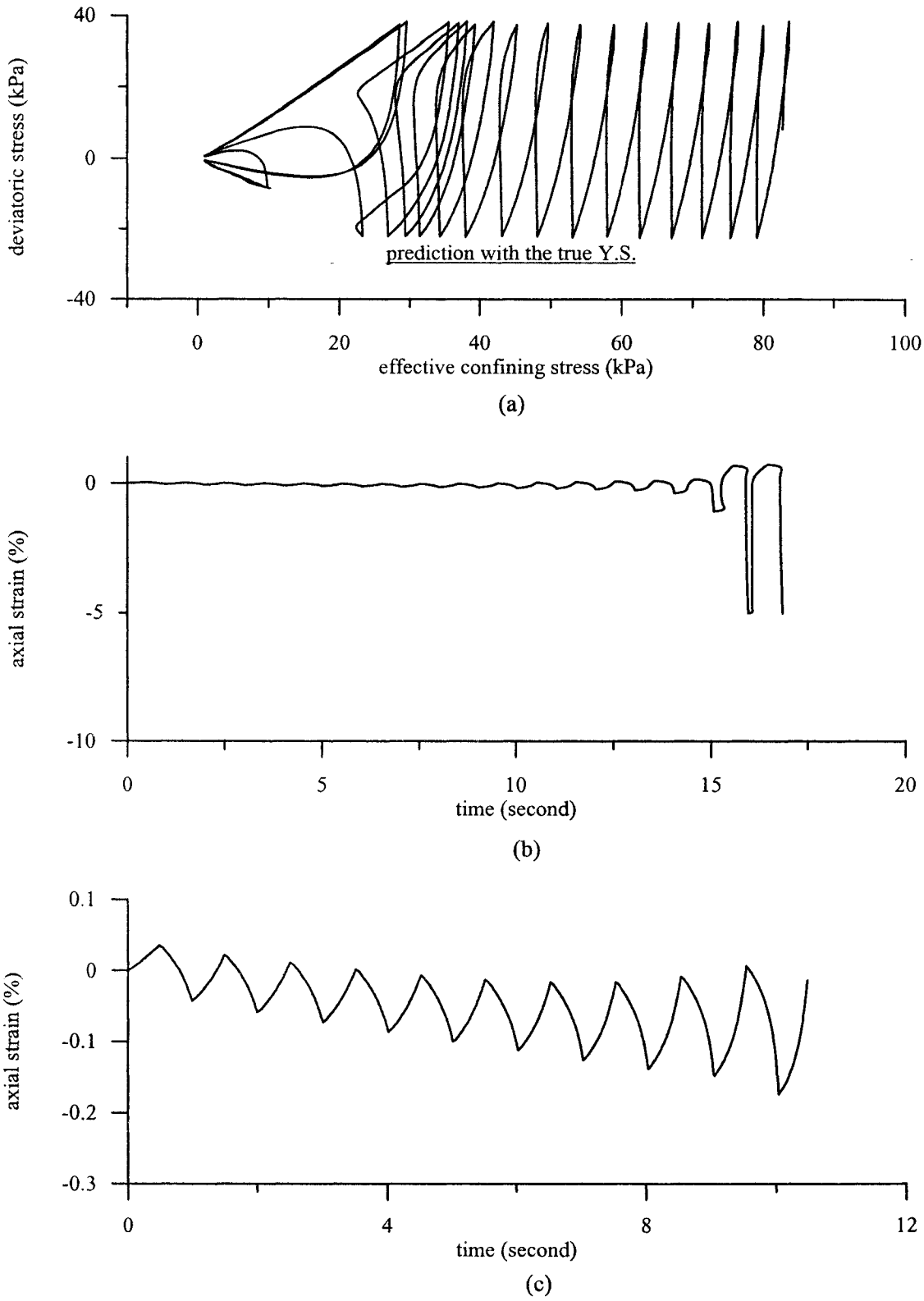

Figure 2.4: undrained cyclic triaxial test predictions for Nevada sand with a relative density of 60% (initial confining stress = 80 kPa)

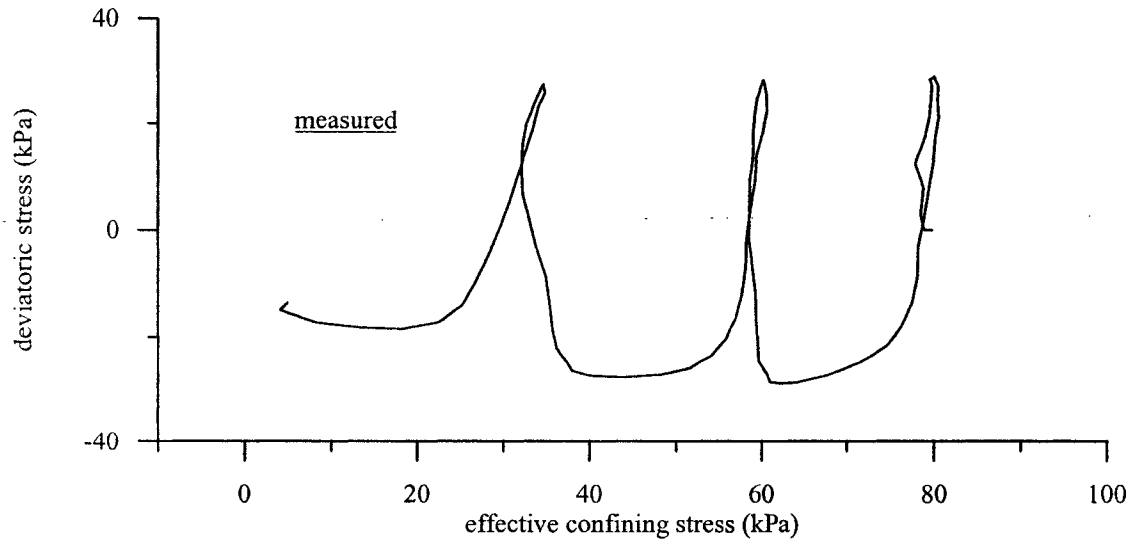

(a)

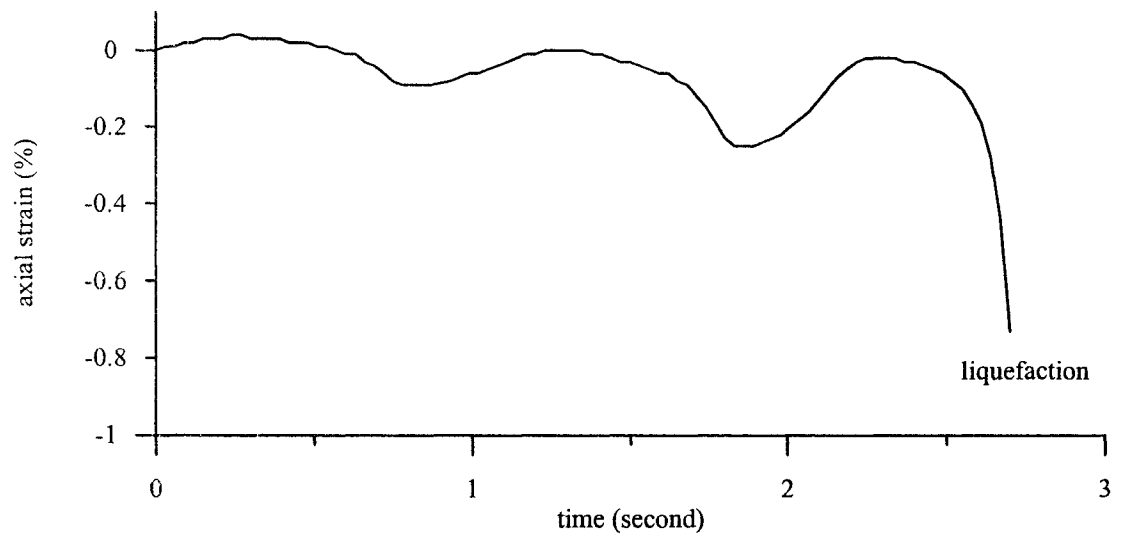

(b)

Figure 2.5: undrained cyclic triaxial test results for Nevada sand with a relative density of 40% (initial confining stress = 80 kPa) (test data after Arulmoli et al., 1992)

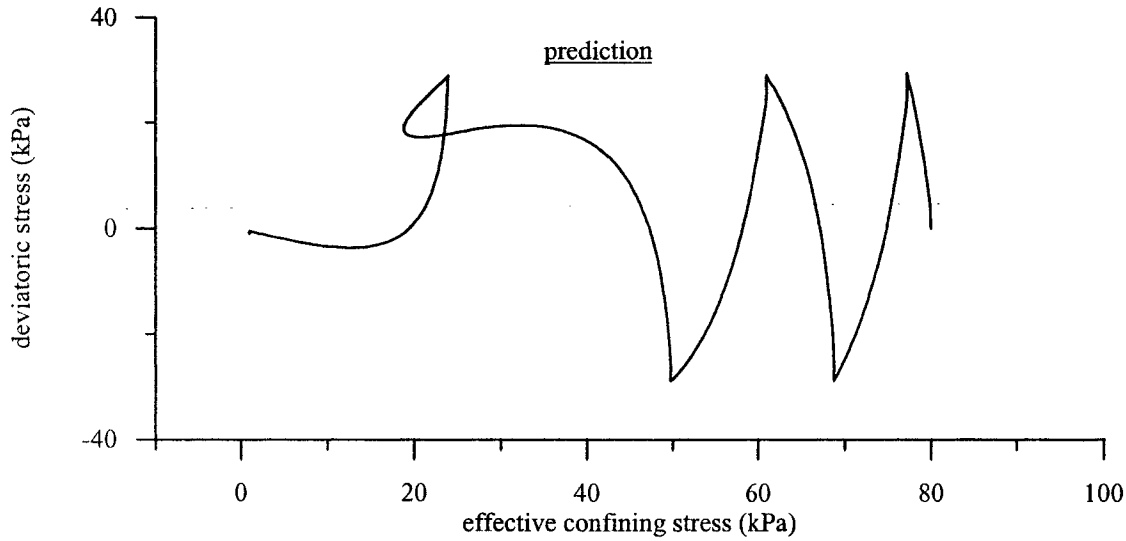

(a)

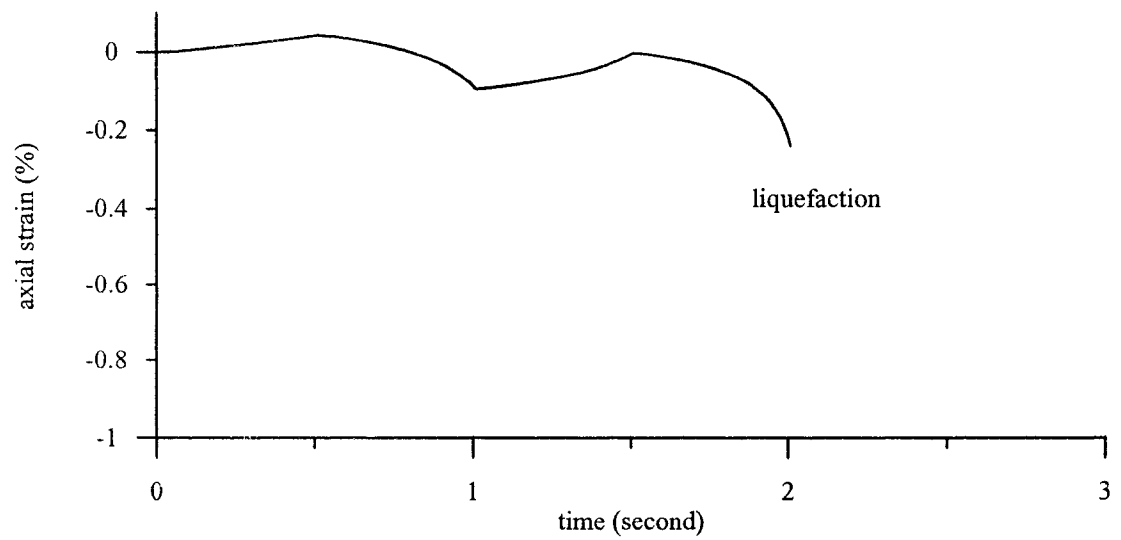

(b)

Figure 2.6: undrained cyclic triaxial test predictions for Nevada sand with a relative density of 40% (initial confining stress = 80 kPa)

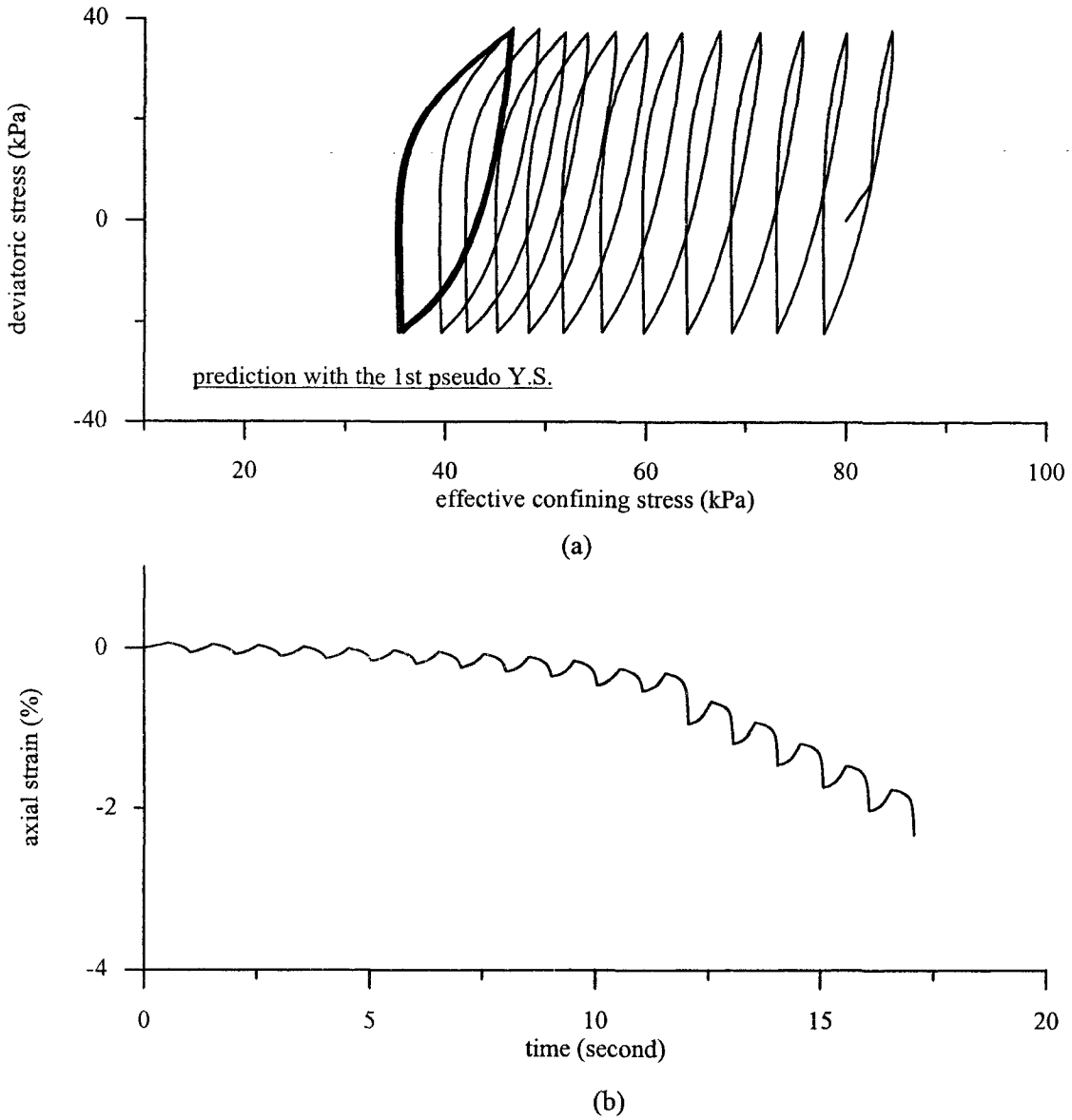

Figure 2.7: undrained cyclic triaxial test predictions for Nevada sand with a relative density of 60% using the first pseudo yield surface

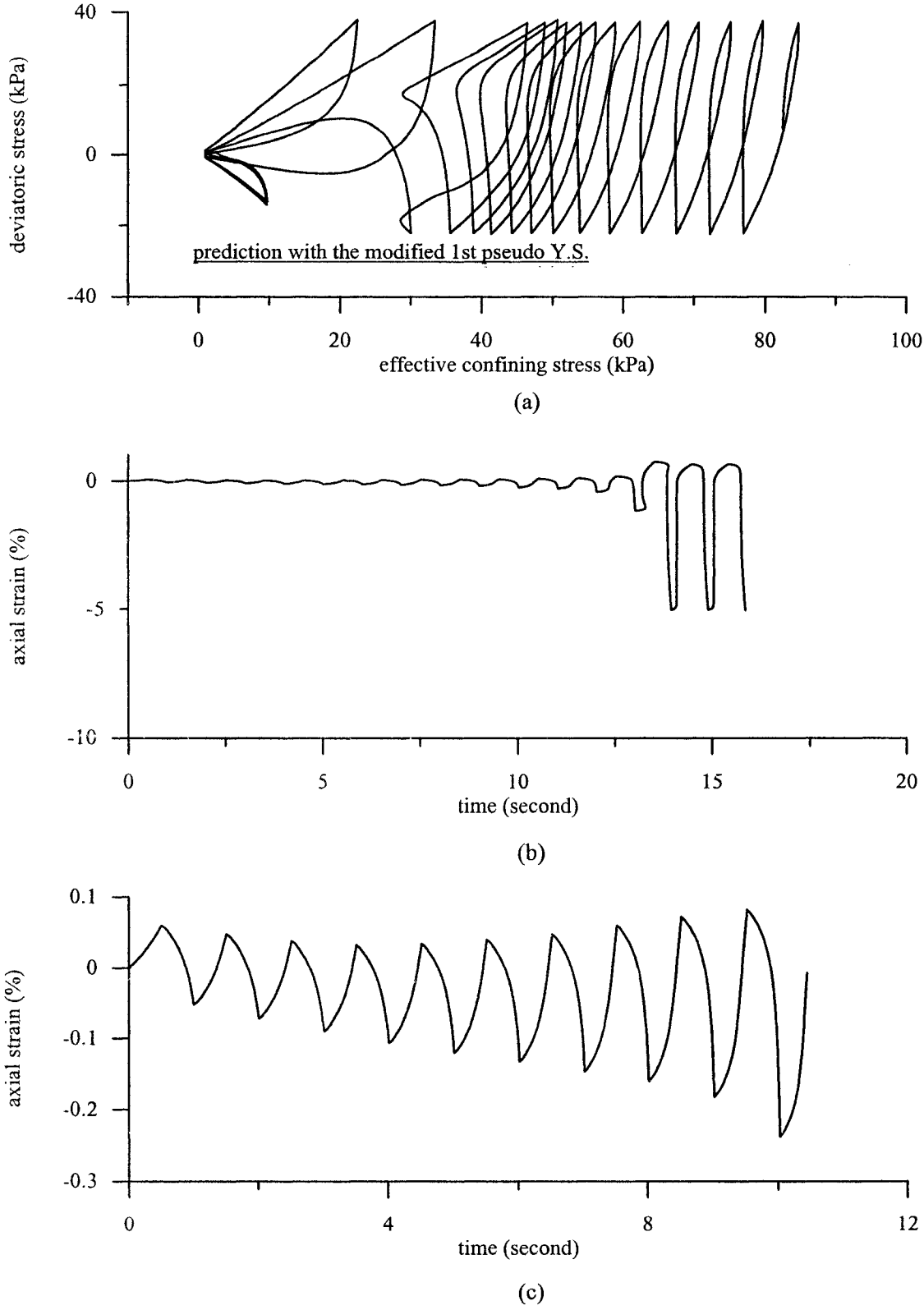

Figure 2.8: undrained cyclic triaxial test predictions for Nevada sand with a relative density of 60% using the modified first pseudo yield surface

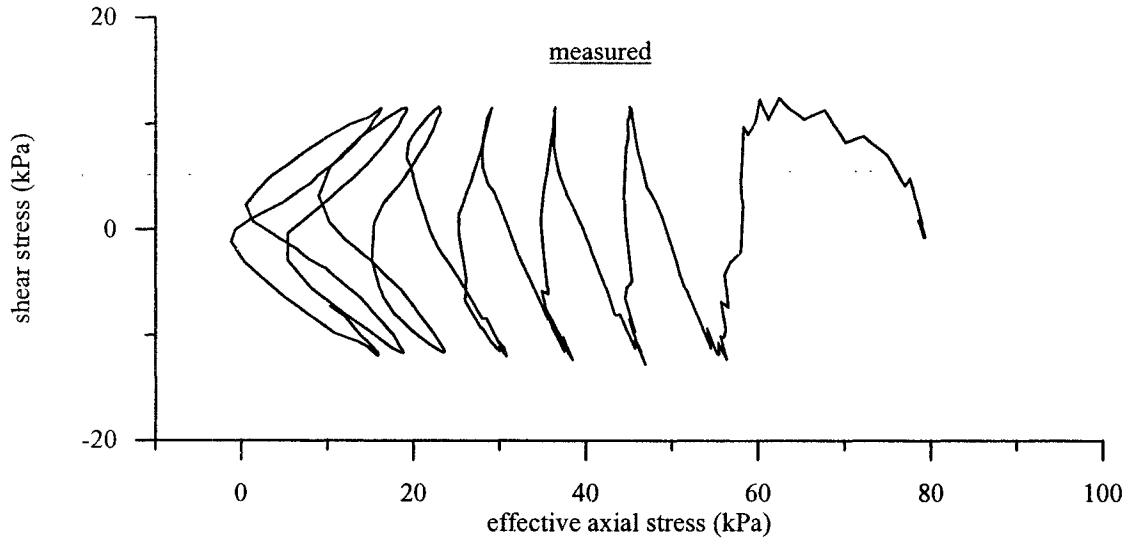

(a)

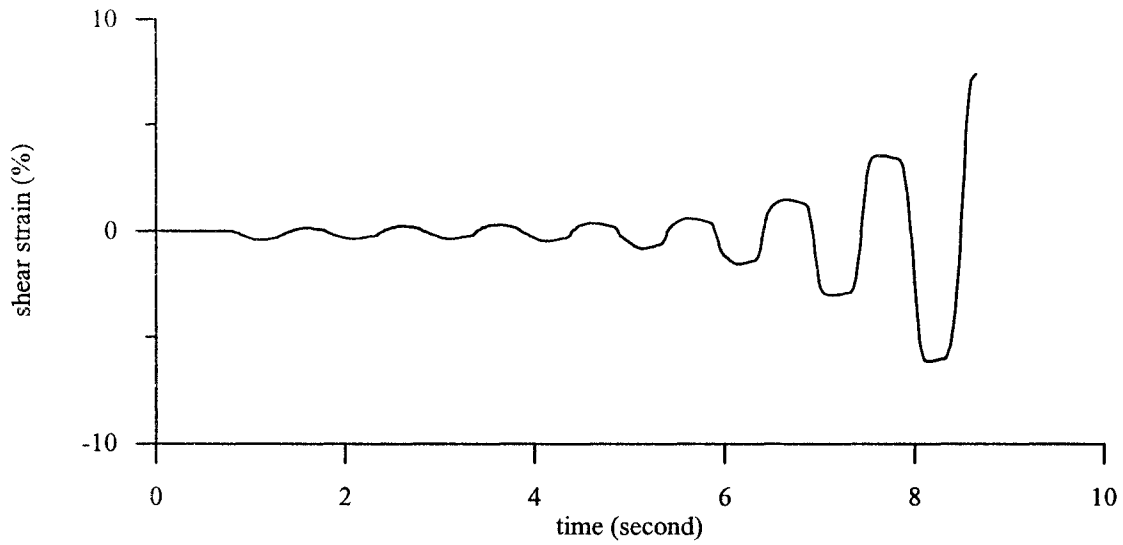

(b)

Figure 2.9: undrained cyclic simple shear test results for Nevada sand with the relative density of 60% (initial axial stress = 80 kPa) (test data after Arulmoli et al., 1992)

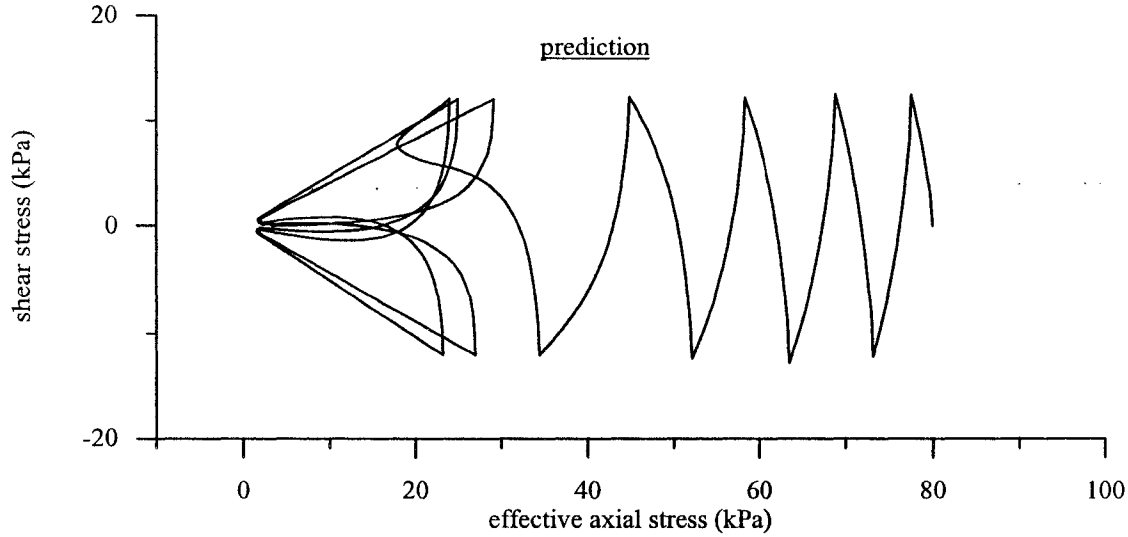

(a)

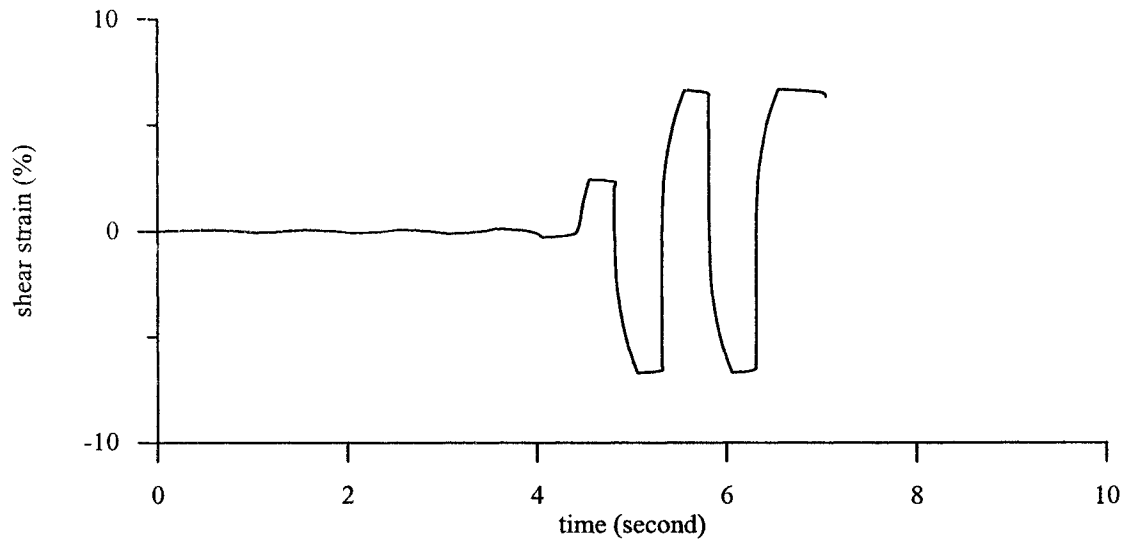

(b)

Figure 2.10: undrained cyclic simple shear test predictions for Nevada sand with the relative density of 60% (initial axial stress = 80 kPa)

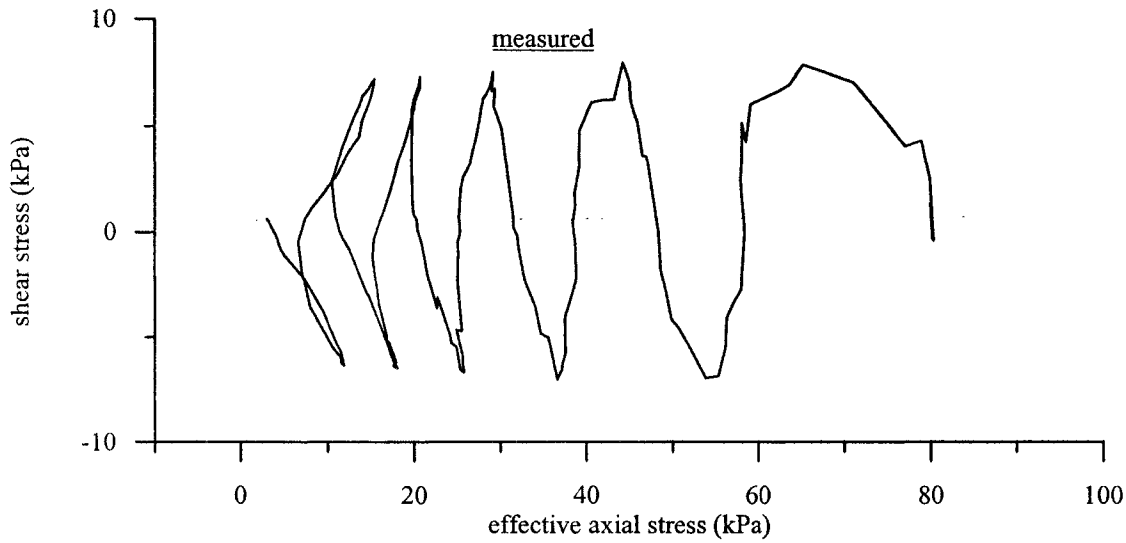

(a)

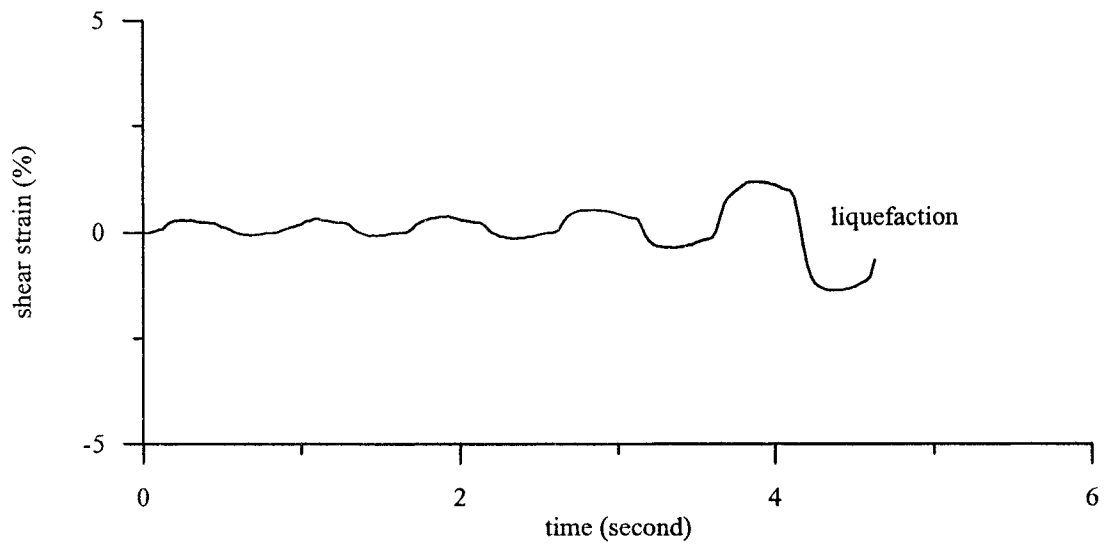

(b)

Figure 2.11: undrained cyclic simple shear test results for Nevada sand with the relative density of 40% (initial axial stress = 80 kPa) (test data after Arulmoli et al., 1992)

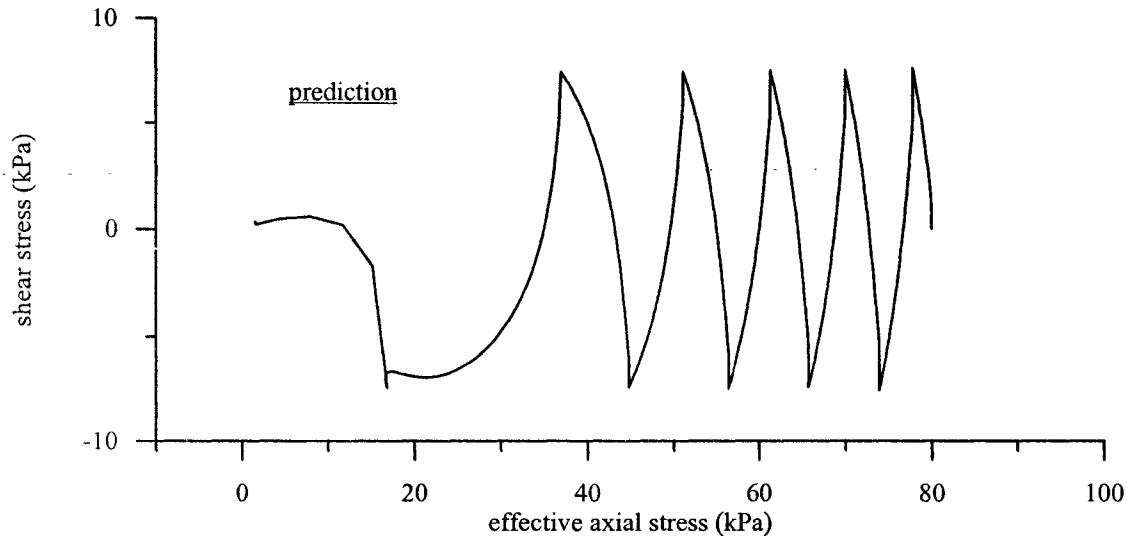

(a)

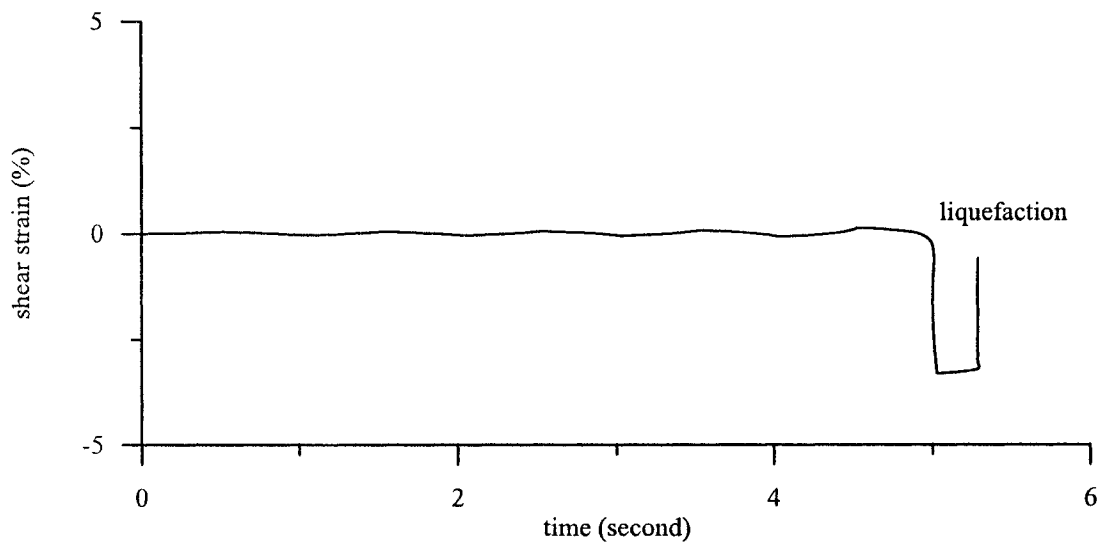

(b)

Figure 2.12: Undrained cyclic simple shear test predictions for Nevada sand with the relative density of 40% (initial axial stress = 80 kPa)

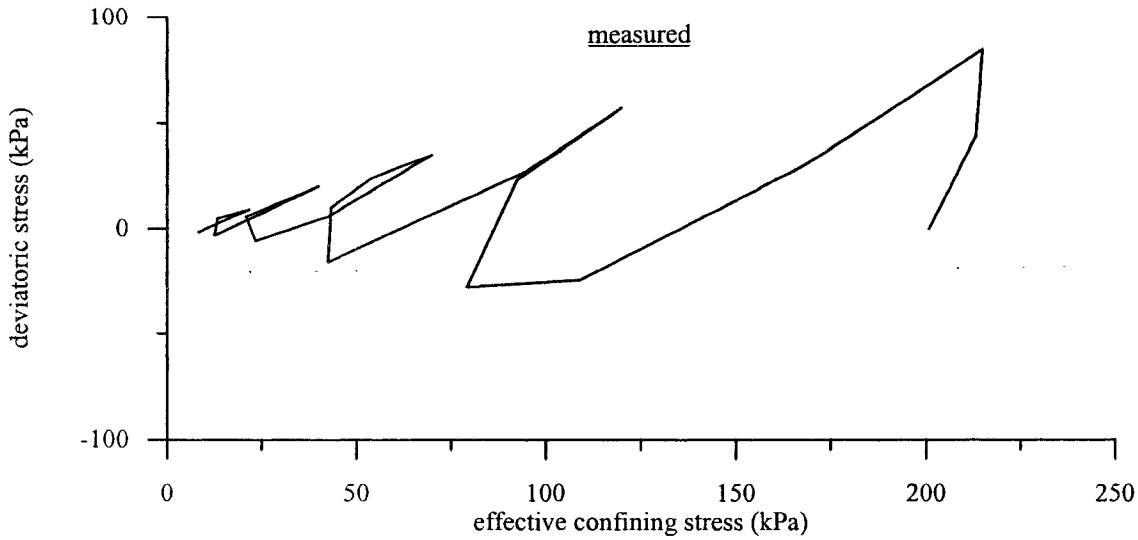

(a)

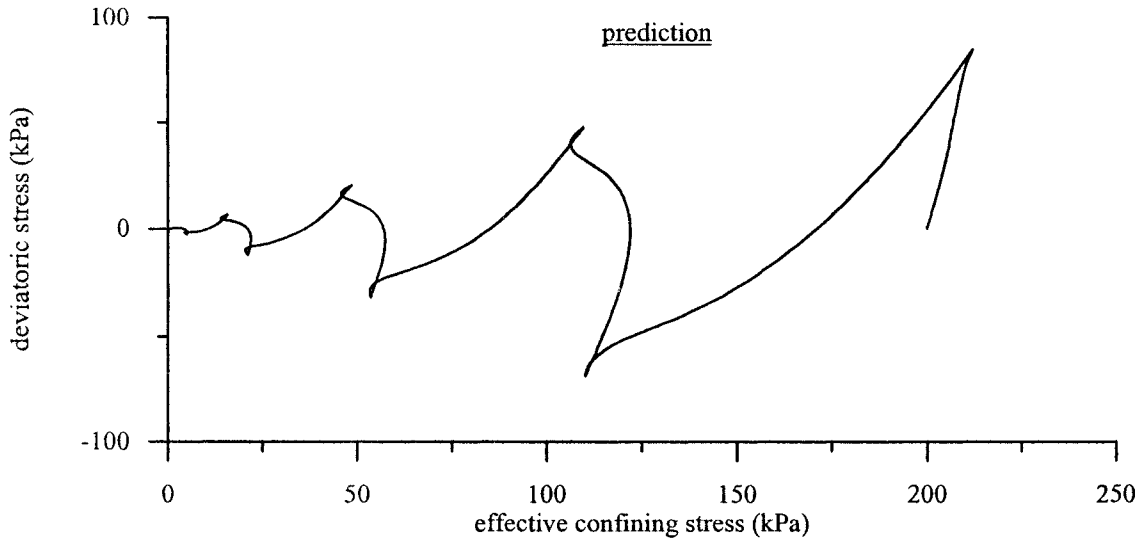

(b)

Figure 2.13: undrained cyclic triaxial test results and predictions for Toyoura sand with a relative density of 50% (initial confining stress = 200 kPa)
(test data after Uchida and Stedman, 2001)
(test data used for calibrating the parameters h1 and h2)

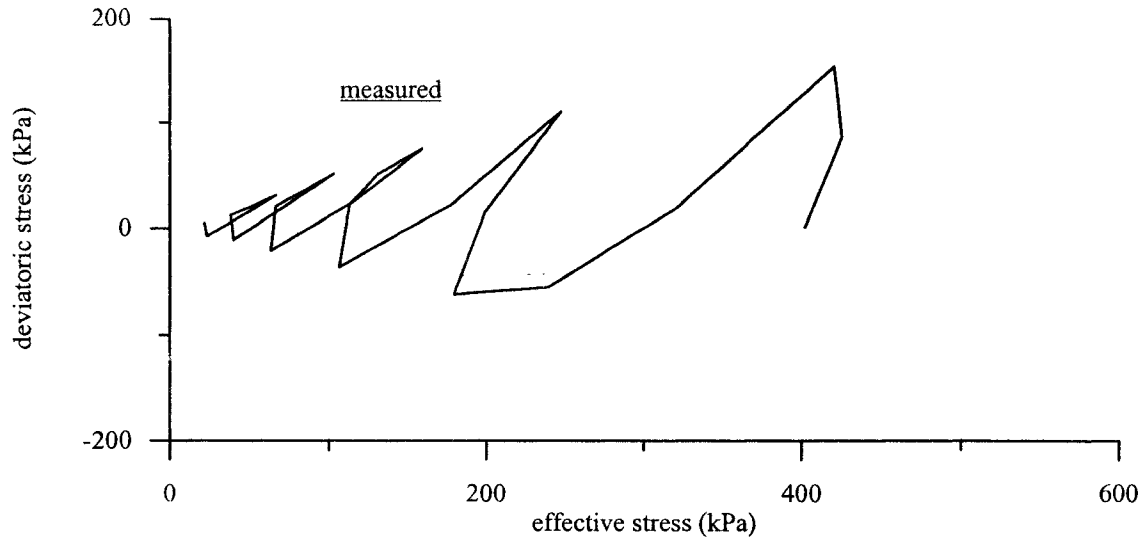

(a)

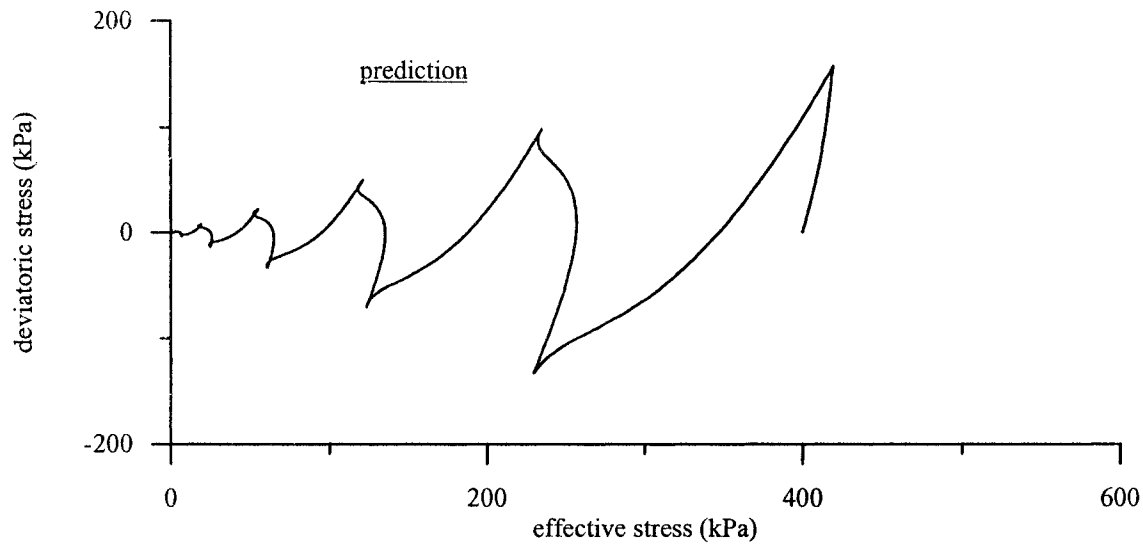

(b)

Figure 2.14: undrained cyclic triaxial test results and prediction for Toyoura sand with a relative density of 50% (initial confining stress = 400 kPa)
(test data after Uchida & Stedman, 2001)

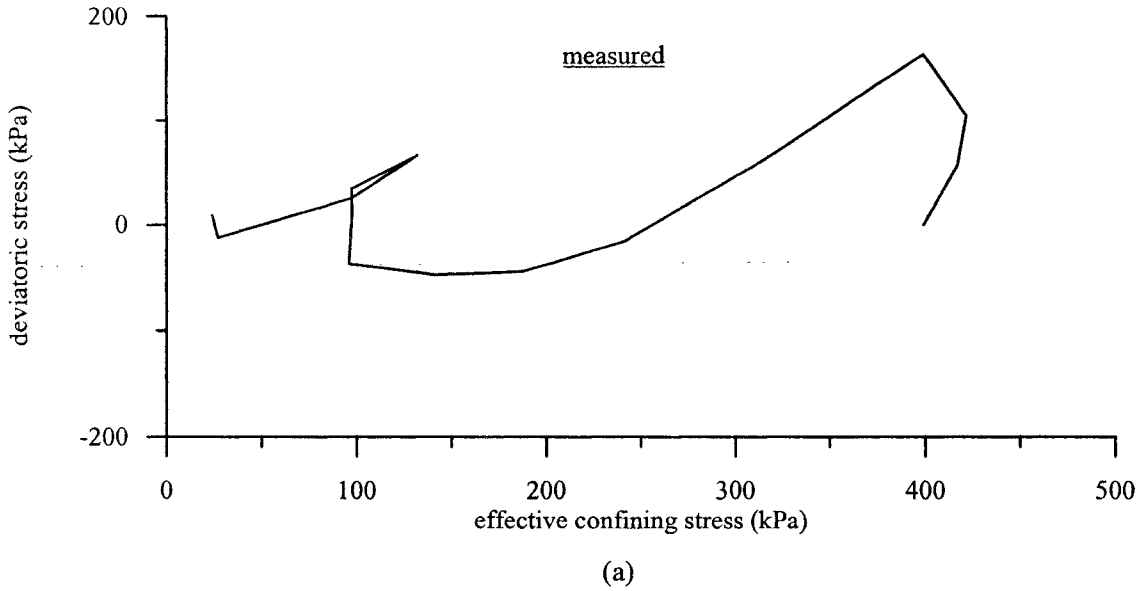

(a)

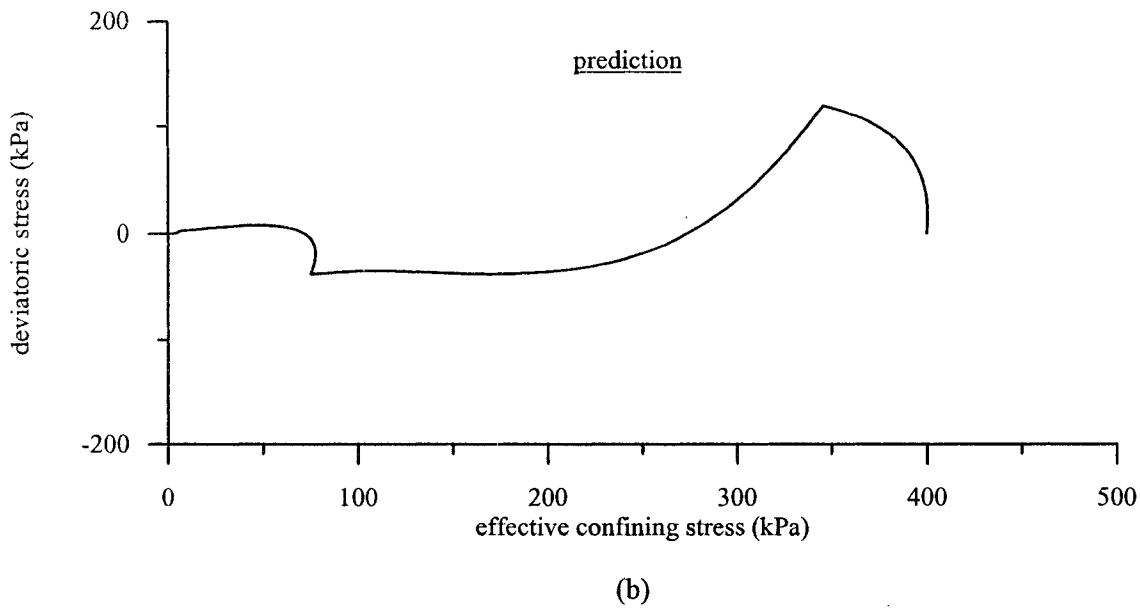

(b)

Figure 2.15: undrained cyclic triaxial test results and predictions for Toyoura sand with a relative density of 30% (initial confining stress = 400 kPa)
(data after Uchida & Stedman, 2001)

Chapter 3

Single Element Numerical Implementation of the MSC Sand Model for Finite Element Applications

3.1 Introduction

A constitutive model is normally formulated in the infinitesimal form. To solve practical engineering problems, the constitutive formulations must be numerically implemented. Therefore, it is essential to investigate whether a model is suited for the numerical implementation. In the case of the MSC, although all the yield surfaces are developed within the framework of classical elastoplasticity theory, the MSC model is different than classical elastoplasticity models in that there are multiple hardening rules and flow rules. Specifically, in the simplified version of the MSC sand model, there are three hardening rules and flow rules. In addition, the hardening rule and flow rule are not only the function of stress states and hardening parameters, but also the function of total strain and plastic strain. The investigation of the numerical implementation of the MSC sand model for a single element or an individual Gauss point in the finite element method is one of the objectives of this chapter.

The numerical implementation in a single element consists of two steps, the numerical integration and the development of the consistent tangent stiffness matrix (Owen and Hinton, 1980; Simo and Hughes, 1998). There are various techniques for the integration of constitutive equations (Wilkins, 1964; Rice and Tracy, 1973; Ortiz and Popov, 1985; Ortiz and Simo, 1986; Simo & Taylor, 1986). Of particular interest is the

generalization of these integration techniques introduced by Ortiz & Popov (1985). They categorized these integration techniques into the generalized trapezoidal and generalized mid-point rules. For the generalized trapezoidal rule, $\alpha = 0$ corresponded to the explicit integration; $\alpha = 1/2$ corresponded to the mean-normal integration; $\alpha = 1$ coincided with the closest point projection algorithm. For the accuracy of the integration by the generalized trapezoidal rule, they derived that $\alpha = 1/2$ led to the second order accuracy while other values of α led to the first order accuracy. For the stability of the generalized trapezoidal rule, they derived that $\alpha \geq 1/2$ led to unconditional stability for von Mises models, and $\alpha = 1$ was the only value of α leading to unconditional stability for those loading surfaces with corners. Their propositions about the integration accuracy corresponding to different values of α were verified by using a simple numerical example. A perfectly plastic von Mises model was used in their example with the strain increment of a single step applied as the input condition, so that analytically exact stress increment could be obtained. The exact stress increment was used to compare with the stress increment computed through the numerical integrations with different values of α. The results of their numerical examples showed that for small strain increments optimal accuracy was obtained for $\alpha = 1/2$. In contrast, when large strain increments were used, higher values of α led to better accuracy. Because the trapezoidal rule has the general nature and some conclusions have been drawn on it, in this chapter, it will be used to integrate the MSC sand model. On the other hand, the elastic moduli were assumed to be constant in the original trapezoidal rule. This assumption is appropriate for metals, but not for soils. Usually, the elastic moduli for soils depend on the confining pressure. In this chapter, the original trapezoidal rule will be expanded to consider the dependence of

elastic moduli on the confining pressure. In addition, as described above, the integration accuracy corresponding to different values of α was verified only by using a relatively simple example by Ortiz & Popov (1985). To apply the trapezoidal rule to solve practical engineering problems, the investigation of the integration accuracy for different values of α in relatively complicated cases is desirable. To this end, the effects of different values of α on the integration accuracy will be analyzed by using the MSC model under various complicated loading conditions.

Another step in the numerical implementation of a model is the development of the stiffness matrix for a Gauss point. The continuum tangent stiffness matrix was commonly used until the introduction of the consistent tangent stiffness matrix (Simo and Taylor, 1985; Braudel et al., 1986). Unlike the continuum tangent stiffness matrix, the consistent tangent stiffness matrix is consistent with the integration algorithm of the constitutive model, and preserves the quadratic rate of asymptotic convergence of iterative solution schemes based upon Newton's method in the global finite element program. Subsequent applications of the consistent tangent stiffness matrix in many models proved its superiority to the continuum tangent stiffness matrix (Borja, 1990; Borja, 1991; Hashash and Whittle, 1992; Macari et al., 1997; Jeremic and Sture, 1997; Manzari and Prachathananukit, 2001). However, the development of the consistent tangent stiffness matrix is more difficult than that for the continuum tangent stiffness matrix, and there are no closed-form solutions for many models. Consequently, approximate techniques have been developed for some models to obtain the closed-form consistent tangent stiffness matrix. Other models have resorted to numerical techniques to develop the consistent tangent stiffness matrix. Due to the comprehensive nature of this

MSC sand model, it is impossible to come up with the closed-form consistent tangent stiffness matrix. Therefore the consistent tangent stiffness matrix is developed numerically.

3.2 Numerically Implemented Formulations of the MSC Sand Model

The detailed formulations for the MSC sand model are presented in Chapter 2. In this section the equations of the model that have to be integrated are briefly described. The quantities with the subscript 12, 2 and 3 represent those for the modified first pseudo yield surface, the second and third pseudo yield surfaces, respectively. The quantities without the subscript represent those for the true yield surface.

Elastic Relationship

$$\dot{p} = K_e \dot{\varepsilon}_v^e = K_e(\dot{\varepsilon}_v - \dot{\varepsilon}_v^p) \tag{3.1}$$

$$\dot{\mathbf{s}} = 2G_e \dot{\mathbf{e}}^e = 2G_e(\dot{\mathbf{e}} - \dot{\mathbf{e}}^p) \tag{3.2}$$

where p and ε_v denote the hydrostatic stress and strain, respectively; and **s** and **e** represent the deviatoric stress and strain tensors, respectively. The superscripts e and p denote the elastic and plastic parts of the strain, respectively. The bold-faced symbols denote tensors. K_e and G_e denote the elastic bulk and shear moduli, respectively, which are defined as :

$$K_e = K_0(\frac{p}{p_{at}})^{a0} \tag{3.3a}$$

$$G_e = G_0(\frac{p}{p_{at}})^{a0} \tag{3.3b}$$

where K_0, G_0, and a_0 are the elastic model parameters, and p_{at} denotes the atmospheric pressure.

Yield Surface

$$f = [(\mathbf{s} - p\boldsymbol{\alpha}) : (\mathbf{s} - p\boldsymbol{\alpha})]^{1/2} - mp = 0 \tag{3.4}$$

where $\boldsymbol{\alpha}$ denotes the hardening parameter. The yield surface has the shape of a cone in the general stress space, and its radius is m on the stress ratio π plane, which is a relatively small constant.

Hardening Rule and Plastic Modulus

The hardening rule for the true yield surface is defined as:

$$\dot{\boldsymbol{\alpha}} = \dot{\Lambda}(\frac{K_p}{p})\mathbf{n} \tag{3.5}$$

where $\dot{\Lambda}$ denotes the loading index. $\mathbf{n}$ is a unit tensor and represents the normal to the yield surface, which is given as:

$$\mathbf{n} = \frac{\mathbf{r} - \boldsymbol{\alpha}}{m} \tag{3.6a}$$

$$\mathbf{r} = \frac{\mathbf{s}}{p} \tag{3.6b}$$

K_p denotes the plastic modulus, which is defined as:

$$K_p = \frac{\xi^p}{b + \xi^p} K_{p12} + \frac{b}{b + \xi^p} K_{p3} + p\frac{b}{(b + \xi^p)^2}\mathbf{n} : (\boldsymbol{\alpha}_{12} - \boldsymbol{\alpha}_3) \tag{3.7a}$$

$$K_{p12} = \frac{d_{12}}{a/2(M_d - 2m - d_{12})} p + h_1 p(\boldsymbol{\alpha}_2 - \boldsymbol{\alpha}_{12}) : \mathbf{n} \tag{3.7b}$$

$$K_{p3} = \exp(-k_1\psi)K_{p12} \tag{3.7c}$$

$$d_{12} = M - m - \boldsymbol{\alpha}_{12} : \mathbf{n} \tag{3.7d}$$

$$\boldsymbol{\alpha}_2 = M\frac{\mathbf{e}^p}{a + |\mathbf{e}^p|} \tag{3.7e}$$

In equation (3.7a), K_{p12} and K_{p3} are the plastic moduli for the modified first pseudo and the third pseudo yield surfaces, and $\boldsymbol{\alpha}_{12}$ and $\boldsymbol{\alpha}_3$ are their hardening parameters, respectively. ξ^p denotes the accumulated plastic deviatoric strain and b is a model parameter. In equation (3.7b), the first part of K_{p12} involves the bounding surface concept. The radius of the bounding surface is M-m, where M denotes the critical stress ratio. M_d-2m represents the diameter of the bounding surface. The distance of $\boldsymbol{\alpha}_{12}$ to the bounding surface is denoted by d_{12}, which is defined in equation (3.7d). a is a model parameter. Due to the use of the bounding surface concept, the unloading and reloading plastic deformation can be represented by K_{p12}. In addition, as the radius of the bounding surface is M-m, the stress ratio is ensured to reach the critical state at the end of loading. The second part of K_{p12} involves the influence of the second pseudo yield surface or the fabric anisotropy. Its hardening parameter $\boldsymbol{\alpha}_2$ represents the evolution of the fabric anisotropy, which is defined in equation (3.7e). The effect of fabric anisotropy on the hardening response is dependent on $(\boldsymbol{\alpha}_2 - \boldsymbol{\alpha}_{12}) : \mathbf{n}$, which is the relative distance between $\boldsymbol{\alpha}_{12}$ and $\boldsymbol{\alpha}_2$. h_1 is a model parameter. In equation (3.7c), K_{p3} is related to K_{p12} by $\exp(-k_1\psi)$, where k_1 is a model parameter. ψ denotes the state parameter, given by:

$$\psi = e - e_{cr} \tag{3.8a}$$

$$e_{cr} = e_{ref} - \lambda \ln(p/p_{ref}) \tag{3.8b}$$

where, e is the current void ratio and e_{cr} is the void ratio at the critical state under the current confining pressure. e_{ref}, p_{ref}, and λ are the model parameters used to define the void ratio at the critical state. It is worth noting that the inclusion of ψ into K_{p3} enables the model to represent the effect of the state parameter on the hardening response.

$\boldsymbol{\alpha}_{12}$ and $\boldsymbol{\alpha}_3$ are related to $\boldsymbol{\alpha}$ by:

$$\boldsymbol{\alpha}_{12} = g_{12}\boldsymbol{\alpha} \tag{3.9a}$$

$$\boldsymbol{\alpha}_3 = g_3\boldsymbol{\alpha} \tag{3.9b}$$

Where g_{12} and g_3 are two scalars. Thus, $\boldsymbol{\alpha}_{12}$ and $\boldsymbol{\alpha}_3$ are simplified, and replaced by two scalars, with respect to $\boldsymbol{\alpha}$. The evolutions of g_{12} and g_3 are defined as:

$$\dot{g}_{12} = \frac{\dot{\Lambda}}{(\boldsymbol{\alpha} : \mathbf{n})}\left[\frac{K_{p12}}{p} - g_{12}\frac{K_p}{p}\right] \qquad \text{when } \boldsymbol{\alpha} : \mathbf{n} \geq (\alpha n)_{min} \tag{3.10a}$$

$$\dot{g}_{12} = 0 \qquad \text{when } \boldsymbol{\alpha} : \mathbf{n} < (\alpha n)_{min} \tag{3.10b}$$

$$\dot{g}_3 = \frac{\dot{\Lambda}}{(\boldsymbol{\alpha} : \mathbf{n})}\left[\frac{K_{p3}}{p} - g_3\frac{K_p}{p}\right] \qquad \text{when } \boldsymbol{\alpha} : \mathbf{n} \geq (\alpha n)_{min} \tag{3.11a}$$

$$\dot{g}_3 = 0 \qquad \text{when } \boldsymbol{\alpha} : \mathbf{n} < (\alpha n)_{min} \tag{3.11b}$$

In equations (3.10) and (3.11), in order to avoid numerical difficulties, g_{12} and g_3 remain constant when $\boldsymbol{\alpha} : \mathbf{n}$ is smaller than $(\alpha n)_{min}$, which is a relatively small value.

Flow Rule

The flow rules for the volumetric and deviatoric plastic strain are defined as:

$$\dot{\varepsilon}_v^p = \dot{\Lambda} D \tag{3.12}$$

$$\dot{\mathbf{e}}^{p} = \dot{\Lambda}\mathbf{n} \tag{3.13}$$

D is the dilatancy ratio, which is defined as:

$$D = D_{12} = D_1 + C_2 D_2 \tag{3.14a}$$

$$D_1 = A(M - m + k_2\psi - \boldsymbol{\alpha}_{12} : \mathbf{n}) \tag{3.14b}$$

$$D_2 = A(M - m + k_2\psi - \boldsymbol{\alpha}_2 : \mathbf{n}) \tag{3.14c}$$

$$C_2 = h_2 \left| (\boldsymbol{\alpha}_{12} - \boldsymbol{\alpha}_2) : \mathbf{n} \right| \tag{3.14d}$$

From equations (3.14b) and (3.14c), it can be seen that D_1 and D_2 are defined based on the distance between $\boldsymbol{\alpha}_{12}$, $\boldsymbol{\alpha}_2$ and the dilatancy surface with the radius of $M - m + k_2\psi$, respectively. C_2 represents the degree of the effect of D_2. A and k_2 are model parameters. The incorporation of state parameter into the dilatancy surface can represent the effect of the state parameter on the dilatancy ratio. In addition, with the stress ratio approaching the critical state, the dilatancy surface approaches the bounding surface. As a result, the state parameter approaches zero, which indicates that the void ratio approaches the critical state. Similar to the definition of the plastic modulus in equation (3.7), the effect of the sand fabric anisotropy on the dilatancy ratio depends on $(\boldsymbol{\alpha}_2 - \boldsymbol{\alpha}_{12}) : \mathbf{n}$ in equation (3.14d), where h_2 is a model parameter.

Lode Angle Dependence

In order to represent the Lode angle dependence, some model parameters are made to be a function of the Lode angle. The Lode angle θ is defined as:

$$\cos 3\theta = \frac{3\sqrt{3}}{2}\left(\frac{\bar{\bar{S}}}{\bar{J}}\right)^3 \tag{3.15a}$$

$$\bar{J} = \left(\frac{1}{2}\mathrm{tr}\bar{\mathbf{r}}\right)^{1/2} \tag{3.15b}$$

$$\bar{S} = \left(\frac{1}{3}\mathrm{tr}\bar{\mathbf{r}}\right)^{1/3} \tag{3.15c}$$

$$\bar{\mathbf{r}} = \mathbf{r} - \boldsymbol{\alpha} \tag{3.15d}$$

The model parameters that depend on the Lode angle are defined as:

$$Q_\theta = g(\theta)Q_c \tag{3.16a}$$

$$g(\theta) = \frac{2c_e}{(1+c_e)-(1-c_e)\cos 3\theta} \tag{3.16b}$$

$$c_e = \frac{Q_e}{Q_c} \tag{3.16c}$$

where Q_θ represents those model constants that are dependent on the Lode Angle θ. Q_c and Q_e denote the model constants for triaxial compression and extension, respectively. The model parameters a, k_2 and M are chosen to depend on the Lode angle in this model.

3.3 Numerical Implementation of the Constitutive Relations

3.3.1 Global Problem

In this section, the MSC sand model is numerically implemented to simulate the responses of sand samples under triaxial and simple shear loadings. The considered sample corresponds to a single Gauss point in the finite element method. Assume the stress increment is given in each step and the problem can be described as:

$$\mathbf{F} = \Delta\boldsymbol{\sigma} - \Delta\tilde{\boldsymbol{\sigma}}(\Delta\boldsymbol{\varepsilon}) = 0 \tag{3.17}$$

where $\Delta\boldsymbol{\sigma}$ denotes the total stress increment given as the input condition, and $\Delta\boldsymbol{\varepsilon}$ denotes the strain increment, which needs to be solved. $\Delta\tilde{\boldsymbol{\sigma}}$ represents the stress increment

computed based on $\Delta\varepsilon$. It should be noted that in some cases the input condition is a combination of stress and strain increments. This can also be considered similar to equation (3.17). Usually, there is not an analytical solution of $\Delta\varepsilon$ for nonlinear elastoplastic problems. Instead, the iterative numerical technique is required to solve the above problem. The most commonly used numerical technique is Newton-Raphson algorithm, which is given as:

$$-\frac{\partial \mathbf{F}}{\partial \Delta\varepsilon} \mathrm{d}(\Delta\varepsilon) = \mathbf{F} \tag{3.18}$$

where $\mathbf{F}$ represents the error of the stress increment, and $\mathrm{d}(\Delta\varepsilon)$ represents the error of the strain increment in the iteration process. According to equation (3.17), equation (3.18) can be further written as:

$$(\mathbf{I}_u + \frac{\partial \Delta\tilde{\boldsymbol{\sigma}}'}{\partial \Delta\varepsilon})\mathrm{d}(\Delta\varepsilon) = \mathbf{F} \tag{3.19a}$$

$$\mathbf{I}_u = \Gamma(1,1,1,0,0,0)^T \otimes (1,1,1,0,0,0) \tag{3.19b}$$

In order to consider the pore water pressure, the effective stress increment in equation (3.19) is expressed with $\Delta\tilde{\boldsymbol{\sigma}}'$. $\frac{\partial \Delta\tilde{\boldsymbol{\sigma}}'}{\partial \Delta\varepsilon}$ denotes the consistent tangent stiffness matrix. $\mathbf{I}_u$ denotes the part of the stiffness matrix caused by the pore water pressure. Γ represents the bulk modulus of water and is set to be 2.2×10^6 kPa, which is much larger than the bulk modulus of the soil skeleton. Under drained conditions, Γ is equal to zero. It should be noted that the solution of the consistent tangent stiffness matrix usually is more complicated than that for the so-called continuum tangent stiffness matrix $\mathbf{D}^{ep}$, given by:

$$\mathbf{D}^{ep}_{ijkl} = \frac{\mathbf{E}_{ijmn}\mathbf{R}_{mn}\mathbf{E}_{klrs}\mathbf{L}_{rs}}{\mathrm{K}_p + \mathbf{L}_{mn}\mathbf{E}_{mnrs}\mathbf{R}_{rs}} \tag{3.20}$$

where **E** denotes the elastic stiffness matrix, **R** denotes the plastic flow direction, **L** denotes the normal to the yield surface, and K_p is the plastic modulus. Because it is simpler to develop the continuum tangent stiffness matrix than the consistent tangent stiffness matrix, the continuum tangent operator is used to replace the consistent one in many cases. However, the use of the continuum tangent stiffness matrix deteriorates the quadratic rate of convergence in the Newton-Raphson iterative solution scheme. In this chapter, the consistent tangent stiffness matrix is employed.

According to the finite element method, the strain increment is passed down from the global program to a subroutine. In the subroutine, based on the strain increment, the constitutive relations are integrated and all the elastoplastic quantities in the new step, including $\Delta\tilde{\boldsymbol{\sigma}}'$, are computed. Following the integration, the consistent tangent stiffness matrix is developed in the subroutine. Finally, the computed stress increment $\Delta\tilde{\boldsymbol{\sigma}}'$ and the consistent tangent stiffness matrix are returned to the global program. In the global program, $\Delta\tilde{\boldsymbol{\sigma}}'$ and the consistent tangent stiffness matrix are used to compute the new strain increment. The iteration process ceases when the errors of the stress and strain increments are smaller than the allowable ones.

3.3.2 Numerical Integration

The integration is performed by using the generalized trapezoidal rule. It is assumed that step n represents the last step and all the quantities at this step are known. With the strain increments $\Delta\varepsilon_v$ and $\Delta\mathbf{e}$ are passed down from the global program, the quantities at step n+1 are to be solved. In this MSC sand model, the constitutive relations needed to be integrated are the elastic relations in equations (3.1) and (3.2), the hardening

rule for the true yield surface in equation (3.5), the hardening rules for two pseudo yield surfaces in equations (3.10) and (3.11), and the flow rules in equations (3.12) and (3.13). In addition, the consistency condition expressed in equation (3.4) needs to be satisfied at step n+1. The results of the integration are given as follows. The subscript "n+1" referring to the quantities for n+1 step is omitted for clear demonstration.

$$R_1 = p - \left[\frac{K_0(1-a_0)}{p_{at}^{a0}} (\Delta\varepsilon_v - \Delta\varepsilon_v^p) + p_n^{1-a0} \right]^{\frac{1}{1-a0}} = 0 \tag{3.21}$$

$$\mathbf{R}_2 = \mathbf{s} - \mathbf{s}_n - \frac{2g_0}{p_{at}^{a0}} \left[(1-\alpha) p_n^{a0} + \alpha p^{a0} \right] (\Delta\mathbf{e} - \Delta\mathbf{e}^p) = 0 \tag{3.22}$$

$$R_3 = \left[(\mathbf{s} - p\boldsymbol{\alpha}) : (\mathbf{s} - p\boldsymbol{\alpha}) \right]^{\frac{1}{2}} - mp = 0 \tag{3.23}$$

$$\mathbf{R}_4 = \boldsymbol{\alpha} - \boldsymbol{\alpha}_n - \Lambda \left[(1-\alpha)(\frac{K_p}{p}\mathbf{n})_n + \alpha(\frac{K_p}{p}\mathbf{n}) \right] = 0 \tag{3.24}$$

$$R_5 = \Delta\varepsilon_v^p - \Lambda\left[(1-\alpha) D_n + \alpha D \right] = 0 \tag{3.25}$$

$$\mathbf{R}_6 = \Delta\mathbf{e}^p - \Lambda\left[(1-\alpha)\mathbf{n}_n + \alpha\mathbf{n} \right] = 0 \tag{3.26}$$

$$R_7 = \left[(1-\alpha)(\frac{p\mathbf{n}}{K_{p12}})_n + \alpha(\frac{p\mathbf{n}}{K_{p12}}) \right] : \left[g_{12}\boldsymbol{\alpha} - (g_{12}\boldsymbol{\alpha})_n \right] - \Lambda = 0 \tag{3.27}$$

$$R_8 = \left[(1-\alpha)(\frac{p\mathbf{n}}{K_{p3}})_n + \alpha(\frac{p\mathbf{n}}{K_{p3}}) \right] : \left[g_3\boldsymbol{\alpha} - (g_3\boldsymbol{\alpha})_n \right] - \Lambda = 0 \tag{3.28}$$

In equations (3.21)-(3.28), α denotes the integration parameter. $\alpha = 0$ indicates the explicit integration, and $\alpha = 1$ indicates the fully implicit integration or the closest point projection technique. It should be noted that in the original trapezoidal rule (Ortiz and Popov, 1985) the elastic moduli are constant, which is applicable to metals, and the trapezoidal integration is not carried out on the elastic relations. On the other hand, the

elastic moduli for sands depend on the confining pressure, and the trapezoid integration is applied to the elastic relations in equation (3.22). This is an expansion of the original trapezoidal rule. The unknown quantities needed to be solved in the above equations are expressed in an array $\mathbf{X} = \{p, \mathbf{s}, \Lambda, \boldsymbol{\alpha}, \Delta\varepsilon_v^p, \Delta\mathbf{e}^p, g_{12}, g_3\}^T$. The above system of equations is highly nonlinear if one recalls the definition of D and K_p and the dependence of some model parameters on the Lode angle in the above section. Therefore, numerical techniques must be used to solve the system of equations. The most widely used technique is Newton-Raphson algorithm, which is described as:

$$-\frac{\partial \mathbf{R}}{\partial \mathbf{X}}\Delta\mathbf{X} = \mathbf{R} \tag{3.29}$$

$$\mathbf{X}_{i+1} = \mathbf{X}_i + \Delta\mathbf{X} \tag{3.30}$$

$\mathbf{R}$ is defined as: $\mathbf{R} = [R_1, \mathbf{R}_2, R_3, \mathbf{R}_4, R_5, \mathbf{R}_6, R_7, R_8]^T$, which is equivalent to the error, in the iteration process. The differentiation of $\mathbf{R}$ with respect to $\mathbf{X}$ is given in the appendix II. The initial value of $\mathbf{X}$ is determined by the so-called elastic predictor, given as $\mathbf{X}_0 = [p, \mathbf{s}, \Lambda_n, \boldsymbol{\alpha}_n, 0, \mathbf{0}, g_{12n}, g_{3n}]^T$, where p and $\mathbf{s}$ are determined only from the elastic stress-strain relation, and Λ_n is the loading index for the last time step. The criteria to judge the cessation of the iteration process are given as:

$$\frac{\|\mathbf{R}\|}{\|\mathbf{X}\|} \le \text{tol1 or,} \tag{3.31a}$$

$$\frac{|R_3|}{m} \le \text{tol2} \tag{3.31b}$$

where $\| \ \|$ represents the length of a vector. Equation (3.31b) corresponds to the error for the consistency condition.

3.3.3 The Development of the Consistent Tangent Stiffness Matrix

After the integration of the model constitutive relations and the solution of the resulted nonlinear equations, the consistent tangent stiffness matrix expressed in equation (3.19) can be developed based on equations (3.21)-(3.28). From the above definition of the constitutive relations and the dependence of some model parameters on the Lode angle, it can be seen that there is no an analytical solution available for the consistent tangent stiffness matrix. Instead, the consistent tangent stiffness matrix is developed numerically. Differentiating equations (3.21)-(3.28) gives:

$$d\mathbf{R} = \frac{\partial \mathbf{R}}{\partial \mathbf{X}} d\mathbf{X} + \frac{\partial \mathbf{R}}{\partial \varepsilon_v} d\varepsilon_v + \frac{\partial \mathbf{R}}{\partial \mathbf{e}} d\mathbf{e} = 0 \tag{3.32}$$

It should be noted that ε_v and $\mathbf{e}$ are considered as two variables in addition to $\mathbf{X}$ in equation (3.32). $d\mathbf{X}$ can be written as:

$$d\mathbf{X} = \left\{dp, d\mathbf{s}, d\varepsilon_v^p, d\mathbf{e}^p, d\Lambda, d\boldsymbol{\alpha}, dg_{12}, dg_3\right\}^T \tag{3.33}$$

Rearranging equation (3.32) leads to:

$$\frac{\partial \mathbf{R}}{\partial \mathbf{X}} d\mathbf{X} = -\frac{\partial \mathbf{R}}{\partial \varepsilon_v} d\varepsilon_v - \frac{\partial \mathbf{R}}{\partial \mathbf{e}} d\mathbf{e} \tag{3.34}$$

From equation (3.34), $d\mathbf{X}$ can be expressed according to $d\varepsilon_v$ and $d\mathbf{e}$ by using the inverse of $\frac{\partial \mathbf{R}}{\partial \mathbf{X}}$, given as:

$$d\mathbf{X} = -\left(\frac{\partial \mathbf{R}}{\partial \mathbf{X}}\right)^{-1}\left(\frac{\partial \mathbf{R}}{\partial \varepsilon_v} d\varepsilon_v + \frac{\partial \mathbf{R}}{\partial \mathbf{e}} d\mathbf{e}\right) \tag{3.35}$$

In equation (3.35), the first two elements dp and ds in $d\mathbf{X}$ can be expressed according to $d\varepsilon_v$ and $d\mathbf{e}$. Thus, the consistent tangent stiffness matrix $\frac{\partial \boldsymbol{\sigma}}{\partial \boldsymbol{\varepsilon}}$ can be obtained. It is worth noting that, although the numerical technique is used to develop the consistent tangent stiffness matrix, the procedure is not complicated in that $\frac{\partial \mathbf{R}}{\partial \mathbf{X}}$ has already been developed in the solution of integrated constitutive relations in equation (3.29).

3.4 Numerical Examples

In this section, the above described numerical solution technique is examined by several examples. The stress-strain responses of Nevada sand with a relative density of 60% under conventional triaxial and simple shear loadings in drained and undrained conditions are simulated. The model constants for Nevada sand are listed in Table 2.1. The focus of this section is to investigate the effectiveness of this numerical procedure and the effects of various values of α on the integration accuracy. The allowable relative error for $\mathbf{R}$ in equation (3.31a) in the local iteration is chosen to be 10^{-6}. The other allowable local error in equation (3.31b) is set to be zero. The relative errors for $\Delta\boldsymbol{\sigma}$ and $\Delta\boldsymbol{\varepsilon}$ in the global iteration are 10^{-4}. If one considers the relative large value of $\|\mathbf{X}\|$, the actual error in the local iteration is usually larger than that in the global iteration. The maximum numbers of global and local iteration are chosen to be ten. To examine the performance of the consistent tangent operator, the stress increment is applied as the input condition in all the four loading conditions considered.

In the triaxial drained and undrained loadings, the radial stress remains constant at 80 kPa and the axial stress keeps increasing until the failure of the sample characterized

by very large strain values. It should be noted that it is the axial stress, rather than the confining pressure, which remains constant. This can result in continuous change of the confining pressure in the drained loading simulation so that the use of the trapezoidal rule in the elastic relations can be investigated. The fully implicit integration procedure with $\alpha = 1$ is used for the simulations. The input axial stress increment at each step is 20 kPa, which is a very large value compared with the radial stress of 80 kPa. Figure 3.1 shows the evolutions of the deviatoric stress and volumetric change with the deviatoric strain in drained loading. The mark of a star in Figure 3.1 and other three following figures denotes the position beyond which convergence doesn't occur with the input of relatively large stress increments. In this case, relatively small stress increments or strain increment inputs are used beyond the symbol of star. Figure 3.2 shows the evolutions of the deviatoric stress and pore water pressure with the deviatoric strain in undrained triaxial loading. For the simple shear simulations under drained and undrained conditions, the axial stress remains constant at 80 kPa. The static lateral pressure coefficient is set to be 0.6 at the start of the loading, which is a typical value for sands. The lateral strain remains at zero throughout the simulation and the shear stress keeps increasing until the failure of the sample characterized by a large strain value. Similar to the triaxial loading simulations, the fully implicit integration procedure with $\alpha = 1$ is used. The shear stress increment at each step is 3 kPa, which is a large value considering only 12 loading steps are required to reach the symbol of the star. Figure 3.3 shows the evolutions of shear stress and volumetric strain with the shear strain in drained loading. Figure 3.4 shows the evolutions of shear stress and pore water pressure with the shear strain in undrained loading.

The above four predictions indicate that this numerical procedure performs very well in both global and local parts. Table 3.1 illustrates the number of global iterations used to reach the allowable global errors for the four predictions before the symbol of star. The number of global iteration by using the continuum tangent operator is also listed in Table 3.1 for comparisons. The fully implicit integration is also employed for the continuum tangent operator. From Table 3.1, it can be seen that despite the large magnitude of the stress increments at each step, the proposed numerical procedure leads to a high convergence rate. In most cases, it requires only four or five iterations to reach the allowable errors. On the other hand, the continuum tangent operator leads to a lower convergence rate than that for the consistent one. Especially for the drained simple shear simulation, the computed stress and strain errors are still larger than the allowable errors even after ten iterations. For the local iteration, the Newton's iterative procedure to solve the system of integrated constitutive equations also leads to a high convergence rate. Consider the fourth step of loading in the drained triaxial loading simulation, where the axial stress is increased from 140 kPa to 160 kPa. The evolution of the relative errors of **R** in the local iterations is shown in Table 3.2. One can see that it takes only four or five local iterations for the relative error of **R** to reduce from an order of 10^{-1} to 10^{-8}.

The effects of α on the integration accuracy are investigated with α equal to 0.5, 0.75 and 1.0, respectively, with various magnitudes of stress increments. The reason to select these values of α is to ensure the stability of the numerical simulation because $\alpha \geq 0.5$ leads to unconditional stability for this problem. The investigation of α effects is limited to the loading path before the symbol of star. Exact solutions cannot be obtained analytically for this model under the loading conditions considered. Instead, the exact

solutions are approximated by using the predictions obtained with a very small magnitude of stress increment for each of the three values of α. The solutions are named exact numerical solutions. The stress increment values used are 0.2 kPa for drained and undrained triaxial loadings, and 0.025 kPa for drained and undraind simple shear loadings. The errors of the simulations compared with the exact numerical solutions, are defined as:

$$\text{Int - error} = \frac{\sum_{1}^{k} |x - x_{exact}|}{\sum_{1}^{k} |x_{exact}|} \tag{3.36}$$

where x denotes the quantity to be examined. In the drained triaxial loading, x represents the deviatoric strain and volumetric strain, respectively. In the undrained triaixal loading, x represents the deviatoric strain and pore water pressure, respectively. In the drained simple shear loading, x represents the shear strain and volumetric strain, respectively. In the undrained simple shear loading, x represents the shear strain and pore water pressure, respectively. x_{exact} represents the numerical exact value. Given a very small step for the exact numerical solution, x_{exact} at any stress is obtained by the interpolation between two adjacent values. k denotes the number of loading steps in equation (3.36).

The integration errors for different values of α are shown in Figure 3.5 to Figure 3.8 for the drained triaxial, undrained triaxial, drained simple shear and undrained simple shear loadings, respectively. In these figures, x-axis represents the ratio between the considered loading increment magnitude and that used to develop the exact numerical solution. y-axis represents the error defined in equation (3.36). Figures 3.5 to 3.8 show that all the integration errors decrease with the decreasing magnitude of stress increment. Overall, the difference of the integration errors between various α in Figure 3.5 to Figure 3.8 is that at larger loading increments, the errors for larger α are smaller than those for

smaller α. In contrast, for smaller loading increments, the errors for smaller α are smaller than those for larger α. This is consistent with the postulates by Ortiz and Popov (1985). Specifically, while $\alpha = 1$ leads to an approximately linear decrease of the errors with the decrease of loading increments, $\alpha = 0.5$ leads to a higher order error decrease. This verifies the postulate by Ortiz and Popov (1985) that $\alpha = 0.5$ leads to the second order accuracy. It is worth noting that the difference of the integration errors between various α for undrained loadings in Figures 3.6 and 3.8 are not as significant as that for drained loadings in Figures 3.5 and 3.7. In addition, for undrained simple shear loading in Figure 3.8, smaller α doesn't lead to smaller errors at smaller loading increments than those for larger α. This is probably related to the bulk water modulus in undrained loadings, which is much larger than soil skeleton modulus. The relatively large bulk water modulus lessens the effects of α on the integration error.

3.5 Conclusions

MSC sand model is numerically implemented within the framework of the finite element method. The numerical implementation is carried out in a single Gauss point, which consists of the numerical integration and the development of the consistent tangent stiffness matrix. The theoretical analysis and numerical examples in this chapter show that, although the MSC is different than the classical elastoplasticity modeling techniques, the MSC and its corresponding sand model are well-suited to numerical techniques used in finite element methods.

The well known generalized trapezoidal integration technique is employed to perform the integration of the model. The originally proposed trapezoidal rule (Ortiz and

Popov, 1985) is expanded in this problem to incorporate the dependence of the elastic moduli on the stress state. The numerical examples under various complicated loading conditions with this comprehensive model substantiate and reconfirm the effects of various α on the integration accuracy proposed originally (Ortiz and Popov, 1985). This will contribute to the wider application of this integration rule to solve real engineering problems.

3.6 References

Borja, R. I. (1990), Cam-Clay Plasticity, Part I: Implicit Integration of Constitutive Relations, *Computer Methods in Applied Mechanics and Engineering*, **78**, 49-72

Borja, R. I. (1991), Cam-Clay Plasticity, Part II: Implicit Integration of Constitutive Equation Based on a Nonlinear Elastic Stress Predictor, *Computer Methods in Applied Mechanics and Engineering*, **88**, 225-240

Braudel, H. J., Abouaf, M. & Chenot, J. L. (1986), An Implicit and Incremental Formulation for the Solution of Elastoplastic Problems by the Finite Element Method, *Comput. Struct.*, **22**, 801-814

Hashash, Y. M. A. & Whittle, A. J. (1992), Integration of the Modified Cam-Clay Model in Non-linear Finite Element Analysis, *Computers and Geotechnics*, **14**, 59-83

Jeremic, B, & Sture, S. (1997), Implicit Integrations in Elastoplastic Geotechnics, *Mechanics of Cohesive-Frictional Materials*, **2**, No. 2, 165-183

Macari, E. J., Weihe. S, & Arduino, P. (1997), Implicit Integration of Elastoplastic Constitutive Models for Frictional Materials with Highly Non-linear Hardening Functions, *Mechanics of Cohesive-Frictional Materials*, **2**, No. 1, 1-29

Manzari, M. T. & Prachathananukit, R. (2001), On Integration of a Cyclic Soil Plasticity Model, *International Journal for Numerical and Analytical Methods in Geomechanics*, **25**, 525-549

Ortiz, M., & Popov, E. P. (1985), Accuracy and Stability of Integration Algorithm for Elastoplastic Constitutive Relations, *International Journal of Numerical Methods in Engineering*, **21**, No. 9, 1561-1576

Ortiz, M., & Simo, J. C. (1986), An Analysis of a New Class of Integration Algortihms for Elastoplastic Constitutive Relations, *Int. J. Num. Meth. In Eng*, **23**, 353-366

Owen, D. R. J. & Hinton, E. (1980), *Finite Elements in Plasticity*, Pineridge, Swansea, U.K., 1980

Rice, J. R. & Tracy, D. M. (1973), Computational Fracture Mechanics, *Proc. Symp. Num. Meth. Struct. Mech.*, Urbana, Illinois, (Ed. Fenves, J.S.), Academic Press, New York

Simo, J. C. & Taylor, R. L. (1985), Consistent Tangent Operator for Rate-Independent Elastoplasticity, *Computer Methods in Applied Mechanics and Engineering*, **48**, 101-118

Simo, J. C. & Taylor, R. L. (1986), Return Mapping Algorithm for Plane Stress Elastoplasticity, *International Journal for Numerical Methods in Engineering*, **22**, 649-670

Simo, J. C. & Hughes, T. J. R. (1998), *Computational Inelasticity*, Spring-Verlag, New York, Inc., 1998

Wilkins, M. L. (1964), Calculation of Elastic-Plastic Flow, *Methods of Computational Physics*, (Ed. B.Alder et al.), Vol. 3, Academic Press, New York

Table 3.1. The Convergence of Global Iteration

(a) Triaxial Loading Simulations

Load No.	Axial Stress	Number of Global Iterations (Triaxial)			
		Drained		Undrained	
		Consistent	Continuum	Consistent	Continuum
1	100	5	7	5	8
2	120	5	8	5	8
3	140	5	8	5	8
4	160	5	8	5	8
5	180	5	8	5	7
6	200	5	11*	5	6
7	220	5	8	4	6
8	240	6	8	4	5
9	260	5	9	4	5
10	280	5	9	4	4
11	300	5	9	4	4
12	320	6	9	5	5
13	340	8	10	4	5
* allowable error wasn't reached (the error in strain was 1.2e-4)					

(b) Simple Shear Simulations

Load No.	Shear Stress	Number of Global Iterations (Simple Shear)			
		Drained		Undrained	
		Consistent	Continuum*	Consistent	Continuum
1	3	5	1.9e-4; 9.8e-5	5	6
2	6	5	1.0e-3; 2.7e-4	5	7
3	9	4	1.7e-3; 3.5e-4	5	7
4	12	5	2.9e-3; 4.6e-4	5	7
5	15	5	4.7e-3; 5.6e-4	5	8
6	18	5	7.0e-3; 6.2e-4	5	9
7	21	5	9.7e-3; 6.9e-4	5	8
8	24	5	1.2e-2; 8.4e-4	5	9
9	27	6	1.4e-2; 1.1e-3	6	10
10	30	6	1.3e-2; 1.2e-3	6	10
11	33	6	3.6e-3; 4.0e-4		
12	36	7	6.5e-2; 4.4e-5		
* allowable error wasn't reached, listed are stress and strain errors after 10 iterations					

Table 3.2. The Convergence of Local Iterations for Drained Triaxial Simulation at the 4th step.

Global Iteration No.	1				2					
Local Iteration No.	1	2	3	4	1	2	3	4	5	
Error of **R**	0.11	2.9e-4	8.6e-6	6.2e-8	0.36	4.2e-3	1.1e-5	1.3e-6	2.2-8	
Global Iteration No.	3					4				
Local Iteration No.	1	2	3	4	5	1	2	3	4	5
Error of **R**	0.39	5.4e-3	4.8e-6	3.7e-6	3.7e-8	0.4	5.6e-3	7.4e-6	1.7e-6	1.7e-8

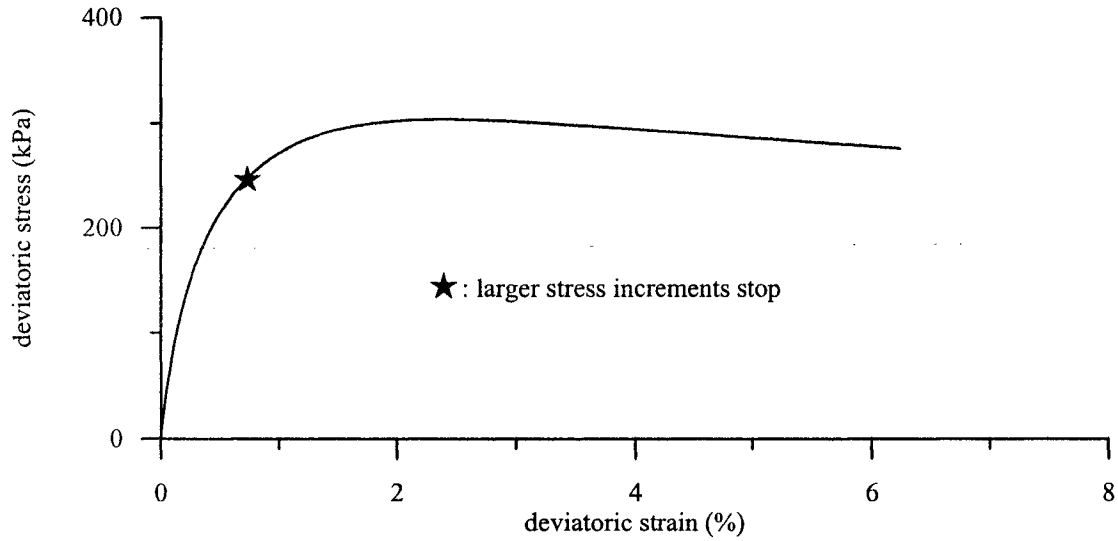

(a)

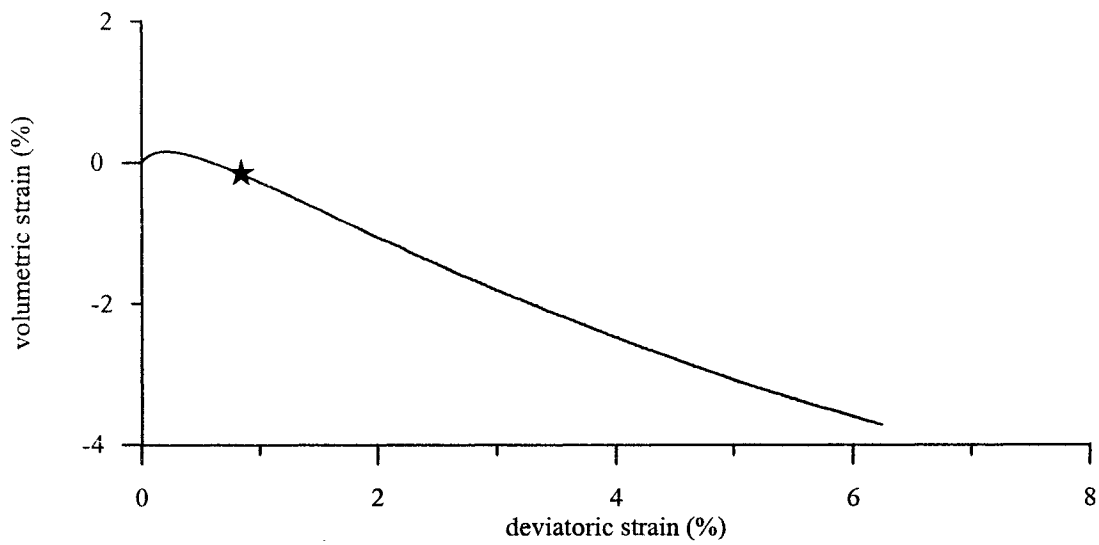

(b)

Figure 3.1: the simulation for conventional drained triaxial loading

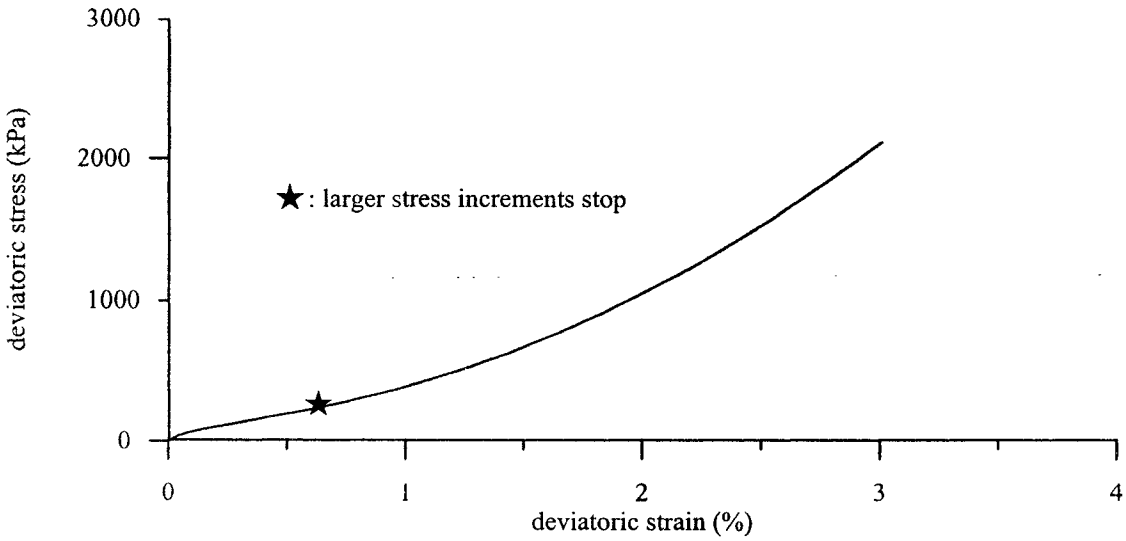

(a)

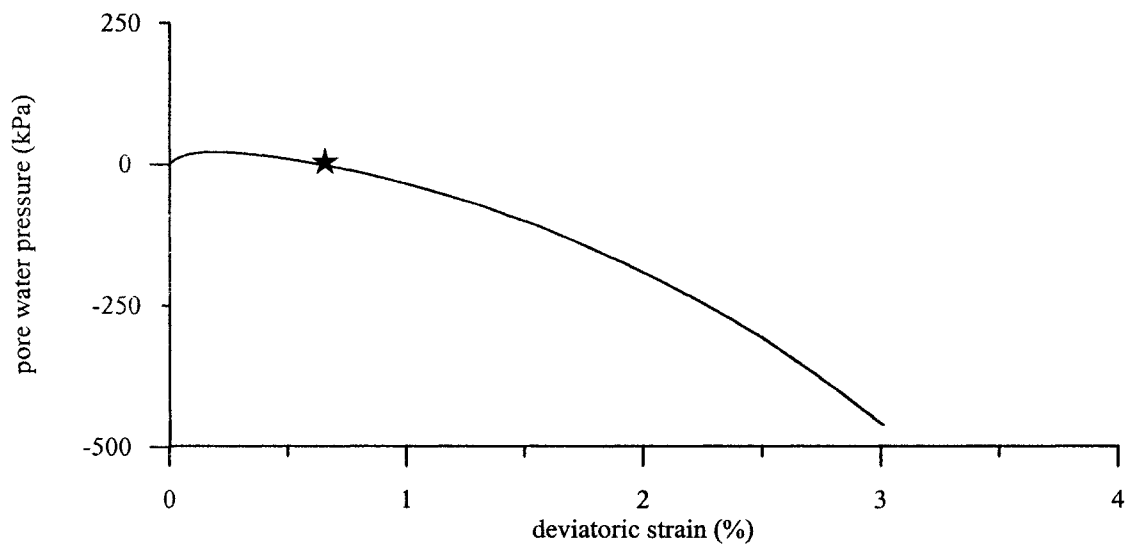

(b)

Figure 3.2: the simulation for conventional undrained triaxial loading

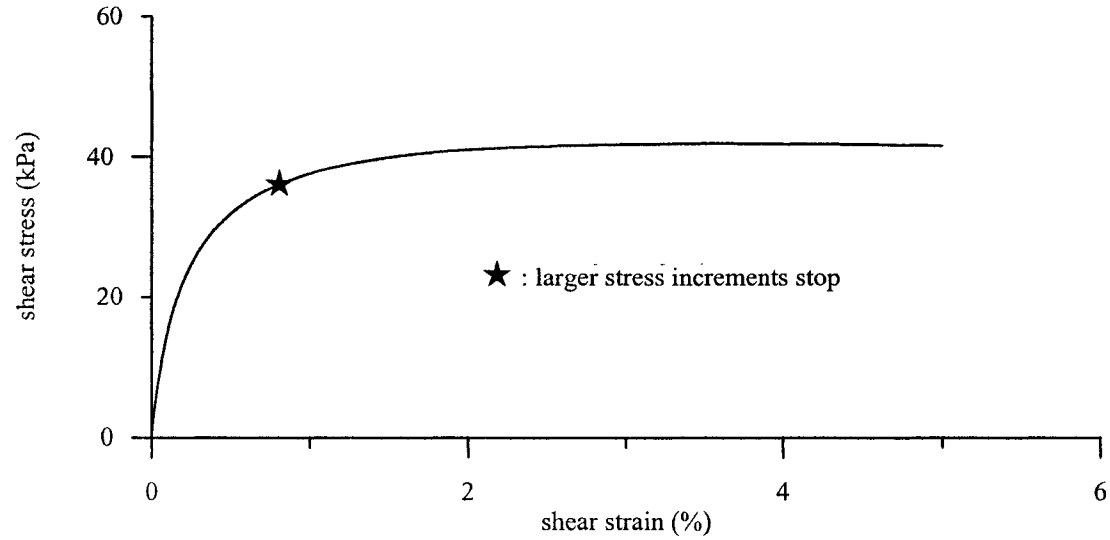

(a)

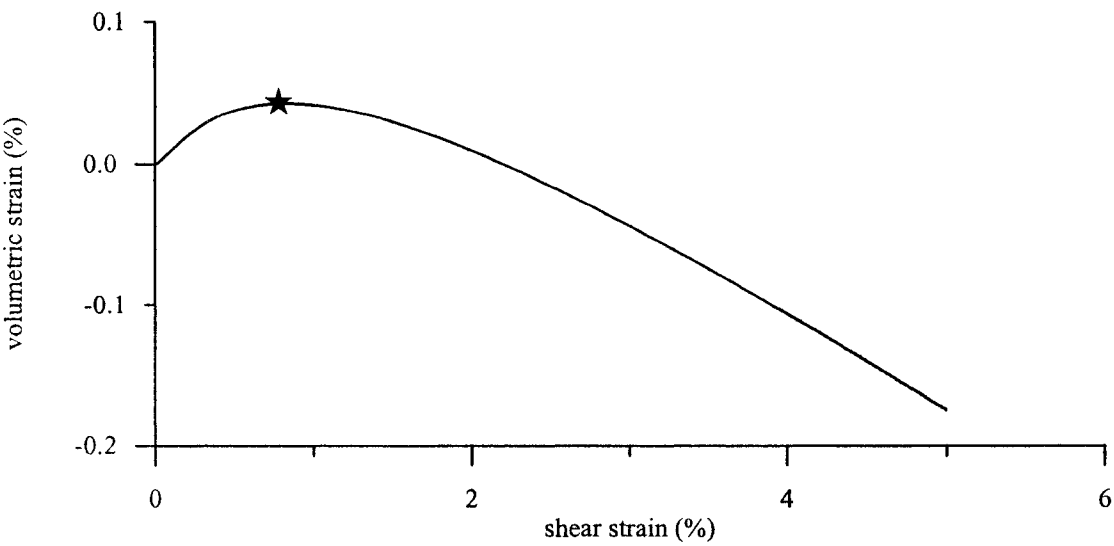

(b)

Figure 3.3: the simulation for drained simple shear loading

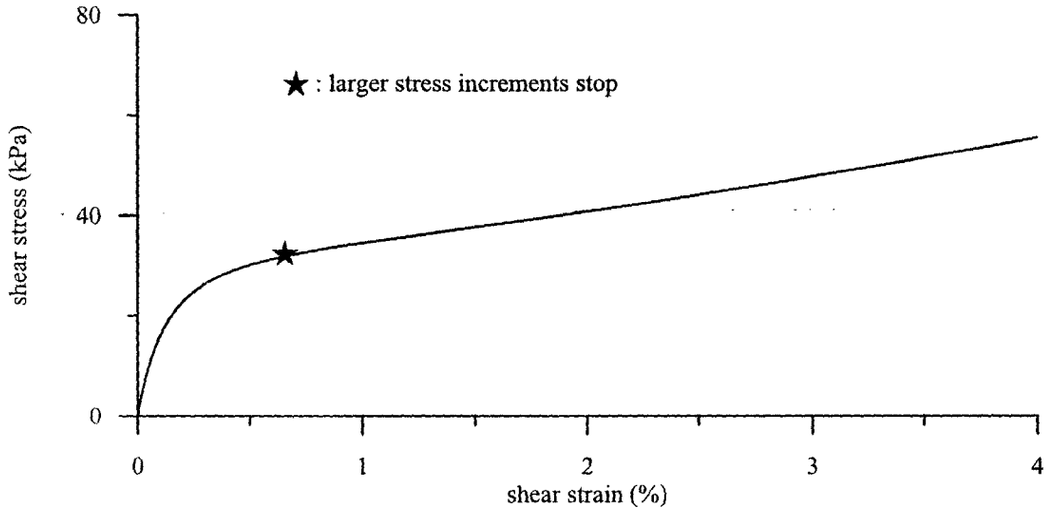

(a)

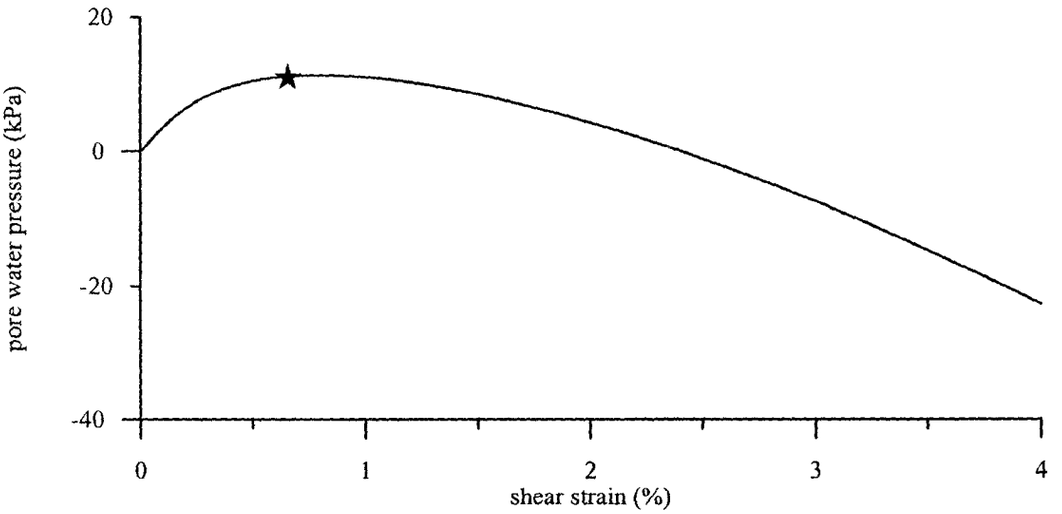

(b)

Figure 3.4: the simulation for undrained simple shear loading

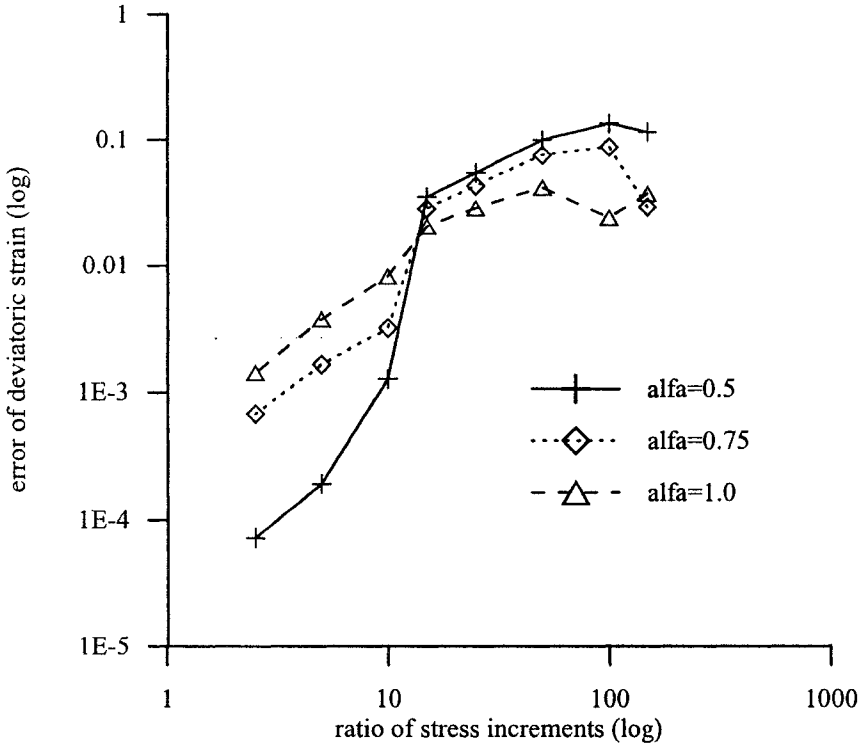

(a)

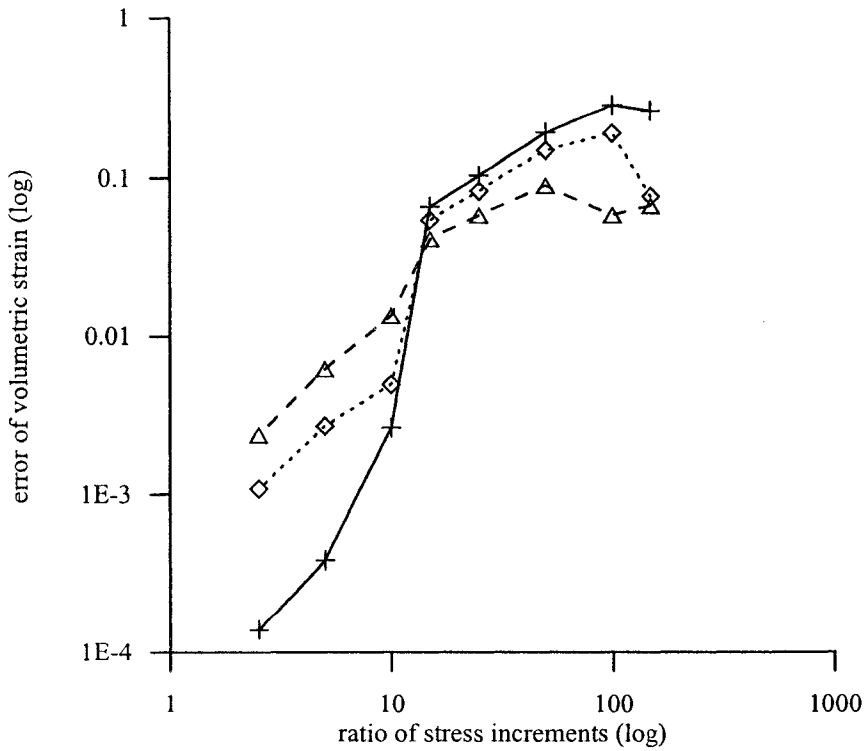

(b)

Figure 3.5: the integration error for conventional drained triaxial loading

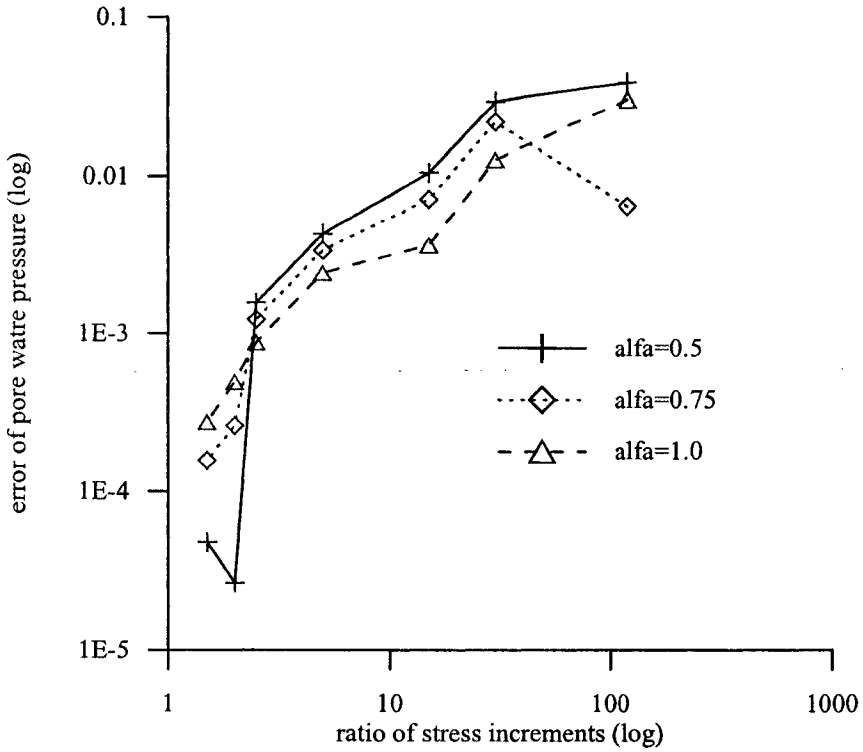

(a)

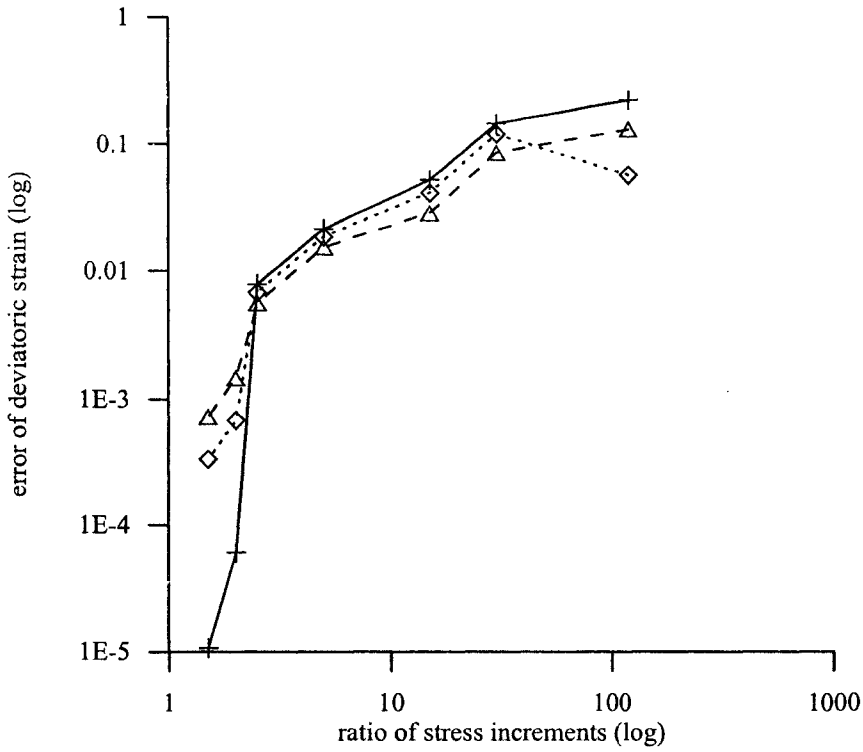

(b)

Figure 3.6: the integration error for conventional undrained triaxial loading

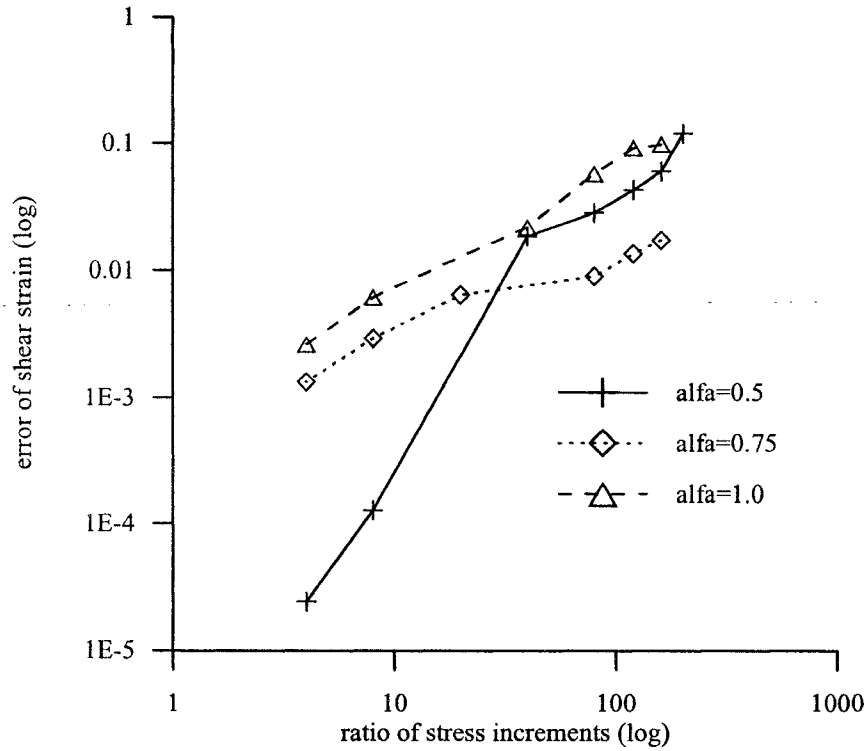

(a)

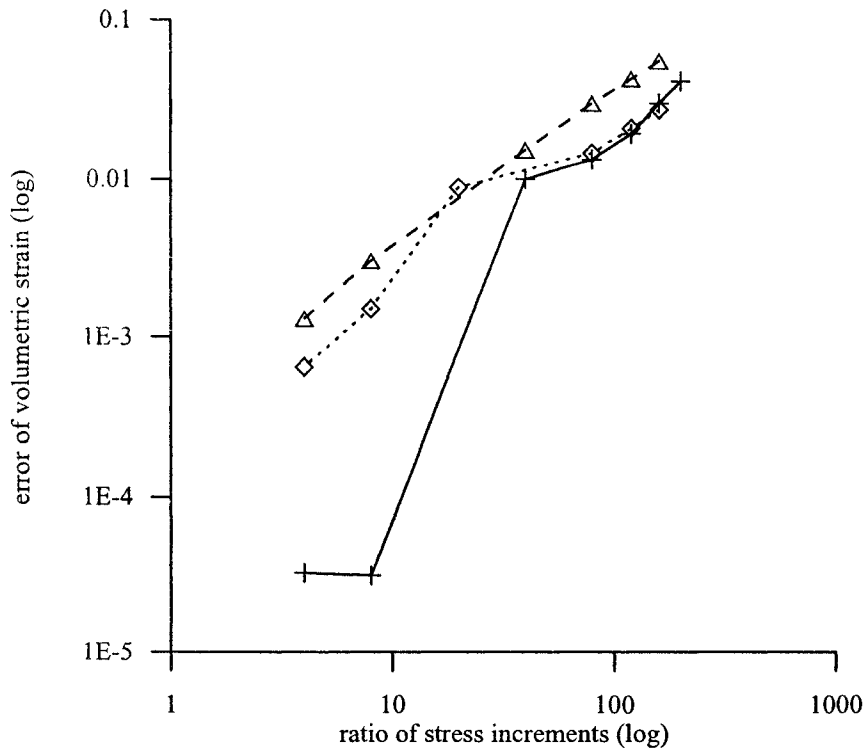

(b)

Figure 3.7: the integration error for drained simple shear loading

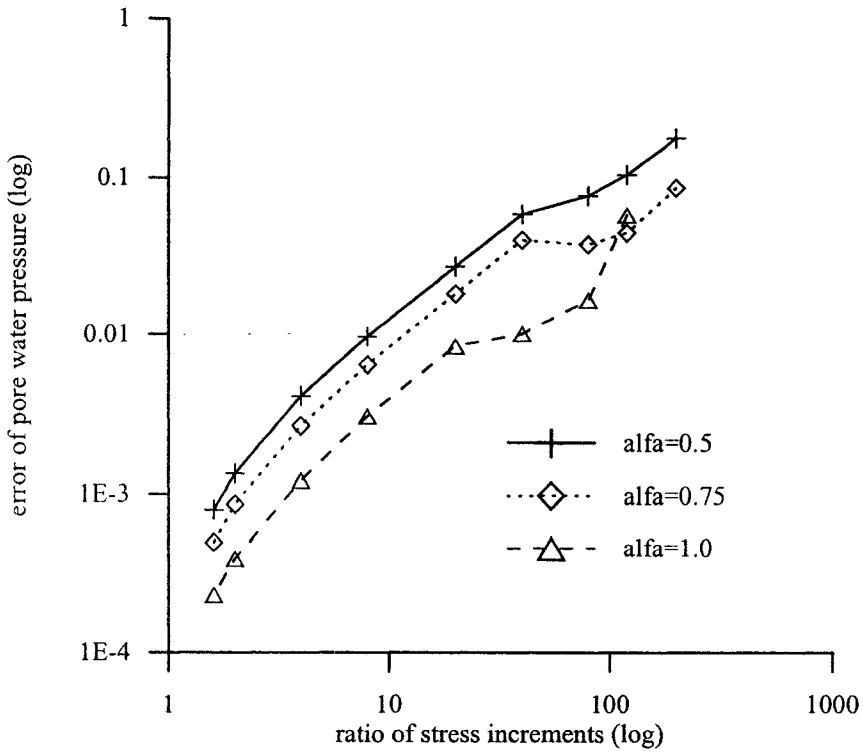

(a)

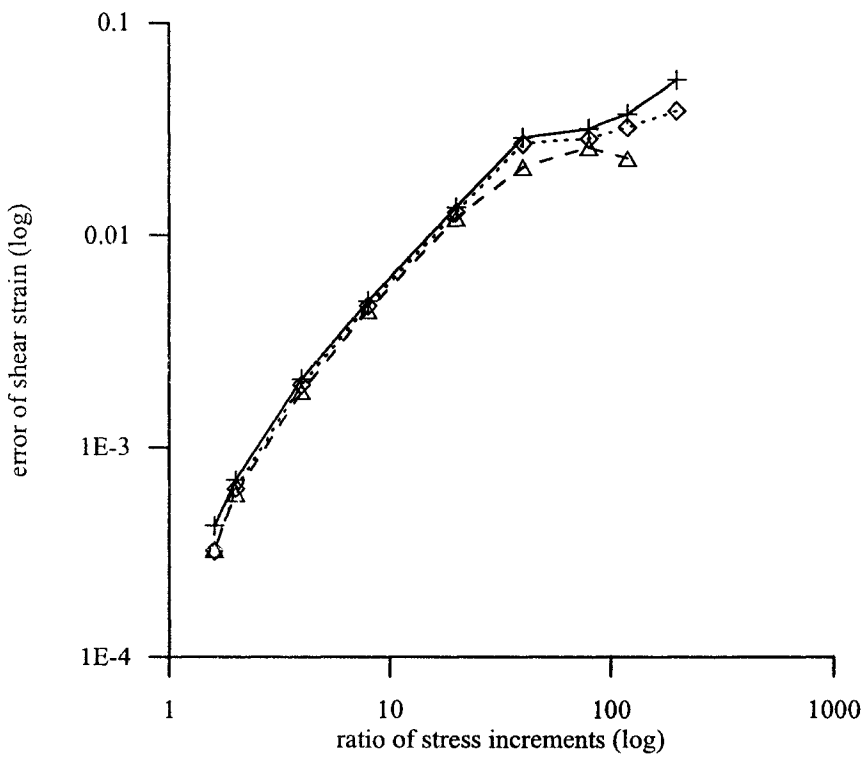

(b)

Figure 3.8: the integration error for undrained simple shear loading

Chapter 4

Solution Existence Conditions for Elastoplastic Constitutive Models of Granular Materials

4.1 Introduction

Classical elastoplasticity theory was initially developed based on the associated flow rule, in which the direction of plastic strain rate coincides with the normal to the yield surface. However, it was found that the associated flow rule is not applicable to many materials, such as granular materials, and a non-associated flow rule needs to be used for these materials (Chen & Baladi, 1985). Unlike the associated flow rule, the use of a non-associated flow rule may encounter the problems of instability, bifurcation, violation of the thermodynamic laws, non-uniqueness, and nonexistence of solutions even in the strain hardening regime (Drucker, 1959; Mroz, 1963, 1966; Mandel, 1964; Maier & Hueckel, 1979). Most of their studies and the subsequent efforts were focused on the plastic modulus (Runesson & Mroz, 1989; Ottosen & Runesson, 1991; Klisinski et al., 1992). Among all these problems brought by non-associated flow rules, the solution nonexistence is the most critical. For example, in the load deformation boundary value problems within the framework of the finite element method, even if the solution doesn't exist at a single Gauss point, it may result in the global failure of the computations. Maier & Hueckel (1979) studied the conditions for solution existence under various conditions when the stress or strain rate is given. They postulated that a solution doesn't exist if the plastic modulus is below a critical value in the strain hardening regime when the strain

rate is given. This critical plastic modulus was derived for mixed stress and strain controlled loading conditions by Klisninski et al. (1992), Nova (1994) and Mroz & Rodzik (1995).

While most of the research efforts on the solution existence for non-associated flow rule models were focused on the plastic modulus, this chapter is aimed at investigating the effects of different flow rules and elastic stress-strain relationship on the solution existence under strain controlled loadings. Because it is the non-associated nature of flow rules that brings the problems, investigation of the flow rules is of particular significance. In this chapter, the original Rowe's and Roscoe's flow rules and their modified versions for granular materials are considered (Rowe et al., 1962, 1964, 1969; Roscoe et al., 1963; Manzari & Dafalias, 1997; Wan & Guo, 1999). It will also be shown that the elastic stress-strain relationship is as important as the flow rules in analyzing the solution existence problem. The elastic stress-strain relationship is characterized by the Poisson's ratio in this chapter. Both isotropic and anisotropic elasticity are investigated. The analysis is performed in the strain hardening regime on the models with Drucker-Prager's yield functions that are widely used to represent granular materials.

4.2 Conditions for the Solution Existence

In classical elastoplasticity theory, the total strain rate $\dot{\varepsilon}_{ij}$ can be decomposed into an elastic part and plastic part, given as:

$$\dot{\varepsilon}_{ij} = \dot{\varepsilon}_{ij}^{e} + \dot{\varepsilon}_{ij}^{p} \tag{4.1}$$

where a superposed dot indicates the rate and the superscripts e and p denote the elastic and plastic parts, respectively. The elastic stress-strain relationship can be expressed as:

$$\dot{\sigma}_{ij} = E_{ijkl}\dot{\varepsilon}^{e}_{kl} \tag{4.2}$$

where the fourth-order tensor E_{ijkl} represents the elastic tangent moduli for an isotropic material, defined as:

$$E_{ijkl} = K\delta_{ij}\delta_{kl} + G\left(\delta_{ik}\delta_{jl} + \delta_{il}\delta_{jk} - \frac{2}{3}\delta_{ij}\delta_{kl}\right) \tag{4.3}$$

where K and G denote the elastic bulk and shear moduli, respectively. δ_{ij} denotes Kronecker delta. The plastic strain rate is defined as:

$$\dot{\varepsilon}^{p}_{ij} = \langle\dot{\lambda}\rangle R_{ij} \tag{4.4}$$

where $\dot{\lambda}$ denotes the loading index, and R_{ij} denotes the direction of $\dot{\varepsilon}^{p}_{ij}$. $\langle\ \rangle$ denotes Macauley brackets. When $\dot{\lambda}$ is positive, $\langle\dot{\lambda}\rangle = \dot{\lambda}$, and indicates the plastic deformation occurs. When $\dot{\lambda}$ is negative, $\langle\dot{\lambda}\rangle$ is zero, and indicates that there is no plastic deformation. The evolution of hardening parameter α_{ij} is defined as:

$$\dot{\alpha}_{ij} = \langle\dot{\lambda}\rangle h_{ij} \tag{4.5}$$

h_{ij} denotes the direction of $\dot{\alpha}_{ij}$. Furthermore, the process of loading and deformation needs to satisfy Kuhn-Tucker conditions, given as:

$$\dot{\lambda} \geq 0, \quad \dot{f}(\sigma_{ij}, \alpha_{ij}) \leq 0, \quad \dot{\lambda}\dot{f}(\sigma_{ij}, \alpha_{ij}) = 0 \tag{4.6}$$

where f denotes the yield surface, which is a function of stress states and hardening parameters. Here, only one hardening parameter α_{ij} is used for the sake of simplicity. When $\dot{\lambda}$ is zero, the material experiences only elastic deformation. $\dot{f}$ can be zero or

negative. Zero $\dot{f}$ indicates that stress state moves on the yield surface, called the neutral loading. Negative $\dot{f}$ indicates that stress state moves towards inside of the yield surface, called unloading. When $\dot{\lambda}$ is positive, the material experiences both elastic and plastic deformation. In this case, $\dot{f}$ must be zero, which is called the consistency condition, written as:

$$\dot{f} = \frac{\partial f}{\partial \sigma_{ij}} \dot{\sigma}_{ij} + \frac{\partial f}{\partial \alpha_{ij}} \dot{\alpha}_{ij} = 0 \tag{4.7}$$

When $\dot{\lambda}$ is positive, by using equations (4.1), (4.2), (4.4), (4.5), (4.7), one can obtain the tangent elastoplastic stiffness tensor D_{ijkl} and the compliance tensor C_{ijkl}, given as:

$$\dot{\sigma}_{ij} = D_{ijkl} \dot{\varepsilon}_{kl} \tag{4.8a}$$

$$\dot{\varepsilon}_{ij} = C_{ijkl} \dot{\sigma}_{kl} \tag{4.8b}$$

$$D_{ijkl} = E_{ijkl} - \frac{P_{ij} Q_{kl}}{B} \tag{4.9a}$$

$$C_{ijkl} = D^{-1}{}_{ijkl} \tag{4.9b}$$

$$P_{ij} = E_{ijab} R_{ab} \tag{4.10}$$

$$Q_{kl} = E_{klrs} L_{rs} \tag{4.11}$$

$$B = K_p + L_{ab} E_{abcd} R_{cd} \tag{4.12}$$

$$L_{ij} = \frac{\partial f}{\partial \sigma_{ij}} \tag{4.13}$$

$$K_p = -\frac{\partial f}{\partial \alpha_{ij}} h_{ij} \tag{4.14}$$

L_{ij} denotes the normal to the yield surface. If L_{ij} is the same as R_{ij}, the flow rule is associated. On the other hand, if L_{ij} is different than R_{ij}, the flow rule is non-associated. K_p denotes the plastic modulus. Positive K_p indicates strain hardening, and negative K_p indicates strain softening. In this chapter, the analysis is restricted within the regime of strain hardening.

Any solution of stress and strain rates must satisfy Kuhn-Tucker conditions, which involve $\dot{f}$ and $\dot{\lambda}$. By using equations (4.1), (4.2), (4.4), (4.5), (4.7), one can also obtain $\dot{\lambda}$, in terms of the stress or strain rate, given as:

$$\dot{\lambda} = \frac{1}{K_p} L_{ij} \dot{\sigma}_{ij} \tag{4.15}$$

$$\dot{\lambda} = \frac{L_{ij} E_{ijkl} \dot{\varepsilon}_{kl}}{B} \tag{4.16}$$

Assume $\dot{\sigma}_{ij}$ is known, the yield surface is convex, the stress state is on the yield surface, and K_p is positive. Equation (4.15) is used to determine $\dot{\lambda}$. If the stress rate is positioned outside of the yield surface, the product of L_{ij} and $\dot{\sigma}_{ij}$ is positive, so that $\dot{\lambda}$ is positive. According to Kuhn-Tucker conditions, $\dot{f}$ needs to be zero. On the other hand, if the stress rate is positioned inside of the yield surface, the product of L_{ij} and $\dot{\sigma}_{ij}$ is negative, so that $\dot{\lambda}$ is also negative. According to Kuhn-Tucker conditions, $\dot{\lambda}$ is reset to zero. Meanwhile, $\dot{f}$ is negative because the stress state tends to move inside of the yield surface. Zero $\dot{\lambda}$ and negative $\dot{f}$ satisfy Kuhn-Tucker conditions.

Consider the strain controlled loading under the same assumptions as in the stress controlled loading. Equation (4.16) is used to determine $\dot{\lambda}$. $E_{ijkl}\dot{\varepsilon}_{kl}$ in equation (4.16) can be denoted by $\dot{\sigma}_{ij}^{*}$, which is equivalent to $\dot{\sigma}_{ij}$ in equation (4.15), in terms of the determination of $\dot{\lambda}$. Two cases need to be considered in terms of the value of B in equation (4.16). When B is positive, it is equivalent to K_p, and the determination of $\dot{\lambda}$ is identical to that for stress controlled loadings. Kuhn-Tucker conditions are always satisfied. The situation becomes complicated when B is negative. If $\dot{\sigma}_{ij}^{*}$ is directed inside of the yield surface, the product of L_{ij} and $\dot{\sigma}_{ij}^{*}$ is negative. As B is negative, $\dot{\lambda}$ is positive. According to Kuhn-Tucker conditions, $\dot{f}$ is zero. This suggests that the material experience the strain softening although K_p is still positive. Furthermore, assume $\dot{\lambda}$ is zero and the plastic deformation doesn't happen. Because $\dot{\sigma}_{ij}^{*}$ is directed inside of the yield surface, $\dot{f}$ is negative. The zero $\dot{\lambda}$ and negative $\dot{f}$ also satisfy Kuhn-Tucker conditions. Therefore, there are two solutions corresponding to negative B when $\dot{\sigma}_{ij}^{*}$ is directed inside of the yield surface. Consider B is negative and $\dot{\sigma}_{ij}^{*}$ is directed outside of the yield surface. In this case, the product of L_{ij} and $\dot{\sigma}_{ij}^{*}$ is positive, which results in negative $\dot{\lambda}$. This doesn't satisfy Kuhn-Tucker conditions. As a result, $\dot{\lambda}$ is reset to zero. Because $\dot{\sigma}_{ij}^{*}$ is directed outside of the yield surface, $\dot{f}$ is positive. The positive $\dot{f}$ violates Kuhn-Tucker conditions. Therefore, when B is negative and $\dot{\sigma}_{ij}^{*}$ is directed outside of the yield surface, there is no admissible $\dot{\sigma}_{ij}$. In another word, the elastoplastic solution doesn't exist.

From the above discussion, the key to the solution existence under strain controlled loadings is to ensure positive B. For associated flow rules, R_{ij} is the same as L_{ij}, and the product of L_{ij}, E_{ijkl}, and R_{kl} is positive. With a positive K_p in the strain hardening regime, B is always positive. However, for granular materials characterized with non-associated flow rules, the product of L_{ij}, E_{ijkl}, and R_{kl} is not necessarily positive. The conditions of the solution existence for the granular material models characterized with Drucker-Prager's yield surfaces are investigated below.

4.3 Solution Existence Conditions for Granular Material Models

4.3.1 Granular Material Models

Drucker-Prager's yield function is widely used to represent granular material behavior. It is expressed as:

$$f = \left[\left(\frac{s_{ij}}{p} - \alpha_{ij}\right)\left(\frac{s_{ij}}{p} - \alpha_{ij}\right)\right]^{1/2} - m = 0 \tag{4.17}$$

where p and s_{ij} denotes the hydrostatic and deviatoric parts of the stress state, respectively. α_{ij} denotes the kinematic hardening parameter, and m denotes the isotropic hardening parameter. Equation (4.17) represents a cone in the principal stress space, where mp is the radius of the cone and α_{ij} represents its axis position. It is convenient to develop the model formulations on the stress ratio π-plane, where the quantity is s_{ij}/p. The flow rules can be expressed in terms of the hydrostatic and deviatoric parts of the plastic strain rate, $\dot{\varepsilon}_v^p$ and $\dot{e}_{ij}^p$, respectively, given as:

$$\dot{\varepsilon}_{ij}^{p} = \frac{1}{3}\dot{\varepsilon}_{v}^{p} I_{ij} + e_{ij}^{p} \tag{4.18a}$$

$$\dot{\varepsilon}_{v}^{p} = \dot{\lambda} D \tag{4.18b}$$

$$\dot{e}_{ij}^{p} = \dot{\lambda} n_{ij} \tag{4.18c}$$

where D denotes the dilatancy ratio between the hydrostatic part and deviatoric part of the plastic strain rate. Positive D indicates the plastic volumetric contraction, and negative D indicates the plastic volumetric expansion. I_{ij} is a second-order isotropic tensor. n_{ij} represents the normal to the yield surface projected on the stress ratio π-plane, defined as:

$$n_{ij} = (r_{ij} - \alpha_{ij})/m \tag{4.19a}$$

$$r_{ij} = \frac{s_{ij}}{p} \tag{4.19b}$$

It should be noted that the associated flow rule is employed on the stress ratio π plane, but not for the hydrostatic plastic strain rate. The normal to the yield surface L_{ij} and the plastic strain rate direction R_{ij} can be written as:

$$L_{ij} = n_{ij} - \frac{1}{3} N I_{ij} \tag{4.20a}$$

$$N = n_{ij} r_{ij} \tag{4.20b}$$

$$R_{ij} = n_{ij} + \frac{1}{3} D I_{ij} \tag{4.21}$$

Substitution of the above model formulations for granular materials into the expression for B in equation (4.12) leads to:

$$B = K_{p} + 2G - KDN \tag{4.22}$$

In elasticity theory, K and G can be expressed as:

$$K = \frac{E}{3(1-2\nu)} \tag{4.23a}$$

$$G = \frac{E}{2(1+\nu)} \tag{4.23b}$$

where E denotes Young's modulus, and ν denotes Poisson's ratio. K_p denotes the plastic modulus and can be determined by any hardening rule. Compared with elastic moduli, the plastic modulus is negligible during most of the loading paths for granular materials. Accordingly, B can be approximated by $\widetilde{B}$, written as:

$$\widetilde{B} = 2G - KDN \tag{4.24}$$

For associated flow rule, D is equal to negative N, and $\widetilde{B}$ becomes,

$$\widetilde{B} = 2G + KN^2 \tag{4.25}$$

In this case, $\widetilde{B}$ is always positive. However, it is well known that non-associated flow rules apply to granular materials, which indicates $\widetilde{B}$ is not necessarily positive. The widely used flow rules for granular materials are Rowe's and Roscoe's flow rules, and those modified based on them. Rowe et al. (1962, 1964, 1969) developed the stress-dilatancy relations for triaxial compression, extension conditions and plane strain condition, under the assumption of the minimum energy criterion. Roscoe et al. (1963) developed the flow rule under triaxial conditions on the basis of the energy dissipation. Thereafter, many flow rules were developed based on them, in order to appropriately represent the effects of confining pressures, void ratios and fabric anisotropy on the dilatancy ratio of granular materials (Wan & Guo, 1999; Dafalias & Manzari, 1997; Manzari & Dafalias, 1999). It is worth noting that most of the flow laws were originally

developed under triaxial loading conditions. Under triaxial loading conditions, n_{ij} and r_{ij} hold the same direction, which results in the largest value of N in equation (4.20). According to the expression of $\widetilde{B}$ in equation (4.24), triaxial loading conditions are the most or nearly most critical condition among all the possible loading paths. Therefore, the examination of $\widetilde{B}$ for various flow rules will be performed under triaxial loading conditions.

Under triaxial loading conditions, the deviatoric parts of stress and strain states can be represented by:

$$q = \sigma_1 - \sigma_3 \tag{4.26a}$$

$$\dot{\gamma}^p = \frac{2}{3}(\dot{\varepsilon}_1^p - \dot{\varepsilon}_3^p) \tag{4.26b}$$

n_{ij} expressed in the form of a vector $\{n_{11}, n_{22}, n_{33}, n_{12}, n_{23}, n_{31}\}^T$ is $\frac{1}{\sqrt{6}}\{2, -1, -1, 0, 0, 0\}^T$ and $\frac{1}{\sqrt{6}}\{-2, 1, 1, 0, 0, 0\}^T$ for triaxial compression and extension, respectively.

Correspondingly, N and D become,

$$N = \pm\frac{\sqrt{6}}{3}\frac{q}{p} \qquad \text{(+: compression; -: extension)} \tag{4.27}$$

$$D = \pm\frac{2}{\sqrt{6}}\frac{\dot{\varepsilon}_v^p}{\dot{\gamma}^p} \qquad \text{(+: compression; -: extension)} \tag{4.28}$$

$\widetilde{B}$ becomes,

$$\widetilde{B} = E\left[\frac{1}{(1+\nu)} - \frac{2}{9(1-2\nu)}\frac{\dot{\varepsilon}_v^p}{\dot{\gamma}^p}\frac{q}{p}\right] \tag{4.29}$$

where E and ν are used to replace K and G.

4.3.2 Examination of Rowe's and Roscoe's Flow Rules

Rowe's flow rule under triaixal compression conditions was originally given as:

$$\frac{\sigma_1}{\sigma_3} = C(\frac{-2\dot{\varepsilon}_3^p}{\dot{\varepsilon}_1^p}) \tag{4.30a}$$

$$C = tan^2(45^0 + \frac{\phi_u}{2}) \tag{4.30b}$$

where ϕ_u denotes the angle of friction between particles. Equation (4.30) can be rewritten as:

$$\frac{\dot{\varepsilon}_v^p}{\dot{\gamma}^p} = \frac{3(C-1)-(C+2)\frac{q}{p}}{\frac{2}{3}(1-C)\frac{q}{p}+(1+2C)} \tag{4.31}$$

Substituting equation (4.31) into equation (4.29), one can obtain $\widetilde{B}$, given as:

$$\widetilde{B} = \frac{2K}{d}\widetilde{B}^* \tag{4.32a}$$

$$\widetilde{B}^* = a(\frac{q}{p})^2 + b(\frac{q}{p}) + c \tag{4.32b}$$

$$d = 2C(3-\frac{q}{p}) + 2\frac{q}{p} + 3 \tag{4.32c}$$

$$a = C + 2 \tag{4.32d}$$

$$b = -3(C-1)(1+x) \tag{4.32e}$$

$$c = \frac{9}{2}(1+2C)x \tag{4.32f}$$

$$x = \frac{1-2\nu}{1+\nu} \tag{4.32g}$$

C is always greater than unity and q/p is usually smaller than 3, which indicates d is positive. As a result, $\widetilde{B}$ and $\widetilde{B}^*$ share the same sign. $\widetilde{B}^*$ represents a parabolic equation with the stress ratio as the variable. This parabolic equation is concave upward as shown in Figure 4.1. A part of $\widetilde{B}^*$ is below zero only if,

$$y = b^2 - 4ac > 0 \tag{4.33}$$

Substitution of equations (4.32d), (4.32e) and (4.32f) into equation (4.33) leads to:

$$y = a^* x^2 + b^* x + c^* > 0 \tag{4.34a}$$

$$a^* = c^* = (C-1)^2 \tag{4.34b}$$

$$b^* = -2(C^2 + 7C + 1) \tag{4.34c}$$

$y > 0$ is satisfied when $x < x_1$ or $x > x_2$, where x_1 and x_2 are two solutions of $y = 0$, which is shown in Figure 4.2. According to the formulations of x and C, x can never exceed x_2 as far as granular materials are concerned. In summary, given a granular material with a specific friction of angle or C, the existence of a solution is dependent on its Poisson's ratio represented by x. The Poisson't ratio corresponding to x_1 is called the critical Poisson's ratio ν_{cr}, expressed as:

$$\nu_{cr} = \frac{1 - x_1}{2 + x_1} \tag{4.35}$$

Substituting x_1 into equation (4.32), one can obtain the critical stress ratio $(q/p)_{cr}$ corresponding to ν_{cr} (Note: this critical stress ratio is different than that in the critical state soil mechanics). When the Poisson's ratio for a granular material is greater than ν_{cr} or $x < x_1$, $\widetilde{B}^*$ is susceptible to be negative. In this case, $\widetilde{B}^*$ is negative when q/p is between $(q/p)_1$ and $(q/p)_2$, which are two solutions of $\widetilde{B}^* = 0$. $(q/p)_{cr}$, as

a reference value, is larger than $(q/p)_1$. In Figure 4.3 the critical Poisson's ratios and the stress ratios corresponding to various angles of friction are given. Figure 4.4 shows the evolution of $\widetilde{B}^*$ with the increase of the Poisson's ratio when the angle of friction is 50 degree. Figure 4.3 shows that the critical Poisson's ratio decreases and the critical stress ratio increases with the increase of friction angles. For granular materials, the angle of friction between particles usually ranges from 10 to 40 degrees. This indicates that the corresponding critical Poisson's ratio ranges from 0.5 to 0.4, in Figure 4.3. In view of the fact that the Poisson's ratio for granular materials normally is between 0.2 and 0.3, a normal Poisson's ratio doesn't cause the problem with solution nonexistence when the original Rowe's flow rule is employed.

Rowe's flow rule under triaxial extension loading conditions can be expressed as,

$$-\frac{\dot{\varepsilon}_v^p}{\dot{\gamma}^p}=\frac{3(C-1)+(2C+1)\dfrac{q}{p}}{\dfrac{2}{3}(C-1)\dfrac{q}{p}+2+C} \tag{4.36}$$

Along the same line as for the triaxial compression, the critical Poisson's ratio and critical stress ratio under extension conditions can also be determined as a function of the angle of friction. It is found that the critical Poisson's ratio for extension under a particular angle of friction is the same as that for compression. But the critical stress ratio for extension is smaller than that for compression, which as shown in Figure 4.3. The smaller critical stress ratio for extension is consistent with the fact that the extension shear strength is smaller than that under compression.

Roscoe's flow rule under triaxial conditions can be written as:

$$\frac{\dot{\varepsilon}_v^p}{|\dot{\gamma}^p|} = M - \frac{|q|}{p} \tag{4.37}$$

where M denotes the critical stress ratio in the critical state soil mechanics. Usually, M for triaxial compression is larger than that for extension. q and $\dot{\gamma}^p$ are positive for triaxial compression and negative for extension. Substitution of equation (4.37) into (4.29) leads to:

$$\widetilde{B} = \frac{2}{3} K \widetilde{B}^* \tag{4.38a}$$

$$\widetilde{B}^* = (\frac{q}{p})^2 - M\frac{|q|}{p} + \frac{9}{2}x \tag{4.38b}$$

where x is the same as in Rowe's flow rule in equation (4.32g). Similar to Rowe's flow rule, a part of $\widetilde{B}^*$ is negative, when the following condition is satisfied:

$$x < \frac{M^2}{18} \tag{4.39}$$

A critical Poisson's ratio can be obtained, when $x = M^2/18$. If the Poisson's ratio of a material is greater than the critical one, the material is susceptible to solution nonexistence. Substituting the critical Poisson's ratio into equation (4.38), one can obtain the corresponding critical stress ratio, $(q/p)_{cr} = M/2$. Figure 4.5 illustrates the critical Poisson's ratios and stress ratios for various values of M. In Figure 4.5, the critical Poisson's ratio decreases and the critical stress ratio increases with the increase of M. Comparing Figures 4.3 and 4.5, one can see that M is equivalent to ϕ_u as far as the existence of a solution is concerned. This is consistent with the fact that the critical stress ratio M in the critical state soil mechanics is dependent on the angle of friction between particles. The evolution of $\widetilde{B}^*$ with the Poisson's ratio for Roscoe's flow rule is similar to

that for Rowe's flow rule in Figure 4.4. M for granular materials usually ranges from 0.5 to 2.0 under triaxial compression and extension conditions. This indicates the corresponding critical Poisson's ratio ranges from 0.5 to 0.35 in Figure 4.5, which is above the normal Poisson's ratios for granular materials. Therefore, Roscoe's flow rule usually doesn't cause the solution nonexistence problem.

4.3.3 Examination of Modified Rowe's and Roscoe's Flow Rules

The volumetric change of granular materials is affected by many factors, such as the inherent anisotropy, stress-induced anisotropy, confining pressure and void ratio. For example, when a sand is subjected to shearing, lower confining pressure and void ratio lead to greater tendency of volumetric expansion than higher confining pressure and void ratio. It is well known that anisotropic fabric in granular materials is produced during the process of deposition or sample preparation. In addition, when the granular material is subject to shearing, anisotropic fabric is produced even if the material initially has an isotropic fabric. After removal of the shear force, a significant amount of fabric anisotropy may still remain. Figure 4.6 shows the effects of fabric anisotropy on the volumetric change under triaxial loading condition. In Figure 4.6, the sample initially has an anisotropic fabric. The fabric in the horizontal direction represented by F_{33} is stronger than that in the vertical direction represented by F_{11}. When the sample is subject to triaxial loading, the compression causes greater volumetric contraction than that under extension due to the fabric anisotropy, shown in Figure 4.6. Although Rowe's and Roscoe's flow rules are concise and widely used in constitutive models for granular materials, they are highly idealized and can not appropriately represent the dependence of

volumetric change on the fabric, confining pressure and void ratio. This is reflected in equations (4.31), (4.36) and (4.37), in which the confining pressure, void ratio and fabric anisotropy are not included. To incorporate the effects of confining pressure, void ratio and fabric anisotropy on the volumetric change, various modifications have been made based on the original Rowe's and Roscoe's flow rules. These modified flow rules were developed so that lower confining pressures and void ratios lead to greater tendency of volumetric expansion. In addition, many modified flow rules incorporate the effects of fabric anisotropy illustrated in Figure 4.6. Without loss of generality, consider two typical flow rules modified based on Rowe's and Roscoe's flow rules, respectively (Wan & Guo, 1999; Manzari & Dafalias, 1997; Dafalias & Manzari, 1999).

The flow rule by Wan & Guo (1999) incorporates the void ratio, confining pressure and fabric anisotropy through energy dissipation considerations at grain contacts during macroscopic deformations. Their flow rule under triaixal compression conditions can be expressed as:

$$\frac{\sigma_1}{\sigma_3} = C^*\left(\frac{-2\dot{\varepsilon}_3^p}{\dot{\varepsilon}_1^p}\right) \tag{4.40a}$$

$$C^* = tan^2\left(45^0 + \frac{\phi_f}{2}\right) \tag{4.40b}$$

$$sin\phi_f = \frac{X(F_{33}/F_{11}) + \gamma^{*p}}{a + \gamma^{*p}}\left(\frac{e}{e_{cr}}\right)^{\alpha} sin\phi_u \tag{4.40c}$$

$$e_{cr} = e_{cr0}\, exp\left[-(p/h_{cr})^{ncr}\right] \tag{4.40d}$$

where F_{33} and F_{11} represent the fabric components in the principal stress directions as shown in Figure 4.6. γ^{*p} denotes the true plastic shear strain. e and e_{cr} denote the current void ratio and the void ratio at the critical state under the current confining

pressure, respectively. X, a are the parameters related to the fabric anisotropy. α is the parameters related to the void ratio and confining pressure. e_{cr0}, h_{cr} and n_{cr} are the parameters for the void ratio at the critical state. ϕ_f is the modified ϕ_u, and is equivalent to ϕ_u in terms of the determination of the critical Poisson's ratio and corresponding stress ratio. When the effects of fabric anisotropy, void ratio and confining pressure are ignored, ϕ_f is equal to ϕ_u and Equation (4.40) becomes the original Rowe's flow rule. Figure 4.3 originally designed for ϕ_u is also applicable to ϕ_f. From equation (4.40), it can be seen that ϕ_f increases with the increase of void ratio, confining pressure and fabric anisotropy F_{33}/F_{11}, which results in the decrease of critical Poisson's ratio.

The volumetric changes of several types of sands under various conditions were predicted by Guo (2000) using Equation (4.40). Critical Poisson's ratios and stress ratios for this flow rule are determined using Figure 4.3 in this section. The effects of void ratios and confining pressures on the volumetric changes of Sacramento River Sand and Toyoura under triaxial compression were investigated using the flow rule given in Equation (4.40). The model parameters are listed in Table 4.1. From the void ratios, confining pressures and the model parameters in Table 4.1, ϕ_f can be determined. From ϕ_f, the critical Poisson's ratios and stress ratios can be determined in Figure 4.3. The results are shown in Tables 4.2 and 4.3, for these two sands under various conditions. It should be noted that the evolution of the void ratio is ignored for the determination of the critical Poisson's ratio because the solution nonexistence usually occurs during the early stages of shearing. Tables 4.2 and 4.3 show that the critical Poisson's ratio decreases with the increase of confining pressures and void ratios. However, the computed critical

Poisson's ratios are still above the normal Poisson's ratios for granular materials. The reason is that only the effects of confining pressure and void ratios are considered for these two sands, but the fabric anisotropy effect is not considered. The effect of fabric anisotropy, as well as the confining pressure and void ratio, is considered in Ottawa Sand using Equation (4.40). The parameters for this flow rule are listed in Table 4.4. Volumetric changes were predicted under the confining pressure of 200 kPa for various void ratios and initial fabric anisotropies. The corresponding critical Poisson's ratios and stress ratios are listed in Table 4.5. It can be seen that the critical Poisson's ratios are quite low and within the range of normal Poisson's ratios for granular materials under some conditions. For example, ν_{cr} is as low as 0.236 when the void ratio is 0.735 and F_{33}/F_{11} is 1.53. ν_{cr} is 0.321 when the void ratio is 0.65 and F_{33}/F_{11} is 1.75. It should be noted that the corresponding critical stress ratios are quite high under these two conditions, at 1.9 and 1.4, respectively. However, the higher the ϕ_f is, the more sensitive $\widetilde{B}^*$ is to the Poisson's ratio. Consider the case in which the void ratio is 0.735 and F_{33}/F_{11} is 1.53. Compared with ν_{cr} at 0.236, when the Poisson's ratio of Ottawa Sand is chosen as 0.3, the solution doesn't exist when the stress ratio is higher than $(q/p)_1$ at 1.1.

The modification of the original Roscoe's flow rule by Manzari & Dafalias (1997) and Dafalias & Manzari (1999) under triaxial compression conditions is given as,

$$\frac{\dot{\varepsilon}_v^p}{\dot{\gamma}^p} = A(M + k\psi - \frac{q}{p}) \tag{4.41a}$$

$$\psi = e - e_{cr} \tag{4.41b}$$

$$e_{cr} = e_{ref} - \lambda ln(p/p_{ref}), \text{ or } e_{cr} = e_{ref} - \lambda(p/p_{at})^{\xi} \tag{4.41c}$$

$$A = A_0(1 + \langle \boldsymbol{f} : \boldsymbol{n} \rangle) \tag{4.41d}$$

where ψ denotes the state parameter, which is the difference between the current void ratio and the void ratio at the critical state e_{cr} under the current confining pressure. $\boldsymbol{f}$ denotes the fabric tensor. It is postulated that A increases only when the material experiences volumetric dilation. k, A_0, e_{ref}, p_{ref}, λ and ξ are model parameters. If k is zero, A_0 is unity and the fabric anisotropy effect is ignored, the flow rule in Equation (4.41) becomes the original Roscoe's flow rule. Along the same line as in the original Roscoe's flow rule, it can be derived that the material is susceptible to solution nonexistence, when

$$x < \frac{M^{*2}}{18} \tag{4.42a}$$

$$M^* = \sqrt{A}(M + k\psi) \tag{4.42b}$$

M^* is equivalent to M in the original Roscoe's flow rule as far as the critical Poisson's ratio is concerned. The critical stress ratio corresponding to the critical Poisson's ratio is $(M + k\psi)/2$. The dependence of the critical Poisson's ratio and stress ratio on M^* is also illustrated in Figure 4.5. Similar to the modified Rowe's flow rule, equation (4.42) indicates that the critical Poisson's ratio decreases with the increase of void ratio, confining pressure and fabric anisotropy, and the critical stress ratio increases with the increase of void ratio and confining pressure.

This modified Roscoe's flow rule was applied to predict Nevada Sand and Toyoura Sand in Chapter 1. The model parameters related to the volumetric change are

listed in Table 4.6. The behavior for medium dense and dense Nevada Sand was predicted under various confining pressures in this study. The critical Poisson's ratios and stress ratios for these medium dense, dense sands, together with the sand at the maximum porosity are determined from Figure 4.5 and shown in Table 4.7. It can be seen that higher void ratios lead to lower critical Poisson's ratios. For the maximum porosity, the critical Poisson's ratio is as low as 0.32. The Poisson's ratio for Nevada Sand in this model is 0.125, which is much lower than the critical one. Therefore, the behavior of Nevada Sand predicted with this model is not susceptible to solution nonexistence. The critical Poisson's ratios and stress ratios for Toyoura Sand under various confining pressures and void ratios are shown in Table 4.8. The same conclusions as for Nevada Sand can be drawn for Toyoura Sand. The minimum critical Poisson's ratio in the Table 4.8 is 0.4 when the void ratio is 0.833 and the confining pressure is 3 MPa. The minimum critical Poisson's ratios for Nevada Sand and Toyoura Sand are 0.32 and 0.4 in Tables 4.7 and 4.8, which are higher than the normal Poisson ratios for granular materials. However, the effect of fabric anisotropy has not been considered for these two sands. If the fabric anisotropy is considered, the critical Poisson's ratios will be smaller than those shown in Tables 4.7 and 4.8.

4.3.4 Consideration of Elastic Anisotropy

The fabric anisotropy influences not only the plastic flow of granular materials, but also their elastic properties. Correspondingly, some models incorporate the elastic anisotropy (Nemat-Nasser & Balendran, 1992). The effects of elastic anisotropy on the

critical Poisson's ratio and solution existence are discussed in this section. Under triaxial isotropic conditions, the elastic stiffness matrix can be written as:

$$\begin{Bmatrix} \dot{\sigma}_{11} \\ \dot{\sigma}_{22} \\ \dot{\sigma}_{33} \end{Bmatrix} = \begin{bmatrix} G & H & H \\ H & G & H \\ H & H & G \end{bmatrix} \begin{Bmatrix} \dot{\varepsilon}_{11} \\ \dot{\varepsilon}_{22} \\ \dot{\varepsilon}_{33} \end{Bmatrix} \tag{4.43a}$$

$$G = \frac{E(1-\nu)}{(1+\nu)(1-2\nu)} \tag{4.43b}$$

$$H = \frac{E\nu}{(1+\nu)(1-2\nu)} \tag{4.43c}$$

Under triaxial conditions, the cross anisotropy, in which the horizontal stiffness is different than the vertical stiffness, is the most common occurrence. One form of the elastic stiffness matrices representing the cross anisotropy can be written as:

$$\begin{Bmatrix} \dot{\sigma}_{11} \\ \dot{\sigma}_{22} \\ \dot{\sigma}_{33} \end{Bmatrix} = \begin{bmatrix} G & H & H \\ \beta H & \beta G & \beta H \\ \beta H & \beta H & \beta G \end{bmatrix} \begin{Bmatrix} \dot{\varepsilon}_{11} \\ \dot{\varepsilon}_{22} \\ \dot{\varepsilon}_{33} \end{Bmatrix} \tag{4.44}$$

where β is an anisotropy parameter. When β is greater than unity, it indicates the horizontal stiffness is greater than the vertical one. In contrast, when β is smaller than unity, the vertical stiffness is greater than the horizontal one. It should be noted that there are many other forms to express the elastic anisotropy (Graham & Houlsby, 1983). The expression in equation (4.44) is used for the sake of clearly demonstrating the effects of elastic anisotropy on the solution existence.

Consider Rowe's flow rule under triaxial compression conditions. Substituting the anisotropic elastic stiffness matrix, Rowe's triaxial compression flow rule into the expression of B in equation (4.12) and ignoring the plastic modulus, one can obtain,

$$\widetilde{B} = \frac{2K}{d}\widetilde{B}^* \tag{4.45a}$$

$$\widetilde{B}^* = a'(\frac{q}{p})^2 + b'(\frac{q}{p}) + c' \tag{4.45b}$$

$$a' = \frac{1}{3}(2\beta+1)(C+2) + \frac{2}{3}(\beta-1)(1-C)x \tag{4.45c}$$

$$b' = (4\beta - 2C - \beta C - 1) + (\beta C + 2\beta - 4C + 1)x \tag{4.45d}$$

$$c' = \frac{3}{2}(\beta+2)(2C+1)x + 3(C-1)(1-\beta) \tag{4.45e}$$

where K, d, x, C are the same as those for the isotropic elasticity in equation (4.32). When β is unity, a', b' and c' become a, b and c in equation (4.32). Along the same line as for the isotropic elasticity, the critical Poisson's ratio and stress ratio for the anisotropic elasticity can be determined as a function of β as well as the friction angle, which are illustrated in Figure 4.7. It can be seen that when β is larger than unity, which indicates stronger stiffness in the horizontal direction than in the vertical one, its critical Poisson's ratio and stress ratio are smaller than those with isotropic elasticity. In contrast, smaller β leads to larger critical Poisson's ratio and stress ratio. Recall β is equivalent to F_{33}/F_{11} for the plastic flow. While stronger stiffness in the horizontal direction reduces the critical Poisson's ratio through plastic flow rule during triaxial compression, it further reduces the critical Poisson's ratio through anisotropic elasticity.

4.4 Conclusions and Discussions

The solution existence is discussed for granular material models with Drucker-Prager's yield surfaces. The emphasis is placed on the effects of various flow rules and

elastic stress-strain relationships. It is found there exists a critical Poisson's ratio during strain controlled loading. When the Poisson's ratio of a material is above the critical Poisson's ratio, the constitutive model is susceptible to solution nonexistence. For the original Rowe's and Roscoe's flow rules, the critical Poisson's ratio is higher than the normal Poisson's ratios for granular materials, and the material doesn't have solution nonexistence problem. On the other hand, for the modified Rowe's and Roscoe's flow rules, the critical Poisson's ratio is lower than that for the original Rowe's and Roscoe's when the void ratio and confining pressure are relatively high and fabric anisotropy is considered. In addition, when the anisotropic elasticity is used, the fabric anisotropy may further reduce the critical Poisson's ratio. Therefore, special attention should be paid to the selection of Poisson's ratio under these conditions, to ensure the solution existence.

In complicated load deformation boundary value problems within the framework of the finite element method, the void ratio, confining pressures and fabric of granular materials may be subject to dramatic changes. Medium dense and dense materials can evolve to loose ones during loading. Therefore, to ensure the solution existence under any condition, the material Poisson's ratio should be selected below the critical Poisson's ratio under the worst possible condition. For example, for Nevada sand represented with the modified Roscoe's flow rule without consideration of fabric anisotropy, the Poisson's ratio should be chosen below 0.3, which corresponds to its maximum void ratio. If the effects of fabric anisotropy on the flow rule and elastic relationship are considered, its Poisson's ratio should be further reduced.

4.5 References

Chen, W. F., & Baladi, G. Y. (1985), *Soil Plasticity: Theory and Implementation*, Elsevier, Amsterdam

Dafalias, Y. F. & Manzari, M. T. (1999), Modeling of Fabric Effect on the Cyclic Loading Response of Granular Soils, *Proceedings of ASCE 13th Engineering Mechanics Conference*, Baltimore, Maryland, 13-16 June 1999

Drucker, D. C. (1959), A Definition of a Stable Inelastic Material, *J. Appl. Mech.* **26**, 101-106

Graham, J. & Houlsby, G. T. (1983), Anisotropic Elasticity of a Natural Clay, *Geotechnique* **33**, No. 2, 165-180

Guo, P. J. (2000), *Modeling Granular Materials with Respect to Stress-Dilatancy and Fabric: A Fundamental Approach*, PhD dissertation, University of Calgary

Klisinski, M., Mroz, Z. & Runesson, K. (1992) Structure of Constitutive Equations in Plasticity for Different Choices of State and Control Variables, *International Journal of Plasticity* **8**, No. 3, 221-243

Maier, G. & Hueckel, T. (1979), Nonassociated and Coupled Flow Rules of Elastoplasticity for Rock-like Materials, *Int. J. Rock Mech. Min. Sci. & Geomech. Abstr.* **16**, 77-92

Mandel, J. (1964), Conditions de Stabilite et Postulat de Drucker, *J. Kravichenko and P.M. Sirieys, eds., Proc. IUTAM Symposium on Rheology and Soil Mechanics*, Springer-Verlag, Berlin, 58-68

Manzari, M. T. & Dafalias, Y. F. (1997), A Critical State Two-Surface Plasticity Model for Sands, *Geotechnique* **47**, No. 2, 255-272

Mroz, Z. (1963), Non-Associated Flow Laws in Plasticity, *J. de Mechanique* **2**, 21-42

Mroz, Z. (1966), On Forms of Constitutive Laws for Elastic-plastic Solids, *Arch. Mech. Stosowanej* **18**, 1-34

Mroz, Z. & Rodzik, P. (1995), On the Control of Deformation Process by Plastic Strain, *International Journal of Plasticity* **11**, No. 7, 827-842

Nemat-Nasser, S. & Balendran, B. (1992), Plastic Flow of Particulate Media, *Plastic Flow and Creep, MD* **31**, 93-105

Nova, R. (1994), Controllability of the Incremental Response of Soil Specimens Subjected to Arbitrary Loading Programmes, *Journal of the Mechanical Behavior of Materials* **5**, No. 2, 193-201

Ottosen, N, & Runesson, K. (1991), Properties of Bifurcation Solutions in Elasto-Plasticity, *Int. J. Solids and Structures* **27**, 401-421

Roscoe, K. H., Schofield, A. N. & Thurairajah, A. (1963), Yielding of Clays in States Wetter than Critical, *Geotechnique* **13**, No. 3, 211-240

Rowe, P. W. (1962), The Stress Dilatancy Relation for Static Equilibrium of an Assembly of Particles in Contact, *Proc., Roy. Soc., London, Series A* **269**, 500-527

Rowe, P. W., Barden, L. & Lee, I. K. (1964), Energy Components During the Triaxial Cell and Direct Shear Tests, *Geotechnique* **14**, No. 3, 247-261

Rowe, P. W. (1969), The Relation Between the Shear Strength of Sands in Triaxial Compression, Plane Strain and Direct Shear, *Geotechnique* **19**, No. 1, 75-86

Runesson, K., & Mroz, Z. (1989), A Note on Nonassociated Plastic Flow Rules, *International Journal of Plasticity* **5**, 639-658

Wan, R. G. & Guo, P. J. (1999), Description of Macroscopic Stress-Dilatancy in a Granular Assembly with Microstructure, *13th ASCE Engineering Mechanics Division Conference*, Baltimore, MD, USA, June 13-16, 1999

Table 4.1: Modified Rowe's Flow Rule Parameters for Sacramento River Sand and Toyoura Sand (After Guo, 2000)

Sand Type	e_{cr0}	h_{cr} (Mpa)	n_{cr}	ϕ_u	α
Sacramento River Sand	1.03	22.139	0.7075	34	1.2828
Toyoura Sand	0.933	15.54	0.8046	31	1.3

Table 4.2: The Critical Poisson's Ratios and Stress Ratios for Sacramento River Sand Under Various Conditions with Modified Rowe's Flow Rule (e_0, p_0 are After Guo, 2000)

e_0	0.61				0.87				
p_0 (Mpa)	0.1	0.3	1.05	2	0.1	0.2	0.45	1.27	2
ϕ_f	17.1	17.7	19.4	21.2	27.6	28.1	29.2	32.3	34.7
ν_{cr}	0.485	0.484	0.481	0.477	0.460	0.459	0.455	0.449	0.436
$(q/p)_{cr}$	0.333	0.345	0.383	0.424	0.578	0.585	0.618	0.673	0.765

Table 4.3: The Critical Poisson's Ratios and Stress Ratios for Toyoura Sand Under Various Conditions with Modified Rowe's Flow Rule (e_0, p_0 are After Guo, 2000)

p_0 (Mpa)	0.1			0.5		
e_0	0.831	0.917	0.996	0.81	0.886	0.96
ϕ_f	26.9	31.0	35.0	27.7	31.5	35.5
ν_{cr}	0.462	0.450	0.435	0.460	0.448	0.433
$(q/p)_{cr}$	0.560	0.665	0.773	0.580	0.678	0.787

Table 4.4: Modified Rowe's Flow Rule Parameters for Ottawa Sand (After Guo, 2000)

e_{cr0}	h_{cr} (Mpa)	n_{cr}	ϕ_u	α	X	a
0.75	11.23	0.6467	33	1.926	0.004	0.004

Table 4.5: The Critical Poisson's Ratios and Stress Ratios for Ottawa Sand Under Various Conditions with Modified Rowe's Flow Rule (e_0, F_{33}/F_{11} are After Guo, 2000)

e_0	0.65				0.735					
F_{33}/F_{11}	0.75	1.0	1.33	1.75	0.75	0.86	1.0	1.16	1.33	1.53
ϕ_f	20.9	28.5	39.3	56.5	26.9	31.3	37.2	44.5	53.4	67.5
ν_{cr}	0.477	0.458	0.418	0.321	0.462	0.449	0.427	0.393	0.342	0.236
$(q/p)_{cr}$	0.417	0.60	0.896	1.467	0.560	0.673	0.835	1.055	1.354	1.904

Table 4.6: Modified Roscoe's Flow Rule Parameters for Nevada Sand and Toyoura Sand

Sand Type	M	λ	e_{ref}	p_{ref} (kPa)	ξ	k	A
Nevada Sand	1.30	0 ($p < 160$ kPa) 0.04 ($p > 160$ kPa)	0.78	160		11	0.8
Toyoura Sand	1.27	0.019	0.934		0.7	6	0.7

Table 4.7: The Critical Poisson's Ratio and Stress Ratio for Nevada Sand Under Various Conditions with Modified Roscoe's Flow Rule

e_0	0.661	0.737	0.887 (maximum e_0)
p_0(kPa)	40-160	40-160	0-160
M^*	0	0.740	2.215
ν_{cr}	0.5	0.477	0.320
$(q/p)_{cr}$	0	0.414	1.238

Table 4.8: The Critical Poisson's Ratio and Stress Ratio for Toyoura Sand Under Various Conditions with Modified Roscoe's Flow Rule

e_0	0.831	0.996	0.810	0.960	0.735	0.833
p_0(kPa)	100	100	500	500	3000	3000
M^*	0.641	1.469	0.734	1.487	1.095	1.587
ν_{cr}	0.483	0.415	0.478	0.413	0.452	0.402
$(q/p)_{cr}$	0.383	0.878	0.439	0.889	0.654	0.948

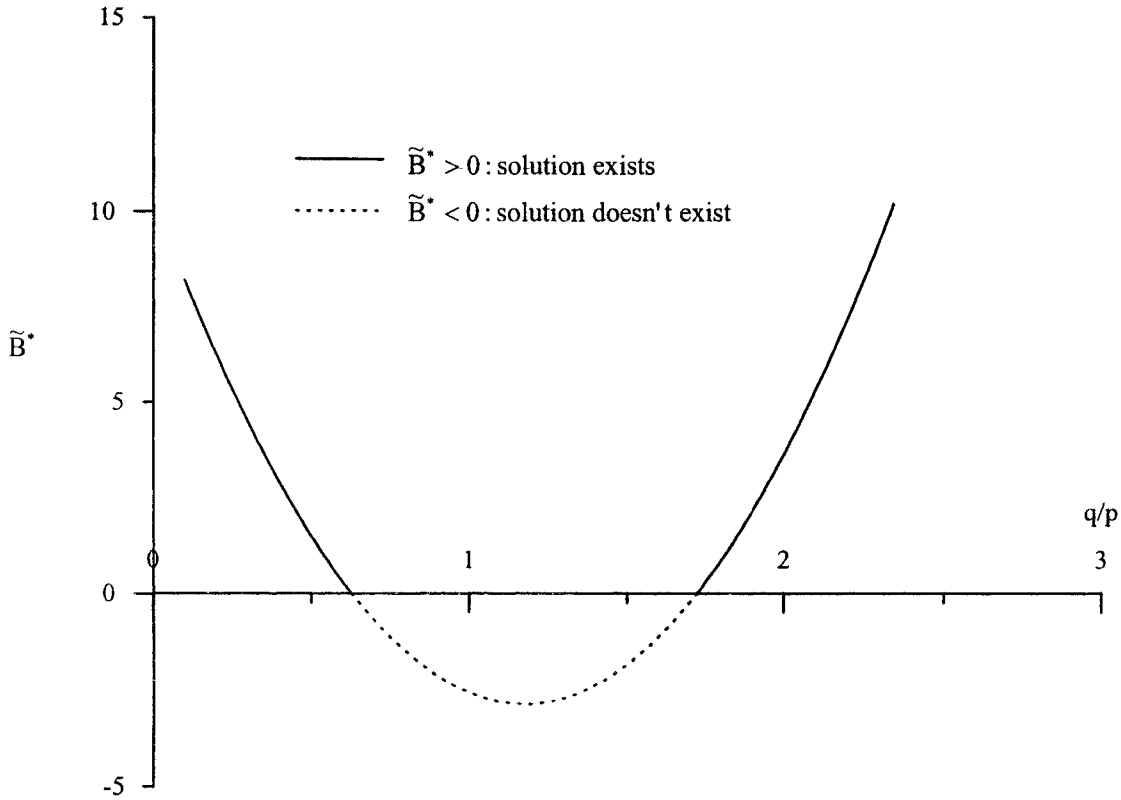

Figure 4.1 : $\widetilde{B}^*$ – q/p and the conditions for solution existence

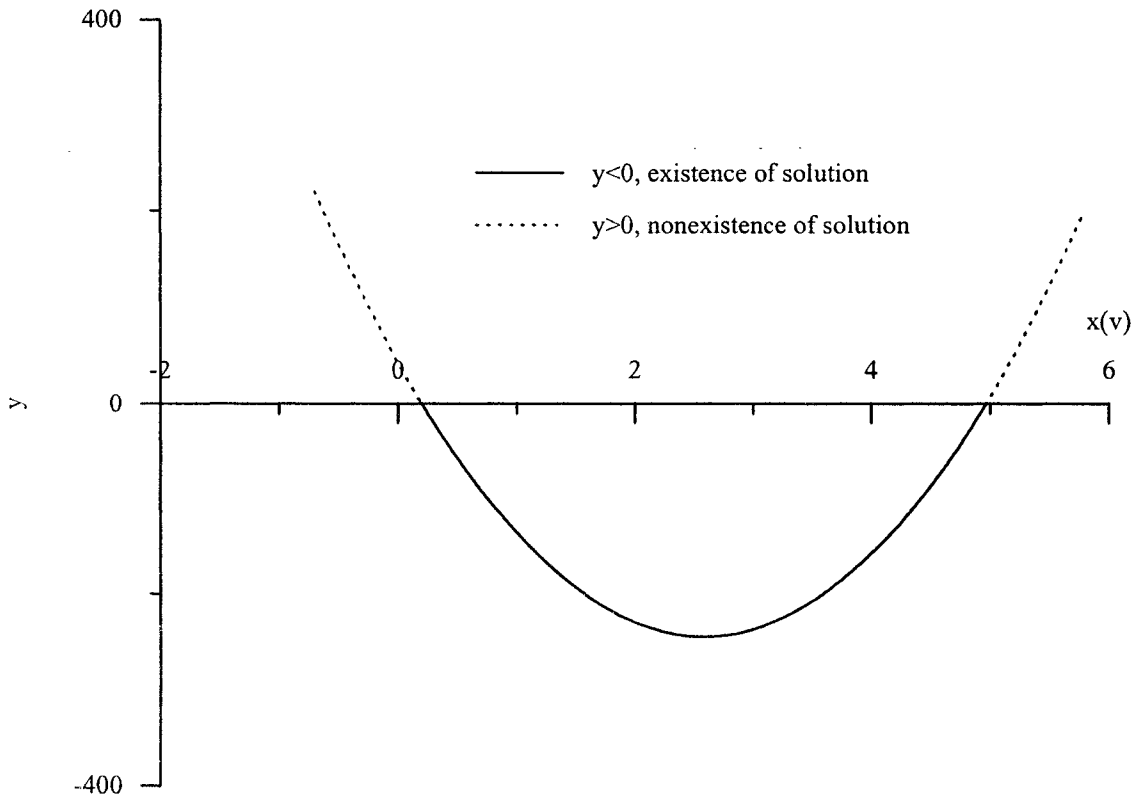

Figure 4.2: y-x(v) and the conditions for solution existence

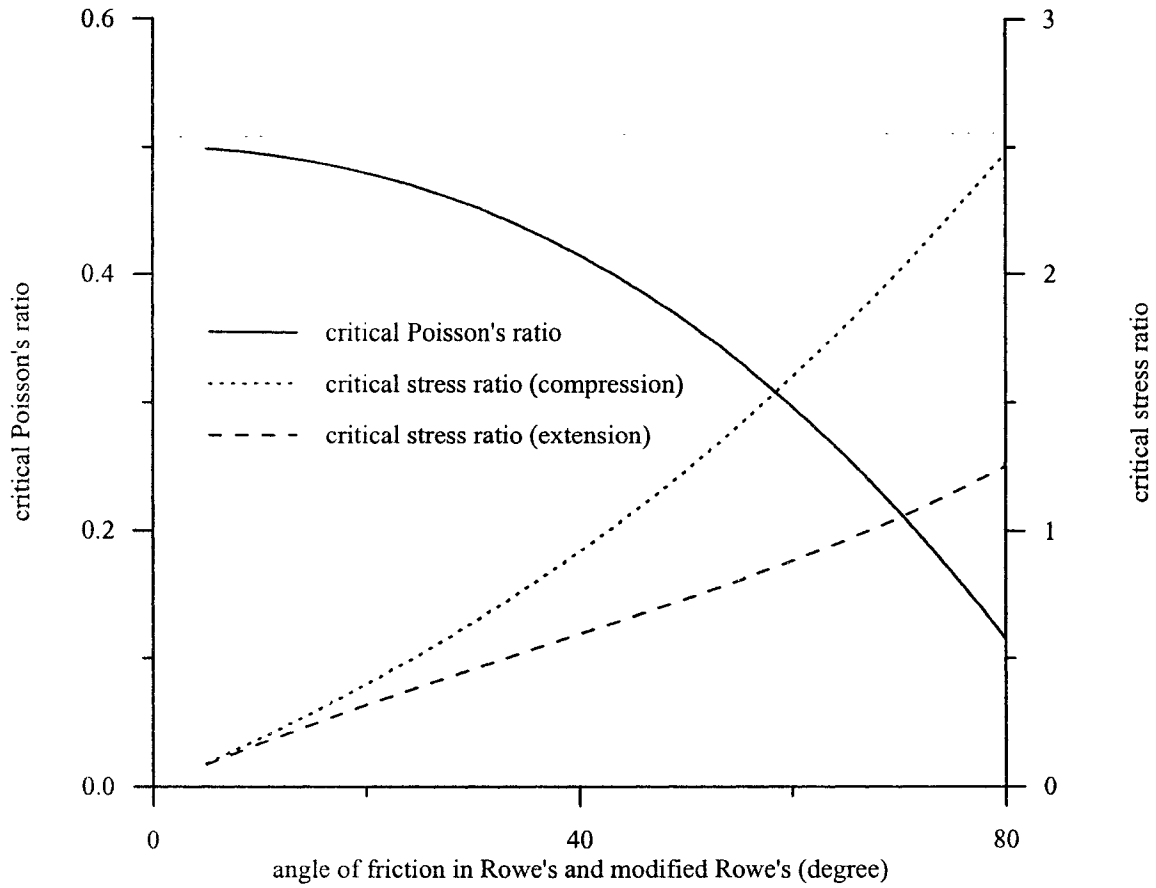

Figure 4.3: the critical Poisson's ratio and stress ratio for Rowe's and modified Rowe's flow rule

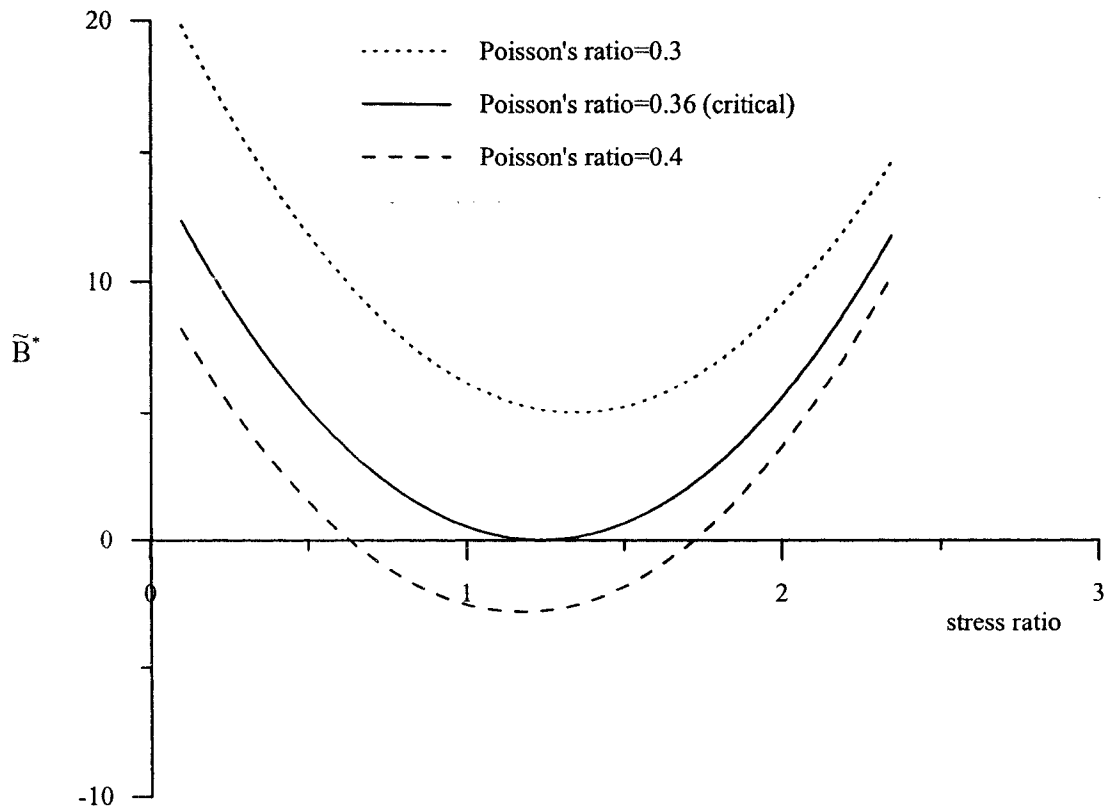

Figure 4.4 : the evolution of $\widetilde{B}^*$ with the Poisson's ratio

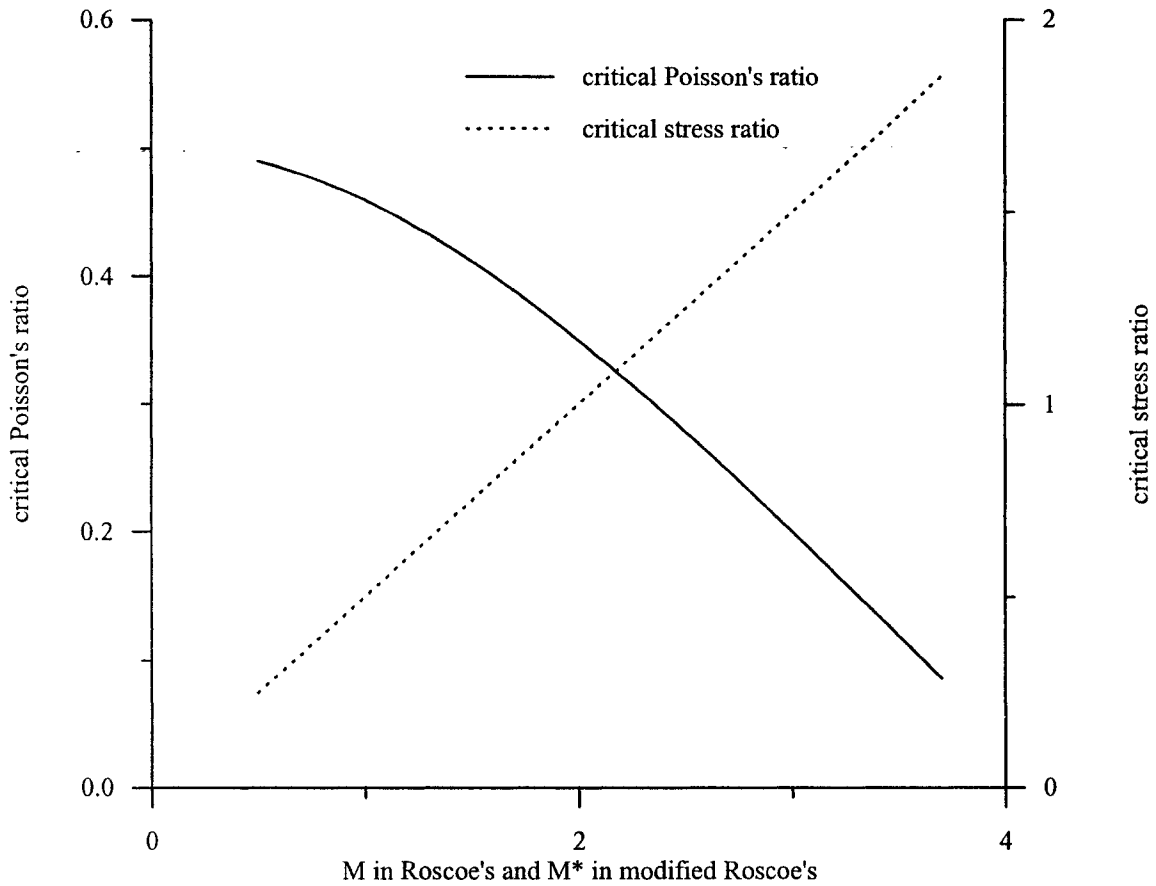

Figure 4.5: the critical Poisson's ratio and stress ratio for Roscoe's and modified Roscoe's flow rule (A=1)

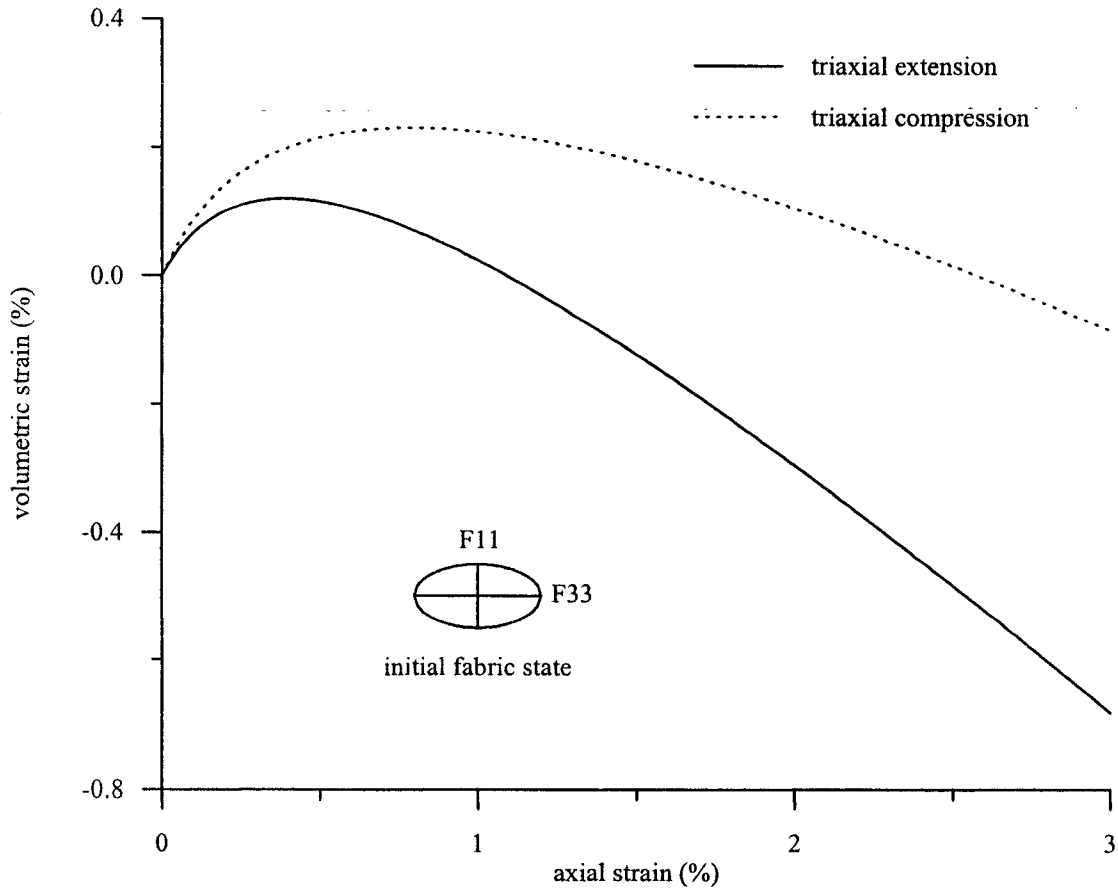

Figure 4.6: the effects of fabric anisotropy on volumetric changes

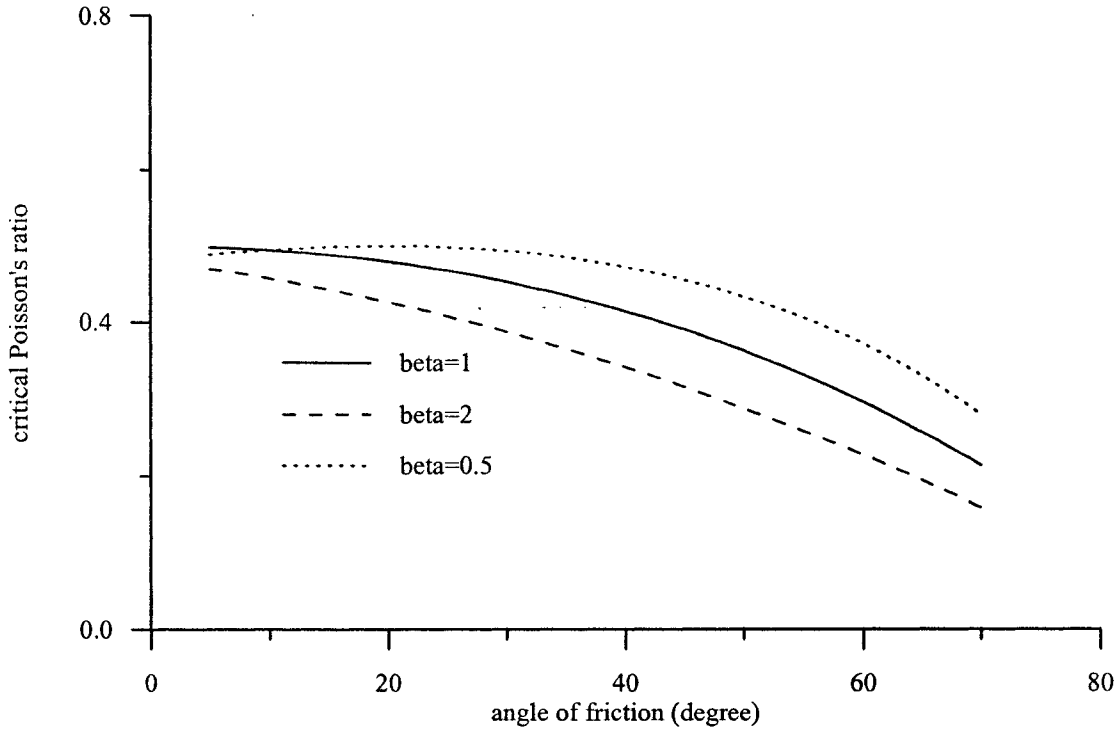

(a)

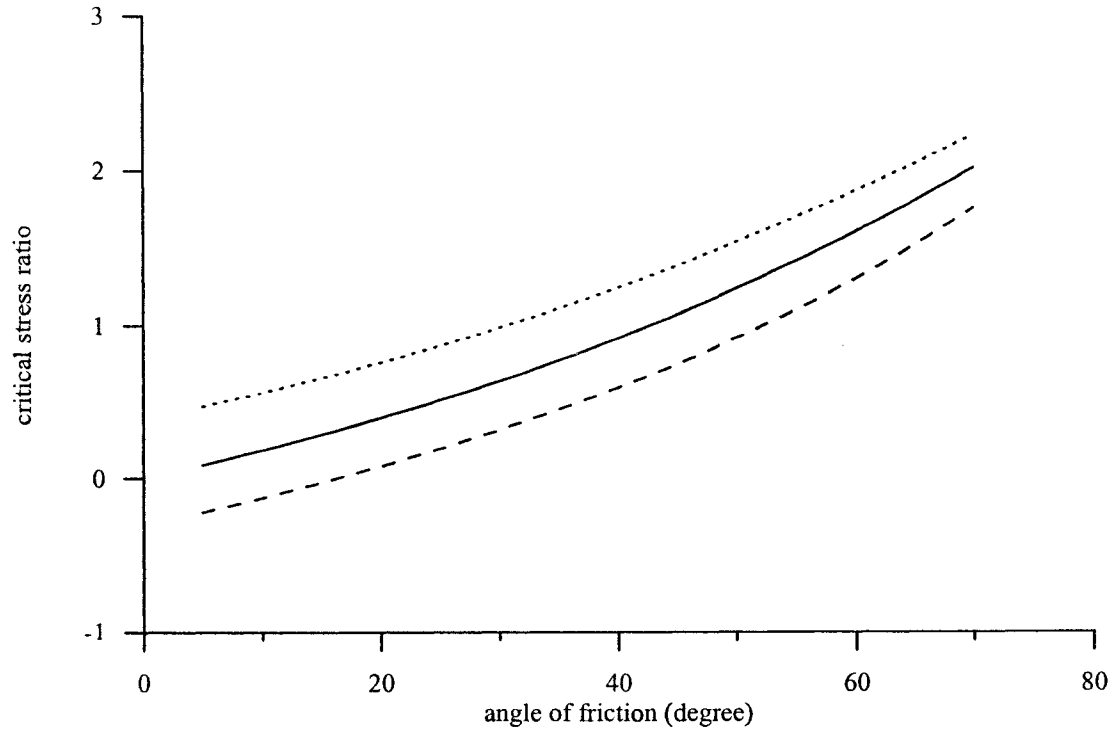

(b)

Figure 4.7: the effects of anisotropic elasticity on the critical Poisson's ratio and stress ratio

Chapter 5

Modeling the Stress-Strain Behavior of Unsaturated Soils Using the Middle Surface Concept

5.1 Introduction

The elastoplastic constitutive models for unsaturated soils are usually developed based on the models for saturated soils and by incorporating the effects of matric suction, s (pore air pressure minus pore water pressure) (Bishop & Blight, 1963; Gens & Potts, 1982; Alonso et al., 1990; Josa et al., 1992; Fredlund & Rahardjo, 1993; Wheeler & Sivakumar, 1995). Of particular interest is the model proposed by Alonso et al. (1990). This model was established in mean net pressure (p') – deviatoric stress (q) - matric suction (s) space. The mean net pressure was defined as the total mean pressure (p) minus the pore air pressure. In $p' - q$ space, the Modified Cam Clay model was used. In $p' - s$ space, the load-collapse (LC) curve was introduced. The LC curve describes the variation of the plastic volumetric strain with the change of mean net pressure and suction. In addition, the critical state line was made to depend on matric suction. This model can predict many response characteristics of unsaturated soils, such as the collapse due to wetting, and increase of shear strength and modulus with suction. In recent years, most of the elastoplastic constitutive models for unsaturated soils are developed within the framework proposed by Alonso et al. (1990).

However, the Modified Cam Clay model is not suitable for many soils. Saturated sands and silts are good examples of soils that won't fit into a framework based on the

Modified Cam Clay model. First, these soils don't have a unique normal consolidation line. Instead, the slopes of their normal consolidation lines vary with their relative densities. Second, the yield surface for dense sands is approximately linear in $p' - q$ space, whereas it is an ellipse for clays. Third, their hardening parameters can be best represented by the plastic deviatoric strain instead of the plastic volumetric strain. Fourth, the large dilation of dense sands cannot be predicted appropriately by using the Modified Cam Clay model. Therefore, it is necessary to develop the models for unsaturated sands or silts based on frameworks other than the Cam Clay type of models.

The objective of this chapter is to develop a constitutive model for unsaturated sands in $p' - q - s$ space based on a typical saturated sand model by using the Middle Surface Concept (MSC) to incorporate the effects of matric suction. Three pseudo yield surfaces are used in the MSC unsaturated sand model presented here. The first pseudo yield surface involves a typical saturated sand model with a linear yield surface and plastic deviatoric strain hardening in $p' - q$ space. The normal consolidation line and the corresponding LC curve are not used in this model. The other two pseudo yield surfaces are used to incorporate the effects of suction in $s - q$ space. The $s - q$ space is selected to represent the effects of suction, instead of $p' - s$ space, in order to avoid the difficulties in using the plastic volumetric strain hardening and a normal consolidation line for sands. The true response is developed by combining the pseudo responses produced by these three pseudo yield surfaces. In this chapter, the model is limited to triaxial monotonic loading conditions and the elastic response is not considered for simplicity. The model is shown to be capable of representing many characteristics of

unsaturated sands and silts. The reference to this model can also be made to Yang and Muraleetharan (2003).

It should be pointed out here that the choice of stress measures to represent the behavior of unsaturated soils is still undergoing considerable research. Furthermore, a theoretical framework to rigorously include the soil-water characteristic curve (SWCC) into the elastoplastic behavior is needed. For example, the concept by Muraleetharan and Wei (2003) provided insight into appropriate stress measures and a rigorous framework to incorporate the SWCC. The model presented in this paper is developed using p', q, and s as stress measures and doesn't explicitly consider the water content. However, the concepts presented by Muraleetharan and Wei (2003) can be easily incorporated with the MSC concepts to develop an appropriate model for unsaturated sands and silts.

5.2 Model Formulations

5.2.1 The Pseudo Yield Surface in $p' - q$ Space

This pseudo yield surface is for saturated sands. While the comprehensive formulations can be found in Chapter 1 and 2, a simplified saturated sand model is used here. This model is developed within the framework of the critical state soil mechanics and incorporates the concept of the state parameter (Been and Jefferies, 1985). The subscript "1" is used for the quantities in this space. The pseudo yield surface is given as:

$$f_1 = q_1 / p' - \alpha_1 = 0 \tag{5.1}$$

where q_1 is the pseudo deviatoric stress, and α_1 denotes the pseudo hardening parameter, which is defined as:

$$\alpha_1 = M_1 \frac{\gamma_1^p}{a_1 + \gamma_1^p} \tag{5.2}$$

where γ_1^p denotes the pseudo plastic deviatoric strain. M_1 denotes the critical stress ratio for saturated conditions and a_1 is a hardening model parameter. The evolution of the pseudo plastic strain is defined as:

$$d\gamma_1^p = L_1 \tag{5.3}$$

$$d\varepsilon_{v1}^p = L_1 D_1 \tag{5.4}$$

$$D_1 = A_1(M_1 + k_1\psi_1 - \alpha_1) \tag{5.5}$$

where L_1 denotes the pseudo loading index. In equation (5.3), the flow direction in the deviatoric part is set to unity. ε_{v1}^p denotes the pseudo volumetric plastic strain, and D_1 denotes the pseudo dilatancy ratio. A_1 and k_1 are model parameters for volume change. Equation (5.5) shows that D_1 depends on the pseudo state parameter ψ_1, which is defined as:

$$\psi_1 = e_1 - e_{cr1} \tag{5.6a}$$

$$e_{cr1} = e_{ref1} - \lambda ln(p'/p_{ref}) \tag{5.6b}$$

where e_1 denotes the pseudo void ratio, and e_{cr1} denotes the pseudo void ratio at the critical state under the current mean net pressure. e_{ref1}, p_{ref} and λ are model parameters defining the critical state under saturated conditions. According to the above defined flow rule, when the pseudo stress ratio q_1 / p' is above the phase transformation line represented by $M_1 + k_1\psi_1$, the sand experiences volumetric dilation. In contrast, when q_1 / p' is below the phase transformation line, the sand experiences volumetric

contraction. Relatively loose sands are characterized with higher phase transformation line, and relatively dense sands have a lower phase transformation line. In addition, the flow rule defined in equation (5.3)-(5.6) guarantees that the pseudo void ratio reaches the critical state for saturated conditions together with the pseudo stress ratio at the end of loading.

5.2.2 The Pseudo Yield Surfaces in $s-q$ Space

Similar to the pseudo yield surface in $p'-q$ space, the pseudo yield surface in $s-q$ space is also developed within the framework of the critical state soil mechanics and the state parameter concept. The subscript "s" is used for the quantities in this space. The shape of the pseudo yield surfaces in $s-q$ space is also linear, and the pseudo plastic deviatoric strain is the hardening parameter. Because the shear strength due to suction is bilinear as shown in Figure 5.1, two pseudo yield surfaces are used in this space. The use of two pseudo yield surfaces also facilitates the representation of the peak of the deviatoric stress followed by strain softening during shearing when suction is relatively large. It is proposed that these two pseudo yield surfaces share the same pseudo plastic deviatoric strain and suction. Their yield surfaces and hardening rules are given as:

$$f_{si} = q_{si} / s - \alpha_{si} = 0 \qquad (i = 1,2) \tag{5.7}$$

$$\alpha_{si} = M_{si} \frac{\gamma_s^p}{a_s + \gamma_s^p} \tag{5.8}$$

where q_{si} and α_{si} denote the deviatoric stresses and hardening parameters for the two pseudo yield surfaces, respectively. γ_s^p denotes the pseudo plastic deviatoric strain, and

a_s denotes the hardening model parameter. M_{si} denotes the critical stress ratios for the two sections, respectively, which are shown in Figure 5.1.

Based on Figure 5.1, the shear strength q_s^f due to suction can be expressed as:

$$q_s^f = M_{s1} s \qquad when\ s \le s_0 \tag{5.9a}$$

$$q_s^f = c_s^f + M_{s2}\, s \qquad when\ s > s_0 \tag{5.9b}$$

where s_0 denotes the air entry value. Usually, M_{s1} is equal to M_1 for the saturated condition. The deviatoric stress q_s is developed based on q_{s1} and q_{s2} in terms of γ_s^p, defined below:

$$q_s = q_{s1} \qquad when\ s \le s_0 \tag{5.10a}$$

$$q_s = exp(-b_s \gamma_s^p) q_{s1} + (1 - exp(-b_s \gamma_s^p))(q_{s2} + c_s^f) \qquad when\ s > s_0 \tag{5.10b}$$

where b_s is a model parameter. In equation (5.10b), when $s > s_0$ and γ_s^p is smaller, q_s is close to q_{s1}. On the other hand, when γ_s^p becomes larger, q_s starts to approach $q_{s2} + c_s^f$. Because q_{s1} is larger than $q_{s2} + c_s^f$, the strain softening due to suction can be represented this way.

The definitions of the flow rules for these two pseudo yield surfaces are similar to that for the first pseudo yield surface and are given below:

$$d\gamma_s^p = L_s \tag{5.11}$$

$$d\varepsilon_{vsi}^p = L_s D_{si} \qquad (i = 1,2) \tag{5.12}$$

$$D_{si} = A_s (M_{si} + k_s \psi_{si} - \alpha_{si}) \tag{5.13}$$

where L_s denotes the pseudo loading index. ε_{vsi}^p and D_{si} denote the plastic volumetric strain and dilatancy ratios for these two pseudo yield surfaces. A_s and k_s are the model

parameters for volume change. In equation (5.13), it can be seen that, similar to the first pseudo yield surface, D_{si} also depend on the pseudo state parameter ψ_{si}, which is defined as:

$$\psi_{si} = e_{si} - e_{crs} \qquad (i = 1, 2) \tag{5.14a}$$

$$e_{crs} = e_{refs} \tag{5.14b}$$

where e_{si} denotes the pseudo void ratios, and e_{crs} denotes the pseudo critical state void ratio. e_{crs} is a constant equal to e_{refs}. e_{refs} is usually larger than e_{cr1} in $p' - q$ space, which leads to smaller ψ_{si} than ψ_1. Correspondingly, the increase of volumetric dilation with suction under shearing with constant suction can be represented this way. ε_{vs}^{p} is obtained by combining ε_{vs1}^{p} and ε_{vs2}^{p} in terms of γ_s^{p}, given as:

$$\varepsilon_{vs}^{p} = exp(-c_s \gamma_s^{p})\varepsilon_{vs1}^{p} + (1 - exp(-c_s \gamma_s^{p}))\varepsilon_{vs2}^{p} \tag{5.15}$$

where c_s is a model parameter. Similar to q_s, during the early stage of loading when γ_s^{p} is relatively small, ε_{vs}^{p} is closer to ε_{vs1}^{p}. With the increase of γ_s^{p}, ε_{vs}^{p} starts to approach ε_{vs2}^{p}. Generally, the volumetric contraction represented by ε_{vs1}^{p} is larger than that of ε_{vs2}^{p} during the early stages of loading. Therefore, during shearing, ε_{vs}^{p} first shows volumetric contraction followed by dilation.

5.2.3 The Development of the True Response

The true response is developed by using these pseudo responses through the links between them. It is worth noting that the true yield surface exists but can't be defined explicitly. It is proposed that all the yield surfaces share the same initial conditions consisting of the same initial stress and void ratio. During the course of loading, all the yield surfaces experience the plastic deformation and the relationships of elastoplastic quantities between various yield surfaces are defined as:

$$\gamma^p = \gamma_1^p = \gamma_s^p \tag{5.16}$$

$$q = q_1 + q_s \tag{5.17}$$

$$\varepsilon_v^p = (1-\beta)\varepsilon_{v1}^p + \beta\varepsilon_{vs}^p \tag{5.18a}$$

$$\beta = q_s^f / (q_1^f + q_s^f) \tag{5.18b}$$

Equation (5.16) indicates that all the yield surfaces share the same plastic deviatoric strain. Equation (5.17) indicates that the true deviatoric stress q is carried by both q_1 and q_s, respectively. From the common plastic deviatoric strain and the definitions of q_1 and q_s in equations (5.1) and (5.7), it can be seen that larger suction leads to larger q_s. On the other hand, larger p' leads to larger q_1. In equation (5.18), q_1^f and q_s^f denote the shear strengths in $p'-q$ and $s-q$ spaces, respectively. q_s^f is defined in equation (5.9), and q_1^f is equal to $M_1 p'$. Because q_1^f and q_s^f depend on p' and s, respectively, equation (5.18) indicates that larger suction leads to larger contribution of ε_{vs}^p to the true volume change ε_v^p. On the other hand, larger p' leads to larger contribution of ε_{v1}^p to ε_v^p. Rewriting equation (5.18), one can obtain: $\varepsilon_v^p = \varepsilon_{v1}^p + \beta(\varepsilon_{vs}^p - \varepsilon_{v1}^p)$. As described previously, the dilation represented by ε_{vs}^p is usually larger than that of ε_{v1}^p under

constant suction shearing. As a result, unsaturated sands have a larger dilation tendency under constant suction shearing than that for saturated sands. It is worth noting that equation (5.18) can lead to the critical state void ratio for the true response, which is given as:

$$e_{cr} = \left[e_{ref1} + \beta(e_{refs} - e_{ref1})\right] - \lambda(1-\beta) ln(p'/p_{ref}) \tag{5.19}$$

Equation (5.19) is consistent with test results regarding the critical state void ratio for unsaturated sands. Because e_{refs} is usually larger than e_{ref1} and β increases with suction, a larger suction leads to a larger reference critical state void ratio and smaller slope of the critical state line.

The above formulations can also simulate the wetting process. Consider the reduction of the suction at a constant stress ratio, where p' and q are held constant. The decrease of suction leads to the decrease of q_s and the increase of q_1 while q is constant. For relatively loose sands, where q_1 / p' is more likely to be below its phase transformation line, the increase of q_1 may lead to volumetric contraction in $p' - q$ space. Although the volumetric expansion may happen in $s - q$ space at the same time, the decrease of β with the decrease of the suction reduces the role of ε_{vs}^{p} in ε_{v}^{p} expressed in equation (5.18). Therefore, the collapse phenomenon can be represented this way. On the other hand, for relatively dense sands, where q_1 / p' is more likely to be above its phase transformation line, the increase of q_1 resulted from the reduction of the suction may lead to volumetric expansion.

5.3 Model Calibration and Prediction

The model calibration can be divided into $p'-q$ space to capture the saturated behavior and $s-q$ space to capture the effects of suction, respectively. The calibration of the model parameters a_1, A_1, k_1, M_1, λ, and e_{ref1} in $p'-q$ space can be performed using saturated soil testing and the details of this calibration procedure can be found in Chapter 1. In the $s-q$ space, M_{s1}, M_{s2} and e_{refs} can be obtained by examining the influence of the suction on the critical state. The model parameter a_s can be calibrated by examining the response under constant suction shearing during the early stages of loading. The parameter b_s mainly controls the peak of the deviatoric stress and strain softening and can be obtained by examining the later stages of loading. The parameters A_s and k_s control the volumetric change during the early stages of loading. The parameter c_s mainly controls the evolution of volumetric change during the later stages of loading. A_s, k_s and c_s can be obtained by curve fitting process.

The model developed is used to simulate the response of an unsaturated compacted Aeolian silt under conventional triaxial compression loading with constant suction (Cui and Delage, 1996). The model parameters are listed in Table 5.1, and the initial void ratio for the tested samples is 0.62. Due to lack of sufficient test results for the critical void ratio, λ is set to zero. This is a reasonable assumption in view of the fact that λ is relatively small under small confining pressures. The test results and predictions under a constant cell pressure of 50 kPa for various values of suctions are shown in Figure 5.2. Because p' undergoes dramatic change during the course of shearing, β is computed by using the value of p' at the critical state to better represent the volumetric change. The test results and predictions agree reasonably well. Larger suction values lead

to larger shear strength and stiffness. The deviatoric stress reaching a peak value followed by strain softening to the critical state can be clearly seen for 800 kPa suction. As shown in Figure 5.2, larger suction values also lead to larger volumetric expansion in the later stages of shearing.

Although no test results are available, the model is used to simulate the wetting process. A sample with a suction value of 400 kPa and a cell pressure 50 kPa is sheared to a stress ratio of 0.94. Then while keeping q and p' constant the suction is reduced from 400 kPa to zero. The same model parameters as given in Table 5.1 are used. Volumetric contraction and the evolutions of q_1 and q_s due to the suction reduction are shown in Figure 5.3. Although the total deviatoric stress q remains constant, the decrease of suction leads to the decrease of q_s and the increase of q_1. Because q_1 / p' is lower than the phase transformation line, the loading in $p' - q$ space leads to the volumetric contraction in $p' - q$ space. On the other hand, the decrease of q_s and s causes the volumetric expansion in $s - q$. Meanwhile, β decreases with the decreasing suction, which decreases the role of ε_{vs}^{p} and increases the role of ε_{v1}^{p} in the true volumetric change ε_{v}^{p}. Therefore, the total effect is volumetric contraction as shown in Figure 5.3. It is worth noting that wetting may cause volumetric dilation for relatively dense silt under exactly same loading condition as described above. If a sample with a lower void ratio of 0.43 is considered under the same loading condition as above, a decrease in suction will cause volumetric dilation as shown in Figure 5.4. This is because the stress ratio q_1 / p' is higher than the phase transformation line for a dense silt.

5.4 Conclusions

A constitutive model for unsaturated sands is proposed within the framework of the Middle Surface Concept (MSC). The multiple response characteristics of unsaturated sands are represented by using a yield surface in the $p' - q$ space and two yield surfaces in the $s - q$ space. The normal consolidation line and volumetric strain hardening for sands are not used. Instead a linear yield surface and plastic deviatoric strain hardening that are more suitable for predicting the response of sands are used. The model is shown to predict many response characteristics of unsaturated sands such as the increase of shear strength and stiffness with the suction. The model predictions are validated in a limited manner using triaxial test results for Aeolian silt. The model also predicts increase of volumetric dilation with the increase in suction under a constant suction shearing. The typical response during wetting process is also successfully predicted. Of particular interest is that this model can predict the dilation of dense sands during the course of wetting under certain loading conditions.

5.5 References

Alonso, E. E., Gens, A., and Josa, A. (1990), A Constitutive Model for Partially Saturated Soils, *Geotechnique* **40**, No. 3, 405-430

Been, K., and Jefferies, M. G. (1985), A State Parameter for Sands, *Geotechnique* **35**, No. 2, 99-102

Bishop, A. W. and Blight, G. E. (1963), Some Aspects of Effective Stress in Saturated and Partly Saturated Soils, *Geotechnique* **13**, No. 3, 177-197

Cui, Y. J., and Delage, P. (1996), Yielding and Plastic Behaviour of an Unsaturated Compacted Silt, *Geotechnique* **46**, No. 2, 291-311

Fredlund, D.G. and Rahardjo, H. (1993), *Soil Mechanics for Unsaturated Soils*, John Wiley & Sons, Inc

Gens, A. and Potts, D. M. (1982), Application of Critical State Soil Models to the Prediction of the Behavior of a Normally Consolidated Low Plasticity Clay, *Proc. 1st Int. Symp. Numer. Mod. Geomech., Zurich*, 312-323

Josa, A., Balmaceda, A., Gens, A. and Alonso, E. E. (1992), An Elastoplastic Model for Partially Saturated Soils Exhibiting a Maximum of Collapse, *Proc. 3rd Int. Conf. Computational Plasticity, Barcelona* **1**, 815-826

Muraleetharan, K. K., and Wei, C. (2003), A Unified Framework for Elastoplasticity of Unsaturated Soils: From Capillary Hysteresis to Soil Skeletal Deformations, *Proceedings, International Conference: From Experimental Evidences Towards Numerical Modelling of Unsaturated Soils*, September 18th – 19th, Weimar, Germany

Wheeler, S.J. and Sivakumar, V. (1995), An Elasto-Plastic Critical State Framework for Unsaturated Soil, *Geotechnique*, **45**, No. 1, 35-53

Yang, Y. and Muraleetharan, K.K. (2003), The Modeling of Unsaturated Soils within the Framework of the Middle Surface Concept, *From Experimental Evidence towards Numerical Modeling of Unsaturated Soils*, September 18th – 19th, Weimar, Germany

Table 5.1. The Model Parameters for Aeolian Silt

$p'-q$ space							$s-q$ space							
a_1	A_1	k_1	M_1	λ	e_{ref1}	p_{ref}	a_s	A_s	k_s	b_s	c_s	M_{s1}	M_{s2}	e_{refs}
0.001	1.0	15	1.0	0	0.5076	100	0.015	1.0	10	40	50	1.0	0.1	0.6959

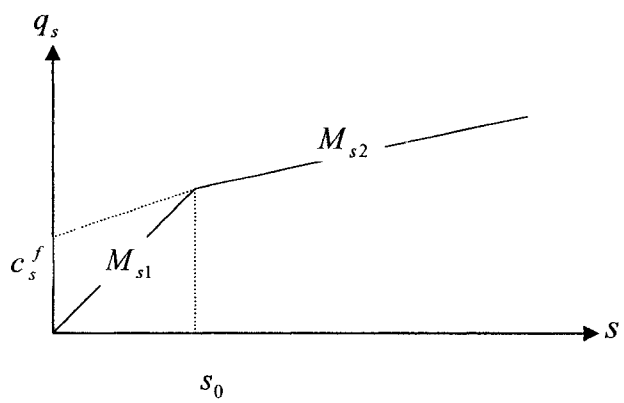

Figure 5.1. Shear Strength Due to Suction

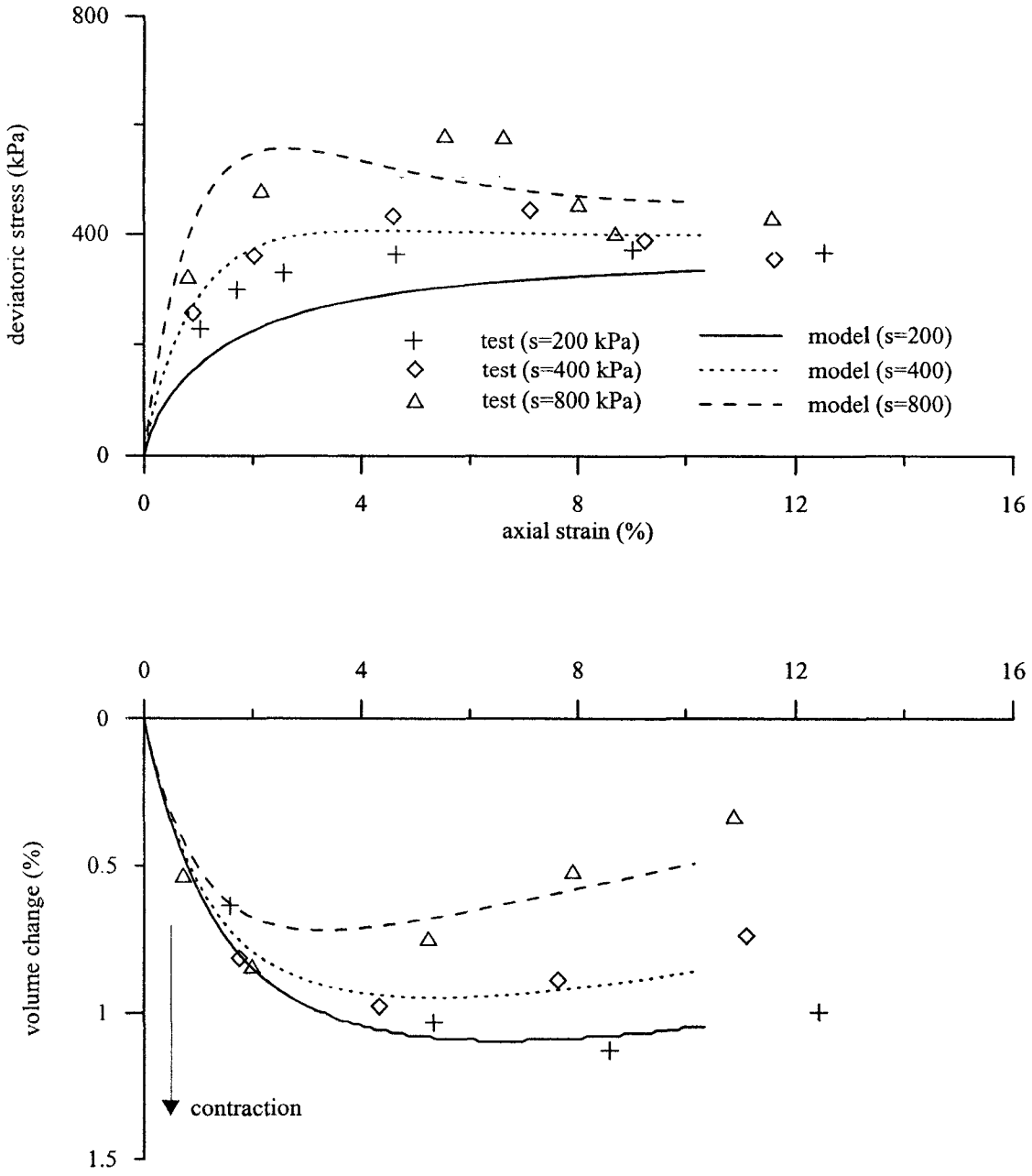

Figure 5.2: the predictions and test results of constant suction shearing (test results after Cui & Delage, 1996)

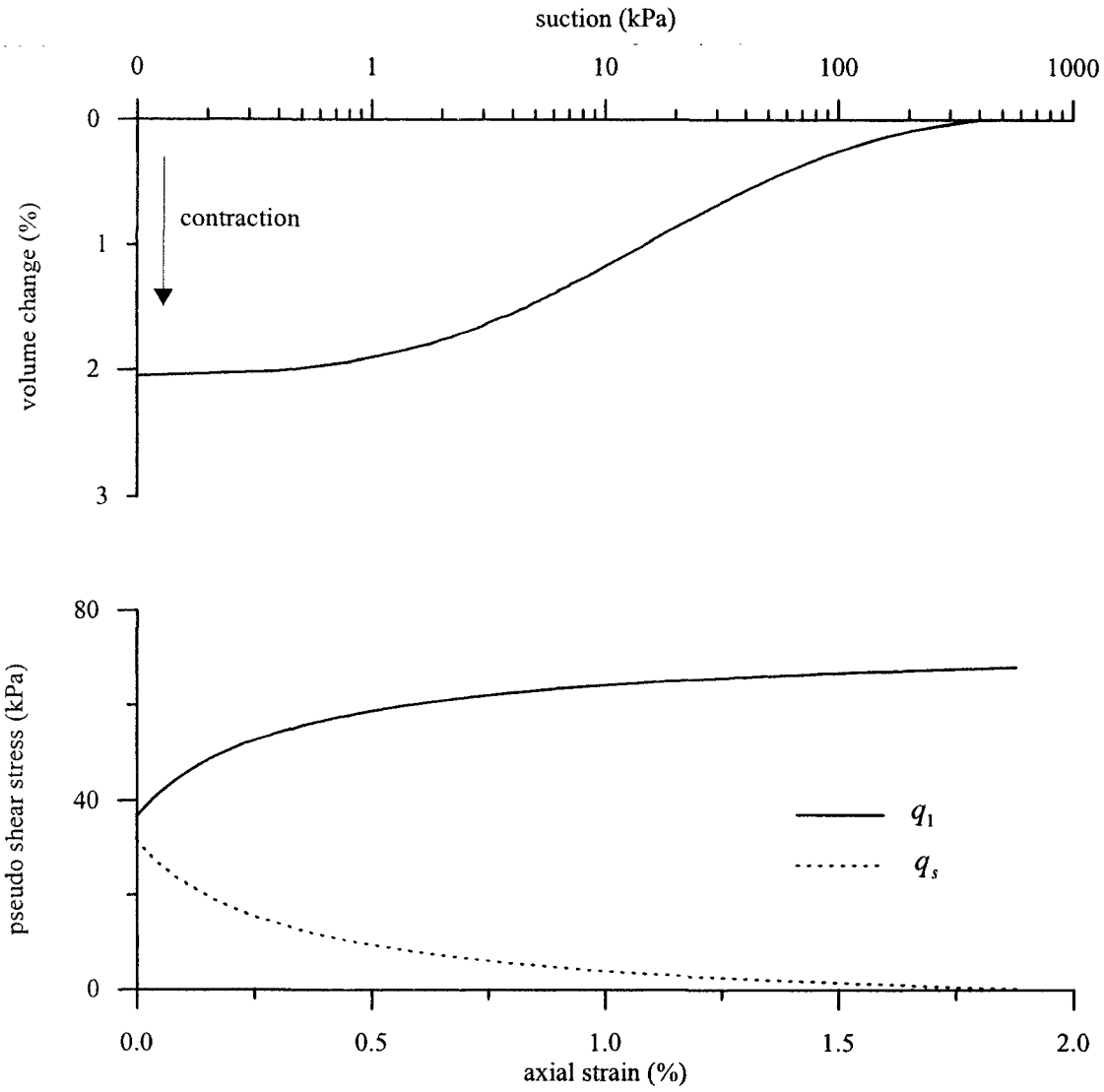

Figure 5.3: simulation of suction decrease for loose silt

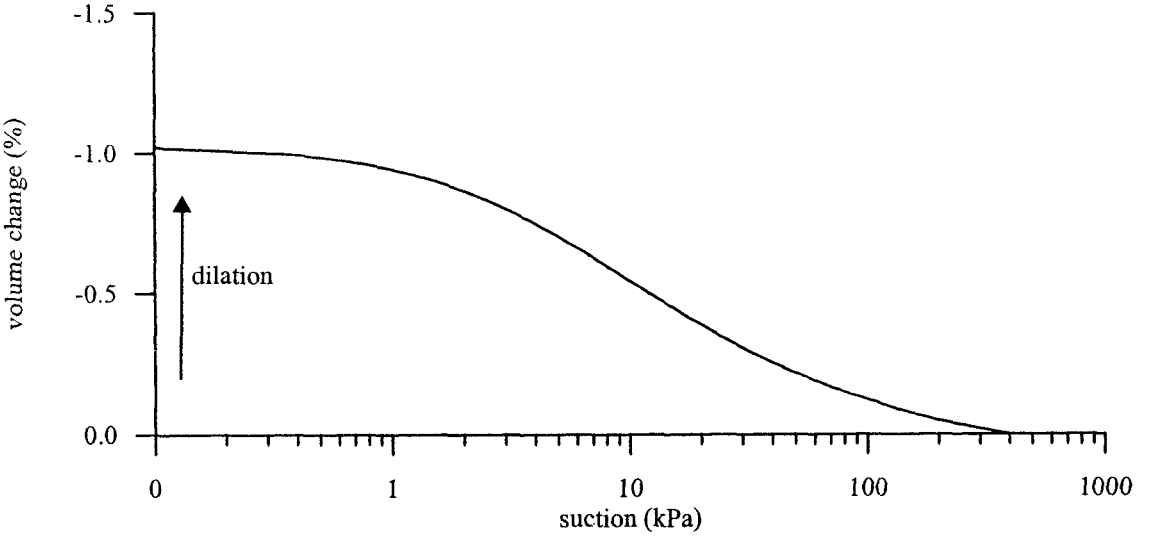

Figure 5.4: simulation of suction decrease for dense silt

Chapter 6

Application of the MSC Based Sand Model in Dynamic Boundary Value Problems

6.1 Introduction

The objective of this chapter is to examine the performance of the MSC sand model in boundary value problems to extend its application to practical engineering problems. The numerical integration of the MSC sand model and the development of consistent tangent stiffness matrix in a single element, as described in Chapter 3, is implemented into a fully coupled finite element program DYSAC2 (Muraleetharan et al., 1988, 1997). A centrifuge model test from the VELACS project (Arulanandan & Scott, 1993) is used to investigate the predictions made by DYSAC2 together with the MSC sand model.

6.2 The Fully Coupled Finite Element Method (FEM)

The fully coupled analysis procedure used in the predictions is based on the finite element solution of the dynamic governing equations for a saturated porous media (soil skeleton and pore fluid). The details of this formulation and numerical implementation are given in Muraleetharan et al. (1994). The two-dimensional numerical implementation of the formulation resulted in the computer code DYSAC2 (Muraleetharan et al. 1988, 1997). Four-noded isoparametric elements with reduced integration for the fluid bulk modulus terms are used in DYSAC2. Nodal variables per node are two soil skeleton and tow fluid displacements. A three-parameter time integration scheme called the Hilber-

Hughes-Taylor α-method (Hilber et al. 1977) is used, together with a predictor/multi-corrector algorithm, to integrate the spatially discrete finite element equations. This time integration scheme provides quadratic accuracy and desirable numerical damping characteristic to damp the high frequency spurious modes. The MSC model time integration and the consistent tangent stiffness development, as described in Chapter 3, are performed within a subroutine.

6.3 Prediction for a Centrifuge Model Test

6.3.1 Model Test Specification

Model No. 3 (Scott et al., 1993) in a series of centrifuge model tests conducted for the VELACS project is used to examine the performance of DYSAC2 together with the MSC sand model. VELACS is a project about Verification of Liquefaction Analysis by Centrifuge Studies (Arulanandan & Scott, 1993). In Model #3, a water-saturated layer of sand deposited as shown in Figure 6.1 in a laminar box was subjected to base motion. The two halves of the box contained loose and dense sand with relative densities of 40% and 70%, respectively. The line of separation was vertical through the center of the box. The depth of soil was approximately equal to 22 cm (model) or 11 m (prototype). The specimen container was a rectangular box constructed of aluminum laminae designed to move freely on top of each other. The laminar box provided a behavior closer to the one-dimensional shear deformation for the soil. A rubber bag molded to the inside dimensions of the laminar box was used to contain the soil and water in the box. The sand was placed in the rubber bag by pluviating dry sand into the model box.

After the specimen was prepared, the centrifuge was started and slowly brought up to 50g and run for about 10 minutes. Afterwards, an earthquake like base motion, as shown in Figure 6.2, was applied to the box base. The longitudinal component of base motion (x-direction) was the major direction of shaking. The peak vertical acceleration (y-direction) was less than 25% of the peak longitudinal acceleration and the transverse direction of shaking was negligible.

A total of 23 transducers were used in the test. Input base accelerations and acceleration-time histories along the height of the soil column were measured with seven accelerometers. Pore pressures at different locations inside the soil mass were measured with ten pore pressure transducers. Six displacement LVDT transducers along the height and at the top of the soil columns were used to measure lateral deformations and settlements. Figure 6.1 shows the locations of transducers and accelerometers installed in the box.

The experiment was performed mainly to investigate effects of major differences in densities of neighboring sand columns on their dynamic response, particularly, their liquefaction susceptibility and post-liquefaction behavior. Soil densification is widely used in practice as a mitigation measure to reduce the negative influences of liquefaction on stability and settlement of structures supported on potentially liquefiable soils. The results of this experiment can be used to study how deep and how far the densification should be made to minimize the adverse effects of liquefaction.

6.3.2 Predictions and Test Results

To model the test, the box is divided into 162 elements as shown in Figure 6.3. The base of the box is fixed to the ground and no vertical water flow is allowed along the base. The nodes on either side of the box are tied up with their adjacent nodes. The tied up nodes have the same movements in order to model the one-dimensional shearing deformation of the soil. Along both sides of the box no horizontal water flow is allowed.

The model parameters for Nevada sand used in the predictions are calibrated in Chapter 2. *The same set of model parameters* are used for the sands with both 40% and 70% relative densities in this problem. From the prediction of triaxial undrained cyclic loading test and simple shear undrained cyclic loading tests in Chapter 2, it can be seen that softening takes place during the later stages of loading when the effective confining pressure approaches zero. It is found that the softening results from relatively large value of model parameters h_1 and h_2. The substantial softening may cause numerical problems in boundary value problems. To avoid this problem, the values of h_1 and h_2 should be reduced compared with those in Chapter 2. The reduction of h_1 and h_2 values doesn't influence the overall predictions of boundary value problems because the softening usually takes place when the effective confining pressure is very small, however, it provides numerical stability. For example, the softening takes place at effective confining pressure of 17 kPa when the initial confining pressure is 80 kPa in the triaxial undrained cyclic loading prediction shown in Figure 2.4. In addition, the effective confining pressure below which softening takes place usually decreases with decreasing initial confining pressure.

In boundary value problems for sands, an important issue is the representation of liquefaction or cyclic mobility. Representation of liquefaction is a complicated problem and there are many techniques available. It is beyond the scope of this paper to thoroughly investigate this problem. Instead, a simple procedure is used to provide numerical stability for the liquefied soil. In this procedure, a cut-off effective confining pressure of 1 kPa is used. When the effective confining pressure reduces below the cut-off value, the liquefied element is shifted to be purely elastic from elastoplastic element. In this case, the elastic shear moduli are very small as they are determined based on the small cut-off confining pressure. The elastoplastic behavior is resumed from the purely elastic behavior when the effective confining pressure in the element increases above the cut-off value.

The measured results and DYSAC2 predictions for the excess pore water pressures, accelerations, and displacements at various locations are shown in Figures 6.4-6.13. All the results and predictions are presented in the prototype scale. Figures 6.4-6.6 show the excess pore water pressure time histories at the bottom, middle and top levels in the box. The overall trends of water pressure development and dissipation are similar between the measured results and predictions. The development of water pressure at the top level is faster than at other levels and makes sands liquefy quickly. In addition, although the development of water pressure is slower in dense sands than that in loose sands in a single element, the difference of water pressure development is slight between dense and loose sands in the laminar box due to the movement of water from loose sand to dense sand. These phenomena are captured well in the predictions. Figures 6.7-6.9 show the water pressure contours at t = 5, 7.5 and 10 seconds for the predictions, which

correspond to the start of shaking, the middle of shaking and the start of liquefaction (excess pore water pressure = initial effective vertical stress), respectively. Figure 6.7 shows that at the start of shaking smaller water pressure is developed on the dense side than that on the loose side. Particularly on the far end of the dense side, the pore water pressure is negative. This is consistent with the laboratory test results on dense and loose sands. Figure 6.7 also shows that the pore water pressure is relatively small compared with those at other times. Figure 6.8 shows the pore water pressure contour in the middle of shaking at 7.5 seconds. It can be seen that pore water pressure at this time is much larger than those at 5 seconds. Below the middle level of the box, the difference of water pressure values between dense and loose sides is distinct. On the loose side below the middle level, a large area of soil mass has the pore water pressure around 55 kPa. On the dense side below the middle level, most areas have the pore water pressure around 40 kPa. The water pressure difference between dense and loose sides will cause pore water to flow from loose side to dense side. Figure 6.9 shows the water pressure contours at 10 seconds right before the liquefaction. It is interesting that the water pressure contour is distinctly divided into multiple layers characterized with various pore water pressures. Similar to the water pressure contour at 7.5 seconds, the pore water pressure is higher on loose side than on dense side. It is worth noting that there are some discrepancies between the measured and predicted pore water pressures in Figures 6.4-6.6. The predicted water pressure is larger than the measured values. The liquefaction is measured only at the top level of the box. However, the whole box of sand is predicted to liquefy. This discrepancy may be caused by the determination of coefficient of permeability for Nevada sand. Experimental evidence shows that the coefficient of permeability for sands

decreases with decreasing effective confining pressure. However, a constant coefficient, 5.7×10^{-6} m/s was used throughout the prediction. This value may correspond to relatively large confining pressures. Another possible reason for this discrepancy may come from the movement of water pressure transducers during shaking. Another discrepancy between measured and predicted pore water pressures is that larger fluctuation of water pressure is predicted after the sand liquefies than that in the measured results. This may be caused by the assumption of elastic material when sand reaches liquefaction. The frequent transition between elastic behavior and elastoplastic behavior around liquefaction causes larger fluctuations in water pressure. In addition, pore pressure transducers used may not have been able to capture the high frequency response.

Figures 6.10 and 6.11 show the measured and predicted acceleration time histories for loose and dense sands at the top level of the box. The predicted accelerations are higher than the measured ones. The exact reasons are not clear. There are several possible explanations. First, the larger predicted accelerations may be caused from the frequent transition between elastoplastic and purely elastic materials. Second, the accelerometers may have undergone substantial movement or rotations during strong shaking.

Figure 6.12 shows the measured and predicted lateral displacements at various levels of the box. Figure 6.13 shows the measured and predicted settlements at the top of the box. The predicted and measured lateral displacements agree well. Positive lateral displacements toward the side of dense sand take place. The displacement increases with the increasing height. However, as shown in Figure 6.13, the measured settlements are larger and stabilize earlier than the predicted ones. The smaller predicted settlements may

be attributed to the plain strain assumption, which gives more restriction to the settlement of sands than that in the laminar box. The longer predicted stabilization time may be due to the continuous elastic compression of sands at the top level during post-liquefaction. In the model, the elastic modulus at the top level, where the confining pressure is relatively small, may be smaller than the real one. While the water drains at the top level, the increase of effective confining pressure brings large elastic compression of sands at the top level in the prediction. Careful investigation of elastic modulus of Nevada sand at small confining pressures is needed.

6.4 Conclusions

The MSC saturated sand model is implemented into a fully coupled FEM program DYSAC2 to analyze boundary value problems. In this model, different characteristics of sand behavior are represented by different pseudo yield surfaces. This makes it possible to use one set of model parameters to represent a sand with different relative densities. The applicability of the model to solve boundary value problems is verified by predicting a centrifuge model test. A reasonable comparison is achieved between test results and predictions.

6.5 References

Arulanandan, K. & Scott, R. F. (1993), Verification of Numerical Procedures for the Analysis of Soil Liquefaction Problems, *Proceedings of the International Conference on the Verification of Numerical Procedures for the Analysis of Soil Liquefaction Problems*, Davis, California, October, 17-20, 1993

Hilber, H. M., Hughes, T. J. R. & Taylor, R. L. (1977), Improved Numerical Dissipation for Time Integration Algorithms in Structural Dynamics, *Earthquake Engineering and Structural Dynamics*, **5**, 283-292

Muraleetharan, K. K., Mish, K. D., Yogachandran, C. & Arulanandan, K. (1988), DYSAC2 (Version 1.0): Dynamic Soil Analysis Code for 2-Dimensional Problems, *Computer Code*, Department of Civil Engineering, University of California, Davis, California

Murlaeetharan, K. K., Mish, K. D. & Arulanandan, K. (1994), A Fully Coupled Non-Linear Dynamic Analysis Procedure and Its Verification Using Centrifuge Test Results, *International Journal for Numerical and Analytical Methods in Geomechanics* **18**, 305-325

Muraleetharan, K. K., Mish, K. D., Yogachandran, C., and Arulanandan, K. (1997), User's Manual for DYSAC2 (Version 7.0): Dynamic Soil Analysis Code for 2-Dimensional Problems, *Technical Report*, School of Civil Engineering and Environmental Science, University of Oklahoma, Norman, Oklahoma

Scott, R. F., Hushmand, B. and Rashidi, H. (1993), Model No 3 Primary Test Description and Test Results, *Proceedings of the International Conference on the Verification of*

Numerical Procedures for the Analysis of Soil Liquefaction Problems, Davis, California, October, 17-20, 1993, 435-462

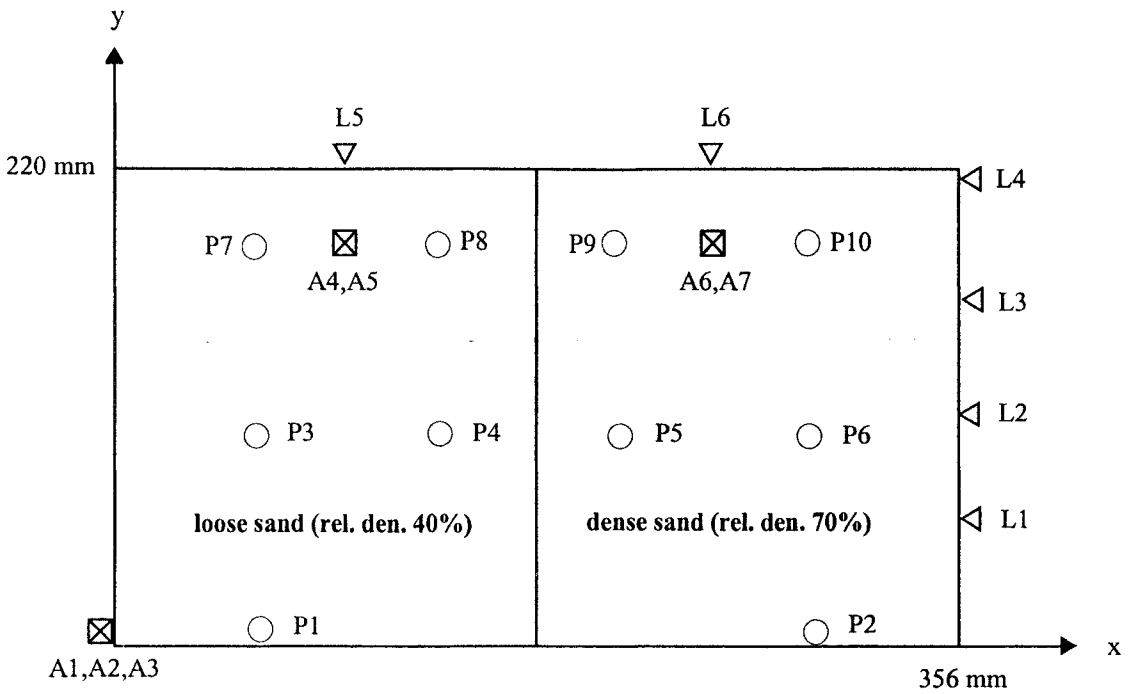

(a) front view elevation

pore pressure transducer

horizontal & vertical accelerometer

displacement transducer

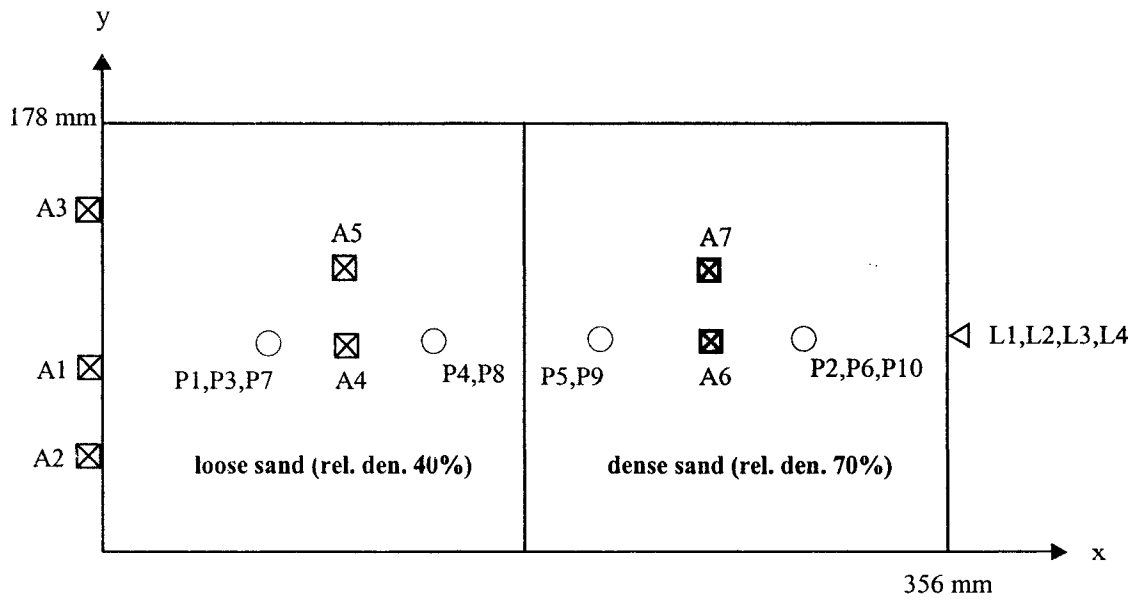

(b) plan view

Figure 6.1: the configuration and instrumentation locations for the centrifuge model test (after Scott et al., 1993)

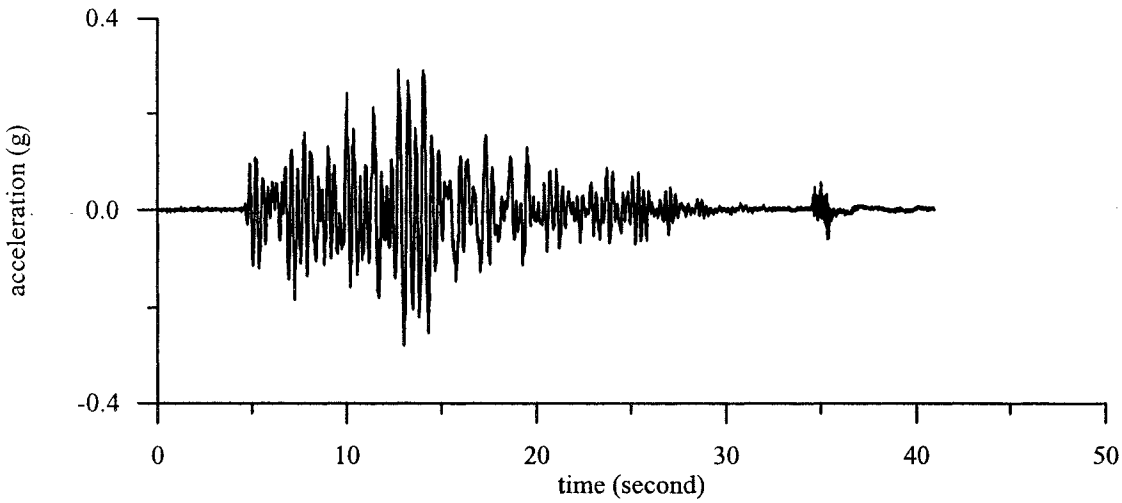

(a) horizontal acceleration time history

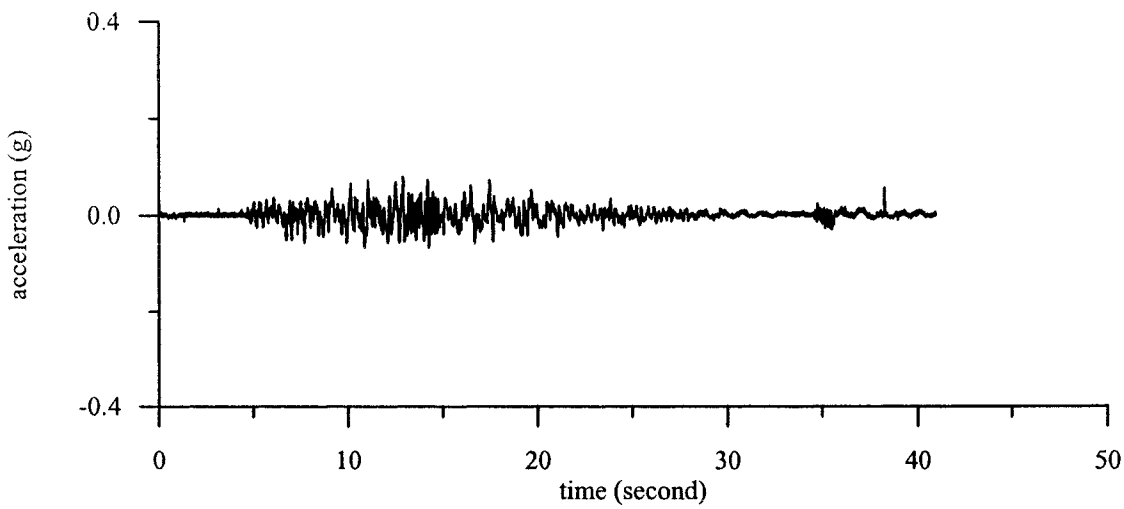

(b) vertical acceleration time history

Figure 6.2: base motion of acceleration for the centrifuge model (after Scott et al., 1993)

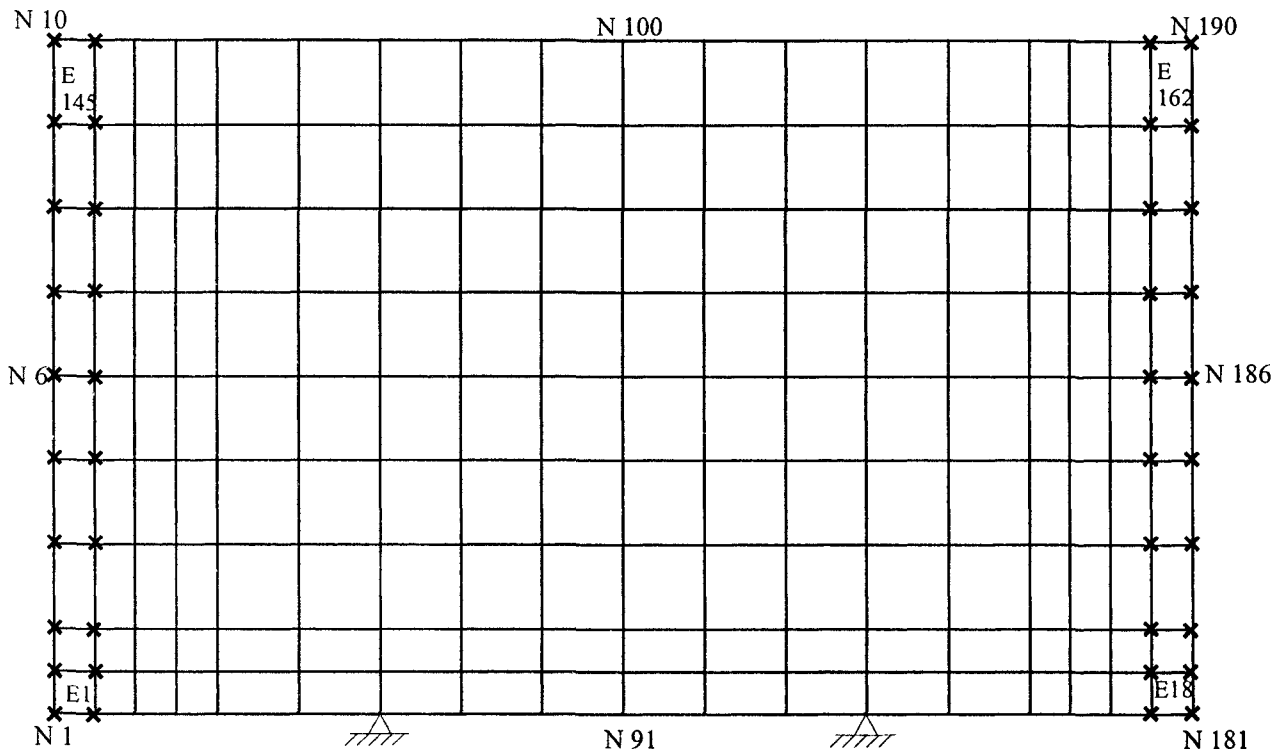

N: nodal point
E: element
×: tied up nodes to simulate laminar box
base: fixed and no vertical water flow
sides: no horizontal water flow

Figure 6.3: elements, nodes and boundary conditions in FEM

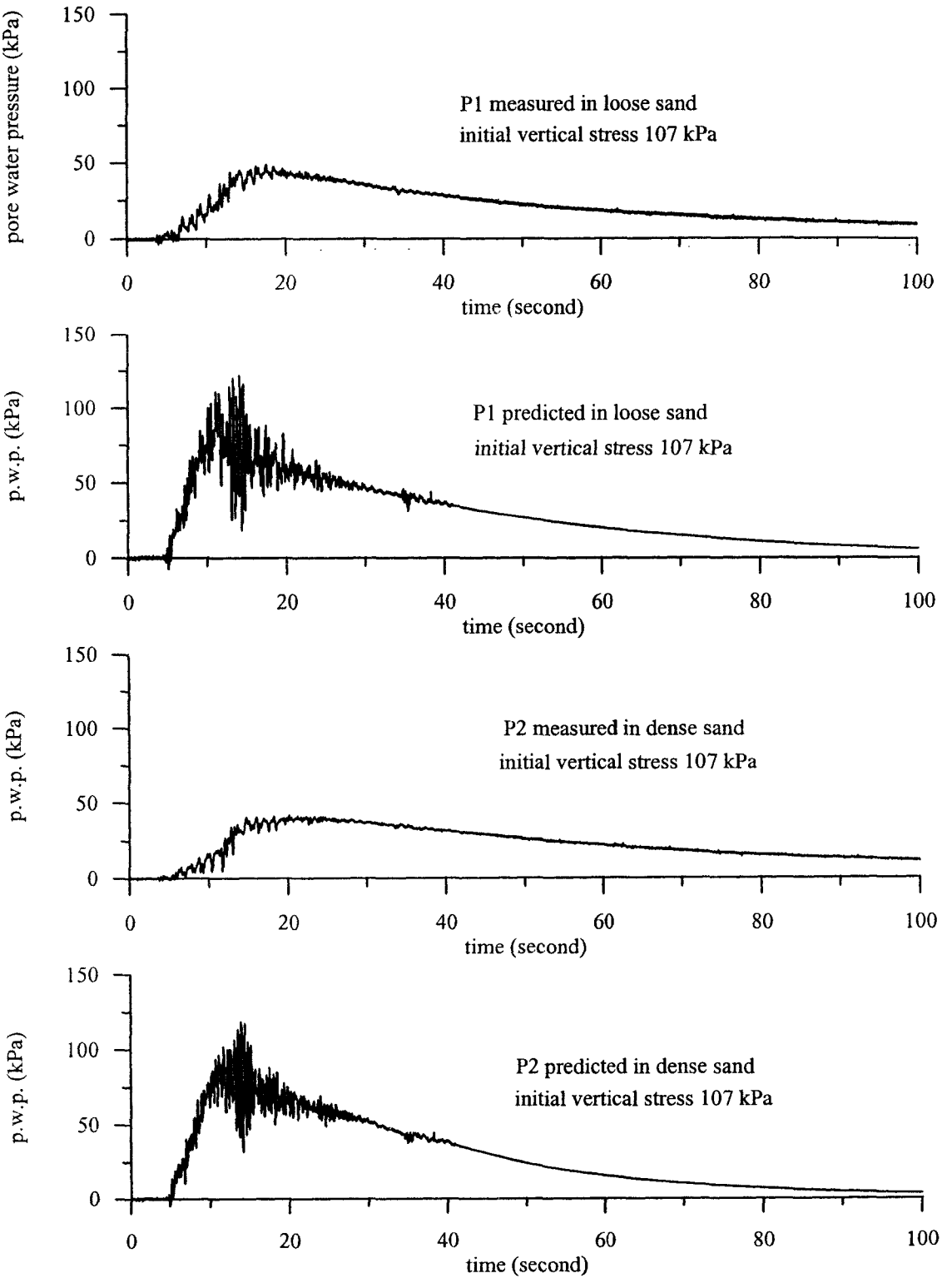

Figure 6.4: the measured and predicted p.w.p. at the bottom level in the centrifuge model (test data after Scott et al., 1993)

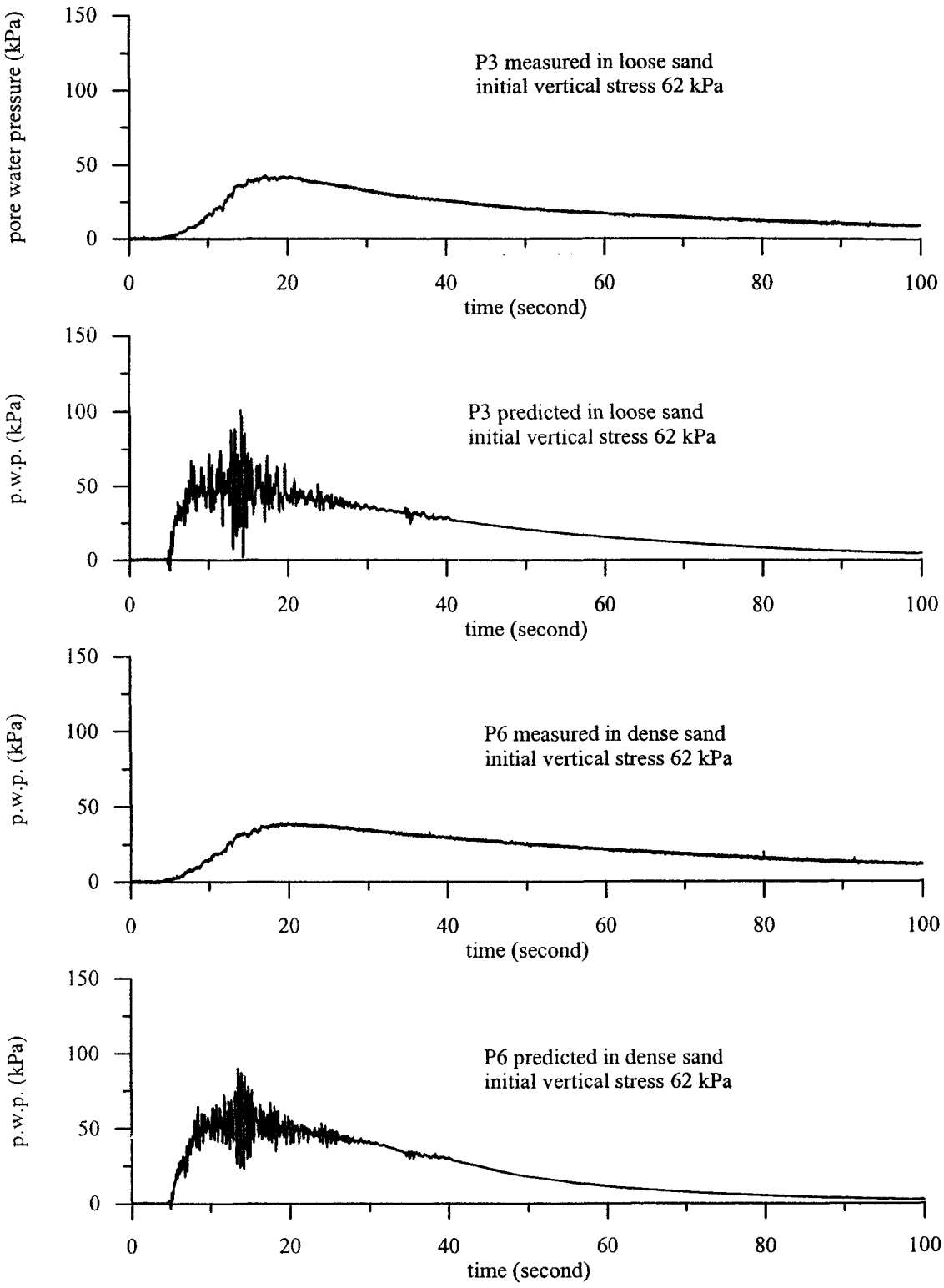

Figure 6.5: the measured and predicted p.w.p. at the middle level in the centrifuge model (test data after Scott et al., 1993)

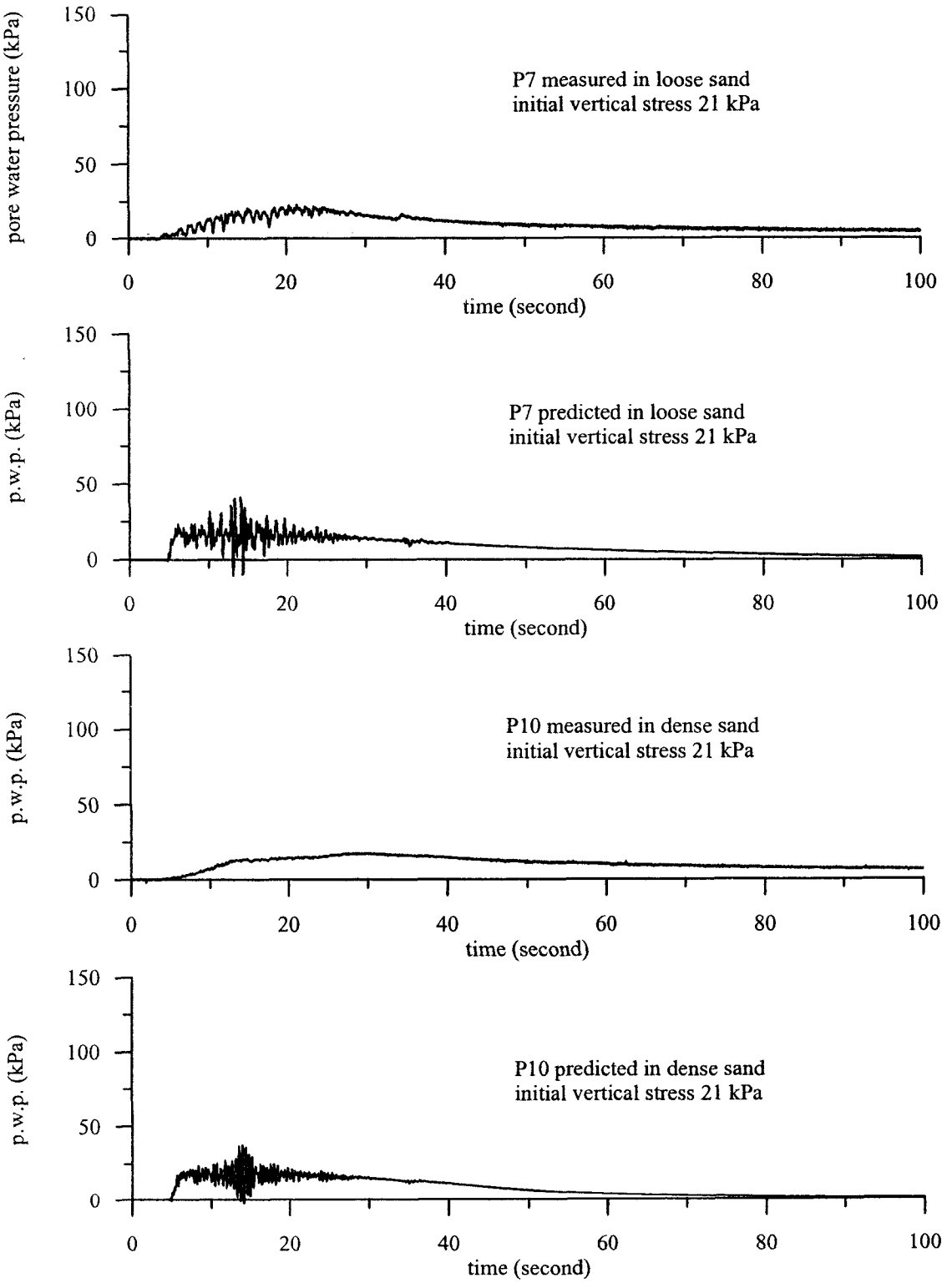

Figure 6.6: the measured and predicted p.w.p. at the top level in the centrifuge model (test data after Scott et al., 1993)

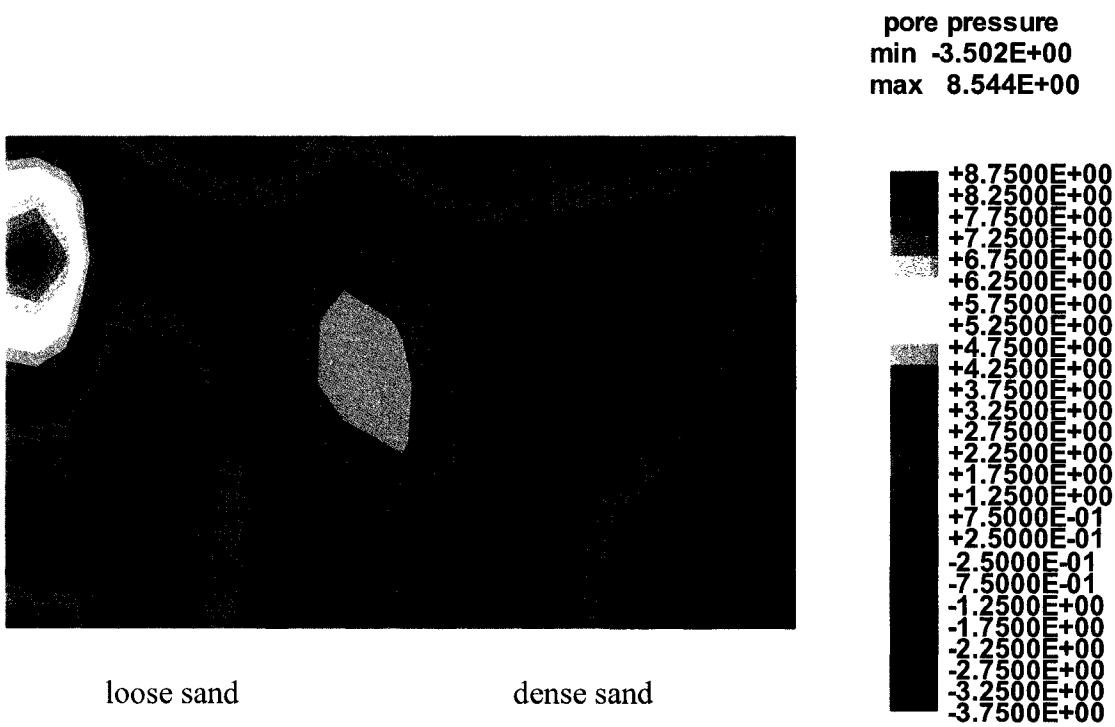

Figure 6.7: pore water pressure contours at t = 5 seconds

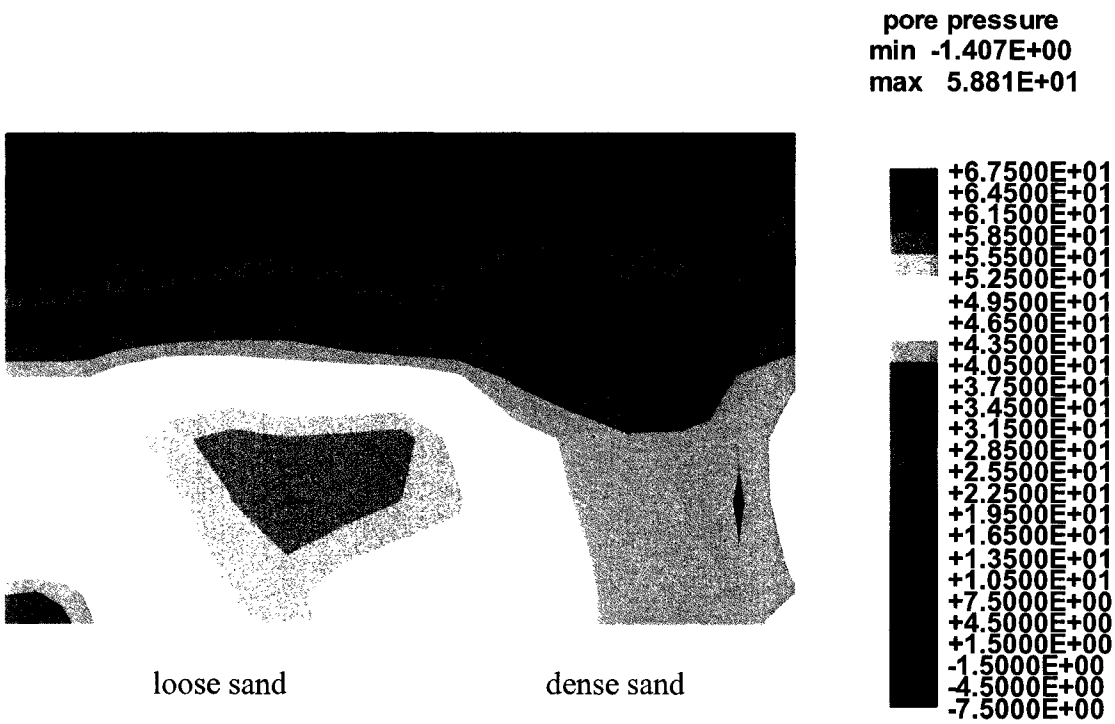

Figure 6.8: pore water pressure contours at t = 7.5 seconds

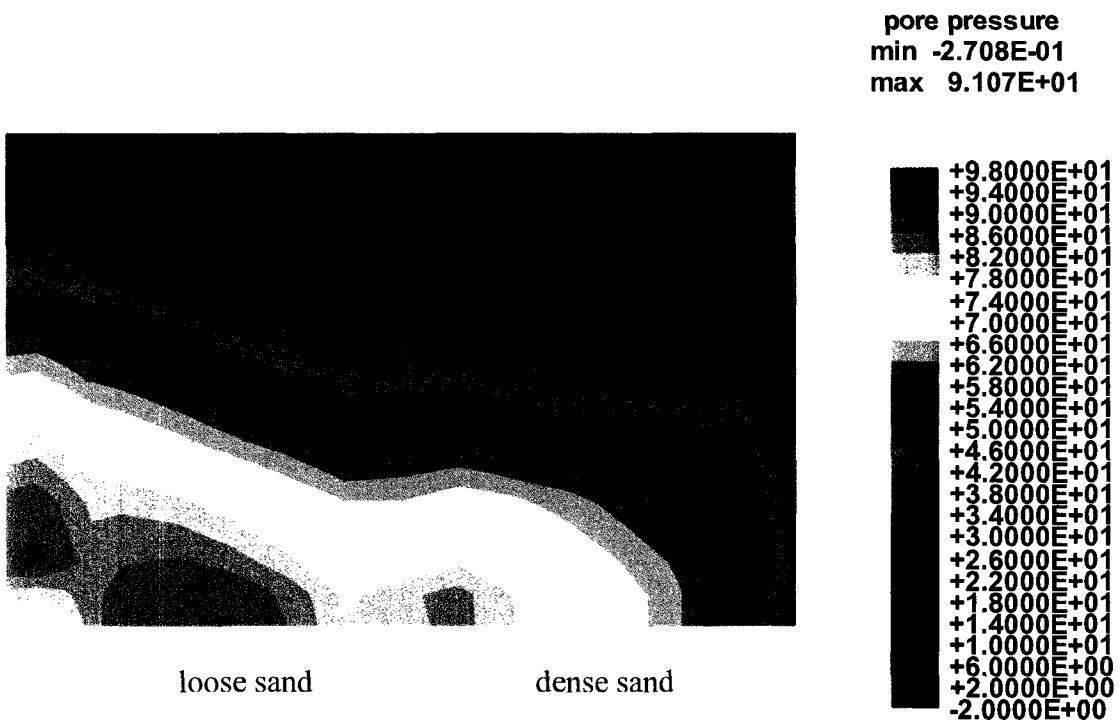

Figure 6.9: pore water pressure contours at t = 10 seconds

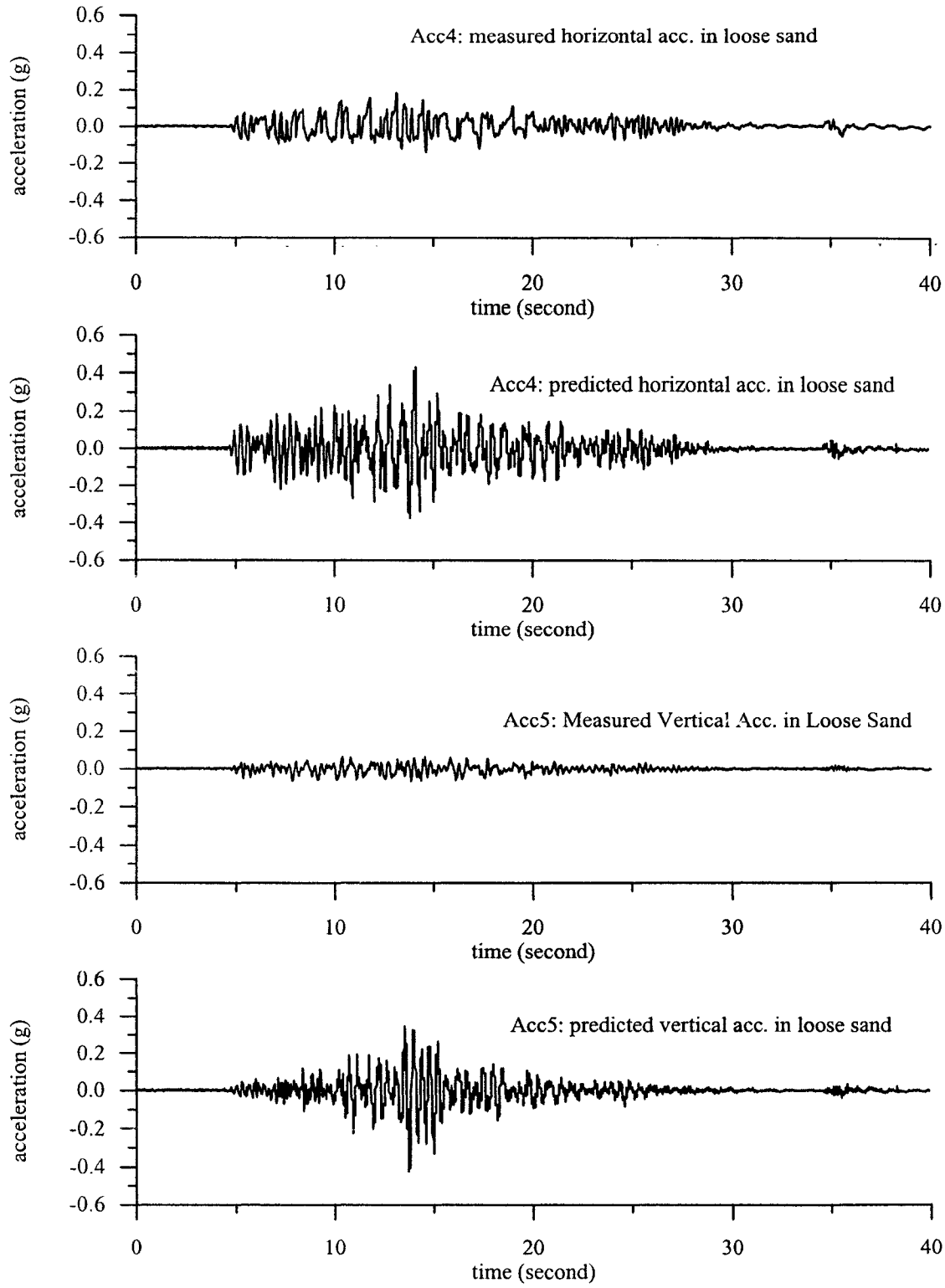

Figure 6.10: the measured and predicted acc. at the top level for loose sand in the centrifuge model (test data after Scott et al., 1993)

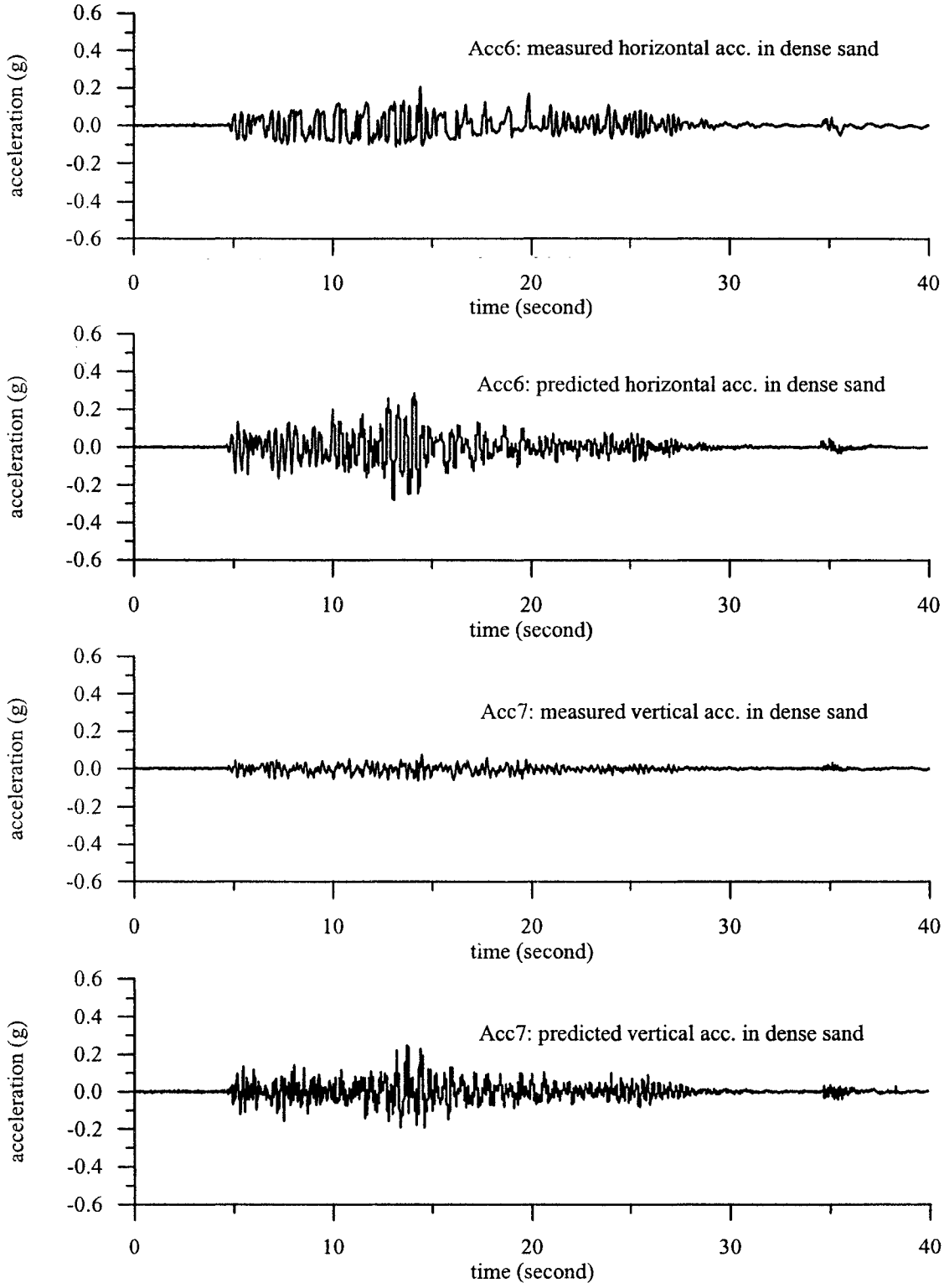

Figure 6.11: the measured and predicted acc. at the top level for dense sand in the centrifuge model (test data after Scott et al., 1993)

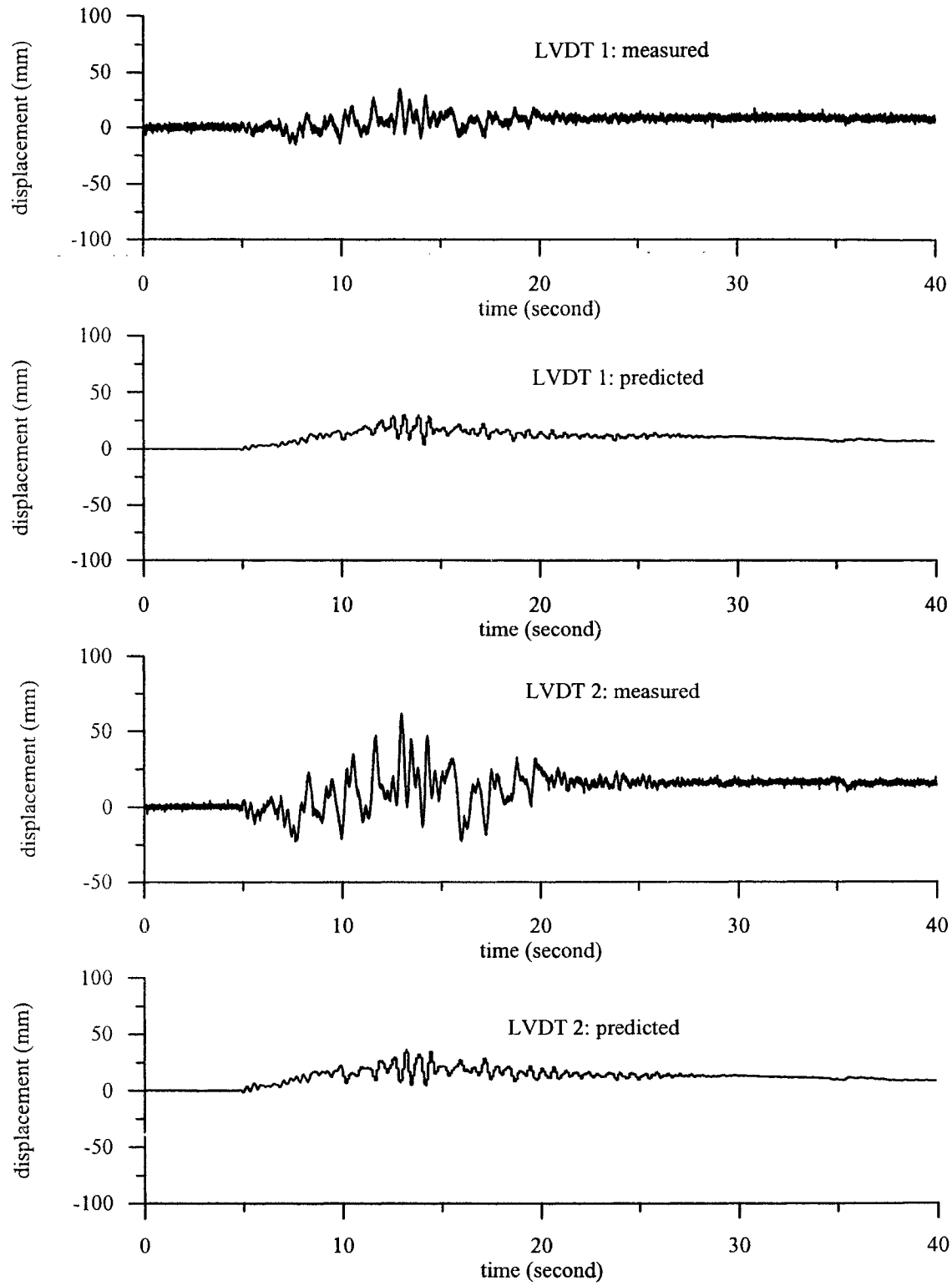

Figure 6.12(a): the measured and predicted lateral displacement in the centrifuge model (test data after Scott et al., 1993)

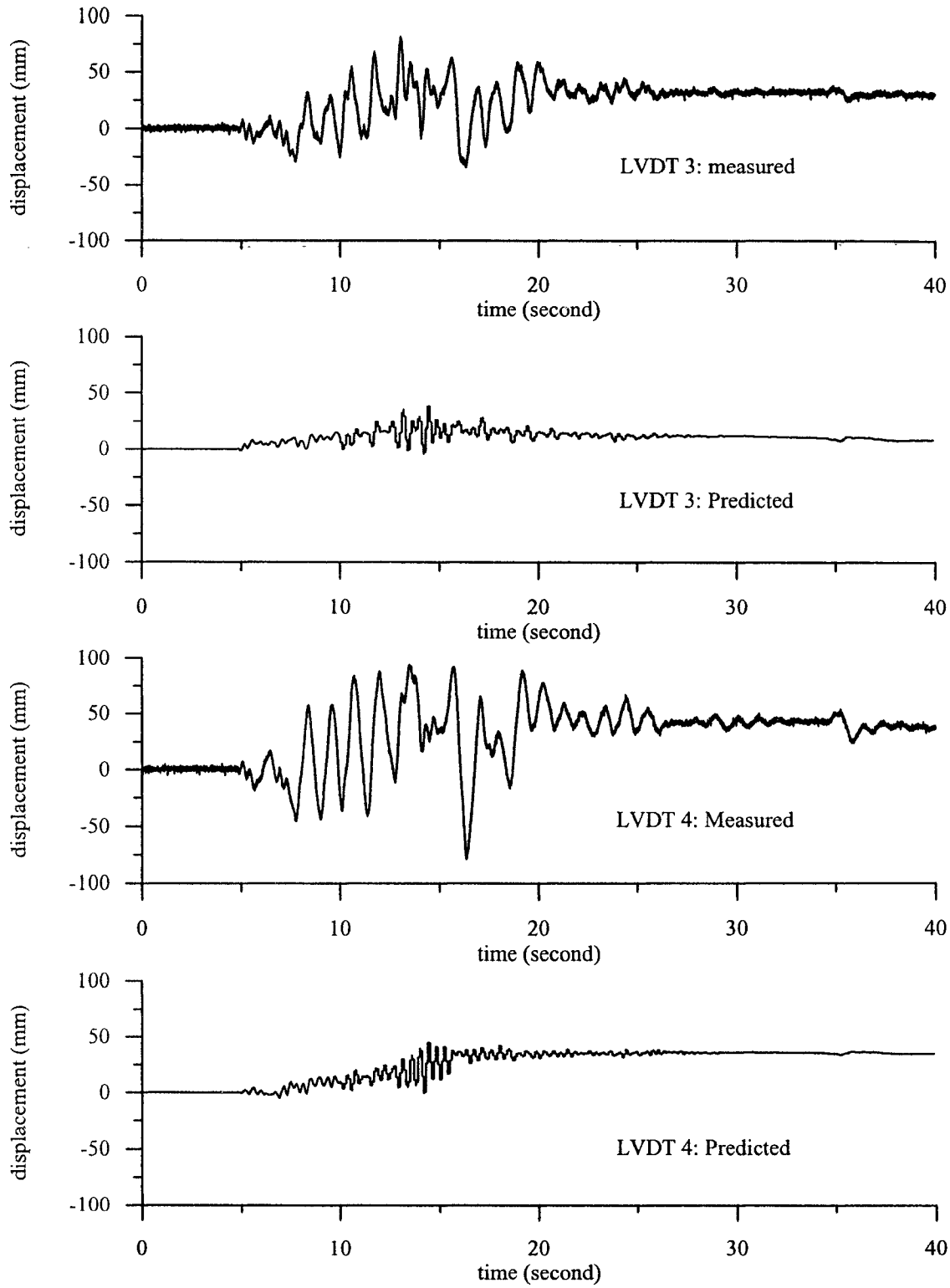

Figure 6.12(b): the measured and predicted lateral displacement in the centrifuge model (test data after Scott et al., 1993)

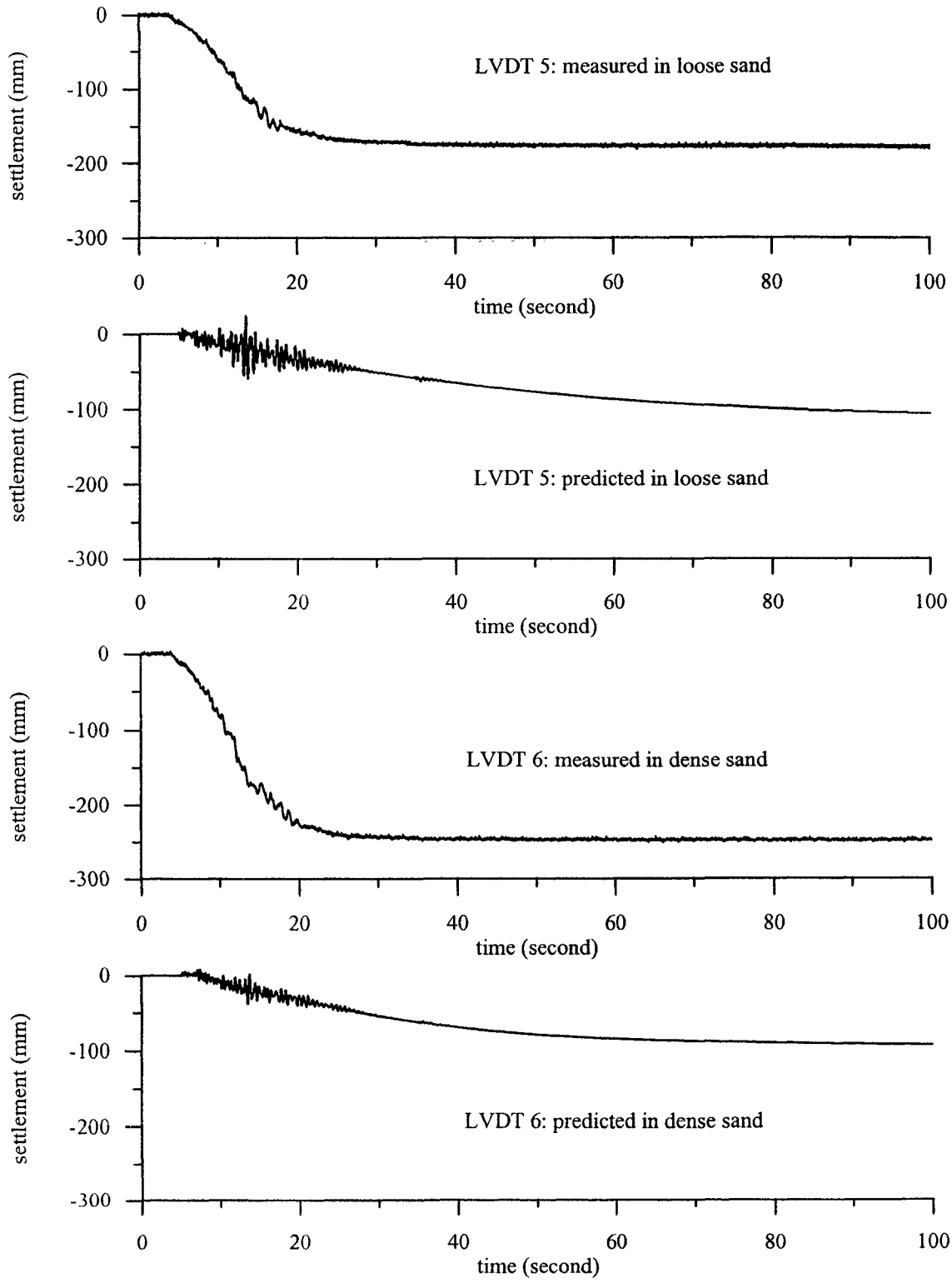

Figure 6.13: the measured and predicted settlement in the centrifuge model (test data after Scott et al., 1993)

APPENDIX I: Conversion of the Model Parameters From Triaxial Space to General Stress Space

The subscript "t" and "g" are used to identify the parameters in the triaxial space and the general stress space, respectively. The model formulations and parameters in triaxial space can be found in Yang and Muraleetharan (2003). The elasticity parameters and the critical state void ratio parameters are identical in these two spaces.

In the triaxial space, the formulations and quantities are listed as follows:

$$\eta = \frac{q}{p} = \frac{(\sigma_1 - \sigma_3)}{1/3(\sigma_1 + 2\sigma_3)} \tag{A1}$$

$$\varepsilon_v^p = \varepsilon_1^p + 2\varepsilon_3^p \tag{A2}$$

$$\gamma^p = 2/3(\varepsilon_1^p - \varepsilon_3^p) \tag{A3}$$

$$\dot{\gamma}^p = \frac{p\dot{\eta}}{K_p^t} \tag{A4}$$

$$\dot{\varepsilon}_v^p = D^t \dot{\gamma}^p \tag{A5}$$

In general stress space under triaxial compression loading, the quantities and formulations are as follows:

$$\boldsymbol{n} = \frac{1}{\sqrt{6}}\{2, -1, -1, 0, 0, 0\}^T \tag{A6}$$

$$\boldsymbol{r} = \frac{(\sigma_1 - \sigma_3)}{1/3(\sigma_1 + 2\sigma_3)}\{2/3, -1/3, -1/3, 0, 0, 0\}^T \tag{A7}$$

$$\dot{\boldsymbol{e}}^p = \frac{2}{\sqrt{6}}\frac{p\dot{\eta}}{K_p^g}\boldsymbol{n} \tag{A8}$$

$$\dot{\varepsilon}_v^p = \frac{2}{\sqrt{6}} \frac{p\dot{\eta}}{K_p^g} D^g \tag{A9}$$

Comparing η and $\|\boldsymbol{r}\|$, one can obtain,

$$M^g = \sqrt{2/3}\, M^t \tag{A10}$$

In view of the fact that $M + k_2\psi$ is used to determine the volumetric change, one can obtain,

$$k_2^g = \sqrt{2/3}\, k_2^t \tag{A11}$$

Considering the same plastic deviatoric and volumetric strain rates are induced in the triaxial space and general stress space when the stress rate is given, one can obtain,

$$K_p^g = \frac{2}{3} K_p^t \tag{A12}$$

$$D^g = \sqrt{2/3}\, D^t \tag{A13}$$

From the relationship in equation (A12) and the formulations of the plastic moduli in the triaxial space and general stress space, one can obtain,

$$a^g = \sqrt{3/2}\, a^t \tag{A14}$$

$$b^g = \sqrt{3/2}\, b^t \tag{A15}$$

$$k_1^g = k_1^t \tag{A16}$$

$$h_1^g = \sqrt{2/3}\, h_1^t \tag{A17}$$

From the relationship in equation (A13) and the formulations of the dilatancy ratio in the triaxial space and general stress space, one can obtain,

$$A^g = A^t \tag{A18}$$

$$h_2^g = \sqrt{3/2}\, h_2^t \tag{A19}$$

APPENDIX II: the Computation of $\frac{\partial \mathbf{R}}{\partial \mathbf{X}}$

$\mathbf{R} = [R_1, \mathbf{R}_2, R_3, \mathbf{R}_4, R_5, \mathbf{R}_6, R_7, R_8]^T$; $\mathbf{X} = \{p, \mathbf{s}, \Lambda, \boldsymbol{\alpha}, \Delta\varepsilon_v^p, \Delta\mathbf{e}^p, g_{12}, g_3\}^T$

∂/∂	R_1	$\mathbf{R}_2$	R_3	$\mathbf{R}_4$	R_5	$\mathbf{R}_6$
p	1	$\mathbf{C}_{21}$	C_{31}	$-\alpha\Lambda(\frac{\partial K_p^*}{\partial p}\mathbf{n} + K_p^*\frac{\partial \mathbf{n}}{\partial p})$	$-\alpha\Lambda\frac{\partial D}{\partial p}$	$-\alpha\Lambda\frac{\partial \mathbf{n}}{\partial p}$
s	0	**I**	$\mathbf{C}_{32}$	$-\alpha\Lambda(\mathbf{n}\frac{\partial K_p^*}{\partial \mathbf{s}} + K_p^*\frac{\partial \mathbf{n}}{\partial \mathbf{s}})$	$-\alpha\Lambda\frac{\partial D}{\partial \mathbf{s}}$	$-\alpha\Lambda\frac{\partial \mathbf{n}}{\partial \mathbf{s}}$
Λ	0	0	0	$-(1-\alpha)(K_p^*\mathbf{n})_n - \alpha K_p^*\mathbf{n}$	$-(1-\alpha)D_n - \alpha D$	$-(1-\alpha)\mathbf{n}_n - \alpha\mathbf{n}$
$\boldsymbol{\alpha}$	0	0	$\mathbf{C}_{34}$	$\mathbf{I} - \alpha\Lambda(\mathbf{n}\frac{\partial K_p^*}{\partial \boldsymbol{\alpha}} + K_p^*\frac{\partial \mathbf{n}}{\partial \boldsymbol{\alpha}})$	$-\alpha\Lambda\frac{\partial D}{\partial \boldsymbol{\alpha}}$	$-\alpha\Lambda\frac{\partial \mathbf{n}}{\partial \boldsymbol{\alpha}}$
$\Delta\varepsilon_v^p$	C_{15}	0	0	0	0	0
$\Delta\mathbf{e}^p$	0	$\mathbf{C}_{26}$	0	$-\alpha\Lambda\mathbf{n}\frac{\partial K_p^*}{\partial \mathbf{e}^p}$	$-\alpha\Lambda\frac{\partial D}{\partial \mathbf{e}^p}$	**I**
g_{12}	0	0	0	$-\alpha\Lambda\frac{\partial K_p^*}{\partial g_{12}}\mathbf{n}$	$-\alpha\Lambda\frac{\partial D}{\partial g_{12}}$	0
g_3	0	0	0	$-\alpha\Lambda\frac{\partial K_p^*}{\partial g_3}\mathbf{n}$	0	0
Note: **I** is a unity tensor. $K_p^* = K_p/p$						

∂/∂	R_7	R_8
p	$\alpha(g_{12}\boldsymbol{\alpha} - g_{12n}\boldsymbol{\alpha}_n) : \dfrac{(K^*_{p12}\dfrac{\partial \mathbf{n}}{\partial p} - \dfrac{\partial K^*_{p12}}{\partial p}\mathbf{n})}{(K^*_{p12})^2}$	$\alpha(g_3\boldsymbol{\alpha} - g_{3n}\boldsymbol{\alpha}_n) : \dfrac{(K^*_{p3}\dfrac{\partial \mathbf{n}}{\partial p} - \dfrac{\partial K^*_{p3}}{\partial p}\mathbf{n})}{(K^*_{p3})^2}$
s	$\alpha(g_{12}\boldsymbol{\alpha} - g_{12n}\boldsymbol{\alpha}_n) : \dfrac{(K^*_{p12}\dfrac{\partial \mathbf{n}}{\partial s} - \dfrac{\partial K^*_{p12}}{\partial s}\mathbf{n})}{(K^*_{p12})^2}$	$\alpha(g_3\boldsymbol{\alpha} - g_{3n}\boldsymbol{\alpha}_n) : \dfrac{(K^*_{p3}\dfrac{\partial \mathbf{n}}{\partial s} - \dfrac{\partial K^*_{p3}}{\partial s}\mathbf{n})}{(K^*_{p3})^2}$
Λ	-1	-1
$\boldsymbol{\alpha}$	$g_{12}\left[(1-\alpha)\dfrac{\mathbf{n}_n}{K^*_{p12n}} + \alpha\dfrac{\mathbf{n}}{K^*_{p12}}\right] +$ $\alpha(g_{12}\boldsymbol{\alpha} - g_{12n}\boldsymbol{\alpha}_n) : \dfrac{(K^*_{p12}\dfrac{\partial \mathbf{n}}{\partial \boldsymbol{\alpha}} - \dfrac{\partial K^*_{p12}}{\partial \boldsymbol{\alpha}}\mathbf{n})}{(K^*_{p12})^2}$	$g_3\left[(1-\alpha)\dfrac{\mathbf{n}_n}{K^*_{p3n}} + \alpha\dfrac{\mathbf{n}}{K^*_{p3}}\right] +$ $\alpha(g_3\boldsymbol{\alpha} - g_{3n}\boldsymbol{\alpha}_n) : \dfrac{(K^*_{p3}\dfrac{\partial \mathbf{n}}{\partial \boldsymbol{\alpha}} - \dfrac{\partial K^*_{p3}}{\partial \boldsymbol{\alpha}}\mathbf{n})}{(K^*_{p3})^2}$
$\Delta\varepsilon^p_v$	0	0
$\Delta\mathbf{e}^p$	$-\alpha(g_{12}\boldsymbol{\alpha} - g_{12n}\boldsymbol{\alpha}_n) : \mathbf{n}\dfrac{(\partial K^*_{p12}/\partial \mathbf{e}^p)}{(K^*_{p12})^2}$	$-\alpha(g_3\boldsymbol{\alpha} - g_{3n}\boldsymbol{\alpha}_n) : \mathbf{n}\dfrac{(\partial K^*_{p3}/\partial \mathbf{e}^p)}{(K^*_{p3})^2}$
g_{12}	$\left[(1-\alpha)\dfrac{\mathbf{n}_n}{K^*_{p12n}} + \alpha\dfrac{\mathbf{n}}{K^*_{p12}}\right] : \boldsymbol{\alpha} -$ $\alpha(g_{12}\boldsymbol{\alpha} - g_{12n}\boldsymbol{\alpha}_n) : \mathbf{n}\dfrac{\partial K^*_{p12}/\partial g_{12}}{(K^*_{p12})^2}$	$-\alpha(g_3\boldsymbol{\alpha} - g_{3n}\boldsymbol{\alpha}_n) : \mathbf{n}\dfrac{\partial K^*_{p3}/\partial g_{12}}{(K^*_{p3})^2}$
g_3	0	$\left[(1-\alpha)\dfrac{\mathbf{n}_n}{K^*_{p3n}} + \alpha\dfrac{\mathbf{n}}{K^*_{p3}}\right] : \boldsymbol{\alpha}$
Note: $K^*_{p12} = K_{p12}/p$, $K^*_{p3} = K_{p3}/p$		

The definitions of $C_{15}, C_{21}, C_{26}, C_{31}, C_{32}$ and C_{34}

$$C_{15} = K_0 p_{at}^{-a0}\left[K_0 p_{at}^{-a0}(1-a_0)(\Delta\varepsilon_v - \Delta\varepsilon_v^p) + p_n^{1-a0}\right]^{\frac{a0}{1-a0}}$$

$$\mathbf{C}_{21} = -2\alpha G_0 a_0 p^{a0-1} p_{at}^{-a0}(\Delta\mathbf{e} - \Delta\mathbf{e}^p) \qquad \mathbf{C}_{26} = 2G_0 p_{at}^{-a0}\left[(1-\alpha)p_n^{a0} + \alpha p^{a0}\right]\mathbf{I}$$

$$C_{31} = \hat{m} - m - \hat{m}^{-1}\mathbf{r} : (\mathbf{r} - \boldsymbol{\alpha}) \qquad \mathbf{C}_{32} = \hat{m}^{-1}(\mathbf{r} - \boldsymbol{\alpha}) \qquad \mathbf{C}_{34} = -p\hat{m}^{-1}(\mathbf{r} - \boldsymbol{\alpha})$$

$$\hat{m} = \left[(\mathbf{r} - \boldsymbol{\alpha}) : (\mathbf{r} - \boldsymbol{\alpha})\right]^{-1/2}$$

The differentiations of $K_p^*, K_{p12}^*, K_{p3}^*$ *with respect to* $p, \mathbf{s}, \boldsymbol{\alpha}, \mathbf{e}^p, g_{12}, g_3$

$$\frac{\partial K_p^*}{\partial p} = \frac{\xi^p}{b+\xi^p}\frac{\partial K_{p12}^*}{\partial p} + \frac{b}{b+\xi^p}\frac{\partial K_{p3}^*}{\partial p} + \frac{b}{(b+\xi^p)^2}(g_{12} - g_3)\boldsymbol{\alpha} : \frac{\partial \mathbf{n}}{\partial p}$$

$$\frac{\partial K_{p12}^*}{\partial p} = \frac{4d_{12}a(M_d^* - d_{12})\dfrac{\partial d_{12}}{\partial p} - 2d_{12}^2\left[(M_d^* - d_{12})\dfrac{\partial a}{\partial p} + a\left(\dfrac{\partial M_d}{\partial p} - \dfrac{\partial d_{12}}{\partial p}\right)\right]}{a^2(M_d^* - d_{12})^2} +$$

$$h_1\left(\frac{\partial \boldsymbol{\alpha}_2}{\partial p} : \mathbf{n} + \frac{\partial \mathbf{n}}{\partial p} : \boldsymbol{\alpha}_2 - g_{12}\boldsymbol{\alpha} : \frac{\partial \mathbf{n}}{\partial p}\right)$$

$$\frac{\partial K_{p3}^*}{\partial p} = \exp(-k_1\psi)\frac{\partial K_{p12}^*}{\partial p} - k_1\frac{\lambda}{p}K_{p12}^*\exp(-k_1\psi)$$

$$M_d^* = M_d - 2m \qquad \frac{\partial d_{12}}{\partial p} = \frac{\partial M}{\partial p} - g_{12}\boldsymbol{\alpha} : \frac{\partial \mathbf{n}}{\partial p}$$

$$\frac{\partial K_p^*}{\partial \mathbf{s}} = \frac{\xi^p}{b+\xi^p}\frac{\partial K_{p12}^*}{\partial \mathbf{s}} + \frac{b}{b+\xi^p}\frac{\partial K_{p3}^*}{\partial \mathbf{s}} + \frac{b}{(b+\xi^p)^2}(g_{12} - g_3)\boldsymbol{\alpha} : \frac{\partial \mathbf{n}}{\partial \mathbf{s}}$$

$$\frac{\partial K_{p12}^*}{\partial \mathbf{s}} = \frac{4d_{12}a(M_d^* - d_{12})\dfrac{\partial d_{12}}{\partial \mathbf{s}} - 2d_{12}^2\left[(M_d^* - d_{12})\dfrac{\partial a}{\partial \mathbf{s}} + a\left(\dfrac{\partial M_d}{\partial \mathbf{s}} - \dfrac{\partial d_{12}}{\partial \mathbf{s}}\right)\right]}{a^2(M_d^* - d_{12})^2} +$$

$$h_1\left(\mathbf{n} : \frac{\partial \boldsymbol{\alpha}_2}{\partial \mathbf{s}} + \boldsymbol{\alpha}_2 : \frac{\partial \mathbf{n}}{\partial \mathbf{s}} - g_{12}\boldsymbol{\alpha} : \frac{\partial \mathbf{n}}{\partial \mathbf{s}}\right)$$

$$\frac{\partial K_{p3}^*}{\partial s} = \exp(-k_1\psi)\frac{\partial K_{p12}^*}{\partial s} \qquad \frac{\partial d_{12}}{\partial s} = \frac{\partial M}{\partial s} - g_{12}\boldsymbol{\alpha} : \frac{\partial \mathbf{n}}{\partial s}$$

$$\frac{\partial K_p^*}{\partial \boldsymbol{\alpha}} = \frac{\xi^p}{b+\xi^p}\frac{\partial K_{p12}^*}{\partial \boldsymbol{\alpha}} + \frac{b}{b+\xi^p}\frac{\partial K_{p3}^*}{\partial \boldsymbol{\alpha}} + \frac{b}{(b+\xi^p)^2}(g_{12}-g_3)(\boldsymbol{\alpha} : \frac{\partial \mathbf{n}}{\partial \boldsymbol{\alpha}} + \mathbf{n})$$

$$\frac{\partial K_{p12}^*}{\partial \boldsymbol{\alpha}} = \frac{4d_{12}a(M_d^* - d_{12})\frac{\partial d_{12}}{\partial \boldsymbol{\alpha}} - 2d_{12}^2\left[(M_d^* - d_{12})\frac{\partial a}{\partial \boldsymbol{\alpha}} + a(\frac{\partial M_d}{\partial \boldsymbol{\alpha}} - \frac{\partial d_{12}}{\partial \boldsymbol{\alpha}})\right]}{a^2(M_d^* - d_{12})^2} +$$

$$h_1(\mathbf{n} : \frac{\partial \boldsymbol{\alpha}_2}{\partial \boldsymbol{\alpha}} + \boldsymbol{\alpha}_2 : \frac{\partial \mathbf{n}}{\partial \boldsymbol{\alpha}} - g_{12}\boldsymbol{\alpha} : \frac{\partial \mathbf{n}}{\partial \boldsymbol{\alpha}} - g_{12}\mathbf{n})$$

$$\frac{\partial K_{p3}^*}{\partial \boldsymbol{\alpha}} = \exp(-k_1\psi)\frac{\partial K_{p12}^*}{\partial \boldsymbol{\alpha}} \qquad \frac{\partial d_{12}}{\partial \boldsymbol{\alpha}} = \frac{\partial M}{\partial \boldsymbol{\alpha}} - g_{12}(\boldsymbol{\alpha} : \frac{\partial \mathbf{n}}{\partial \boldsymbol{\alpha}} + \mathbf{n})$$

$$\frac{\partial K_p^*}{\partial e^p} = (K_{p12}^* - K_{p3}^*)\frac{b}{(b+\xi^p)^2}\frac{\Delta e^p}{|\Delta e^p|} + \frac{\xi^p}{b+\xi^p}\frac{\partial K_{p12}^*}{\partial e^p} + \frac{b}{b+\xi^p}\frac{\partial K_{p3}^*}{\partial e^p}$$

$$\frac{\partial K_{p12}^*}{\partial e^p} = h_1\mathbf{n} : \frac{\partial \boldsymbol{\alpha}_2}{\partial e^p} \qquad \frac{\partial K_{p3}^*}{\partial e^p} = \exp(-k_1\psi)\frac{\partial K_{p12}^*}{\partial e^p}$$

$$\frac{\partial K_p^*}{\partial g_{12}} = \frac{\xi^p}{b+\xi^p}\frac{\partial K_{p12}^*}{\partial g_{12}} + \frac{b}{b+\xi^p}\frac{\partial K_{p3}^*}{\partial g_{12}} + \frac{b}{(b+\xi^p)^2}(\mathbf{n} : \boldsymbol{\alpha})$$

$$\frac{\partial K_{p12}^*}{\partial g_{12}} = \frac{-(\boldsymbol{\alpha} : \mathbf{n})\left[4d_{12}(M_d^* - d_{12}) + 2d_{12}^2\right]}{a(M_d^* - d_{12})^2} \qquad \frac{\partial K_{p3}^*}{\partial g_{12}} = \exp(-k_1\psi)\frac{\partial K_{p12}^*}{\partial g_{12}}$$

$$\frac{\partial K_p^*}{\partial g_3} = \frac{-b(\mathbf{n} : \boldsymbol{\alpha})}{(b+\xi^p)^2}$$

The differentiations of D *with respect to* p, **s**, **α**, $\mathbf{e}^p$, g_{12}, g_3

$$\frac{\partial D}{\partial p} = \frac{\partial D_1}{\partial p} + C_2\frac{\partial D_2}{\partial p} + D_2\frac{\partial C_2}{\partial p}$$

$$\frac{\partial D_1}{\partial p} = A(\frac{\partial M}{\partial p} + k_2 \frac{\lambda}{p} + \psi \frac{\partial k_2}{\partial p} - g_{12}\boldsymbol{\alpha} : \frac{\partial \mathbf{n}}{\partial p})$$

$$\frac{\partial D_2}{\partial p} = A(\frac{\partial M}{\partial p} + k_2 \frac{\lambda}{p} + \psi \frac{\partial k_2}{\partial p} - \mathbf{n} : \frac{\partial \boldsymbol{\alpha}_2}{\partial p} - \boldsymbol{\alpha}_2 : \frac{\partial \mathbf{n}}{\partial p})$$

$$\frac{\partial C_2}{\partial p} = \frac{h_2(\boldsymbol{\alpha}_2 - \boldsymbol{\alpha}_{12}) : \mathbf{n}}{|(\boldsymbol{\alpha}_2 - \boldsymbol{\alpha}_{12}) : \mathbf{n}|}(\mathbf{n} : \frac{\partial \boldsymbol{\alpha}_2}{\partial p} + \boldsymbol{\alpha}_2 : \frac{\partial \mathbf{n}}{\partial p} - g_{12}\boldsymbol{\alpha} : \frac{\partial \mathbf{n}}{\partial p})$$

$$\frac{\partial D}{\partial s} = \frac{\partial D_1}{\partial s} + C_2 \frac{\partial D_2}{\partial s} + D_2 \frac{\partial C_2}{\partial s}$$

$$\frac{\partial D_1}{\partial s} = A(\frac{\partial M}{\partial s} + \psi \frac{\partial k_2}{\partial s} - g_{12}\boldsymbol{\alpha} : \frac{\partial \mathbf{n}}{\partial s}) \qquad \frac{\partial D_2}{\partial s} = A(\frac{\partial M}{\partial s} + \psi \frac{\partial k_2}{\partial s} - \mathbf{n} : \frac{\partial \boldsymbol{\alpha}_2}{\partial s} - \boldsymbol{\alpha}_2 : \frac{\partial \mathbf{n}}{\partial s})$$

$$\frac{\partial C_2}{\partial s} = \frac{h_2(\boldsymbol{\alpha}_2 - \boldsymbol{\alpha}_{12}) : \mathbf{n}}{|(\boldsymbol{\alpha}_2 - \boldsymbol{\alpha}_{12}) : \mathbf{n}|}(\mathbf{n} : \frac{\partial \boldsymbol{\alpha}_2}{\partial s} + \boldsymbol{\alpha}_2 : \frac{\partial \mathbf{n}}{\partial s} - g_{12}\boldsymbol{\alpha} : \frac{\partial \mathbf{n}}{\partial s})$$

$$\frac{\partial D}{\partial e^p} = (-AC_2 + \frac{h_2(\boldsymbol{\alpha}_2 - \boldsymbol{\alpha}_{12}) : \mathbf{n}}{|(\boldsymbol{\alpha}_2 - \boldsymbol{\alpha}_{12}) : \mathbf{n}|} D_2)(\mathbf{n} : \frac{\partial \boldsymbol{\alpha}_2}{\partial e^p})$$

$$\frac{\partial D}{\partial \boldsymbol{\alpha}} = \frac{\partial D_1}{\partial \boldsymbol{\alpha}} + C_2 \frac{\partial D_2}{\partial \boldsymbol{\alpha}} + D_2 \frac{\partial C_2}{\partial \boldsymbol{\alpha}}$$

$$\frac{\partial D_1}{\partial \boldsymbol{\alpha}} = -Ag_{12}(\boldsymbol{\alpha} : \frac{\partial \mathbf{n}}{\partial \boldsymbol{\alpha}} + \mathbf{n}) \qquad \frac{\partial D_2}{\partial \boldsymbol{\alpha}} = -A(\mathbf{n} : \frac{\partial \boldsymbol{\alpha}_2}{\partial \boldsymbol{\alpha}} + \boldsymbol{\alpha}_2 : \frac{\partial \mathbf{n}}{\partial \boldsymbol{\alpha}})$$

$$\frac{\partial C_2}{\partial \boldsymbol{\alpha}} = \frac{h_2(\boldsymbol{\alpha}_2 - \boldsymbol{\alpha}_{12}) : \mathbf{n}}{|(\boldsymbol{\alpha}_2 - \boldsymbol{\alpha}_{12}) : \mathbf{n}|}(\mathbf{n} : \frac{\partial \boldsymbol{\alpha}_2}{\partial \boldsymbol{\alpha}} + \boldsymbol{\alpha}_2 : \frac{\partial \mathbf{n}}{\partial \boldsymbol{\alpha}} - g_{12}\boldsymbol{\alpha} : \frac{\partial \mathbf{n}}{\partial \boldsymbol{\alpha}} - g_{12}\mathbf{n})$$

$$\frac{\partial D}{\partial g_{12}} = -A(\boldsymbol{\alpha} : \mathbf{n}) - D_2 \frac{h_2(\boldsymbol{\alpha}_2 - \boldsymbol{\alpha}_{12}) : \mathbf{n}}{|(\boldsymbol{\alpha}_2 - \boldsymbol{\alpha}_{12}) : \mathbf{n}|}(\boldsymbol{\alpha} : \mathbf{n})$$

The differentiations of $\boldsymbol{\alpha}_2$, $\mathbf{n}$ *with respect to* $p, \mathbf{s}, \boldsymbol{\alpha}, \mathbf{e}^p$

$$\frac{\partial \boldsymbol{\alpha}_2}{\partial x} = \frac{\mathbf{e}^p}{a + |\mathbf{e}^p|} \frac{\partial M}{\partial x} - M^* \frac{\mathbf{e}^p}{(a + |\mathbf{e}^p|)^2} \frac{\partial a}{\partial x} \qquad (x = p, \mathbf{s}, \boldsymbol{\alpha})$$

$$\frac{\partial \boldsymbol{\alpha}_2}{\partial \mathbf{e}^p} = \frac{M^*}{(a+|\mathbf{e}^p|)^2}\left[(a+|\mathbf{e}^p|)\mathbf{I} - \frac{\mathbf{e}^p \otimes \mathbf{e}^p}{|\mathbf{e}^p|}\right]$$

$$\frac{\partial \mathbf{n}}{\partial p} = \frac{-\mathbf{r}}{p\hat{m}} + \frac{(\mathbf{r}-\boldsymbol{\alpha})}{p\hat{m}^3}[(\mathbf{r}-\boldsymbol{\alpha}):\mathbf{r}] \qquad \frac{\partial \mathbf{n}}{\partial s} = \frac{\mathbf{I}}{p\hat{m}} - \frac{(\mathbf{r}-\boldsymbol{\alpha})\otimes(\mathbf{r}-\boldsymbol{\alpha})}{p\hat{m}^3}$$

$$\frac{\partial \mathbf{n}}{\partial \boldsymbol{\alpha}} = \frac{-\mathbf{I}}{\hat{m}} + \frac{(\mathbf{r}-\boldsymbol{\alpha})\otimes(\mathbf{r}-\boldsymbol{\alpha})}{\hat{m}^3}$$

The differentiations of model parameters $Q(a, M, \text{and } k_2)$ *with respect to* $p, s, \text{and } \boldsymbol{\alpha}$

$$\frac{\partial Q}{\partial p} = -Q_c^* \frac{\partial \cos(3\theta)}{\partial \bar{\mathbf{r}}} : \frac{\mathbf{s}}{p^2} \qquad \frac{\partial Q}{\partial s} = Q_c^* \frac{\partial \cos(3\theta)}{\partial \bar{\mathbf{r}}} \frac{1}{p} \qquad \frac{\partial Q}{\partial \boldsymbol{\alpha}} = -Q_c^* \frac{\partial \cos(3\theta)}{\partial \bar{\mathbf{r}}}$$

$$Q_c^* = \frac{2c_e(1-c_e)Q_c}{[(1+c_e)-(1-c_e)\cos(3\theta)]^2}$$

$$\frac{\partial \cos(3\theta)}{\partial \bar{r}_{ij}} = \frac{9\sqrt{3}\bar{S}^2}{2\bar{J}^4}\left(\frac{\bar{J}}{3\bar{S}^2}\bar{\mathbf{r}}_{ik}\bar{\mathbf{r}}_{kj} - \frac{\bar{S}}{2\bar{J}}\bar{\mathbf{r}}_{ij}\right)$$